2023-12-01

Enhancing Damage Tolerance Of The Constituents Of Sandwich Composites

Zackery Nieto
University of Texas at El Paso

ENHANCING DAMAGE TOLERANCE OF THE CONSTITUENTS OF SANDWICH COMPOSITES

ZACKERY RYAN NIETO

Doctoral Program in Mechanical Engineering

APPROVED:

Alejandra Castellanos, Ph.D., Chair

Md Mahamadur Rahman, Ph.D.

David Roberson, Ph.D.

Joel Quintana, Ph.D.

Stephen L. Crites, Jr., Ph.D.
Dean of the Graduate School

ENHANCING DAMAGE TOLERANCE OF THE CONSTITUENTS OF SANDWICH COMPOSITES

by

ZACKERY RYAN NIETO

DISSERTATION

Presented to the Faculty of the Graduate School of

The University of Texas at El Paso

in Partial Fulfillment

of the Requirements

for the Degree of

DOCTOR OF PHILOSOPHY

Department of Mechanical Engineering

THE UNIVERSITY OF TEXAS AT EL PASO

December 2023

Acknowledgements

I would like to thank my adviser, Dr. Alejandra Castellanos from the Aerospace and Mechanical Engineering Department at the University of Texas at El Paso, for her guidance, patience, and constant help throughout my journey.

I would like to thank my friends and family for their support and understanding over the years. Thank you from the bottom of my heart.

Abstract

Composite structures have become a lucrative material choice for researchers throughout various sectors such as green energy, arctic travel, and aerospace application due to their light weight, high-bending to stiffness ratio, and job tailorable applications through material selection. With the increasing demand for new and better composite technologies growing each year it is imperative to investigate new materials and analytical options to help the composite field as a whole grow. In this report various materials and statistical applications have been studied regarding the constituent materials in sandwich composites. For core materials an additive manufactured photoreactive resin has been characterized for quasi-static properties at room and arctic temperature to pave the road for future geometric core implementations designed for arctic naval transportation. Uncertainty quantification has been applied to attach a statistical representation to vinyl-ester resin matrix systems to highlight influential parameters towards impact damage. Several systems of interlaminar reinforcement have been studied in the forms of Kevlar® pulp and vertically aligned carbon nanotubes (VACNT) in an effort to increase the damage tolerance within composite systems. Kevlar® pulp studies investigated the impact damage mitigation at room and arctic temperatures and a brief review was performed on the current state of vertically aligned carbon nanotube interlaminar reinforcement technologies.

Table of Contents

List of Tables

List of Figures

Chapter 1: Quasi-Static Properties of Photoreactive Resin at Arctic Temperatures

INTRODUCTION

Over the years, massive melting of the Arctic Circle has opened new naval passages [1] respectively increasing naval travel for resource procurement, tourism, and fishing [2, 3]. However, navigating these Arctic waters poses substantial challenges for naval ships, including exposure to harsh environmental conditions such as corrosive saltwater [4], ice debris hazards [5], and extreme cold with temperatures plunging as low as -60°C [6]. These conditions can lead to the degradation of chemical and mechanical properties, jeopardizing the structural integrity and safety of naval structures [7]. These inhospitable conditions have the capacity to trigger the degradation of the chemical and mechanical properties of naval structures, thereby imperiling their structural integrity and safety. Consequently, the materials utilized in naval structures must meet the dual mandate of resilience in the face of Arctic harshness while preserving their mechanical attributes. In response to these formidable requirements, sandwich composites have emerged as a compelling solution for naval structures. These composites offer an array of advantages, marked by their lightweight nature, high stiffness-to-weight ratio, and an impressive strength-to-weight ratio [8]. At their core, sandwich composites comprise two thin yet remarkably stiff face sheets, responsible for carrying in-plane and bending forces [9], and a lightweight core tasked with managing the transverse loads [10].

Emphasizing the vital role of the core material, it stands as an essential element in sandwich composites, profoundly influencing the overall performance of the composite structure while working collaboratively with the face sheets. Over the years, a great deal of research has covered a variety of traditional core materials, wood, cork, polymeric foam, and syntactic foam. Wood cores have been studied using balsa [11]–[18], beech [19], birch [20], oak [21], plywood [22], and

spruce [23], [24]. Wood cores offered economical renewable resource which observes in increase in mechanical properties at lower temperature resulting from hardening of the wood cell walls and stabilization of the crystalline structure [25]–[27], however the mechanical properties severely decreased in the presence of water moisture ingress softening the wooden cells [28]. Cork cores [16], [29], [30] were studied as another alternative for a renewable resource material. Cork cores observed an increase in mechanical properties at lower temperatures resulting from the embrittlement effect and stiffening of the crystalline arrangement [31]. The cork cores, however, suffer a decrease in mechanical properties when influenced by water due to plasticizing of the cork caused by water molecules [32]. Polymeric foam cores have been studied using polyester (PES) [33], polyethylene terephthalate (PET) [34], phenolic [35], polyimide (PIF) [36], polymethacrylimide (PMI) [37], [38], polypropylene [39], polyurethane (PUF) [40]–[56], and polyvinyl chloride (PVC) [57]–[75] due to their good corrosion resistant properties [33], light weight, and low water absorption [36]. The lower temperatures increased the mechanical properties of the foam core by stiffening the polymer cellular structure, however the embrittlement of the cellular structure resulted in foam breakage and crushing of the foam through deformation during loading and recovery/relaxation during unloading. Syntactic foam cores are formed using hollow particles or particulates dispersed within a matrix system. Studies have been conducted using various materials to develop these cores, such as Aluminum [76]–[78], cenospheres (fly ash) [67], [79]–[81], and hollow-glass [82]–[84], due to their tailor-made properties. Syntactic foams behaved similarly to polymeric foams under low temperature conditions, where an increase in mechanical properties is observed from the stiffened cell walls, but with the introduction of catastrophic failure induced by the embrittlement of the foam with no signs of deterioration before failure occurs [81].

Outside of the traditional core materials, wood, cork, and foams, there has been a great interest in studying new material selections utilizing alternative core geometries. The new functional cores aim to reduce the overall weight of the core material [85] while maintaining/enhancing mechanical performance [86] through geometric designs. Studies investigating alternative core geometries have been performed using Nomex fibers [87]–[93], ABS plastic [94]–[96], acrylic [97], ASA plastic [96], carbon fiber [98], [99] cardboard [100], ceramic resin [101], E-Glass [102], Jute [103], PC plastic [95], PLA plastic [104]–[107], polyester [108], [109], shape memory polymers [110], Silicon Carbide (SiC) [111], [112], Titanium alloy [113], and tough nylon resin [99]. Using these materials, researchers have investigated studies using core geometries based on simpler designs such as, honeycomb cells [114]–[117] and pyramidal truss lattices [118]–[123], and novel designs such as auxetic lattices [124]–[130]. Simpler designs like honeycomb and pyramidal truss lattice cores are implemented to reduce the core weight while improving stiffness-to-weight ratios, and mechanical properties of the composite [119], [131]–[138] More complex designs like the novel auxetic lattice studies aim to develop multi-purposed structures which can increase mechanical properties [139]–[142], enhance acoustic dampening [143], and increase energy absorption [144] resulting from its geometric design inciting a negative Poisson's ratio [145]–[149].

While the arctic influence on the alternative geometry core studies is limited compared to traditional cores, the potential for use has been reported for simpler geometries. Li et al. [98] studied the influence of varying temperatures on mechanical properties for composite sandwich panels with pyramidal lattice truss cores (CSPPLTC). Shear tests and out-of-plane compression tests were performed in a range of temperatures from -90 °C to 180 °C using carbon fiber/epoxy systems for the face sheets and core. Their results illustrated an increase in compressive modulus

and strength at low temperature by 9.48% and 14.23% when compared to room temperature, and an increase to shear modulus and strength by 10.94% and 11.02% respectively when compared to room temperature. In the low temperature environment brittle failure was observed within the composite truss and is appropriated to the molecular chain mobility within the matrix being hindered by the lower temperature.

St-Laurent et al. [91] performed compression after impact (CAI) studies on carbon epoxy composite sandwich panels with Nomex honeycomb cores at 25 °C, -70 °C, and -150 °C. Striker size and mass consisted of different combinations of 12.7 mm and 25.4 mm diameter and 5 kg, 10 kg, and 20 kg mass to simulate various damage types and sizes. Their findings concluded that while the lower temperature resulted in more induced damage, the overall influence temperature had on compressive strength was negligible.

As the limitations of traditional core materials are increasingly evident, and the potential of new core materials are emerging through geometric modification exhibited by simpler geometries, additive manufacturing (AM) emerges as an attractive avenue for the development of lightweight composite cores using more complex novel designs. AM processes, such as fused deposition modeling (FDM) and selective laser melting (SLM), offer the advantages of intricate core designs and a broad array of material choices [108]. Nevertheless, they are not without their challenges, including issues related to layer adhesion, thermal warping, and geometric irregularities, which necessitate careful consideration in the when manufacturing AM cores [150], [151]. Stereolithography (SLA), however, selectively cures photopolymer resins using UV light, creating a chemical bond between layers. This process diverges from traditional additive manufacturing techniques, such as FDM and SLM, which rely on heat. The reduction of layer

adhesion issues, material shrinkage, and warping presents an appealing prospect for photopolymer resins application towards complex core geometries [94].

This study aims to evaluate the potential of a photopolymer resin known as "Durable resin" as a core material for sandwich composites in Arctic conditions. Specimens were manufactured through SLA and tested to assess their quasi-static responses, including tensile, flexural, and compressive behaviors, at both room temperature (25°C) and Arctic temperature (-60°C). The investigation delves into the variations in mechanical properties due to temperature changes, examining modulus, strengths, and strain at failure. Finite element computational models were employed to predict the quasi-static responses of the Durable resin under different temperatures and validated against experimental data.

METHODS

This section discusses the specimens' manufacturing system, material selection, specimens' fabrication process, and test methods.

Manufacturing System

Specimens were manufactured using the SLA AM process using Formlabs' Form 3 printer operating with uses UV light to selectively cure the photopolymer resin, developing polymer networks through a chemical process. When photoreactive resins are exposed to UV light, the molecular chains join together, polymerizing monomers and oligomers into solidified parts [49]. Form 3 SLA printing machine is illustrated in Figure 1.1 and has the following components: a) resin cartridge, b) resin tank, c) UV permeable layer, and d) build platform. The resin cartridge stores the photopolymer resin. The resin tank is transparent with a UV permeable layer. UV beams that are always perpendicular to the building platform are delivered to the resin through the UV permeable layer. The resin cartridge transfers the resin to the resin tank through a slow drip

method. Once the resin tank is completely filled with resin, the manufacturing process begins. First, the building platform lowers to the resin tank, and a UV light selectively cures the resin into the building platform. Once a layer has been cured, the building platform raises, and a mixing rod slides across the resin in the resin tank to level the resin for the next layer, so there is uniformity between the print layers. This process prevents geometric irregularities that are observed in the FDM process. The building platform lowers, and the next layer is cured and chemically adhered to the previously cured layer. This process is repeated until all the layers are cured.

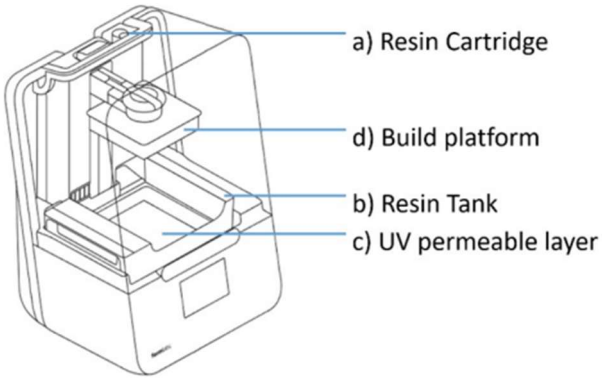

Figure 1.1 Formlabs Form 3 SLA Printer [152]

Material Selection

The core material for sandwich structures must meet specific criteria, including being lightweight and capable of withstanding mechanical loadings such as tension, flexural, and compression, even at extremely low temperatures (e.g., -60 °C). Among the various resins offered by FormLabs, Durable resin emerged as the optimal choice. Table 1.1 highlights its remarkable impact properties, significantly outperforming all other FormLabs resins, with impact strengths averaging 4.5 times higher.

Table 1.1 FormLabs Resin Properties [152]

Resin	Tensile Strength (MPa)	Flexural Strength (MPa)	Notched IZOD (J/m)
Durable	28	24	114
Tough 1500	33	39	67
Tough 2K	46	65	40
Rigid 10K	65	126	16
Rigid 40K	69	105	23
Grey Pro	61	86	19

Specimen Fabrication

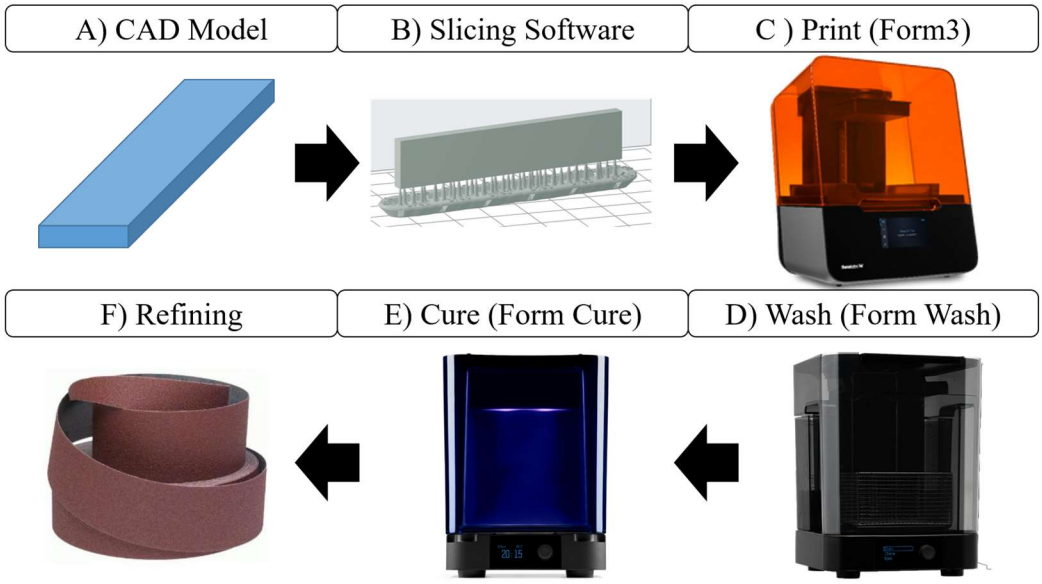

Figure 1.2: Specimen Flowchart: A) CAD Model, B) Slicing Software, C) Form 3, D) Form Wash, E) Form Cure, and F) Refining.

Figure 1.2 illustrates the specimen fabrication process. A) Specimens were designed using Autodesk Fusion 360 computer-aided design (CAD) software and saved as STL files. B) STL files were imported into FormLabs' "PreForm" slicing software to select printing parameters. The orientation of the models aimed to maximize specimen quantity per print run, as preliminary testing revealed isotropic behavior of Durable resin. A resolution of 50 microns, the slowest yet most accurate option recommended by the manufacturer, was used. Default support structures

generated by the software were employed to ensure uniformity. C) Specimens were 3D printed using a Form 3 SLA printer. Following printing, specimens were washed and cured in a UV bath to optimize their mechanical properties. D) Specimens, along with their supports, were removed from the build plate and placed in the "Form Wash." Here, specimens underwent a 20-minute agitation bath in a 90% isopropyl alcohol (IPA) solution, as per FormLabs' recommendations. E) After excess resin removal and drying, specimens were transferred to the "Form Cure," where they were subjected to a 60-minute UV bath at 60°C, following FormLabs' guidelines. Once cured, the specimens were cooled to room temperature (RT) for post-processing. F) During post-processing, supports were cautiously removed from specimens using flat-edged clippers to prevent damage. Subsequently, specimens were sanded with 80-grit, 120-grit, 220-grit, and 400-grit sandpaper to meet the dimensions required by the relevant ASTM standards. Specimens were randomly divided into two groups: one for testing at RT and the other for testing at AT. A total of 35 specimens were manufactured for tensile testing, 20 for compression, and 10 for flexural testing.

Tensile Testing

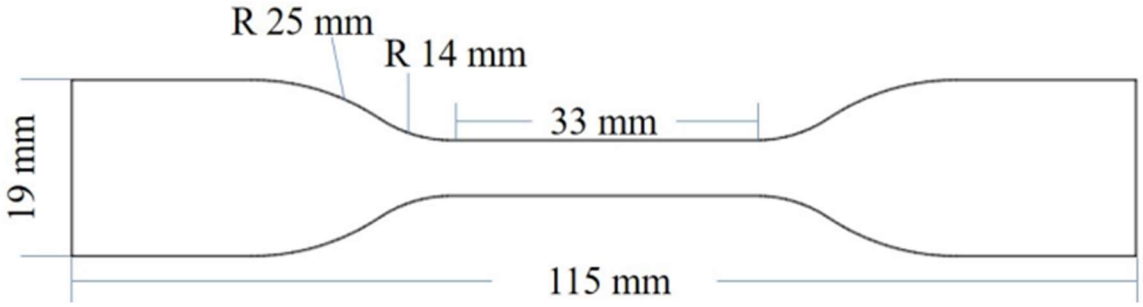

Figure 1.3: Tensile Specimen Type IV

Tensile tests were conducted at both room temperature (RT) and Arctic temperature (AT). The tensile specimens were designed in compliance with ASTM standard D638-14: "Standard Test Method for Tensile Properties of Plastics" [153]. As shown in Figure 1.3, the type IV tensile specimen featured overall dimensions of 115 mm in length, 19 mm width at the grip section, 33 mm in length, 6 mm width at the narrow section, and a thickness of 4 mm.

Tensile testing was conducted using an Instron 5969 universal testing apparatus equipped with a 50 kN load cell. A consistent crosshead rate speed of 5 mm/min was maintained for both RT and AT testing. Physical Epsilon 25365 extensometers with a 25.4-mm gauge length were attached to the specimens to measure strain. The BlueHill software managed data acquisition, recording displacement, load, strain, and time.

A total of 35 specimens were manufactured for tensile testing. Of the 35 specimens, 25 were designated for preliminary orientation tests at room temperature, and 10 specimens were designated for temperature tests according to the optimal orientation identified from the preliminary study. Temperature studies were conducted using five samples subjected to testing at RT, while the remaining five were tested at AT.

Printing Orientation

In the realm of SLA printing, it is crucial to emphasize that, in comparison to FDM and SLM, SLA boasts superior printing resolution, demonstrating notable reductions in material shrinkage, geometric irregularities, and warping. Although there exists literature exploring the impact of build orientation on SLA components [154]–[157], investigations specifically dedicated to durable resin have been constrained to single-axis rotation tests, yielding conflicting outcomes. Researchers have labeled the material as both anisotropic [158] and isotropic [159]. In this study, initial tests were conducted to ascertain optimal printing orientations, laying the foundation for guiding the manufacturing design of subsequent experiments.

Five tensile specimens were printed at five different orientations: 0° flat, 0° vertical, 45° flat, 90° flat, and 90° vertical, as illustrated in Figure 1.4 to determine isotropic or anisotropic tendencies. Isotropy was defined using the 95% confidence interval (CI) method [95] to statistically determine whether the tensile properties showed significant differences attributed by the change in print orientation.

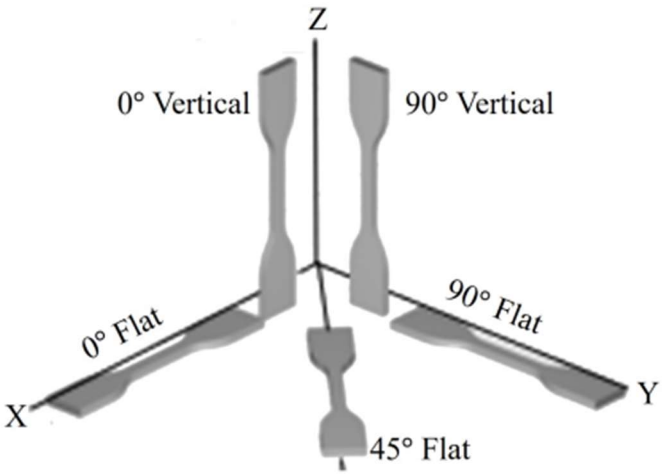

Figure 1.4: Print Orientations of Durable Resin for the Preliminary Tensile Orientation Study

Environmental Conditioning

The specimens tested at room temperature (RT) did not require any specific environmental conditioning. In contrast, the specimens designated for testing at Arctic Temperature (AT) underwent a specific preparation procedure. These AT specimens were placed in plastic bags to prevent moisture buildup on the surface and stored within an on-site ThermoScientific chiller (TSU 600) maintained at -60°C for a duration of 48 hours, ensuring that the specimens reached the desired test temperature.

For the actual testing, a temperature-controlled environmental chamber (Instron 3119-609) was connected to the Instron 5969 universal testing apparatus equipped with a 50 kN load cell. The environmental chamber was conditioned for 30 minutes using Liquid Nitrogen (LN2) to achieve and maintain a temperature of -60°C before testing commenced. A total of five specimens were tested, following the guidelines of ASTM D638-14 [153].

Flexural Testing

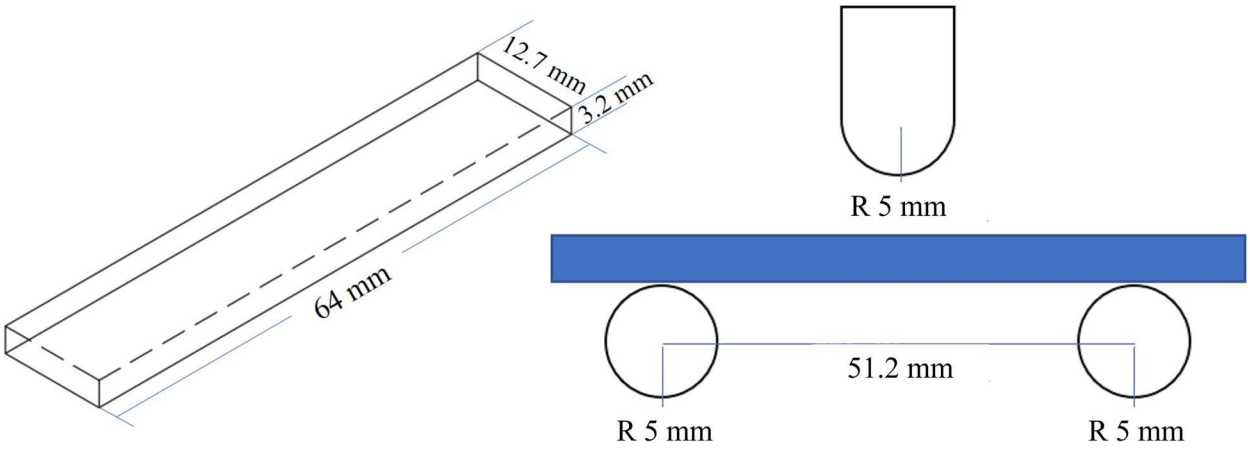

(a) Flexural Specimen Dimensions (b) Flexural Fixture Dimensions

Figure 1.5: Design and Dimensions for Flexural Specimen and Flexural Testing

Flexural testing was conducted at both room temperature (RT) and Arctic Temperature (AT). The flexural specimens were designed in accordance with the ASTM D790 – 17 standard, titled "Standard Test Methods for Flexural Properties of Unreinforced and Reinforced Plastics and Electrical Insulating Materials" [160]. The rectangular flexural specimens featured dimensions of 12.7 mm in width, 64 mm in length, and a thickness of 3.2 mm, as depicted in Figure 1.5a. The span length between supports was set at 51.2 mm, as illustrated in Figure 1.5b. For the flexural tests, an Instron 5969 universal testing apparatus equipped with a 50 kN load cell was employed. A preliminary study with an initial crosshead rate of 1.3 mm/min was tested based on specimen geometry and in accordance with the ASTM D790-17 [160] (Procedure A). During testing, the specimen the specimen is deflected until rupture or until a maximum flexural strain of 5% is reached, whichever occurs first. However, as specimen failure did not occur within the 5% flexural strain range, a faster crosshead speed was required. The crosshead rate speed was set to 13 mm/min, following Procedure B outlined in ASTM D790-17 [160], and was consistent for both RT and AT tests.

During testing, the data acquisition system recorded displacement, load, and time, all of which were managed through the BlueHill software. In total, ten specimens were tested, with five tested at RT and five tested at AT.

Environmental Conditioning

For the specimens tested at Arctic Temperature (AT), a specific environmental conditioning procedure was followed. The specimens were placed in plastic bags to prevent moisture buildup on the surface, and then stored in an on-site ThermoScientific (TSU 600) chiller maintained at -60 °C for a period of 48 hours prior to testing. To facilitate testing at the designated Arctic temperature, a temperature-controlled environmental chamber (Instron 3119-609) was connected to the Instron 5969 testing apparatus. The environmental chamber underwent a 30-minute pre-conditioning process with Liquid Nitrogen (LN2) to reach the desired temperature of -60 °C. The preconditioning time was selected as a result from preliminary studies showing thermal equilibrium was reached by the environmental chamber within 30 minutes.

A total of 5 specimens subjected to Arctic Temperature conditions were tested in accordance with the ASTM D790-17 Procedure B.

Compression Testing

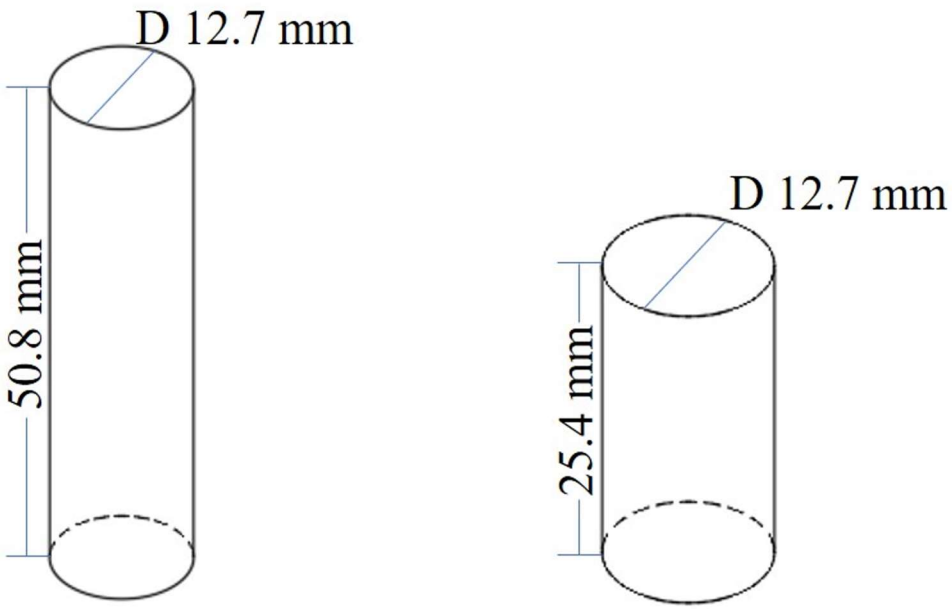

(a) Compressive Modulus Dimensions (b) Compressive Strength Dimensions

Figure 1.6: Specimen Dimensions for Compressive Modulus and Compressive Strength Tests

Compression tests were conducted at both Room Temperature (RT) and Arctic Temperature (AT). As per the ASTM D695-23 standard, "Standard Test Method for Compressive Properties of Rigid Plastics" [161], two distinct specimen types were employed to determine the compressive modulus and strength. The cylindrical specimen used to measure the compressive modulus had dimensions of 12.7 mm in diameter and 50.8 mm in length, as depicted in Figure 1.6a. For measuring compressive strength, a cylindrical specimen with dimensions of 12.7 mm in diameter and 25.4 mm in length, as shown in Figure 1.6b, was utilized.

The tests were carried out using an Instron 8801 Servohydraulic fatigue testing system, equipped with compression plates and a load capacity of 100 kN. A consistent crosshead rate speed of 1.3 mm/min was maintained for both RT and AT tests.

Compressive modulus and strength were computed based on the results from five specimens for each scenario. The Instron machine's data acquisition system recorded key parameters, including displacement, load, strain, and time, through the WaveMatrix software. A total of 20 specimens were tested, with ten specimens at RT and ten specimens at AT, five for assessing compressive modulus and five for measuring compressive strength.

Environmental Conditioning

For the compression tests, specimens evaluated at Room Temperature (RT) did not necessitate any special environmental conditioning. However, those specimens intended for testing at Arctic Temperature (AT) were subjected to a specific preparation process. Specimens designated for AT testing were securely sealed in plastic bags to prevent moisture buildup on the surface, and stored within an on-site ThermoScientific (TSU 600) chiller at a temperature of -60 °C. These specimens were kept in these conditions for an extended period of 48 hours prior to testing to ensure they reached the desired temperature.

To execute the tests at the extreme AT, a temperature-controlled environmental chamber was connected to the Instron 8801 testing machine. This chamber was methodically conditioned

for a duration of 30 minutes using Liquid Nitrogen (LN2) until the target temperature of -60 °C was consistently achieved, ensuring an accurate and controlled testing environment.

EXPERIMENTAL RESULTS AND DISCUSSION

The displacement, load, strain, and time data were used to characterize the tension, flexural, and compression behavior of the Durable resin at RT and AT.

Tensile Tests

The data collected, including displacement, load, strain, and time, served as the basis for characterizing various mechanical properties of the specimens at both Room Temperature (RT) and Arctic Temperature (AT). The properties analyzed included the modulus of elasticity, tensile yield stress, ultimate tensile stress, and strain at failure for samples tested under these different conditions.

The discussion will begin by examining the influence of the printed orientation on the specimens' behavior, followed by an exploration of the effects of temperature variation, and an analysis of the observed failure mechanisms.

Orientation Influence

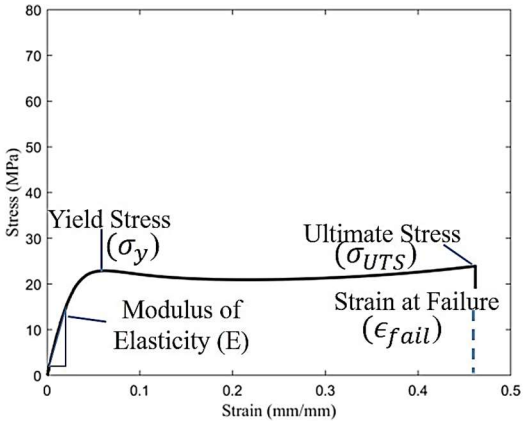

Figure 1.7: Representative Tensile Stress-Strain Graph of Durable Resin at RT

Figure 1.7 provides a typical stress-strain curve for Durable resin at room temperature, depicting the material's behavior under tensile loading. Several key mechanical properties were derived from this curve. Modulus of Elasticity (E): Calculated from the linear segment of the stress-strain curve. Yield Stress (σ_y): Identified at the point where the material first exhibits increased strain without a corresponding increase in stress. Ultimate Tensile Strength (σ_{UTS}): Determined as the maximum stress reached in the test. Strain at Failure (ε_{fail}): Measured at the point of specimen fracture. Each of these properties were evaluated for all the different printing orientations using the 95% confidence interval (CI) method. The 95% CI was determined for each test by finding the standard deviation of the measured properties, respective to their print orientation. The margin of error, corresponding to 95% of the area under a normal distribution, was calculated by multiplying the standard deviation by the critical value of 1.96. This margin of error was then added and subtracted from the respective orientation property sample mean to construct the 95% CI. Table 1.2 provides a summary of the Durable resin's tensile properties, demonstrating that the properties displayed isotropic behavior and mostly fell within a 95% confidence interval. The respective 95% CI ranges are as follows: E: 750 - 801 MPa, σ_y: 22.2 - 23.2 MPa, σ_{UTS}: 24.2 - 25.1 MPa, and ε_{fail}: 0.448 - 0.489.

Table 1.2: Durable Resin Tensile Mechanical Properties (with 95% CI) at RT

Orientation	0° Flat	0° Vertical	45° Flat	90° Flat	90° Vertical
E (MPa)	783 ± 21	759 ± 53	789 ± 46	795 ± 48	755 ± 24
σ_y (MPa)	22.9 ± 0.71	21.5 ± 0.77	22.9 ± 0.81	23 ± 0.55	23.2 ± 0.67
σ_{UTS} (MPa)	24.1 ± 1.0	25.4 ± 0.81	24.6 ± 1.4	24.9 ± 0.92	24.5 ± 0.56
ε_{fail} (%)	44.9 ± 4.1	51.3 ± 2.3	44.9 ± 4.1	47.2 ± 1.7	46.9 ± 1.5

The evaluation of the different printing orientations revealed the following. Modulus of Elasticity (E): There was no statistically significant difference among the print orientations (meaning all the representative means for each orientation behaved in the 95% CI range [162]).

The 90° flat specimens exhibited the highest value, but this was only about 5% higher than the lowest modulus observed in the 90° vertical specimens.

Tensile Yield Strength (σ_y): The yield strength did not show a clear correlation with orientation. The 0° vertical and 90° vertical specimens had the lowest and highest values, respectively. The difference in yield strength between the 90° vertical and 90° flat specimens was less than 1%.

Ultimate Tensile Strength (UTS): The UTS also did not exhibit a statistically significant difference between print orientations, as all values were within the confidence interval.

Strain at Failure: The most significant difference was observed in the strain at failure, with 0° vertical specimens showing an average strain at failure of 0.513 ± 0.023, while 0° flat specimens had an average of 0.449 ± 0.041. However, with average strain to failure overlapping within 10% of the total average between tests [163] and no clear designation correlating to the vertical versus flat orientations (90° vertical specimens having a lower strain to failure than 90° flat specimens), this difference should not be attributed to print orientation influences [162].

In summary, the results, as detailed in Table 1.2 and illustrated in Figure 1.8 for tensile testing at room temperature, indicate that Durable resin exhibited isotropic behavior, and print orientation had minimal influence on its mechanical properties. Therefore, for all subsequent tensile, flexural, and compressive tests at both room temperature and Arctic temperature, specimens were printed in a single orientation.

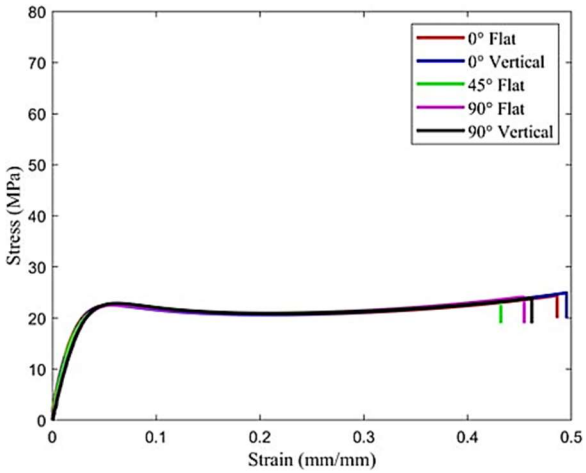

Figure 1.8: Representative Tensile Stress-Strain Graph of Durable Resin at RT for each Tested Orientation

Arctic Temperature Influence

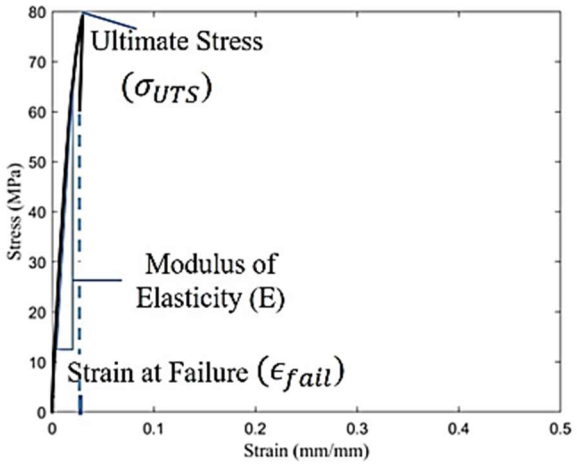

Figure 1.9: Representative Tensile Stress-Strain Graph of Durable Resin at AT

The stress-strain curve shown in Figure 1.9 illustrates the typical behavior of the Durable resin specimens at AT. At Arctic temperatures (AT), all the specimens exhibited brittle failure, illustrated by an increase in modulus and strength with a decrease in strain to failure, which is a characteristic of materials at low temperatures. The mechanical properties of the Durable resin specimens at Arctic temperatures are summarized in Table 1.3. The modulus of elasticity (E), ultimate tensile strength (σ_{UTS}), and strain at failure (ε_f) were calculated for the AT specimens.

Table 1.3: Tensile Mechanical Properties of Durable Resin at AT

E (MPa)	2500 ± 215
σ_{UTS} (MPa)	80.1 ± 1.6
ε_f (%)	3.23 ± 0.3

Comparison between Room and Arctic Temperature

The mechanical properties of the specimens tested at Arctic temperatures (AT) demonstrated significant changes compared to those tested at room temperature (RT). The modulus of elasticity (E) increased by 318% for the AT specimens compared to the RT specimens. The ultimate tensile strength (σ_{UTS}) increased by 322% for the AT specimens compared to the RT specimens. The strain at failure ($\varepsilon_{\text{fail}}$) decreased by 93% for the AT specimens compared to the RT specimens.

These changes can be attributed to the increased rigidity and embrittlement of materials at Arctic temperatures [63]. The increase in modulus of elasticity and ultimate tensile strength indicates a more rigid response, while the significant decrease in strain at failure reflects the reduced ductility and increased brittleness of the material under low-temperature conditions.

Failure Analysis

The failure mechanisms of the specimens tested at both room temperature (RT) and Arctic temperatures (AT) were evaluated. Regardless of the printed orientation, the specimens tested at RT exhibited fractures at the midsection of the sample. Additionally, all these specimens showed a clean fracture in the plane perpendicular to the loading direction, as depicted in Figure 1.10. Similarly, the specimens tested at AT also experienced a clean fracture toward the center of the specimen, as shown in Figure 1.11. While the experimental results illustrated the Durable resin behaved in a ductile fashion at room temperatures, the consistent observation of clean fractures in both RT and AT specimens suggests that the material exhibits brittle failure characteristics at the time of rupture. This ductile-to-brittle transition is attributed to the lack of polymer chain mobility

at the time of rupture. During room temperature tests, as the specimen is placed under tensile loading the polymer chains progressively stretch during the linear-elastic region, begin to buckle after the yield stress, and eventually collapse at the time of rupture [164]. During the arctic temperature tests, the low temperature hinders chain mobility resulting in an earlier rupture [165]. In both cases, the lack of chain mobility at the point failure results in the brittle failure mechanisms [166] and illustrates the ductile-to-brittle transition [167].

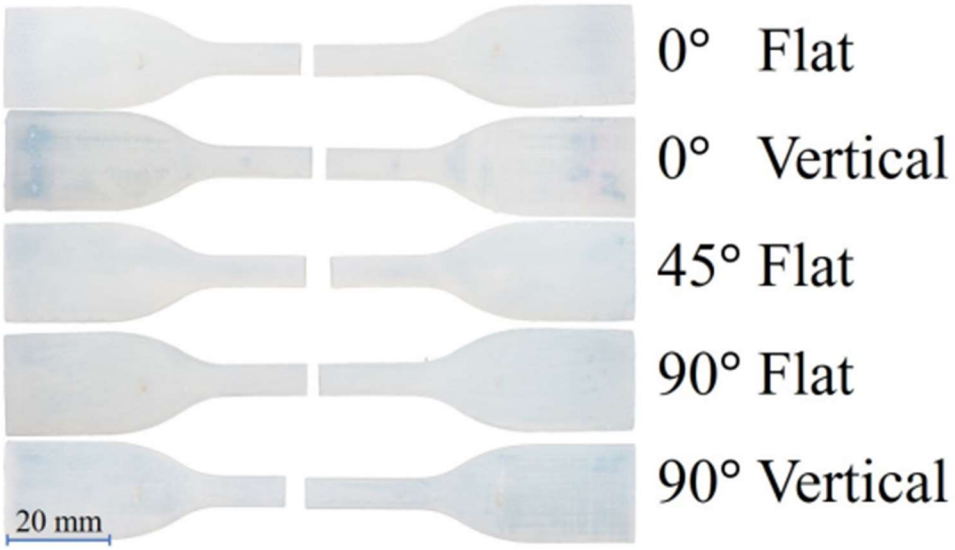

Figure 1.10: Typical Failure Mode of Durable Resin Tensile Specimens Tested at RT

Figure 1.11: Typical Failure Mode of Durable Resin Tensile Specimens Tested at AT

Flexural Tests

The displacement, load, and time data were used to characterize the flexural modulus, flexural strength, and strain at failure for RT and AT. The flexural stresses and strains were obtained with the following formulas:

$$Flexural\ Sress\ (\sigma_f) = \frac{3PL}{2bd^2} \quad (1)$$

$$Flexural\ Strain\ (\varepsilon_f) = \frac{6Dd}{L^2} \quad (2)$$

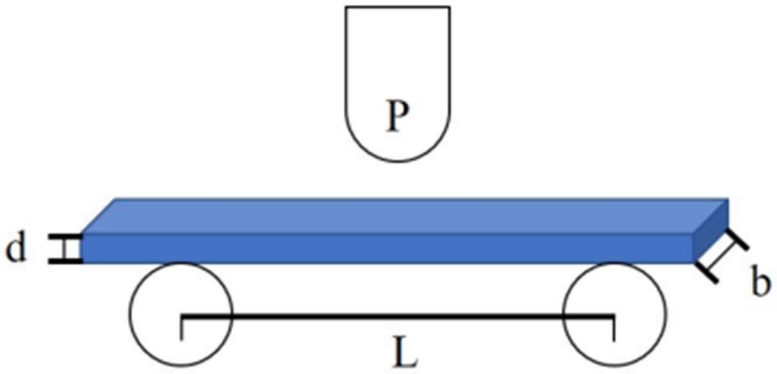

Figure 1.12: Free Body Diagram for Flexural Stress

Where P stands for load at a given point (N), L stands for support span (mm), b stands for the width of the beam (mm), d stands for the depth of the beam (mm), D stands for maximum deflection of the center of the beam (mm), illustrated in Figure 1.12. For both room and arctic temperature tests, specimens were loaded until rupture occurred, or a maximum flexural strain of 5% was reached, whichever occurred first according to the ASTM standards. The flexural response at RT will be discussed first, followed by the flexural response at Arctic temperature and failure mechanisms.

Room Temperature

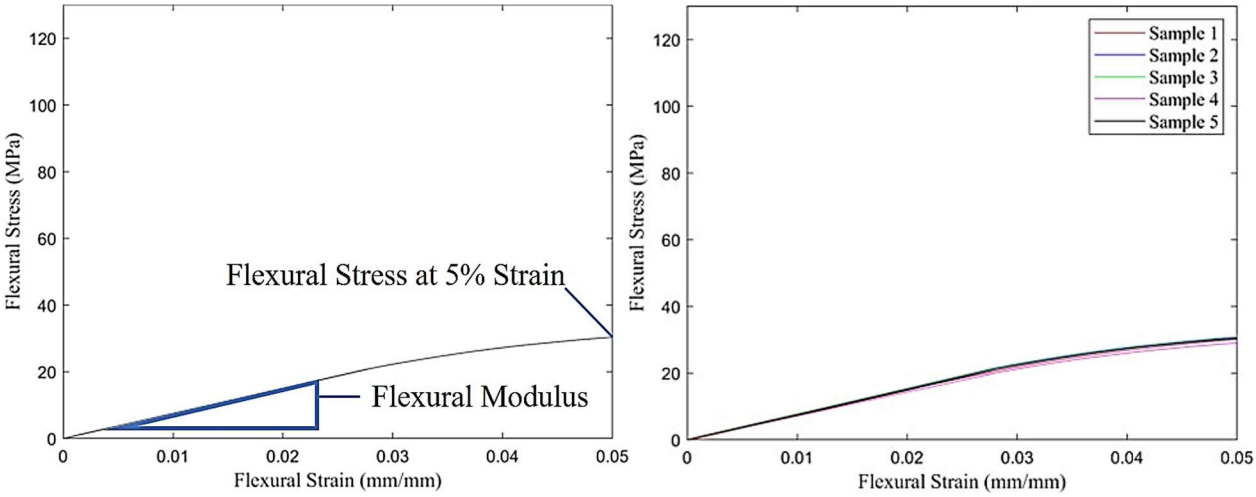

(a) Representative Flexural Stress-Strain Graph (b) Flexural Stress-Strain Test Results

Figure 1.13: Flexural Stress-Strain Relations for Durable Resin Tested at Room Temperature

Figure 1.13a shows a representative flexural stress-strain graph of Durable resin at room temperature (RT). The analysis for flexural properties, following ASTM D790-17 guidelines, focused on the 5% flexural strain region where testing ends because of rupture or reaches the 5% flexural strain limit. Figure 1.13b displays the results of the RT flexural tests, with flexural modulus, flexural strain, and flexural strength determined for each specimen tested. The flexural modulus was calculated from the linear portion of the stress-strain curve, and the flexural stress was calculated at the 5% flexural strain limit as rupture did not occur. The average flexural mechanical properties of the specimens tested at RT are summarized in Table 1.4.

Table 1.4: Flexural Mechanical Properties for Durable Resin Tested at RT

Flexural Modulus (MPa)	819.6 ± 21.6
Flexural Strength (MPa) at 5% Flexural Strain	30.3 ± 0.92

Arctic Temperature

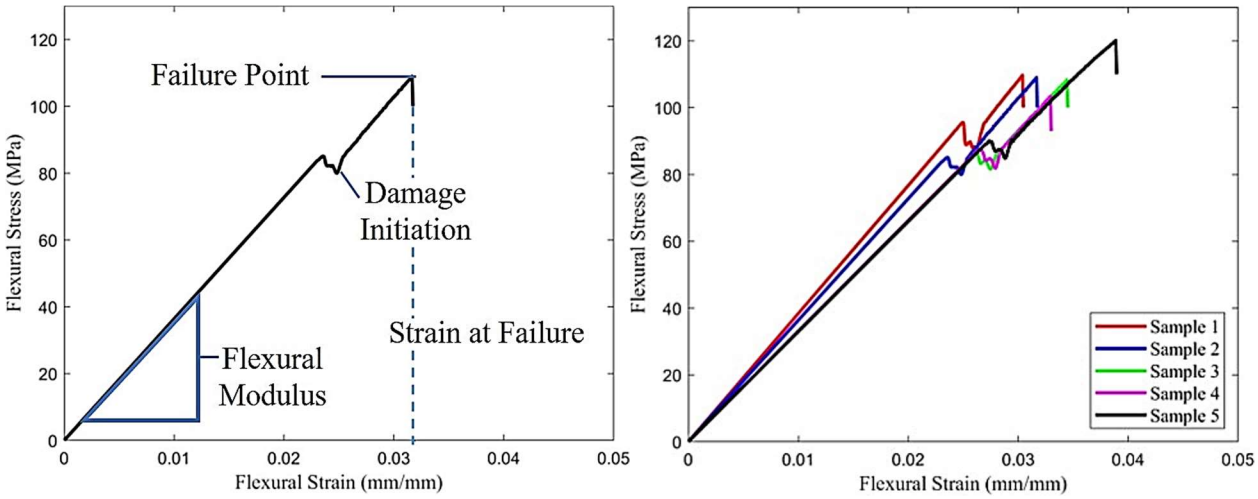

(a) Representative Flexural Stress-Strain Graph (b) Flexural Stress-Strain Test Results

Figure 1.14: Flexural Stress-Strain Relations for Durable Resin Tested at Arctic Temperature

Figure 1.14a depicts a representative flexural stress-strain graph of Durable resin at Arctic temperatures (AT). In the analysis of flexural properties following ASTM D790-17 guidelines, the focus was on the 5% flexural strain region, where testing ends at specimen rupture or flexural strain has reached the 5% limit. During arctic temperature tests, specimen rupture occurred before

reaching the 5% flexural strain limit. Figure 1.14b shows the results of the AT flexural tests, with the determination of flexural modulus, flexural strain, and flexural strength for each specimen tested. The flexural modulus was calculated from the linear portion of the stress-strain curve, the flexural stress was calculated at the maximum stress value, and the strain at failure was determined at specimen failure. Table 1.5 provides an overview of the average flexural mechanical properties of the specimens tested at AT.

Table 1.5: Flexural Mechanical Properties of Durable Resin Tested at Arctic Temperature

Flexural Modulus (MPa)	3690 ± 229
Maximum Flexural Strength (MPa)	110.4 ± 6.06
Maximum Flexural Strain (%)	3.37 ± 0.33

Comparison between Room and Arctic Temperature

When comparing room temperature and Arctic temperature (AT) tests, it should be noted that room temperature (RT) tests were concluded by reaching the 5% flexural strain limit, while AT tests were concluded upon specimen rupture. For comparative analysis, the RT data will use maximum stress observed during the 5% strain limit, while AT data will use maximum stress before failure. Under Arctic temperature conditions, the specimens exhibited increased stiffness but also became more brittle when compared to the specimens at room temperature. This shift is evident in the flexural modulus, which increased by approximately 450%, and the flexural strength, which increased by about 360%, for the AT specimens in comparison to the RT specimens. The AT specimens had a failure strain of approximately 3.37%, while the RT specimens did not experience any breakage.

Failure Analysis

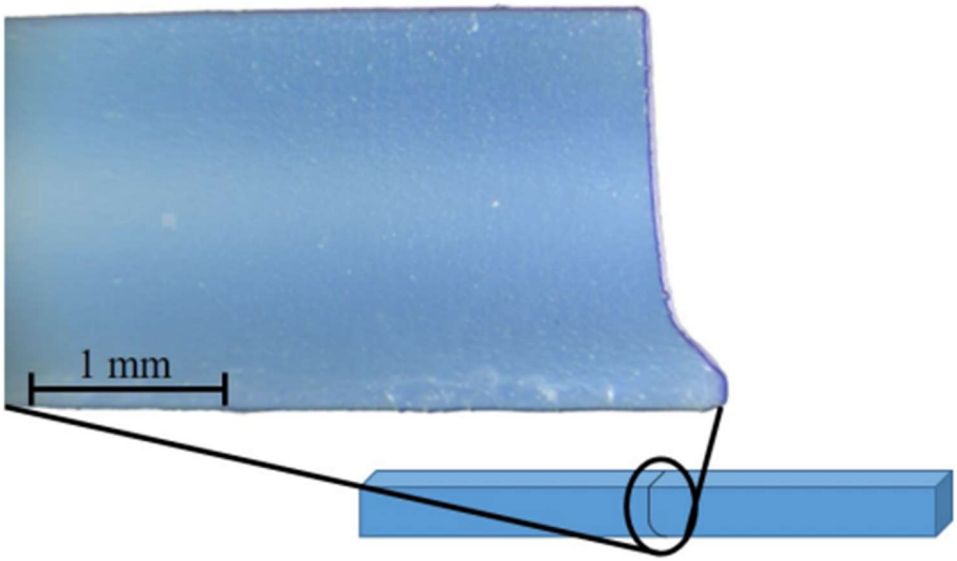

Figure 1.15: Representative Arctic Temperature Flexural Test Failure (Side View)

At room temperature (RT), the flexural specimens did not exhibit yielding or failure before the 5% flexural strain limit was reached. Following testing, the specimens were observed to return almost identically to their original pre-loading state, demonstrating no noticeable changes, damage, or permanent deformation.

In contrast, the flexural specimens subjected to Arctic temperatures (AT) consistently demonstrated a brittle failure mechanism in all tests. AT Specimens observed an increase to flexural strength and modulus with a decrease to flexural strain as failure occurred within the 5% flexural strain limit. The failure was attributed to the development of a crack on the face opposite to the loading plane where tensile forces were dominant, resulting in the formation of a shear lip [168]–[170] followed by a smooth break iconic with brittle failure. Notably, every AT flexural specimen displayed this distinctive midsection crack and shear lip, as depicted in Figure 1.15.

Compression Tests

The displacement, load, strain, and time data were used to characterize the compressive modulus and strength at RT and AT.

Compressive Modulus Tests

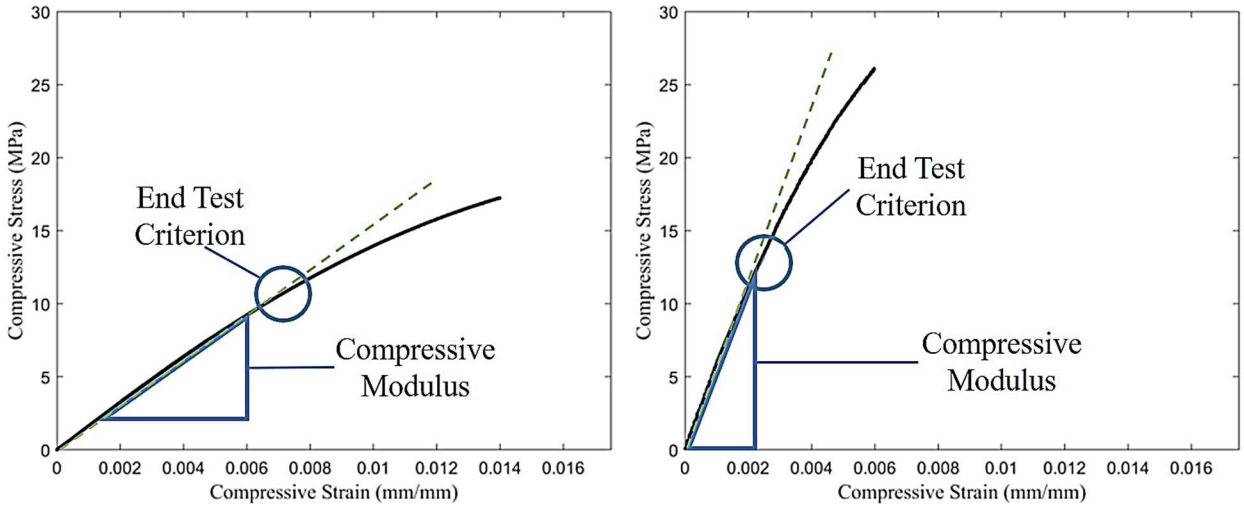

(a) Room Temperature Compressive Modulus (b) Arctic Temperature Compressive Modulus

Figure 1.16: Representative Compressive Stress-Strain Graphs of Durable Resin Tested at Room and Arctic Temperature (Compressive Modulus)

Figure 1.16 depicts the representative compressive stress-strain graphs of Durable resin at both room temperature (RT) 1.16a, and Arctic temperatures (AT) 1.16b. For both temperature conditions, the end criterion for the modulus test was defined as the shift from the linear elastic region, illustrated by the deviation from the initial linear slope, as specified in ASTM D695. Table 1.6 provides data on the RT and AT compressive modulus. As anticipated, the compressive modulus at AT increased compared to the RT values.

Table 1.6: Compressive Modulus Properties of Durable Resin at Room and Arctic Temperature

	RT	AT
Compressive Modulus (MPa)	1100 ± 300	5100 ± 220

Compressive Strength Tests

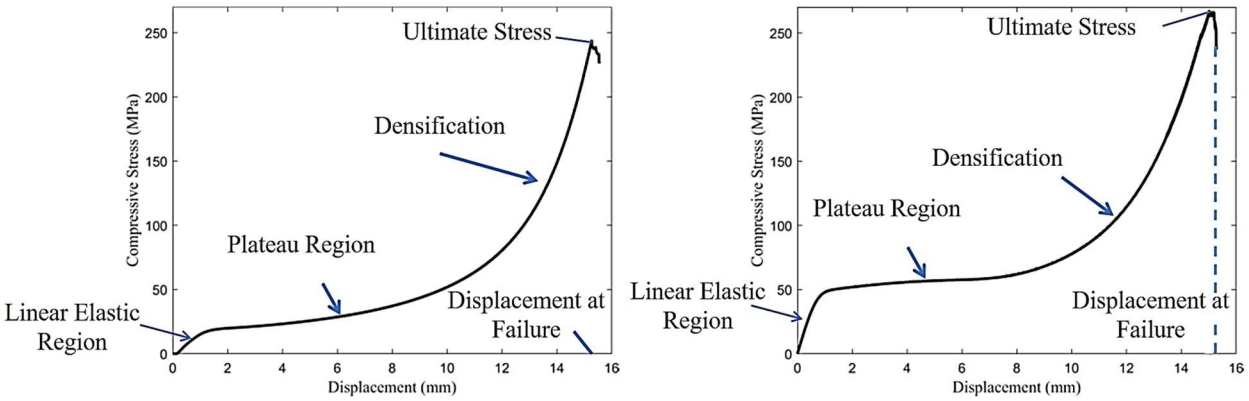

(a) Representative: RT Strength Test (b) Representative: AT Strength Test

Figure 1.17: Representative Stress-Displacement Graphs of Durable Resin Tested at Room and Arctic Temperature (Compressive Strength)

The displacement, load, strain, and time data were utilized to characterize the strength of Durable resin at both room temperature (RT) and Arctic temperatures (AT). Figure 1.17 presents a representative compressive strength stress-displacement graph for Durable resin at RT (Figure 1.17a) and AT (Figure 1.17b). The observed trends in these graphs suggest that the polymer chains, acted similar to universal joints [171], exhibit behavior like that of cells in polyurethane and elastomeric foams [57], [172]. This suggests that Figure 1.17a and Figure 1.17b illustrate different regions: a linear elastic region controlled by the stretching of polymer chains, a plateau region governed by elastic buckling and polymer chain collapsing, and a densification region caused by the majority of polymer chains collapsing, leading opposing chains to come into contact and compressing the solid, rapidly increasing the stress [172]. During the compressive strength tests, stress-displacement data were collected to determine the maximum compressive stress before failure, which corresponded to the maximum stress on the graph, and the displacement at failure, identified as any sharp decrease in load, as recommended by ASTM D695. Table 1.7 displays the average values for maximum compressive stresses and displacements at failure for the specimens tested at both RT and AT.

Table 1.7: Compressive Strength Properties of Durable Resin at Room and Arctic Temperature

	RT	AT
Max Compressive Stress (MPa)	243 ± 31	250 ± 25
Displacement at Failure (mm)	15.3 ± 0.4	15.4 ± 0.3

Comparison between Room and Arctic Temperature

The compressive modulus and strength at AT increased by approximately 460% and ≈3%, respectively, compared to RT. However, the displacement at failure decreased by ≈0.5% when compared to RT. This behavior can be attributed to the increased rigidity and embrittlement of Durable resin at AT.

Failure Analysis

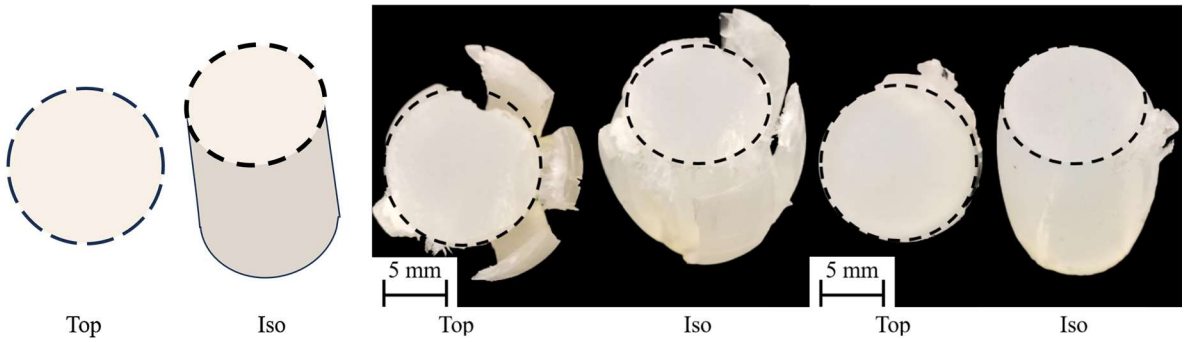

(a) Non-Deformed (a) Room Temperature (b) Arctic Temperature

Figure 1.18: Representative Compressive Strength Failure Mechanism for Durable Resin Specimens: a) Non-Deformed Example b) RT Tests and c) AT Tests

Figure 1.18a illustrates a non-deformed representative sample, with a black dashed outline highlighting the original top surface geometry for top a top-down view and isometric view. Figure 1.18b illustrates the failure of a representative RT compressive strength specimen, while Figure 1.18c illustrates the failure of representative AT compressive strength specimens. Images in Figure 1.18 were contrasted to aid in the illustration of failure for readers. During room temperature compressive strength tests, as the compressive load on the top face of the specimen increased, radial expansion was observed. The expansion, known as barreling [173] occurred during the densification stage resulting from the compressed polymer chains expanded radially,

perpendicular to the applied compressive load [174], [175]. Failure of RT specimens occurred when expansion caused the walls of the specimen to separate from the core by radial cracking, observed by the peeling mechanism [176] illustrated in Figure 1.18b. Compressive strength specimens tested under AT conditions did not fail from barreling, as the reduced polymer chain mobility from lower temperatures did not allow for rapid expansion. Arctic specimens failed through axial splitting, similar to brittle materials [177]. Axial splitting nucleates from microflaws present at the loading site and grow in the direction of the axial load [178]–[180]. This is observed in Figure 1.18c, by the minimal change to the surface geometry of the top plane of the specimen, and the cracks formed in the axial (vertical) direction. The change in failure modes illustrates the influence of Arctic temperatures on changing the material from ductile (RT) to brittle (AT) in failure mechanisms.

Finite Element Modeling

Anticipating the future use of SLA with Durable resin for the manufacturing and testing of intricate core structures, it became essential to develop a computational model that could accurately capture the influence of temperature on material properties. Consequently, an elastic-plastic finite-element model (FEM) was created to replicate the tensile, flexural, and compressive strength tests, and linear-elastic FEM models were created to replicate the compressive modulus tests using ABAQUS 6.14, a commercial finite-element software. These models were intricately designed based on the mechanical responses of Durable resin obtained during experimental tests at both room temperature (RT) and Arctic temperature (AT). To ensure their utility, each simulation was meticulously validated against the corresponding experimental data, serving as a crucial step in assessing the accuracy and reliability of the models.

Uniaxial Tension Simulation

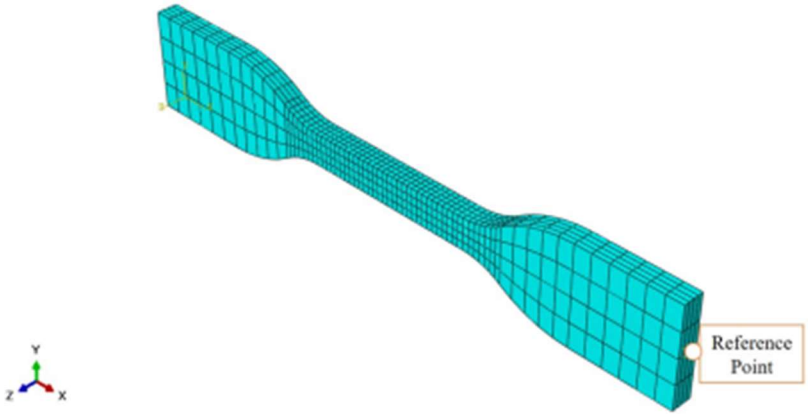

Figure 1.19: Uniaxial Tension Test Model Diagram

Figure 1.19 displays the 3D finite-element model used for uniaxial tension. In this model, the Durable resin specimen was represented as a deformable material. To simulate the gripping area, encastre fixed boundary conditions (U1=U2=U3=UR1=UR2=UR3) were applied at the left end surfaces. Furthermore, a coupling constraint was employed between a reference point (RP) and the right gripping area surfaces to simulate the 15 mm ramp displacement in the x-direction (U1). This coupling constraint ensured that the elements associated with the clamp location during testing moved with the same x-displacement as the RP to represent the loading mechanism within the model.

A refined mesh was used specifically at the gauge length, which is the critical zone in the tensile model. The entire model was assigned eight-node brick elements with reduced integration (C3D8R), resulting in a total of 1056 elements. To determine the optimal element size at the gauge length, a mesh convergence study (Figure 1.20) was conducted. Mesh seed sizes of 2.5 (blue dots), 2.0 (red dashes), 1.1 (magenta circles), and 0.6 (green squares) were studies and revealed that an element size of 1.1 mm was optimal. A load drop was observed at the yield point within coarser meshes (2.5- and 2.0-mm seed size) as the material transitioned between the linear-elastic to plastic properties within the model. This was attributed to convergence issues related to the transition in properties resultant of the coarser mesh size. Finer meshes reduced and eventually removed this

error as the overall material transition gradient was smoother in the model. Reducing the mesh seed size from 1.1- to 0.6-mm showed negligible differences (highlighted in Figure 1.20).

The computational model utilized experimental tensile data to calculate the material's yield stress, Young's modulus, and ultimate stress using the elastic-plastic calibration tool in ABAQUS. The mechanical properties for both room temperature (RT) and Arctic temperature (AT) are summarized in Table 1.8.

Table 1.8: Material Properties for Tension Simulations

	RT	AT
Young's Modulus (MPa)	851	3680
Poisson's Ratio	0.33	0.33
Yield Stress (MPa)	19.39	36.9
Ultimate Stress (MPa)	24.6	78.3

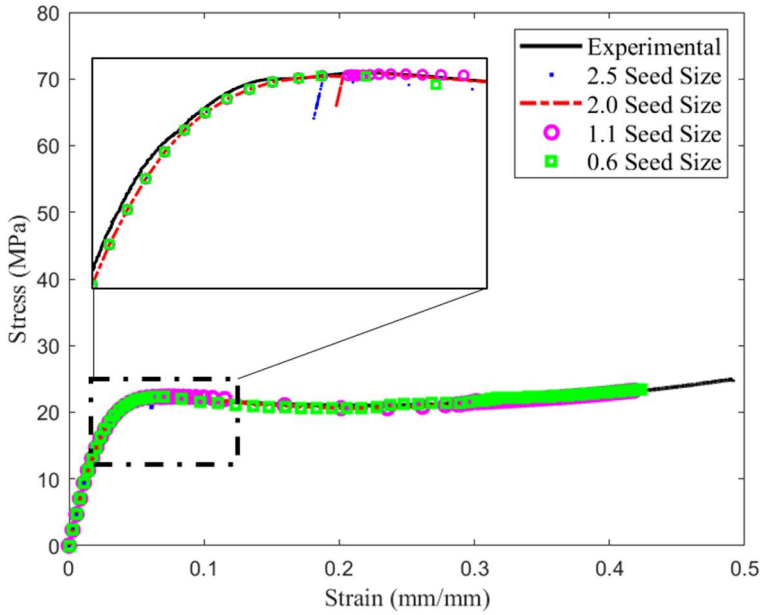

Figure 1.20: Tensile Test Mesh Convergence Study Results

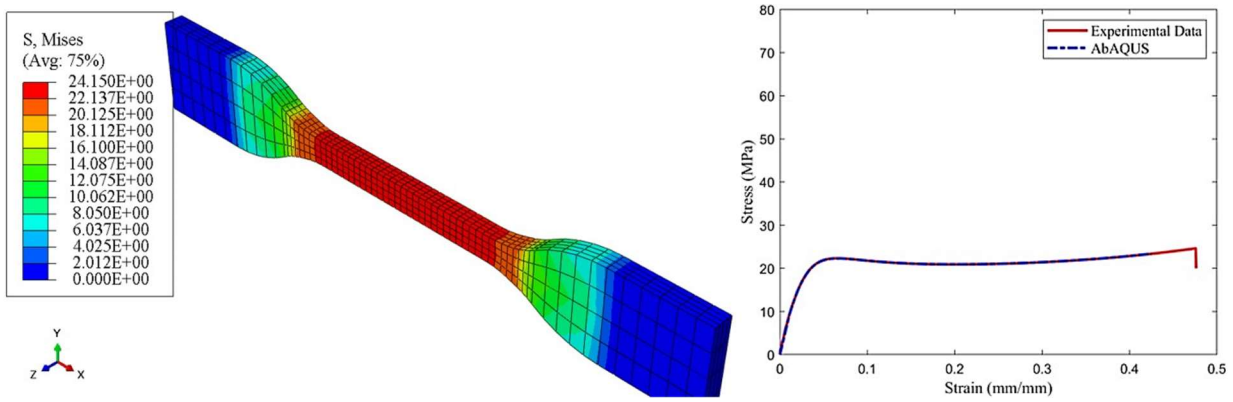

(a) Room Temperature Tensile Simulation (b) Room Temperature Stress-Strain Graph
Figure 1.21: Stress-Strain Comparison for Tension at Room Temperature

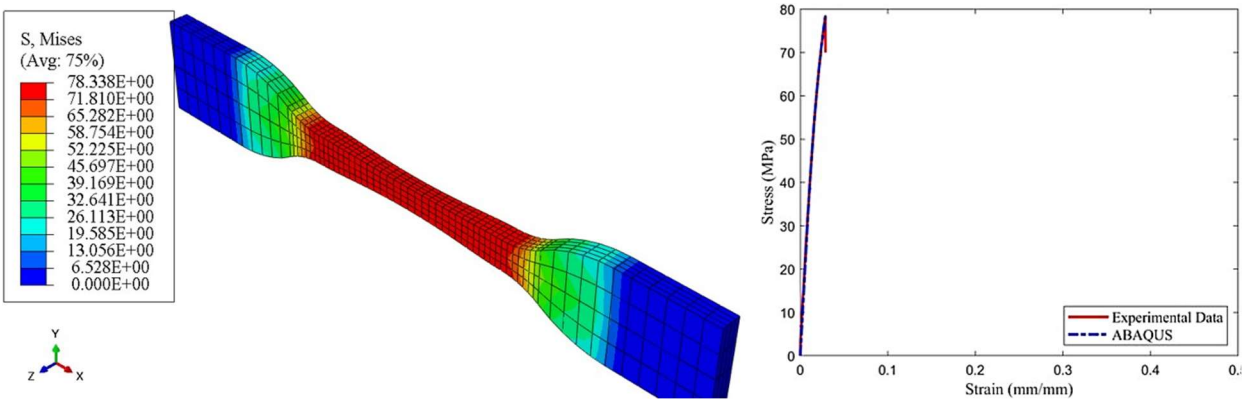

(a) Arctic Temperature Tensile Simulation (b) Arctic Temperature Stress-Strain Graph
Figure 1.22: Stress-Strain Comparison for Tension at Arctic Temperature

Figures 1.21 and 1.22 illustrate the comparison between the stress-strain data from the simulation and the experimental results. The simulation results show good agreement with the experimental data. At room temperature (RT), both Young's modulus and yield strength were accurately predicted by the simulation. Similarly, at Arctic temperature (AT), the simulation successfully replicated the Young's modulus and ultimate stress as shown in the experimental data.

Flexural Simulation

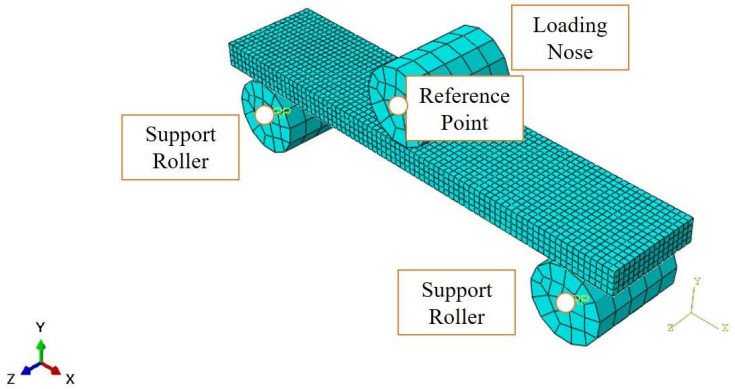

Figure 1.23: Flexural Test Model Diagram

Figure 1.23 shows the model used for the flexural simulation. The Durable resin specimen was modeled as a deformable material. The support and loading rollers were modeled as rigid body parts. The support rollers were fixed using Encastre boundary conditions (U1=U2=U3=UR1=UR2=UR3) to prevent rigid body motion. The loading roller was fixed to prevent translation and rotation in all directions (U1=U3=UR1=UR2=UR3), except for the Y-direction (U2) displacement. Surface-to-surface interactions were created between the rollers (support and loading) and the flexural specimen. The master surfaces were assigned to the rollers, and slave surfaces were assigned to the specimen surfaces. Tangential and normal constraints were applied to ensure no penetration between the rollers and the specimen. The flexural part was meshed with eight-node brick with reduced integration (C3D8R) elements and seed size of 1.1 mm, defined by the convergence during the tensile simulation for consistency. The total number of elements was 2124. The roller parts were meshed with three-dimensional quadrilateral rigid (R3D4) elements. The mechanical properties were specified using the isotropic elastic-plastic properties from the experimental tension tests because ABAQUS only allows Young's modulus or compression modulus in the material properties. Displacement-loading was designated using the experimental data as a reference to simulate the maximum displacement seen in experimental tests (6.9 mm for RT and 5.2 mm for AT). Displacement was applied by the loading nose using a reference point constraint similar to the tensile model ensuring the entire loading nose body moved uniformly to replicate the physical test apparatus. As seen in Figure 1.24 and Figure 1.25, the

simulation had a good agreement with the experimental data, however there was deviation from the experimental results. This deviation was resultant from elastic-plastic behavior being defined only by the tensile data due to the program limitations stated previously.

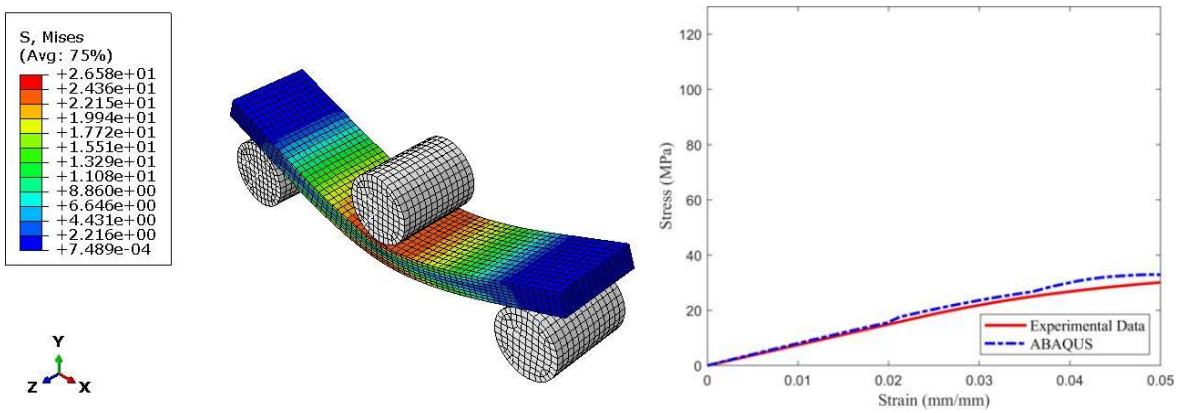

(a) Room Temperature Flexural Model (b) Room Temperature Stress-Strain Relation

Figure 1.24: Stress-Strain Comparison for Flexural Test at Room Temperature

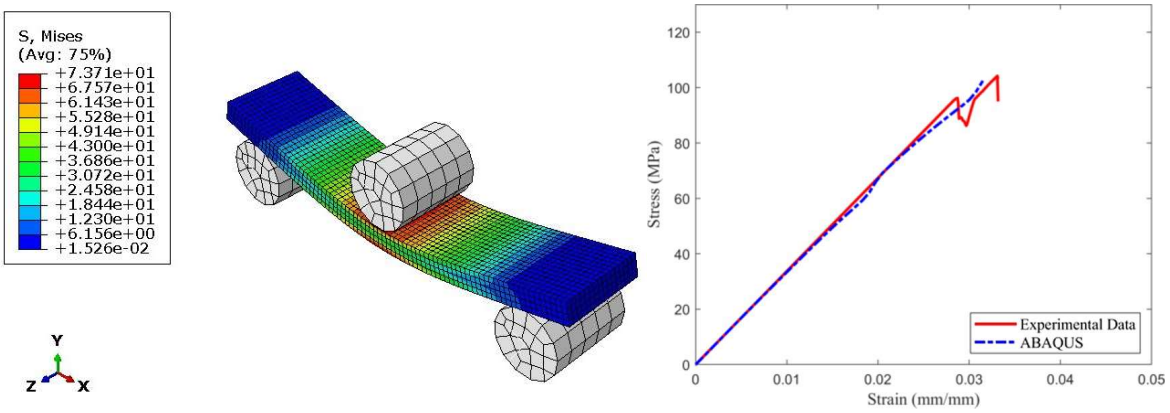

(a) Arctic Temperature Flexural Model (b) Arctic Temperature Stress-Strain Relation

Figure 1.25: Stress-Strain Comparison for Flexural Test at Arctic Temperature

Compression Simulations

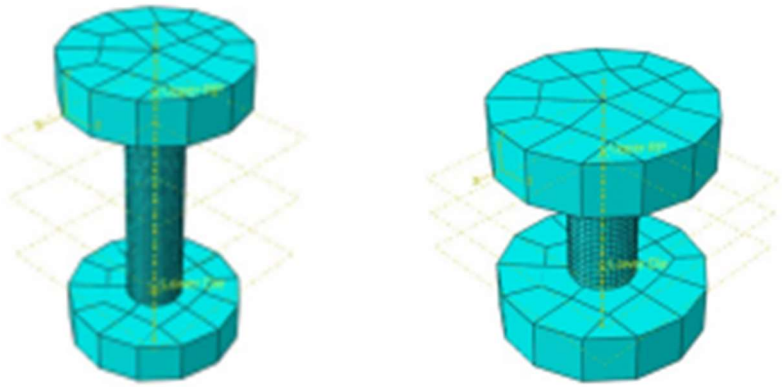

(a) Compressive Modulus (b) Compressive Strength

Figure 1.26: Compressive Test Models for Compressive Modulus and Compressive Strength

Figure 1.26 illustrates the model used for the compression simulation. The lower and upper plate fixtures had the same dimensions as those used in the experimental setup. The Durable resin specimens were represented as deformable materials, while the lower and upper plate fixtures were modeled as rigid shell parts. The compressive model was meshed using eight-node brick elements (C3D8R) with a seed size of 1.1 mm defined by the convergence during the tensile simulation for consistency, resulting in a total of 7222 elements. The lower and upper plate fixtures were meshed with three-dimensional quadrilateral rigid elements (R3D4) using a mesh seed size of 10 mm, resulting in a total mesh of 53 elements for each plate. The lower and upper plates were developed using a coarser mesh as the contact boundary conditions observed a finer mesh was not necessary for this model. Mechanical properties for the compression simulations were based on the experimental compressive data, and ABAQUS determined the material's elastic modulus, yield point, and plastic points using an elastic-plastic calibration tool. The mechanical properties for the RT and AT compression simulations are detailed in Table 1.9

.

Table 1.9: Material Properties for Compression Simulations

	Modulus (RT)	Modulus (AT)	Strength (RT)	Strength (AT)
Young's Modulus (MPa)	1338	5186	450	1716
Poisson's Ratio	0.3	0.3	0.3	0.3
Yield Stress (MPa)	16.0	20.8	14.0	33.0
Ultimate Stress (MPa)	16.0	20.8	294	222

General contact and tie constraints were applied between the fixtures (upper and lower plates) and the compressive specimen to simulate the compressive contact exhibited by the plated during experimental testing. The plates were treated as master surfaces, and the top and bottom specimen surfaces were treated as slave surfaces as seen in Figure 1.26. Tangential and normal constraints were applied to ensure no penetration between the plates and the compressive specimen. The simulation was created using two steps. The boundary conditions were applied in the initial step. For the lower plate, Encastre boundary conditions were applied (U1=U2=U3=UR1=UR2=UR3). For the upper plate, translations and rotations were fixed in all directions (U1=U3=UR1=UR2=UR3), except for Y-displacement (U2). The second step was associated with compressive displacement, which was applied in the U2 direction. The displacement used for the simulations was taken from the experimental tests (3 mm for modulus tests and 15.5 mm for strength tests).

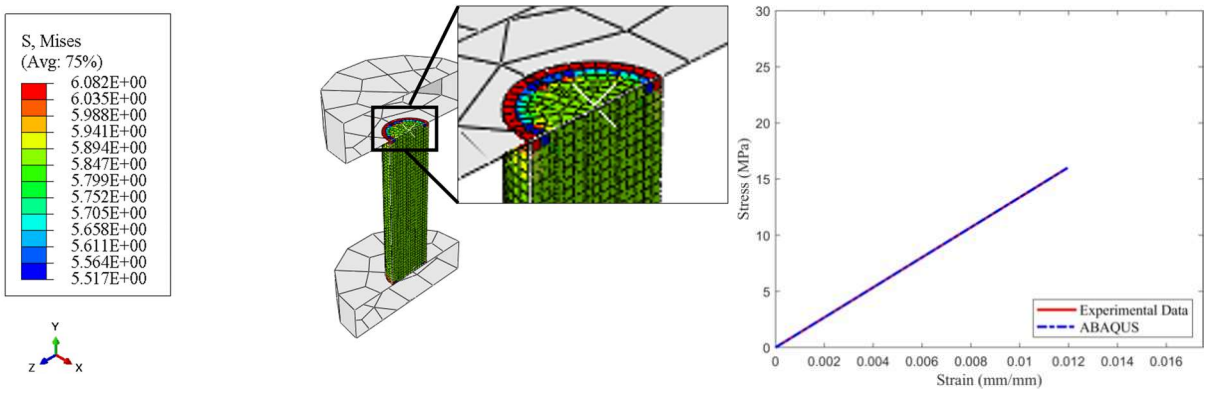

(a) RT Compressive Modulus Simulation (b) RT Compressive Modulus Stress-Strain Relation
Figure 1.27: Stress-Strain Comparison for Compressive Modulus Test at Room Temperature

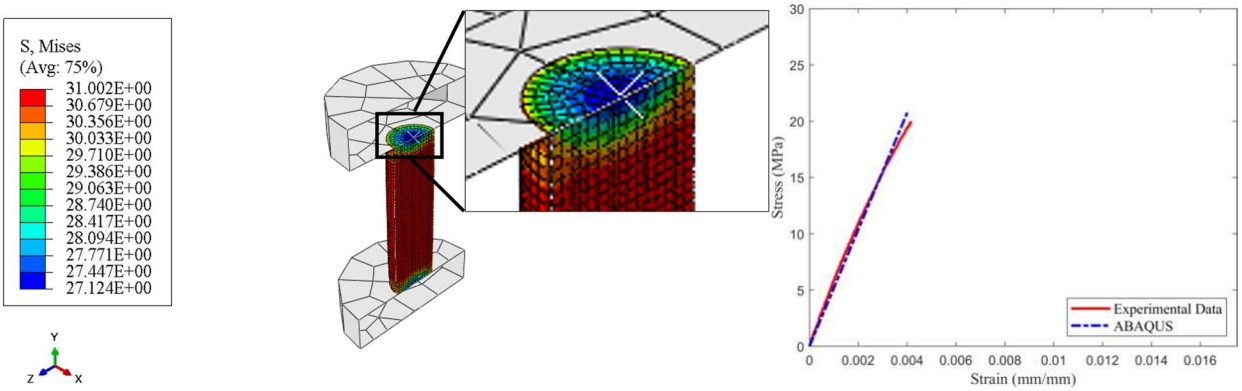

(a) AT Compressive Modulus Simulation (b) AT Compressive Modulus Stress-Strain Relation
Figure 1.28: Stress-Strain Comparison for Compressive Modulus Test at Arctic Temperature

Figure 1.27 and Figure 1.28 show the experimental and simulation stress-strain graphs for the compressive modulus. Figure 1.27a shows the stress distribution in the sample at RT and Figure 1.28a shows the stress distribution in the sample at AT. From the figures, it was noted that there is good agreement between both of them, with the simulation modulus values being almost exactly that of their experimental counterparts.

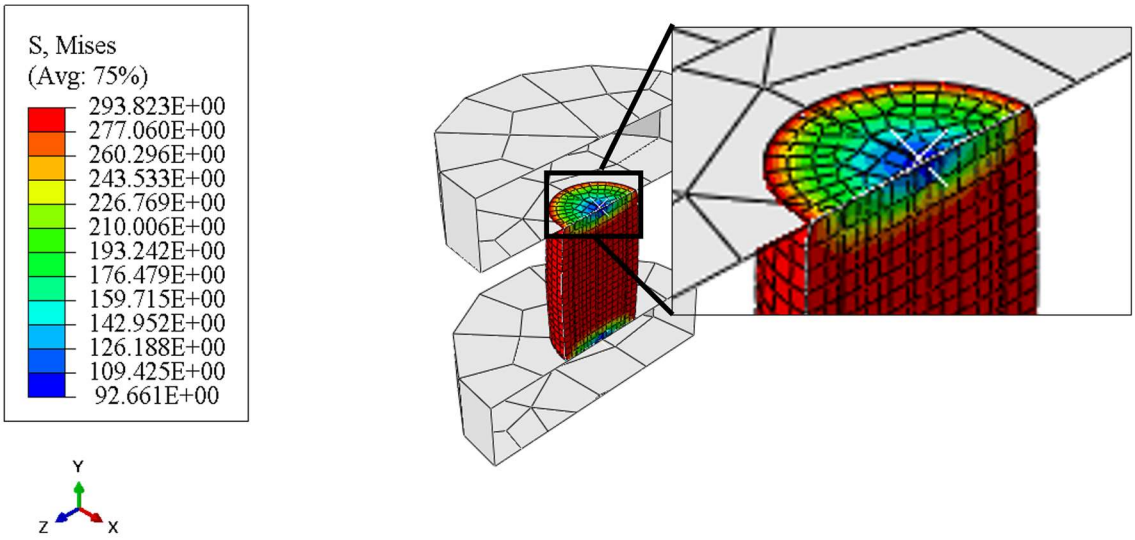

Figure 1.29: End of Simulation for Room Temperature Compressive Strength Model

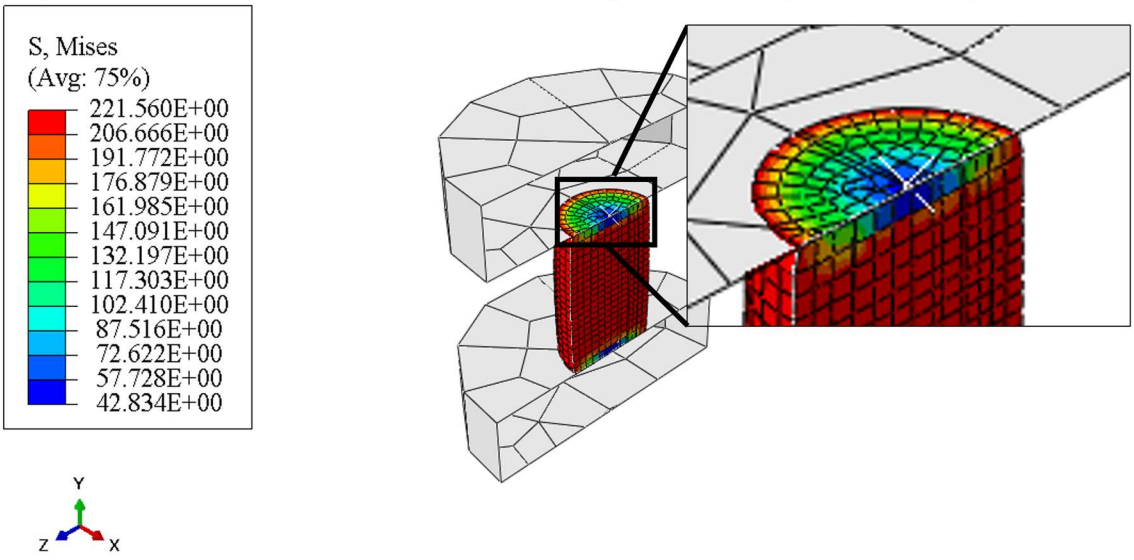

Figure 1.30: End of Simulation for Arctic Temperature Compressive Strength Model

Figure 1.29 shows the stress distribution in the sample subjected to compressive loading at room temperature. Figure 1.30 shows the stress distribution in the sample subjected to compressive loading at arctic temperature. From the images, the simulation illustrated an increase in stress caused by the compressive force, however it failed to capture the failure mechanisms observed during testing. For the RT specimens, failure occurred after the specimen expanded outwards through a barreling mechanism before rupturing caused by radial cracking. Specimens compressed under AT environments during experimental testing saw failure caused by cracking initiation at the compression plate contact face, which evolved into axial splitting. The simulation failed to

capture the barreling of the room temperature tests, as well as the axial stress concentration associated with the arctic temperature tests. This discrepancy highlights further testing should be performed regarding the compressive strength tests to develop a more accurate model.

CONCLUSION

In this report, a comprehensive study on FormLabs' photoreactive resin "Durable resin" was conducted. The material was characterized for its quasi-static properties, including tensile, flexural, and compressive properties, at both room and arctic temperatures. Additionally, post-test failure analyses were performed for each of the quasi-static tests to compare behavior at different temperatures. The key findings and conclusions of this study are as follows:

- **Isotropic Behavior**: Tensile orientation tests confirmed that specimens manufactured using Durable resin via stereolithography exhibited isotropic behavior. This means that the material's properties were consistent regardless of the printing orientation.
- **Temperature Effects**: Tests conducted at arctic temperatures revealed a significant increase in mechanical properties compared to room temperature conditions. The arctic specimens exhibited a substantial improvement in properties, including a 318% increase in tensile modulus, a 322% increase in ultimate tensile stress, a 450% increase in flexural modulus, a 360% increase in flexural strength, a 460% increase in compressive modulus, and a 3% increase in ultimate compressive strength.
- **Polymer Chain Behavior**: The experimental compressive tests indicated that the polymer chains in Durable resin exhibited properties similar to foam cells, with the polymer chains acting as universal joints [181]. This behavior was evident from the compressive stress-strain graphs, which displayed distinct regions, including an elastic region, plateau region, and densification region [164].
- **Failure Modes**: The failure analyses of quasi-static tests showed that arctic temperature specimens had an increased tendency for shear failure modes in both

flexural and compressive tests. This shift in failure modes was attributed to the influence of temperature reducing chain mobility and inducing brittle behavior [166]. Failure mechanisms observed during room temperature tensile tests highlighted the ductile-to-brittle behavior resulting from lack of chain mobility under loading [167].

- **Simulation Accuracy**: Elastic-plastic finite-element models aimed to replicate quasi-static scenarios for tension, compression, and flexural tests were implemented. The purpose was to establish a computational framework capable of predicting the mechanical behavior of Durable resin at both room temperature (RT) and Arctic temperature (AT). Tensile models were able to capture an almost identical representation for both RT and AT tests. Flexural models had limitations due to a constraint in allowing only one set of material properties (either tensile or compressive), the simulations, nevertheless, demonstrated effectiveness by performing within 10% of their experimental counterparts when using tensile elastic-plastic properties. Compressive modulus models were able to capture their experimental RT and AT counterparts, however, the compressive strength models were incapable of capturing the stress concentrations associated with their failure mechanisms.

Based on these findings, this study has validated the potential use of Durable resin for sandwich composite core materials. The material's ability to be fabricated through additive manufacturing, its enhanced mechanical properties at arctic temperatures, and the accuracy of computational modeling have emphasized the need for further research and exploration in the context of sandwich composites.

Chapter 2: Uncertainty Quantification for the Manufacturing of Carbon Fiber/Vinyl Ester Laminates

INTRODUCTION

In many applications that require lightweight structures, such as aerospace, green energy, and naval transportation, carbon fiber reinforced polymer (CFRP) composites have become an attractive option due to their high stiffness-to-weight ratio, high strength-to-weight ratio, and tailorable mechanical properties [182]–[184]. CFRP composites are usually composed of two constituents, bulk material (polymer matrix), and carbon fiber reinforcement. Fibers carry the majority of transverse loads, while the matrix effectively transfers the loads between fibers and houses them from the environment [77]. During manufacturing of CFRP composites, there exists a multitude of methods one can take to develop the end-product with more common methods [185] being hand-layup [186], vacuum-assisted resin transfer molding [187], autoclave [188], [189], and filament winding [190]. With each process however, due to the complexity of composites the manufactured component can drastically change in performance due to uncertainties developed by unavoidable manufacturing imperfections such as voids, incomplete resin curing, excess resin pockets, porosity, variation in ply-thickness, and fiber parameters [191]. Designers by convention use a factor of safety in attempts to combat this variance which can lead to ultraconservative designs or unsafe designs. Ultraconservative designs developed to ensure safety during use can result in larger components than needed, which increases weight, increases cost, and decreases fuel efficiency for vehicles [192]. In efforts to combat this variance in components, quantifying the degrees of uncertainty is imperative [193].

Uncertainty quantification (UQ) serves as a process to identify, quantify, and reduce uncertainties associated with numerical algorithms, experiments, and predicted outcomes or quantities of interest through statistics and numerical analysis theory [194]. Uncertainty can be divided into three groups, aleatoric, epistemic, and prejudicial uncertainties [195]. Aleatoric uncertainty is a result of the inherent system variabilities [196], with an example being components

developed on the same production line not resulting in the exactly identical product. This form of variability can be characterized statistically through probability density functions if there are enough components present [197]. Epistemic uncertainty, results from the lack of knowledge on a system, due to the complexity within [198]. Probabilistic approaches to attempt quantifying these uncertainties are based on interval algebra [199], convex sets [200], Dempter-Schafer theory [201], and fuzzy sets [202]. Prejudicial uncertainty regards the variability which cannot be characterized as the variance is unknown [203]. This can result from random error, user or measuring bias, and generalization/assumptions made regarding the problem. Additional work can be employed in attempts to group the prejudicial uncertainties to treat them as an aleatoric uncertainty [204].

Statistical attempts at quantifying these uncertainties exist in two general forms, deterministic and stochastic. Deterministic studies [205]–[207] represent identical outputs for identical inputs, disregarding any form of randomness. With the lack of uncertainty accounted for in the model, exclusively deterministic approaches can result higher safety factors required, or result in serious overestimations in reliability of the structure [208]. To overcome this, there is a continued interest towards implementing stochastic or probabilistic approaches within FRP studies and frameworks [209]–[211]. Stochastic methods involve the incorporation of random variables applied in the study, meaning identical input does not always give identical output. Another form of statistical study which can accompany uncertainty quantification is a sensitivity analysis (SA), which helps to identify dominant variables through a culmination of weighted variables during the analysis [212].

Composite hierarchy has been the respective guide for researchers performing uncertainty quantification towards composites. On the macro-scale, where the focus towards uncertainty is on composite structures [213], [214] or plates [191], [212], [215]–[226], the data used to drive predictive models is based on already manufacture material. The macro-scale studies primarily focus on the modeling the distribution of fibers [227], fiber alignment [228], and variance in material properties to represent their effects on job oriented properties such as mechanical strength [229], thermal resistance [230], and thermal conductivity [231]. Uncertainties developed during

manufacturing are significantly influenced by their constitutive elements (matrix and fibers), through the volume fractions of matrix and fiber [232], [233], excess resins between plies [234], incomplete curing [235], voids/porosity of the matrix [236], alignment of fibers [237], and temperature effects [238]–[241]. Primarily studies focus on the meso- to macro-scale of composites, where they investigate fiber geometry [242], cure kinetics [243], [244], infiltration [245], and defects to define the mechanical properties of the composite [246]. Micro- to meso-scale studies [247]–[250] build their models from the constituent level up primarily focusing on fiber volume fraction [251], fiber misalignment [252], and yarn angles for woven composites [253]. While they do focus on constituent materials to build their models, the constituent materials in their isolated setting are ignored. Micro-scale studies have focused on the interaction of the matrix with fibers through RVEs [254], [255]. However, there have been no observed studies focusing on the constituents at an individual scale.

Literature shows a vast range of numerical analysis methods and techniques for composites throughout its hierarchal scale. Methods such as Monte Carlo [256], are robust, however, the Monte Carlo based UQ methods are not desirable in industrial applications as they exhibit a very slow convergence rate and need a vast number of simulations to predict statistical results accurately [257]. Methods using trained algorithms and machine learning require large data sets for testing [258], and a majority of the models rely on categorizing mathematical guidelines to the behavior of the composite scale.

While there are more robust methods such as Monte Carlo, simpler less intensive approaches can be performed with adequate results. Wang et al. [259] conducted a quantitative sensitivity analysis on fiber-reinforced composites (FRCs) using a global sensitivity analysis (GSA) approach based on the variance-based method. The analysis incorporated Random Sampling-High Dimensional Model Representation (RS-HDMR) expansion with a unique Diffeomorphic Modulation under Observable Response Preserving Homotopy (D-MORPH) regression. The study aimed to explore the impact of fiber path, treated as the design variable, on the formability and structural performance of FRCs, addressing spring-back and load-carrying capacity. Two FRC

scenarios, an L-shaped part with a straight fiber path using autoclave manufacturing and a variable stiffness composite cylindrical shell under pure bending, were investigated. The GSA algorithm revealed that spring-back in FRCs using autoclave manufacturing is highly sensitive to fiber orientation angles on plies close to the tool, while the buckling performance of the variable stiffness cylinder is influenced by fiber orientation angles at tension/compression regions. The D-MORPH-HDMR GSA algorithm effectively quantified the contributions of fiber orientation angles to the buckling load, with promising results validated against analytical solutions.

Thapa et al. [260] introduced a framework for stochastic progressive failure analysis (PFA) of fiber-reinforced composites, addressing the significant impact of material property randomness on nonlinear structural responses. To mitigate the computational intensity of PFA using finite element analysis (FEA), the study employs the polynomial chaos expansion (PCE) technique, allowing for efficient uncertainty analysis. The framework is validated against 5000 Latin Hypercube Sampling (LHS) simulations, demonstrating cost-effectiveness and high accuracy. Global sensitivity analysis (GSA) is performed as a post-processing step, identifying influential random material properties correlated with failure modes. The presented approach is applied to a composite laminate with a circular cutout under various load cases, revealing its cost-effectiveness, accuracy, and utility in decision-making for further experimental tests. The study emphasizes the importance of GSA in reducing computational efforts and facilitating optimization by identifying non-influential inputs. The framework's potential for enhancing composite structure design and reliability is highlighted, with future work proposed to extend its applicability to complex structures and incorporate additional factors like interlaminar failure and uncertainties in ply characteristics.

Bogdanor et al. [261] explored the application of Bayesian statistical methods for the calibration and uncertainty quantification in rate-dependent damage modeling of composite materials. The study addresses epistemic and aleatory uncertainties arising from model parameter uncertainty, model form error, solution approximations, and measurement errors. Gaussian process surrogate models replace computationally expensive finite element models, facilitating analysis

within a commercial finite element software package (Abaqus). Calibration of a viscous damage model is performed using experimental data from monotonic load tests on glass fiber-reinforced epoxy composite samples. Bayesian inference is employed to derive distributions for material parameters and measurement errors. Gaussian process models serve as surrogate models, allowing the quantification of approximation errors. The study highlights challenges in predicting composite material response due to nonlinear behavior, limited test data, and incomplete material understanding. To improve accuracy, the manuscript suggests further experimental testing and additional training points for Gaussian process models. The conclusion emphasizes the need for extending the viscous damage evolution to multiscale applications, especially in the context of fatigue loading, to comprehensively address uncertainty propagation across spatial and time scales in the design of composite materials.

Resulting from the lack of studies performed on individual constituent materials, this study aims to perform an exploratory uncertainty quantification paired with a sensitivity analysis on a vinyl-ester resin matrix system subjected to impact loads. In efforts to minimize the computational resources required and the number of tested specimens, the investigation utilizes the polynomial regression method to develop local trends of manufacturing parameters. Polynomial regression acts as a flexible analytical tool which can define local trends on smaller quantity sample sizes [262] and evolve into a robust tool with future studies [263]. After defining local trends, global trends are then employed using multi-linear/multi-variate regression (MLR/MVR) to identify the influence parameters have on one another in conjunction with global sensitivity analysis. Global sensitivity approaches have been observed in the past to help define critical points of interest [264], [265] and MLR similar to polynomial regression allows for a low sample size entry point [266] which can evolve into a more robust system with future testing [267], [268]. The following sections highlight the material selection, process of variable identification, specimen fabrication, impact testing, impact test results and the development of numerical models, and how the numerical predictions compare to experimental data.

METHODS AND MATERIALS

This section discusses material selection, variable identification, specimen manufacturing, and test methods.

Material Selection

In this study, the focus was on investigating the impact of the curing process on the mechanical response of vinyl-ester resin when subjected to low-velocity impact damage. This research aimed to lay the groundwork for uncertainty quantification (UQ) in future studies, particularly for carbon fiber-reinforced polymer (CFRP) composites. Vinyl-ester resin was chosen as the material of interest due to its favorable characteristics compared to other polyester resins. Notably, it has lower water absorptivity and greater UV tolerance [183], [184]. The hardening agent employed in the curing process was methyl ethyl ketone peroxide (MEKP). Vinyl-ester resin exhibits the following mechanical properties: tensile strength = 82 MPa, tensile modulus = 3720 MPa, tensile elongation at yield = 4.6%, tensile elongation at break = 7.9%, flexural strength = 131 MPa, flexural modulus = 3450 MPa, and heat distortion = 98 °C [62].

Uncertainty Quantification

Variable Identification

Definition of specimen fabrication and testing methods first required the identification of variables that were isolatable variables and inevitable/miscellaneous variables [269]. These variables were identified using the three previously mentioned forms of uncertainty, aleatoric, epistemic, and prejudicial. Aleatoric uncertainty, resulting from the inherent system variabilities, was used to define unavoidable variance to classify the miscellaneous variable. Epistemic

uncertainty, resulting from the lack of knowledge of the system, was used to classify variables that may influence the material, but are unknown, to aid in the definition of the miscellaneous variable. Prejudicial uncertainty, regarding the variance that is unknown, was used to define the variables for testing. By testing said variables, the prejudicial uncertainty transforms into future aleatoric uncertainty as the variance becomes defined.

Aleatoric uncertainties consisted of the devices and tools implemented during manufacturing and testing of the specimens. During manufacturing the measuring scale, resin mixture time, silicon molds, and an environmental chamber all helped to maintain an identical manufacturing process. After manufacturing specimen removal and post-processing followed identical procedures. Testing was performed with identical procedures in terms of striker shape, mass, and velocity. While these steps were performed to minimize variance, the complete occlusion of effect cannot be stated, thus the variance caused by these variables was grouped into a "miscellaneous" variable identifier.

Epistemic uncertainties consisted of variables which were unknown whether they would affect the resin system or not. These variables coincided with the resin hardening mechanism as the hardener chemically interacted with the resin during curing and potential influences from the materials during development by the manufacturer. While it was believed that these had negligible influence they were also grouped into the "miscellaneous" variable group.

Prejudicial uncertainties which would require testing to determine the variance effect within the material were treated as the isolatable variables. In this study, the two isolatable variables of focus existed in the resin to hardener mixture ratio and the cure time of specimens prior to testing. Both variables can heavily influence the chemical composition of the specimens during the curing process. The mixture ratio can result in incomplete curing resulting in excess resin or hardener in the specimen. The time of cure to testing can illustrate whether the specimens are fully cured or if longer time is needed for a complete cure. In conjunction with their potential influence on mechanical properties, both variables are easily isolated to aid in the designation of uncertainty variance.

Isolated Variables

Defining the manufacturing methods to analyze variance within the isolated variables consisted of using the manufacturer recommendation for the base studies, and then two alternative manufacturing methods for each case to see the influence. The vinyl-ester resin to methyl-ethyl ketone peroxide hardener (MEKP) recommended ratio was 1.25% hardener to resin by weight [270]. This ratio served as the baseline reference for study. Ratios of 1.00% and 1.50% were selected for variance identification. The two additional ratios were chosen to represent lesser and greater quantities of the hardener present during the chemical reaction process which could be easily overlooked during manufacturing. The deviation from the baseline ratio could result in variance from either an excess of hardener, or resin present after the complete cure of the specimen. The recommended cure time before testing was 24 hours [270]. This served as the baseline reference for testing. Two additional cure times were selected to coincide with 48 hours and 96 hours. The cure times studied purposefully only increased in time by 2x and 4x the baseline reference to ensure the specimens were cured, as lesser time could potentially result in incomplete cure of the specimens.

Through the reduction of stochastic variables using the aforementioned procedure, two specific variables were able to be categorically tested using three sets of each variable for statistical identification [269]. Further identification towards implementing the techniques towards uncertainty is highlighted in the subsequent sections.

Specimen manufacturing

The manufacturing process of the vinyl-ester resin specimens was carried out systematically to ensure consistency and control over the key variables being tested. Here is an overview of the process:

Batch Preparation: Each batch consisted of 626 grams of vinyl-ester resin. The amount of MEKP (Methyl Ethyl Ketone Peroxide) added to the resin was based on the desired resin-to-hardener mixture ratio (1%, 1.25%, or 1.5%). The mixing of MEKP initiated an exothermic reaction. The resin and hardener mixture was stirred for 1 minute in a large container. This mixing step ensured that the hardener was uniformly distributed throughout the resin.

Specimen Molding: The resin-hardener mixture was poured into silicone molds (Figure 2.1) to create specimens. Each specimen had specific dimensions, measuring 102 mm in length, 102 mm in width, and 9.23 ± 0.1 mm in thickness. These dimensions were designed to mitigate geometric influences on the mechanical properties, as mentioned earlier in the study. Once the mixture was poured into the molds, the specimens were placed in a level and enclosed environment to prevent environmental contamination and maintain the geometric stability of the fluid mixture during the curing process.

Curing: The specimens were allowed to cure in the controlled environment at room temperature until they reached the specified curing time (24, 48, or 96 hours). The use of silicone molds and a controlled curing environment aimed to minimize external factors that could affect the specimens' properties.

Cataloging and Refinement: After curing, each specimen was cross-cataloged with its initial mixing time to ensure uniform testing conditions. To prepare the specimens for testing, any sharp edges caused by the concave curing nature of vinyl-ester resin were removed using a low-revolution-per-minute (rpm) sander. The sanding process was limited to the specimen edges to avoid heat-related uncertainties.

This systematic manufacturing process ensured that the specimens were consistent in terms of composition, curing time, and geometry, allowing for a reliable evaluation of the variables under investigation and their impact on the mechanical response of the vinyl-ester resin to low-velocity impact damage.

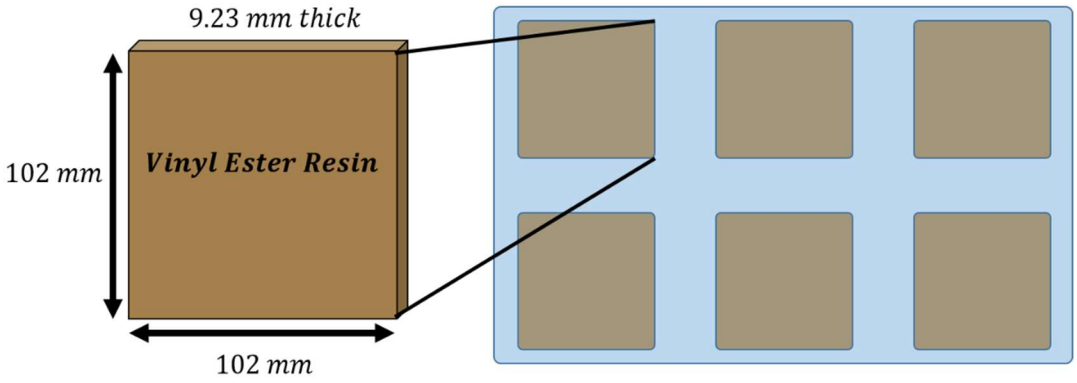

Figure 2.1: Specimen Dimensions and Silicone Mold Representation

Experimental Testing

Drop-weight impact tests were conducted using the CEAST 9340 Drop Tower Impact System. A metal support fixture with a 76 mm (diameter) circular hole was used for all the specimens as shown in Figure 2.2. A hemispherical striker with a fixed mass of 3.1 kg and a diameter of 12.1 mm was used to impact the specimens at the center of the top face. The impact energy chosen was 3.3 J with an impact velocity of 1.46 m/s. An impact energy of 3.3 J coincided with the highest energy to produce BVID within the specimen as preliminary tests at 3.5 J impact energy induced complete failure within the specimens. Energy-time responses for the impact event were recorded via the "CEAST DAS 8000 Junior" data acquisition system. Table 2.1 shows the testing matrix for all the tests that were performed. Three different MEKP concentrations were tested at 1.0%, 1.25% (recommended by manufacturer), and 1.5%. Three different cure/rest times before testing were tested at 24 hours, 48 hours, and 96 hours. This allowed for 9 test batches, with 6 specimens per batch for a total of 54 specimens. Batch manufacturing and testing served to aid in identifying the influences from resin-to-hardener ratio, cure time to testing, and the miscellaneous variables with respect to the impact response of vinyl-ester samples.

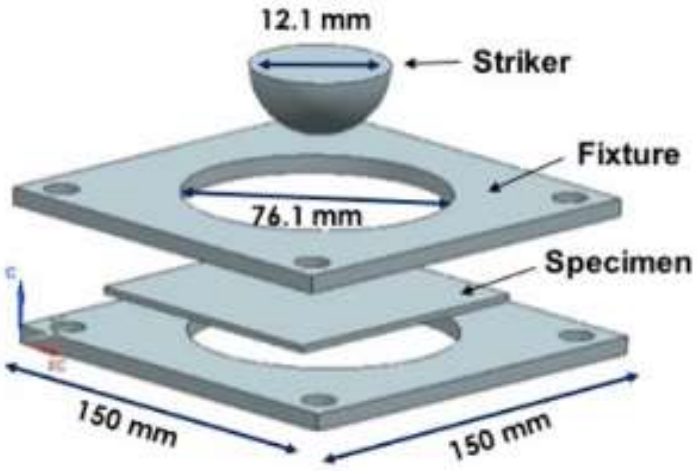

Figure 2.2: Impact Fixture

Table 2.1: Specimen Batch Representation

	1.00 % MEKP	1.25% MEKP	1.50% MEKP
24 Hours	Batch a	Batch b	Batch c
48 Hours	Batch d	Batch e	Batch f
96 Hours	Batch g	Batch h	Batch i

EXPERIMENTAL RESULTS

In this section, the experimental impact results were evaluated using their respective energy-time graphs recorded from testing. This is done to identify how each variable (MEKP % concentration and cure/rest time before testing) influences the degree of damage of vinyl-ester resin samples when subjected to impact loading.

Degree of Damage Evaluation

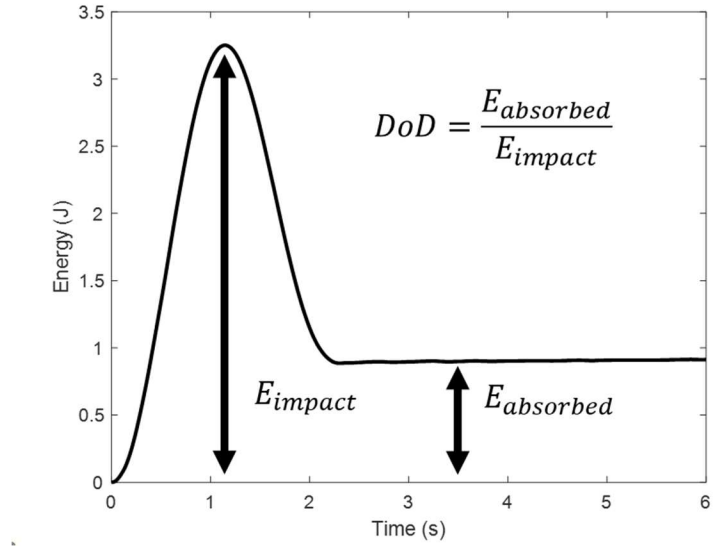

Figure 2.3: Representative Energy/Time Graph for Impact Degree of Damage

Figure 2.3 illustrates a representative energy vs time graph for the impact responses, where: E_{impact} illustrates the impact energy, $E_{absorbed}$ illustrates the absorbed energy, and DoD illustrates how degree of damage is calculated.

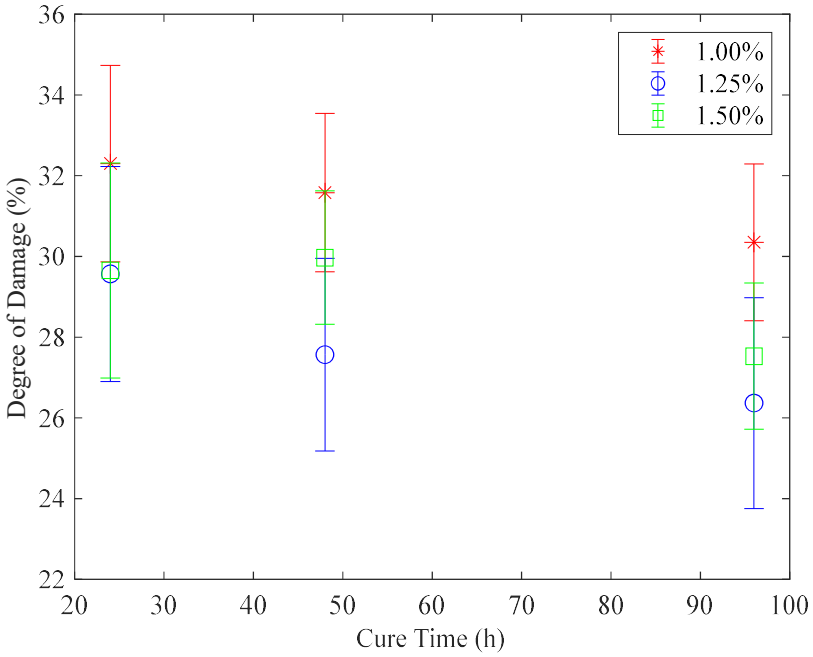

Figure 2.4: Degree of Damage for all 9 Batches (Mean and Standard Deviation)

Table 2.2: Degree of Damage Mean and Standard Deviation for all Test Batches

	1.00 % MEKP	1.25% MEKP	1.50% MEKP
24 Hours	32.3 ± 2.4	29.6 ± 2.6	29.6 ± 2.4
48 Hours	31.7 ± 2.16	27.6 ± 2.4	30.4 ± 1.6
96 Hours	29.7 ± 1.71	26.4 ± 2.6	27.5 ± 1.8

Figure 2.4 illustrates the degree of damage for each batch. Specimen batches made from 1.00%, 1.25% and 1.50% MEKP ratio are illustrated in red star, blue circle, and green square, respectively. Each batch marker illustrates the mean value of degree of damage, with the bars illustrating the standard deviation. From Figure 2.4 and Table 2.2 trends regarding the tested variables, concentration percentage and cure time to testing were observed. As the concentration percentage of MEKP deviated from the recommended percentage, the degree of impact damage increased. With the lowest concentration of MEKP (1.00 %) receiving the highest degree of damage on average. As the time of cure before testing increased, the degree of damage observed was reduced. The longest tested time of 96-hour cures resulting in the least degree of damage on average.

Uncertainty Quantification

This section provides a comprehensive explanation of the processes involved in theoretical modeling of the uncertainty quantification regarding the manufacturing uncertainties of vinyl-ester resin specimens. Theoretical models were employed to coincide with minimal computational resources required and work with a smaller data set following guidelines mentioned by Lin et al. [269]. Identification of local trends exhibited by the prejudicial variables of study associated by the isolatable variables was performed using polynomial linear regression, allowing the observance of the individual variances witnessed during testing. After local trends were identified for the cure-to-hardener ratio and cure time testing parameters, a global trend analysis approach

similar to Wang et al. [259] and Thapa et al. [260]. The MLR approach was selected as it can build a variance sensitivity analysis with smaller data sets by incorporating all of the tested variables and their relation to the degree of damage.

The global trend equation derived from the MLR approach then served as a foundational model that incorporated both independent variables, as well as a unique UQ coefficient derived from the miscellaneous variables' influence. This equation is central to building a sensitivity analysis and a UQ predictive model. The UQ model is particularly significant as it addresses manufacturing uncertainties related to factors like MEKP concentration and cure/rest time before testing in vinyl-ester samples subjected to low-velocity impact loading. Notably, the UQ model underwent experimental validation to ensure its accuracy and reliability.

This in-depth explanation highlights the meticulous process of theoretical modeling and underscores the significance of the UQ model in accounting for uncertainties stemming from various manufacturing factors.

Polynomial Regression

Polynomial regression formulas were calculated using the programming computational software MATLAB in the form of $Y = A_n X^n + A_{n-1} X^{n-1} \dots A$, with the primary objective of discerning potential trends in single-variable data. In this equation, Y represents the dependent variable, A corresponds to the linear coefficient or weighted value, X denotes the independent variable, and n serves as the power identifier. When identifying the power identifier for an unknown variable, it is important to identify the power which develops the closest representation using the smallest magnitude. To identify the optimal power identifier illustrated by trendlines which encompass the experimental data, three different powers, 1, 2, and 3 in the polynomial regression analysis were tested. analysis was tested. The following were the most relevant trends, each accompanied by its respective polynomial function.

INFLUENCE ON DEGREE OF DAMAGE CAUSED BY CURING TIME

To explore potential trends related to curing time before testing, the specimens were categorized into three distinct MEKP concentration groups (1%, 1.25%, and 1.5%). This approach provided a more precise focus on the time-related impact. Figures 2.5, 2.6, and 2.7 depict the experimental data, illustrating the degree of damage (DoD) (%) in relation to cure/rest time before testing (hours), along with the polynomial regression trends.

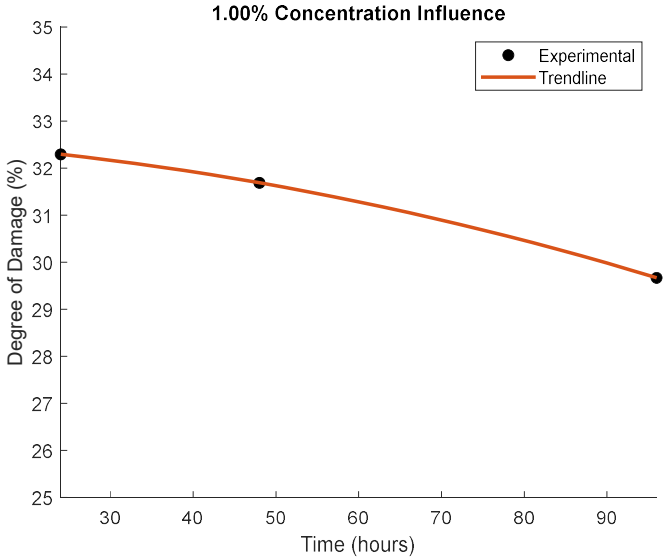

Figure 2.5: DoD Vs. Time (1.00% MEKP), $\boldsymbol{DoD = -.002x^3 - .0084x^2 + 32.6314}$

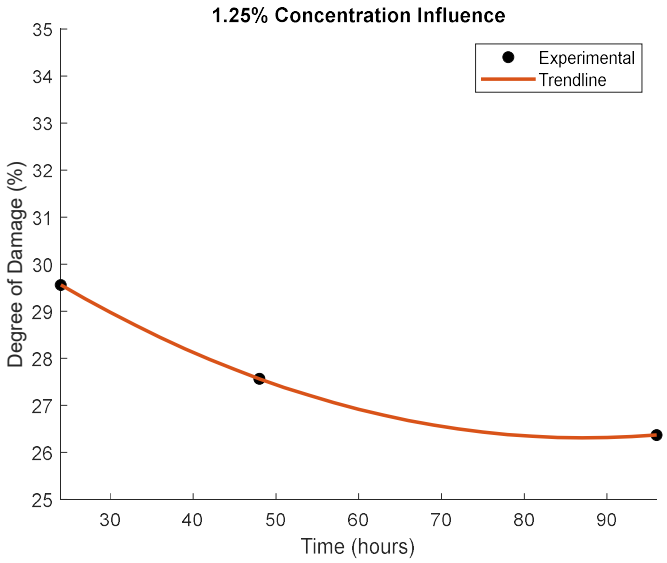

Figure 2.6: DoD Vs. Time (1.25% MEKP), $\boldsymbol{DoD = 0.0008x^2 - .1414x + 32.4911}$

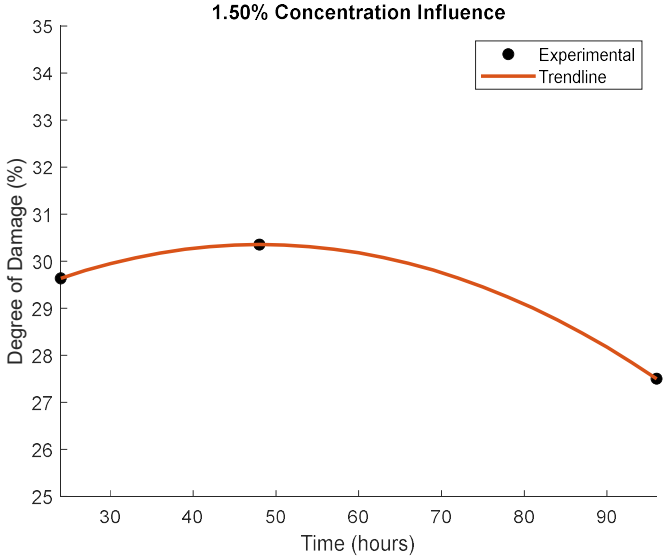

Figure 2.7: DoD Vs. Time (1.50% MEKP), $\boldsymbol{DoD = -0.0012x^2 + .1192x + 27.4909}$

Figures 2.5, 2.6, and 2.7 clearly indicate a consistent pattern: as the duration of curing time increased, the degree of damage decreased. This trend was observed across all cases, with one exception in the 1.5% concentration group, where 48 hours showed a slightly higher degree of damage compared to 24 hours. Nevertheless, the 96-hour mark demonstrated a substantial reduction in the degree of damage, aligning it with the overarching trend seen in the other cases.

Influence on degree of damage caused by MEKP concentration

To investigate the influence of MEKP concentration, the specimen tests were divided into three distinct MEKP concentrations: 1%, 1.25%, and 1.5%. Plots of the degree of damage (%) versus MEKP Concentration (%) were generated to assess this impact. Figures 2.8, 2.9, and 2.10 depict the relationship between the degree of damage (DoD) (%) and MEKP Concentration (%) using the experimental data, along with their respective polynomial regression trends.

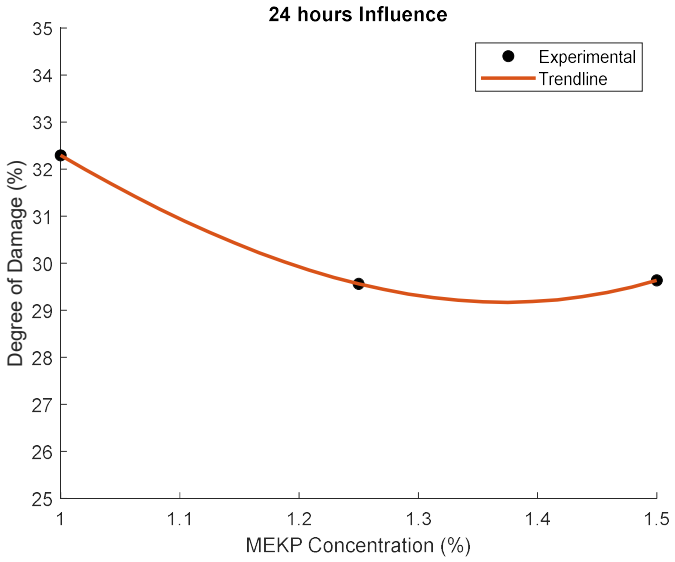

Figure 2.8: DoD Vs. Concentration (48 hours), $\boldsymbol{DoD = 13.2940 - 27.3848x^2 + 46.3869}$

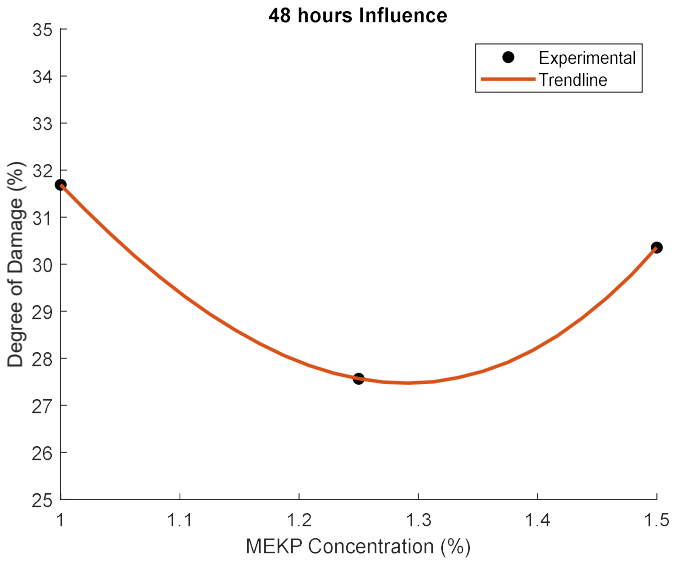

Figure 2.9: DoD Vs. Concentration (48 hours), $\boldsymbol{DoD = 30.4740x^3 - 58.9683x^2 + 60.1853}$

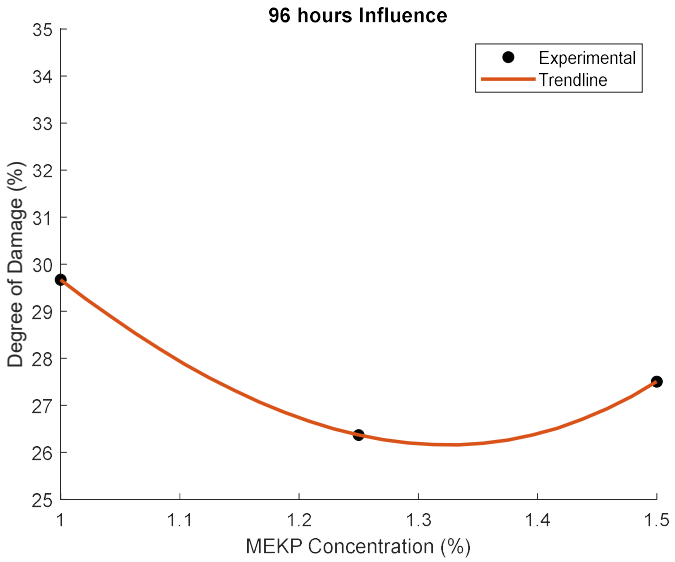

Figure 2.10: DoD Vs. Concentration (48 hours), $\boldsymbol{DoD = 20.1140x^3 - 39.9499x^2 + 49.5079}$

Figures 2.8, 2.9, and 2.10 clearly demonstrate that deviations from the manufacturer's recommended MEKP concentration (1.25%) led to an increase in the degree of damage. Specimens with lower MEKP concentration exhibited a higher degree of damage compared to those with

higher MEKP concentration. This can be attributed to incomplete curing in the samples with lower MEKP concentrations and excess hardener present in higher MEKP concentrations.

Multilinear Regression (MLR)

As mentioned previously, multilinear regression was selected for the global scale analysis due to its minimal test case requirements to develop the statistical model while still incorporating multiple variables. MLR was employed to incorporate the different influences the isolatable variables (cure time before testing and hardener concentration) had with one another and their overall effect on degree of damage. The multilinear regression formula developed using MATLAB followed the equation format: $DoD_{Global} = G + B_1\ t + B_2\ c$. In this equation, DoD_{Global} represents the predicted degree of damage (%), G is the y-intercept (a constant), B_1 and B_2 are calculated weights for the variables, t denotes time (in hours), and c stands for MEKP concentration (%).

To account for the influence exhibited by the miscellaneous variables, it is imperative to identify methods for its isolation and incorporation. In this study, the incorporation of isolating each batch's variance to define the miscellaneous variable is employed and utilized to form a global miscellaneous influence, assuming the variance within a batch is caused by the miscellaneous influence. Definition of miscellaneous influence in each batch was incorporated using the coefficient of variation (CV) [271], [272], by dividing the average value within the respective batch by its standard deviation to develop a percentile influence caused by the miscellaneous variables. After each batch's miscellaneous variance was defined, the overall average and standard deviation for the miscellaneous influence was calculated. By performing this step for all 9 batches, a percentile range of miscellaneous uncertainty was classified on average to be 13.7% with a standard deviation of 2.9%.

Combining DoD_{Global} with the percentile range influence, the final theoretical equation was obtained: $DoD_{Global} = (G + B_1\ t + B_2\ c) * (13.7 \pm 2.9\%)$. This final equation was then populated within MATLAB using the values of time ranging from 24 to 96 hours, and MEKP

concentrations (%) ranging from 1.00% to 1.50% to compare with the experimental data. The raw experimental data is illustrated within Figure 2.11, the development of the statistical representation and envelope are illustrated in Figure 2.12, and the comparison of the experimental data and the statistical representation is illustrated in Figure 2.13.

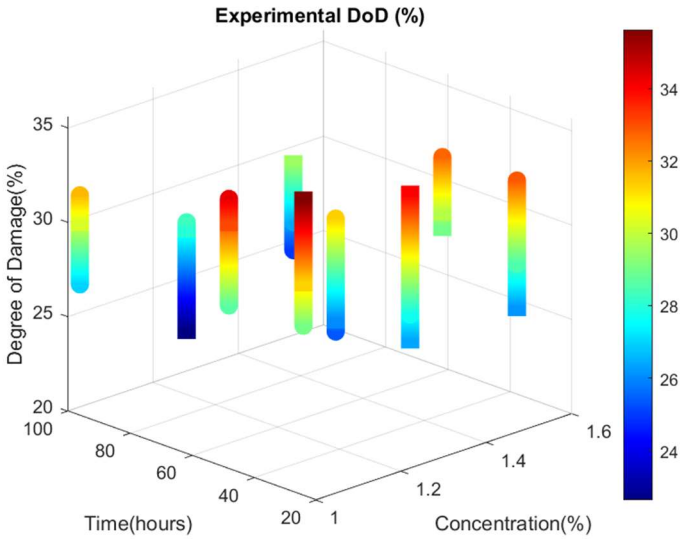

Figure 2.11: Experimental Degree of Damage from the 9 Tested Specimen Batches

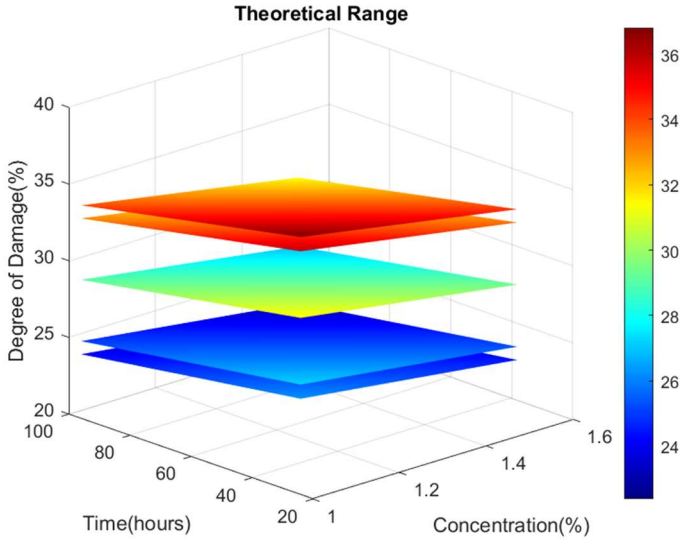

Figure 2.12: Theoretical Range for the Degree of Damage Developed by DoD_{Global}

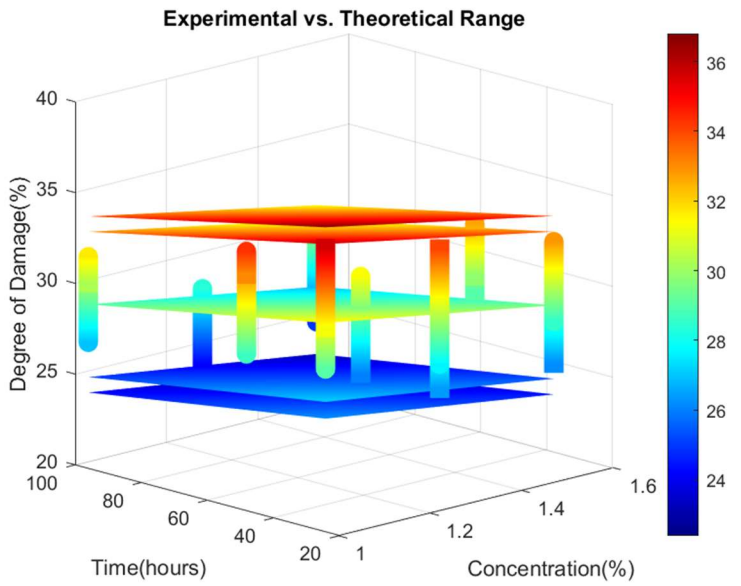

Figure 2.13: Evaluation Graph the Batch Testing Results and the Developed Theoretical Range

$$\boldsymbol{DoD_{Global} = (36.6779 - 0.0347t - 4.3130c) * (13.7 \pm 2.9\%)}$$

Figure 2.11 displays the experimentally obtained degree of damage values, with each column representing a batch of samples, as previously detailed in Table 2.1. Each column shows the maximum and minimum degree of damage at the top and bottom, while the middle portion represents the mean degree of damage for that specific batch.

Figure 2.12 represents the theoretical range of the degree of damage (DoD), derived from the DoD_{global} equation. The middle plate (Turquoise) signifies the predicted averages of DoD with relation to independent variables using the DoD global equation before applying the miscellaneous uncertainty variance. The top two plates (red) and bottom two plates (blue) represent the average coefficient of variance caused by the miscellaneous variables (second from the top and second from the bottom) and its standard deviation (top and bottom). The overall probabilistic envelope is defined by the extrema plates (top and bottom), with the identification from the standard deviations stating experimental results should exist in between them with 95% confidence.

Figure 2.13 illustrates how all of the experimental batches test data fit within the predictive range of the probabilistic envelop, displaying a strong correlation with the global mean and

standard deviation. Analysis of the DoD global equation and the respective coefficients applied to variables reveal the global sensitivity with respect to each variable. The absolute value of the coefficient highlights the overall influence on the degree of damage, with a higher magnitude carrying a higher influence. The miscellaneous variables had the highest influence accounting for a 13.7% variance on average. The MEKP concentration had the second highest influence with a coefficient magnitude of 4.31. Cure time before testing had the least influence with a coefficient magnitude of 0.0347.

CONCLUSION

To investigate the influence of uncertainty within constituent materials, this study delved into the uncertainty quantification of vinyl-ester resin samples. Within the study, two variables of prejudicial uncertainty which could be tested to identify their variance within system were identified as the resin to hardener concentration percentage and the cure time before testing. A third miscellaneous variable was used to encompass the variance caused by unknown variables while still enabling them to be accounted for within probabilistic study. These factors were systematically examined to gain insights into their impact on the mechanical behavior of vinyl-ester specimens subjected to impact loading at room temperature (25 °C). Notable findings from this inquiry are as follows:

- Interactions of the miscellaneous variable introduced variations of approximately ±13% across the batches tested.
- While cure kinetics studies have shown that the overall degree of cure is achieved within 10 hours at room temperature [273], the results showed increasing the time between curing of the specimen and testing resulted with a decrease in the degree of damage by up to 3% at 96 hours. This increase in mechanical properties has been observed when comparing specimens cured at room temperature and tested in a range of 24 to 168 hours after [274].

- Deviations from the recommended MEKP concentrations of 1.25% resulted in an increase in damage, this is attributed to a decrease in hardener resulting in insufficient crosslink promotion [275], and an increase in hardener leading to an upsurge in the crumble of peroxides and the creation of highly reactive free radicals [276] resulting in a reduction to the stiffness of the material.
- Multilinear regression (MLR) proved adept at capturing the sensitivities of the degree of damage, with short-term tests showing MEKP concentration (%) to exert greater influence than cure time before testing, as evidenced by a greater coefficient magnitude of 4.31 from the DoD_{Global} equation.
- By incorporating a miscellaneous global mean and standard deviation, multilinear regression (MLR) generated a theoretical predictive equation that closely aligned with the experimental data.

These initial investigations underscore the substantial potential for uncertainty quantification within a polymer resin matrix, such as vinyl-ester resin. As further research is conducted, and more variables with uncertain variances are tested the overall influence of miscellaneous variance will diminish. A comprehensive understanding of the effects of various sources of uncertainty on the mechanical properties of composites is imperative for establishing guidelines for optimal composite manufacturing.

Chapter 3: Kevlar Pulp Interlaminar Reinforcement for Carbon Fiber Reinforced Polymer Composites

INTRODUCTION

Due to the ice melting in the Arctic, new navigation routes have been created, and it is projected an increase in transportation [2], [277]. The naval vessels traveling these routes will be subjected to a plethora of extreme environmental conditions, such as temperatures as low as -60 ◦C, seawater, and impact events (dropped tools, hail, submerged ice) [278], [279]. Carbon fiber reinforced polymer (CFRP) composites have been widely used in the naval industry due to their lightweight, high specific strength, and high specific stiffness [280]–[284]. A major concern of CFRP laminates used for naval vessels in Arctic navigation is their low resistance to impact damage due to their layered nature and the Arctic temperature effect on them. Low-velocity impact (LVI), which occurs at velocities below 10 m/s [285], produces barely visible impact damage (BVID) on the composite surface but with the potential of significant internal damage [286].

LVI response of CFRP laminates at room temperature (RT) [287]–[308] and low temperatures [64], [73], [309]–[314] have been studied extensively in the past. They have reported that during an impact event, the most common failure mechanisms are matrix-cracking, fiber pullout, and delamination due to their poor toughness in the resin-rich region (interlaminar region) between the layers [315]–[321]. Delamination is one of the most dangerous forms of damage in composites because of its drastic reduction in material strengths while being difficult to detect [322]. Gomez-del Rio et al. (2005) [323] performed LVI tests to identify the influence of different stacking sequences (unidirectional, cross-ply, quasi-isotropic, and woven) and low temperatures on carbon fiber reinforced epoxy matrix laminates. Samples were tested at 20 °C, -60 °C, and -150 °C using impact energies ranging from 1 J to 13 J. It was reported that as the temperature decreased, the damaged area increased. Papa et al. (2019) [324] performed LVI tests on carbon fiber reinforced composites using two different matrix materials: vinyl-ester and epoxy resin. Samples were subjected to 5, 10, and 20 J impact energies at 25 °C and -25 °C. They concluded that as the

temperature decreased, the epoxy resin samples exhibited a damage increase, while the specimens with vinyl ester resin showed lesser amounts of delamination at lower temperatures. Castellanos et al. (2018) [309] investigated the LVI response of woven carbon vinyl ester samples subjected to 20, 25, 30, and 35 J at 25 °C and -50 °C. They reported that at -50 °C, the main damage mechanism was fiber breakage, while at 25 °C it was matrix cracking. In an encompassing report with literature from 1994-2020 regarding the low-temperature effects on CFRP composites, Sapi et al. (2020) [325] reported that colder temperatures had a positive effect on CFRPs' strength, modulus, and fatigue properties, with adverse effects in the form of reductions to ductility, failure strain, and impact strength.

A deep understanding of the failure mechanisms involved when composites are subjected to LVI at Arctic temperature (-60 °C) is necessary to design lightweight and damage tolerant structures for Arctic naval applications. There is always the need to improve the interlaminar region to strengthen the overall through-thickness properties of the composites. In an effort to improve the through-thickness properties of CFRP laminates, there have been many studies on interlaminar reinforcement methods including, Z-pinning [325]–[333], Carbon Nanotubes [[282], [334]–[339], Vertically Aligned Carbon Nanotubes, [340]–[343], 3D Weaving [16], [61], [344]–[347], Stitching [348]–[351], Tufting [352]–[356], Interleaving/ShortFibre [357]–[360], Graphene Nanoplatelets [361]–[365], and ZnO Nanowires [366]–[369]. While these methods have been shown to increase the through-thickness mechanical properties, they substantially increase the cost and complexity of manufacturing, and decrease the in-plane mechanical properties of the composites [370]. Micro-length aramid fibers (Kevlar® pulp) have been studied recently as interlaminar reinforcement that can increase the delamination toughness and improve the through-thickness properties without adding significant changes to the manufacturing process [371]–[373]. Ye 2021 et al. [373] investigated the compression-after-impact (CAI) of carbon fiber composites with interlays of Aramid pulp micro-/nanofibers. The samples were subjected to impact energies of 3.8 and 9.3 J. After impact, CAI tests were performed on the impacted specimens. They concluded that delamination was reduced due to the bridging effects of the aramid microfibers that

produced a “linking” effect with the layers of carbon fibers, localizing the damage, and absorbing impact energy. In addition, they concluded that the Aramid pulp increased the CAI strength up to 86.7%. Yang et al. [374] investigated the enhancement of Basalt Fiber Reinforced Polymer (BFRP) composites by introducing Aramid Pulp (AP) fibers with micro-fiber trunk and nano-fiber branches as interleaving at BFRP interlayers. This innovative approach strengthened the flexural strengths and elastic moduli and promoted quasi-vertical fiber bridging behaviors in the interfacial transition region. The introduced AP fibers illustrated fiber bridging preventing crack propagation along the bonding interface of BF/epoxy. Three-point bending tests reveal that the 4 g/m2 AP interleaving exhibits the most significant improvement, yielding a 63.4% increase in flexural strength and a 47.1% increase in elastic modulus compared to the base composites. In addition to the strengthening effect in the through-thickness properties of composite materials, Kevlar® pulp offers the benefit of being easy on manufacturing. Due to the reinforcement existing in the form of matrix modification through micro-fibers, it can be implemented in a quickly large-scale operation for commercially reinforced prepreg composites [372]. While there have been several studies regarding Aramid pulp, there is a lack of research regarding the implementation of Kevlar® pulp as an interlaminar reinforcement in CFRP composites subjected to LVI at Arctic temperatures.

This study investigates the feasibility of Kevlar® pulp as an interlaminar reinforcement for CFRP laminates subjected to LVI at Arctic temperatures (AT). Woven carbon fiber and vinyl-ester resin samples were manufactured with Kevlar® pulp interlaminar reinforcement (reinforced) and without interlaminar reinforcement (pristine). Drop-weight impact events were performed using an Instron CEAST 9340 drop tower impact system, with impact energies of 5, 10, 15, and 20 J. The LVI responses of unreinforced and Kevlar® pulp reinforced CFRPs at room (RT) and AT were elucidated. For each energy and each temperature, four samples were tested. The impact responses were evaluated based on impact duration time (ms), contact force (N), velocity (m/s), energy (J), and displacement (mm). In addition, the BVID at the impacted and back face of the CFRP composites were evaluated with an optical microscope.

MATERIALS AND COMPOSITE FABRICATION

Material Selection

Compared to unidirectional fibers, woven carbon fiber's fiber architecture has an inherent crack propagation mitigation [375]. Therefore, 3K plain weave woven carbon fiber from FibreGlast [270] was selected for this study. Matrix material selection consisted of #1110 vinyl-ester resin from FibreGlast. Vinyl-ester resin is a commonly used matrix system for marine applications due to its UV resistance and corrosive resistance [183], [184]. Methyl-Ethyl Ketone Peroxide (MEKP) was used as the hardening agent for vinyl-ester resin. Kevlar® pulp (fibrillated) was obtained from FibreGlast. The microfibers were about 10-20 μm in diameter and 0.5-1.7 mm in length [283]. Table 3.1 shows the mechanical properties of the material system:

Table 3.1 Woven Carbon Fiber, Vinyl-Ester Resin, and Kevlar® pulp Mechanical Properties

	Woven Carbon Fiber [60]	Vinyl-Ester Resin [270]	Kevlar® pulp [270]
Tensile Modulus (GPa)	227.5-240.6	3.7	58.8
Tensile Strength (GPa)	4.2 - 4.4	82.7	-----
Density (kg/m^3)	1750 - 2000	1.80	1.40
Nominal Thickness (mm)	0.3048	-----	-----

Design and Fabrication of CFRP Composites

Two different CFRP laminates were manufactured pristine (no interlaminar reinforcements) and reinforced (Kevlar® pulp interlaminar reinforcement). For both laminates, 16 layers of plain weave woven carbon fiber with a stacking sequence of [0/90] with the size of 330 x 330 mm were cut.

Unreinforced Matrix Preparation

The matrix mixture consisted of vinyl-ester resin and MEKP as the hardening agent at a ratio of 100:1.25 by weight to follow manufacturer specifications. The resin was mixed for approximately 2 minutes mixing time to ensure the fibers were adequately dispersed within the resin matrix system. Adequate dispersion was identified visually by a uniform consistency throughout the matrix and a homogenous change in color was observed.

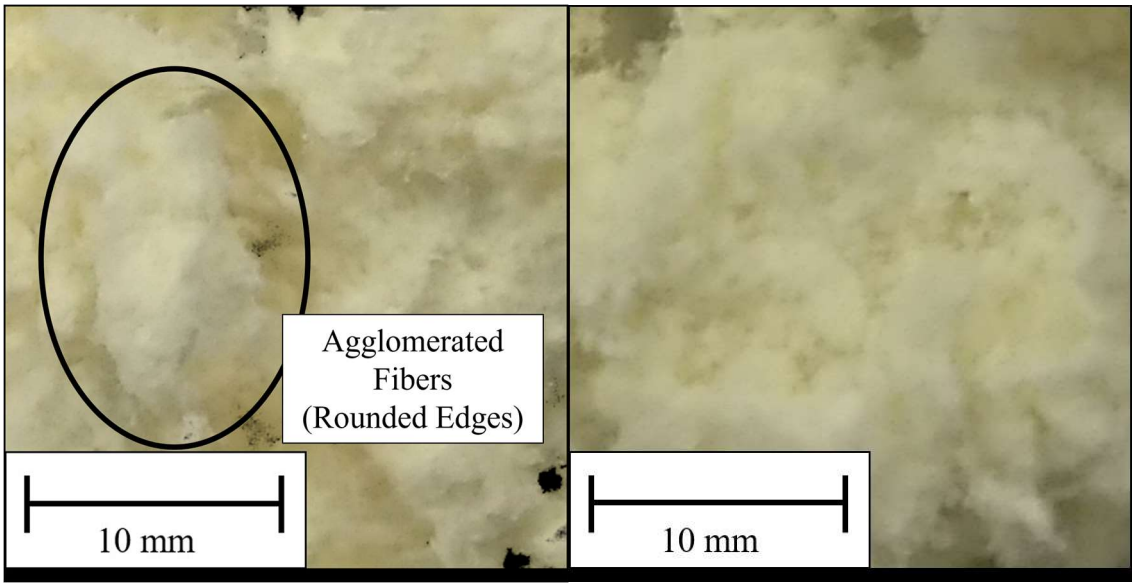

a) Closed/Agglomerated Kevlar® Pulp b) Open Kevlar® Pulp

Figure 3.1: Forms of Kevlar® Pulp: a) Closed, b) Open

Reinforced Matrix Preparation

Kevlar® pulp arrives from the manufacturer as conglomerated pellets (also known as clumps/closed pellets), seen in Figure 3.1a where the micro-fibers are clumped into individual masses. To ensure micro-fiber dispersion within the resin for matrix modification, these conglomerations need to be broken apart (also termed separated/opened). To ensure micro-fiber dispersion and break apart the conglomerated pulp, a Krupps flat blade commercial-grade coffee bean grinder with 20,000 revolutions per minute (RPM) is used to break them apart mechanically and to ensure uniform dispersion. The conglomerated pulp is placed inside of the Krupps blender,

not exceeding half of the blender's volume capacity. This allows the blender's blades to break the masses apart without the pulp compacting due to volume increase as the fibers disperse. The blender is operated in 20-second bursts, with a pause to reposition fibers clinging to the roof of the container due to static cling and repeated for a total of 3 cycles of 20-second bursts. This process proved to be sufficient to break apart the conglomerated Kevlar® pulp and was visualized by loose Kevlar® pulp fibers that appear more voluminous without rounded edges caused by clumping (Figure 3.1b). After the Kevlar® pulp had been sufficiently broken apart, it was added to the vinyl-resin/MEKP mixture, which was mixed previously for five minutes. The ratio of the resin to Kevlar® pulp was 15:1 by volume as advised by the manufacturer FibreGlast.

Laminate Manufacturing (Pristine and Reinforced)

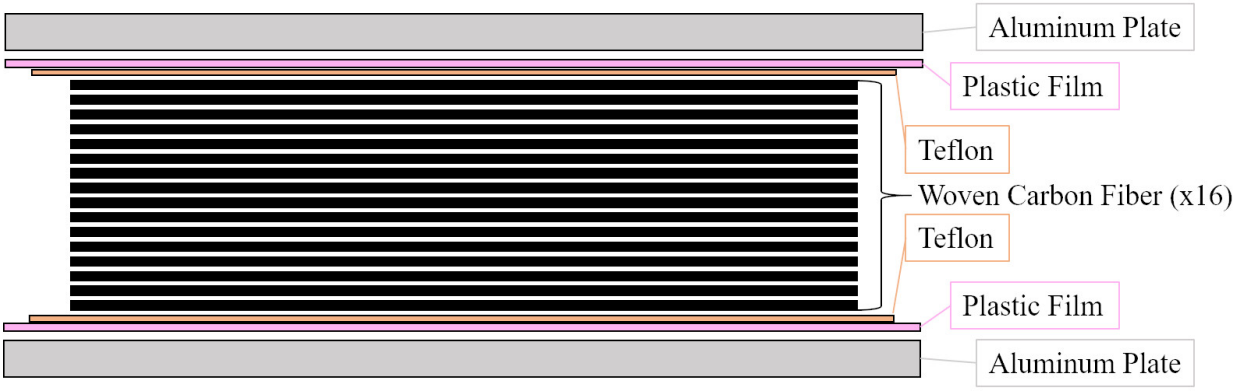

Figure 3.2: Laminate Layup Representation

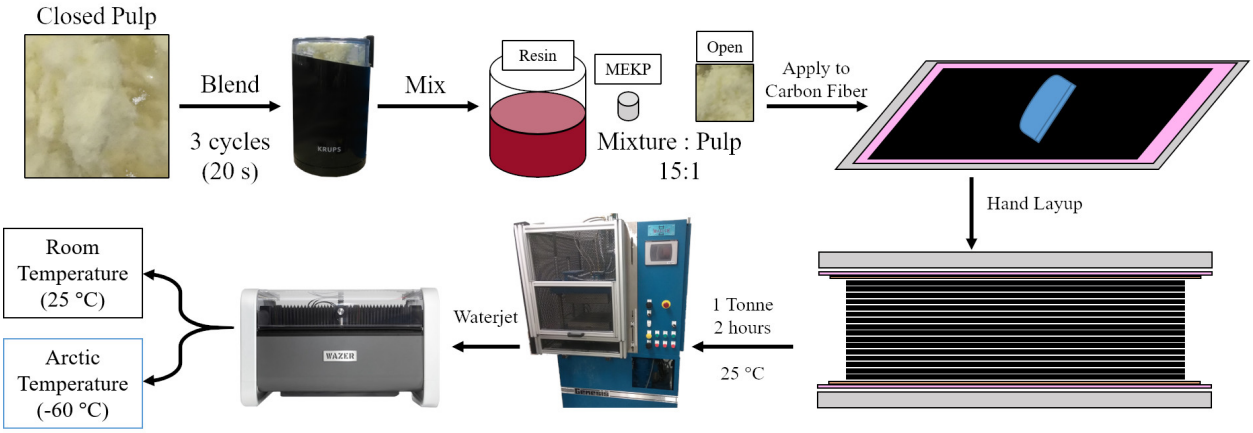

Figure 3.3: Kevlar® Pulp Reinforced CFRP specimen fabrication

The hand lay-up method was used for both laminates (pristine and reinforced). Two flat aluminum molds were wrapped with Stretchlon® 800 Bagging film. Then on top of one aluminum mold, a Teflon sheet of 350 x 350 mm was placed to aid with the laminate removal after curing. After that, the first woven carbon layer was laid, and resin was applied and distributed with a silicone squeegee. This process was repeated 16 times with the corresponding resin for pristine and reinforced laminates. Once the lay-up was completed, the Teflon sheet and second aluminum mold were placed on the top of the laminate, as seen in Figure 3.2. Finally, the laminate was placed in a Wabash Genesis hydraulic press, with a uniaxial pressure of 2 MPa for 2 hours at room temperature to cure. After the 2-hour cure time, the lay-up system was removed from the press and left to rest for 24 hours to ensure the laminate had fully cured as recommended by the manufacturer FibreGlast. Then specimens were cut to the dimensions of 150 mm x 100 mm using an in-house Wazer desktop waterjet cutter to ensure smooth edges and reduce the risk of delamination. These dimensions were based on the ASTM D7136M-20 "Standard Test Method for Measuring the Damage Resistance of a Fiber-Reinforced Polymer Matrix Composite to Drop-Weight Impact Event" [376]. After cutting, specimens were set aside for another 24 hours to completely dry. Then specimens were placed into individual plastic bags to avoid environmental contamination and conditioned to their respective test temperatures. The pristine and reinforced samples had a thickness of 4.2 ± 0.2 mm and 4.2 ± 0.3 mm, respectively. Representation for the manufacturing process is illustrated in Figure 3.3. A total of 48 samples were obtained, which allowed 3 pristine and 3 Kevlar® pulp reinforced specimens to illustrate representative data for each impact energy/temperature combination.

Laminate Conditioning

Conditioning of RT specimens consisted of the bagged specimens sitting inside a closed container at 25 °C for 48 hours. Bagged specimens marked for arctic temperature tests were placed into a Thermo-Scientific (TSU 600) chiller at -60 °C for 48 hours prior to testing.

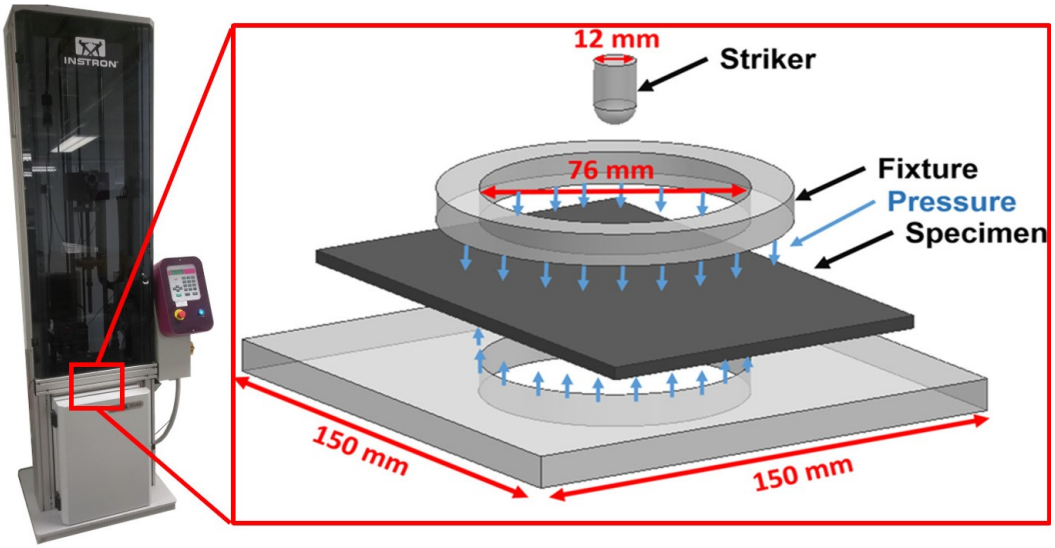

Figure 3.4: Impact Machine Setup

LVI tests were performed using an Instron CEAST 9340 drop tower impact machine. Specimens rested within a steel clamp system with a 76 mm diameter cutout acting as simple support during impact events, as seen in Figure 3.4. A steel hemispherical striker with a 12 mm diameter and a mass of 3.1 kg was used for all impact events. The impact energies were calculated according to the kinematic energy equation (Eq 1):

$$KE = \frac{1}{2} * m * v^2 \quad (1)$$

Where, KE represents kinetic energy or impact energy, m represents striker mass, and v represents the striker's velocity. The impact energies selected were 5J, 10J, 15J, and 20J, to coincide with low impact velocities of 1.82 m/s, 2.57 m/s, 3.16 m/s, and 3.65 m/s, respectively. The Instron impact machine calculated the striker's velocity by altering the initial height of the striker relative to its internal photocell using the potential energy equation (Eq. 2):

$$PE = mgh \quad (2)$$

Where, PE represents potential energy, m represents striker mass, g represents the gravitational constant (9.81 m/s 2), and h represents the height of the striker relative to the top of

the laminate specimen. Impact response data was recorded using the data acquisition system (DAS 8000 Junior) where time (ms), contact force (N), velocity (m/s), energy (J), and displacement (mm) were recorded during the impact event at 666 (kHz) . The BVID on the impacted and back face of the laminates was evaluated with an AmScope optical microscope with 100x magnification, where the failure mechanisms in the form of matrix cracking, fiber pullout, and fiber breakage were identified.

Arctic temperature tests followed the previously mentioned setup for impact tests, but with the addition of an environmental chamber, which was conditioned to -60 °C for 20 minutes prior to each impact test with liquid nitrogen LN2. Previous studies have shown that by preconditioning the chamber for a minimum of 20 minutes before testing, thermal equilibrium can be ensured for the AT environment.

RESULTS AND DISCUSSION

The LVI responses of the laminates were analyzed based on the contact force (N), displacement (mm), energy (J), and time (ms) for the impact energies of 5, 10, 15, and 20 J. In addition, post-impact visual inspection was performed using an optical microscope to identify the BVID on the surface of the impacted and back face of the samples.

Contact Force-Time Histories

Figure 3.5 shows the representative force-time graphs of pristine (no reinforce) and Kevlar® pulp reinforced specimens subjected to impact energy of 20 J at RT and AT. The curves of the samples (RT-Reinforced, AT-Pristine, and AT-Reinforced) have smooth, similar profiles. This behavior was also observed for all the samples (pristine and reinforced) impacted at 5, 10, and 15 J at both temperatures. For this reason, only the 20 J impact sample graphs are shown. The RT-Pristine impacted at 20 J were the only samples that exhibited a sudden drop in load. This is associated with the loss in stiffness of the laminate due to fiber fracture and delamination [326]. During LVI events, the force increased rapidly to the maximum value as soon as the striker was in

contact with the laminate. The oscillations observed in the increasing portion of the force-time graph were produced due to internal damage such as matrix cracking, fiber breakage and delamination [282]. After the maximum impact force (peak force) was reached, the striker rebounded from the specimen. In the case of the 20 J RT-Pristine samples, the striker rebounded after the drop in load. Then the force dropped to 0, signifying that the striker detached from the specimen. This post-peak behavior is only observed for laminated composites subjected to LVI events, where the striker rebounded. The peak force for the pristine and reinforced samples tested at all the impacted energies at both temperatures is presented in Figure 3.6. The peak force increased as the impact energy increased. At AT, the matrix became stiffer and rigid. For this reason, the samples tested at AT (AT-Pristine and AT-Reinforced) exhibited higher impact forces as compared to their RT counterparts (RT-Pristine and RT-Reinforced). The addition of interlaminar reinforcements to the laminates increased their rigidity. Therefore, all the reinforced samples experienced higher peak forces than pristine specimens. The explanation of the AT and reinforcement stiffening effect in the laminates is provided in section 4.6.

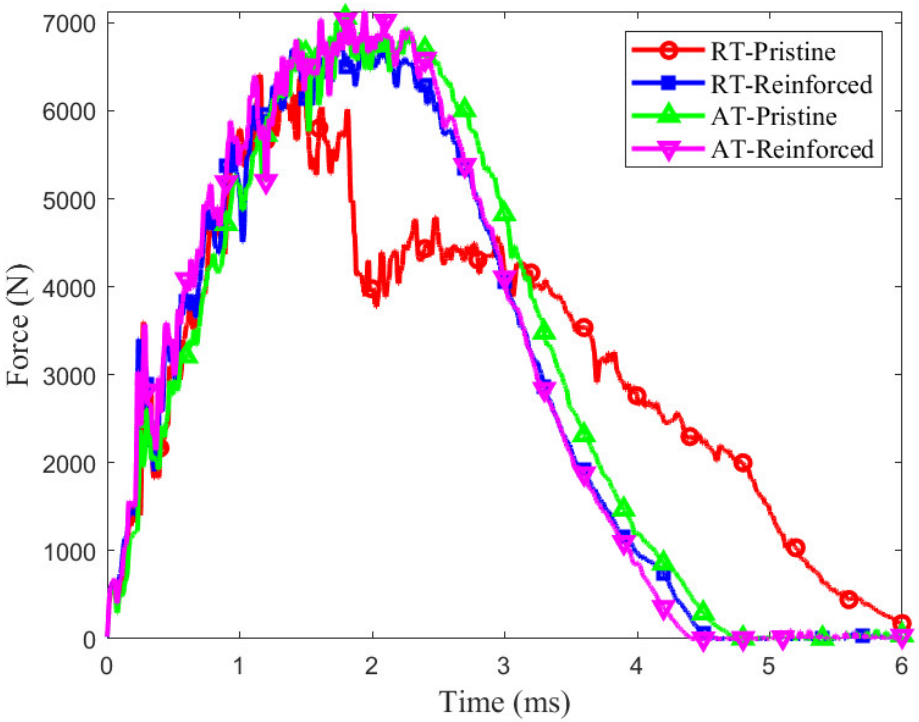

Figure 3.5: Representative force-time graphs of pristine and reinforced composites subjected to 20 J at RT and AT.

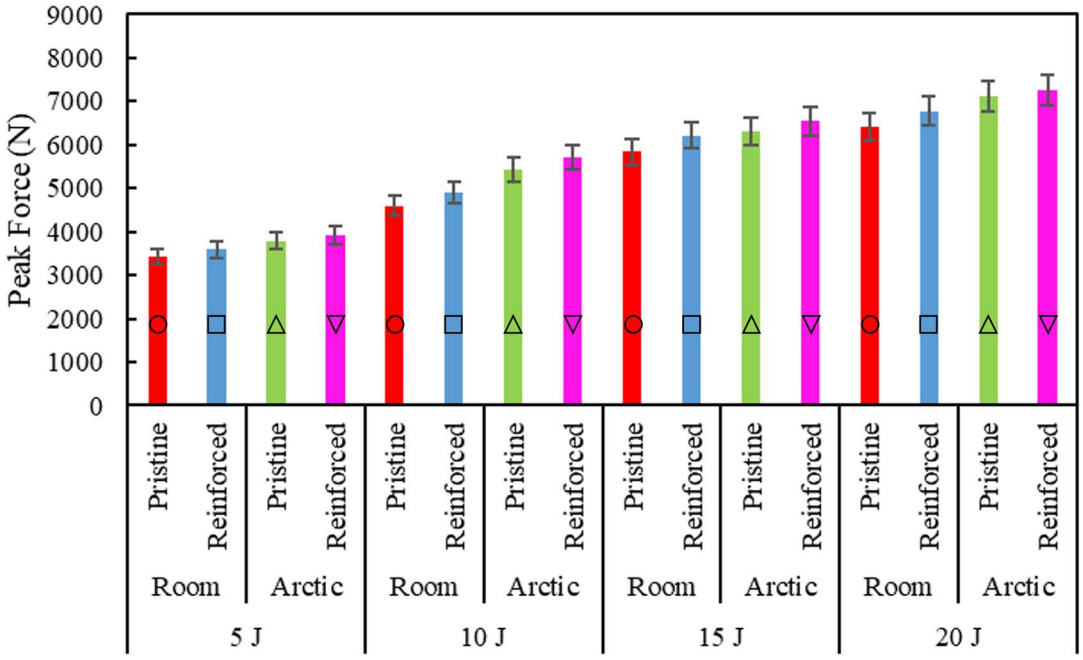

Figure 3.6: Average peak force of all the reinforced and pristine samples tested at both temperatures (RT and AT) and at all impacted energies (5, 10, 15, and 20 J).

Contact Force-Displacement Histories

Figure 3.7 shows the representative force-displacement graphs of pristine and Kevlar® pulp reinforced specimens subjected to impact energy of 20 J at RT and AT. The initial slope of the force-displacement curve represents the bending stiffness. The bending stiffness for the pristine and reinforced samples tested at all the impacted energies at both temperatures is presented in Figure 3.8. The bending stiffness for the samples impacted at AT was higher than their RT counterparts due to the matrix's increase in stiffness and rigidity at low temperatures. All the reinforced samples experienced higher bending stiffness than their pristine counterparts due to the stiffening effect of the Kevlar® pulp reinforcement. As the impact energy increased, the samples impacted at AT showed a decreasing trend in their bending stiffness. This is because, at low temperatures, the matrix became stiffer and more brittle [282]. This decrease in bending stiffness is attributed to the increase in damage at low temperatures. On the other hand, the RT samples

showed an increasing trend in their bending stiffness as the impact energy increased. This increase in bending stiffness is attributed towards the rate-dependency exhibited by many polymers [377].

The maximum displacement for the pristine and reinforced samples tested at all the impacted energies at both temperatures is presented in Figure 3.9. As the impacted energy increased, an increasing trend was observed in the maximum displacement of all the samples. Due to the stiffening effect of the AT and the Kevlar® pulp reinforcement, the AT-Reinforced samples experienced the lowest deflection. Conversely, the RT-Pristine samples experienced the highest deflection. The enclosed area of the force-displacement graph represents the absorbed energy by the samples. The AT-Reinforced had the lowest enclosed area of all the graphs. Therefore, the laminate experienced the least amount of damage of all the tests. Conversely, the RT-Pristine experienced the highest damage of all the samples. This can be seen in the large area under the curve and the drop in load. The energy absorption of the samples is discussed in more detail in the following section.

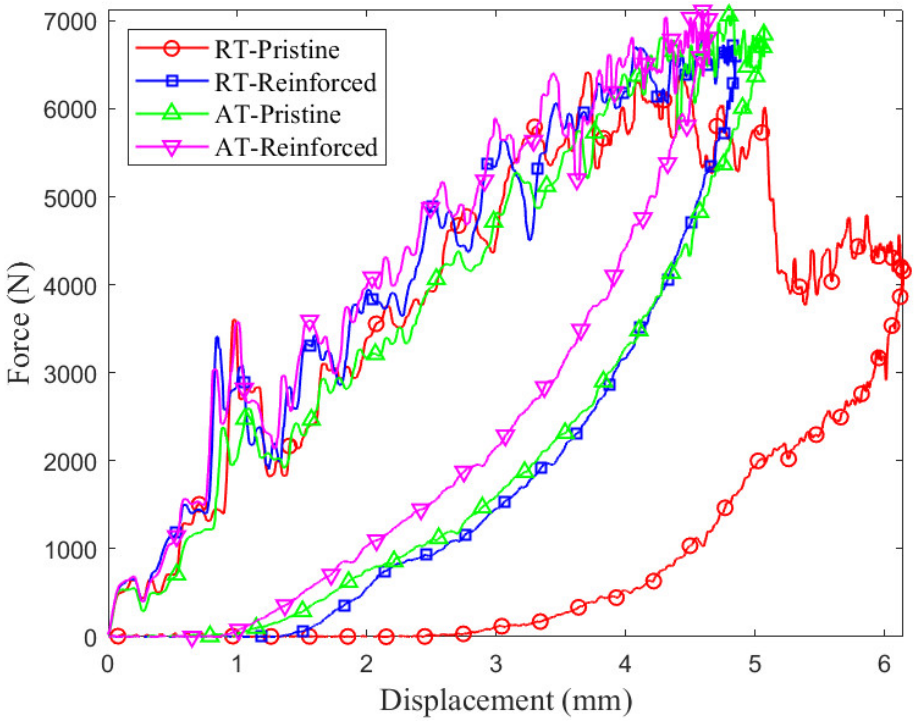

Figure 3.7: Representative force-displacement graphs of pristine and reinforced composites subjected to 20 J at RT and AT.

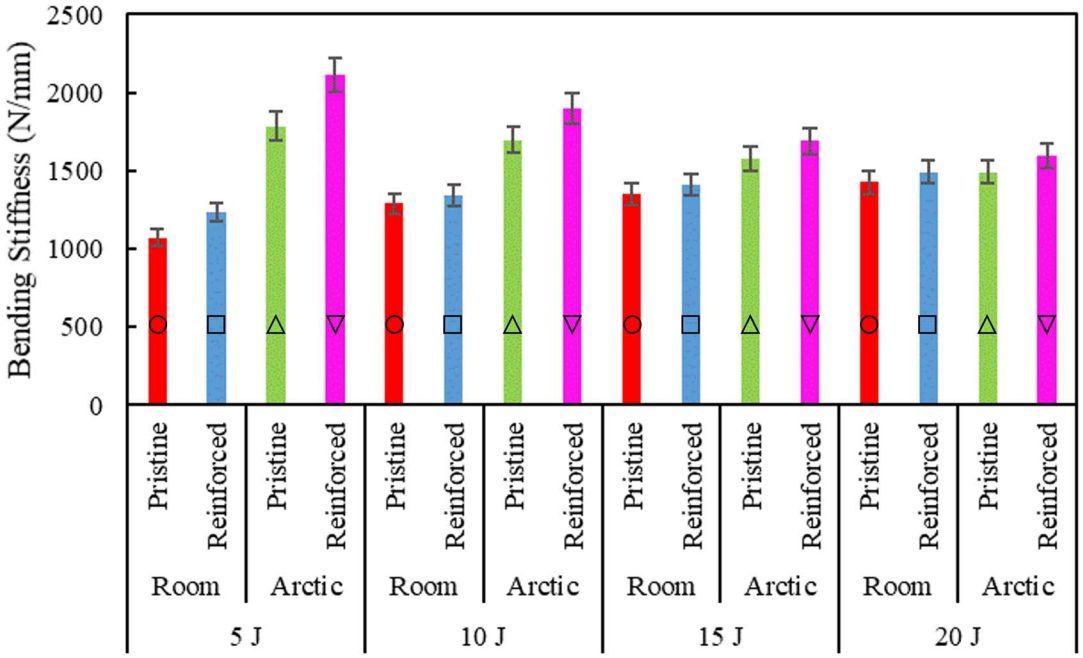

Figure 3.8: Average bending stiffness of all the reinforced and pristine samples tested at both temperatures (RT and AT) and at all impacted energies (5, 10, 15, and 20 J).

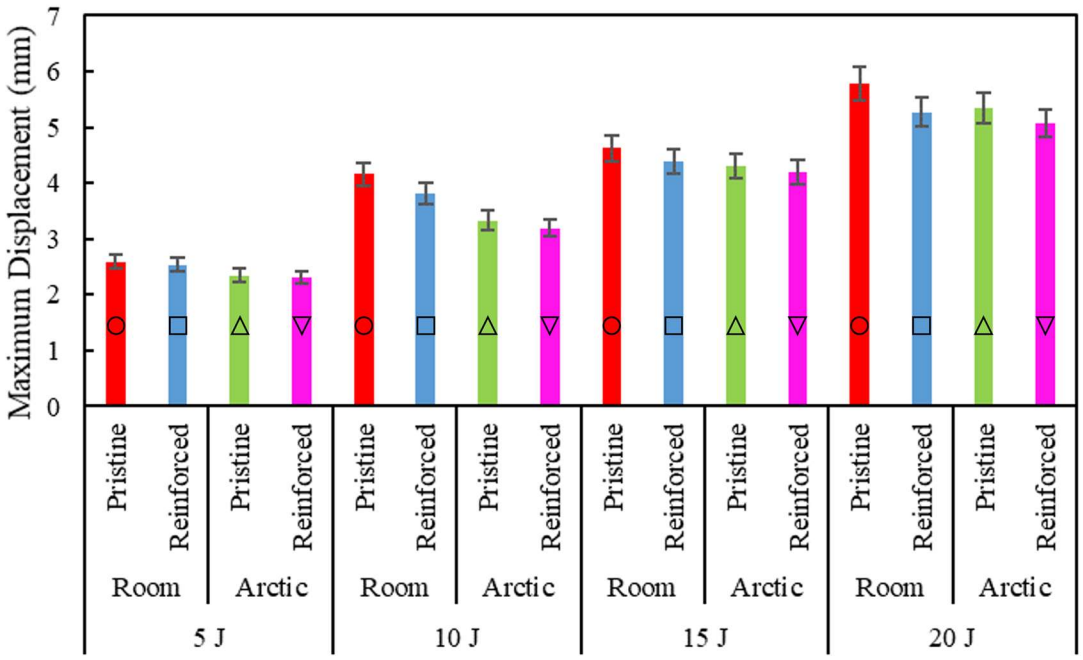

Figure 3.9: Average maximum displacement of all the reinforced and pristine samples tested at both temperatures (RT and AT) and at all impacted energies (5, 10, 15, and 20 J).

Impact and Absorbed Energy

Figure 3.10 illustrates a representative energy-time graph of a composite laminate that was subjected to an LVI event. The maximum energy corresponds to the impacted energy. The absorbed energy by the laminate corresponds to the plateau region of the graph, and it is the energy that is dissipated in the composite structures by failure mechanisms, such as crack propagation, delamination, or perforation [378]. The elastic energy is calculated as the difference between the impact energy and absorbed energy, as seen in Eq. 3. This is the energy that goes back to the system through the striker's rebound. The degree of damage (DoD) represents the scale of damage a laminated composite could receive during an LVI event on a scale of 0 to 1, where 0 illustrates no damage has occurred and 1 illustrates perforation of the flat panel. Any value within the 0 to 1 scale represents that the laminate has received permanent damage through failure mechanisms (e.g., matrix cracking, fiber failure, fiber pullout, delamination). DoD is calculated as the ratio of absorbed energy to impact energy, as seen in Eq. 4.

$$Elastic\ Energy = Impact\ Energy - Absorbed\ Energy \tag{3}$$

$$Degree\ of\ Damage = \frac{Absorbed\ Energy}{Impact\ Energy} \tag{4}$$

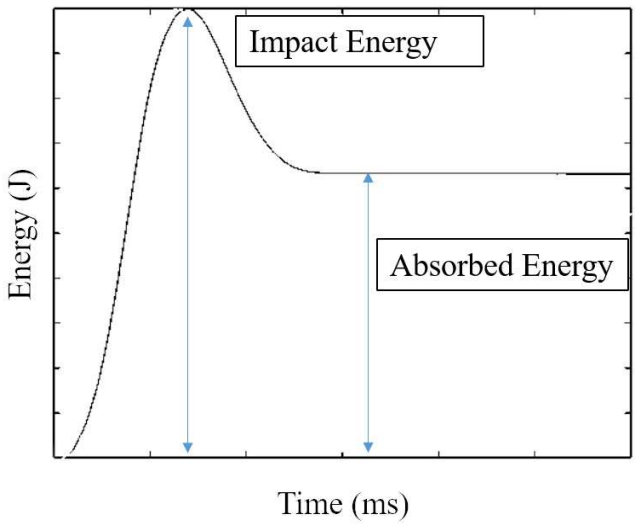

Figure 3.10: Representative energy-time graph.

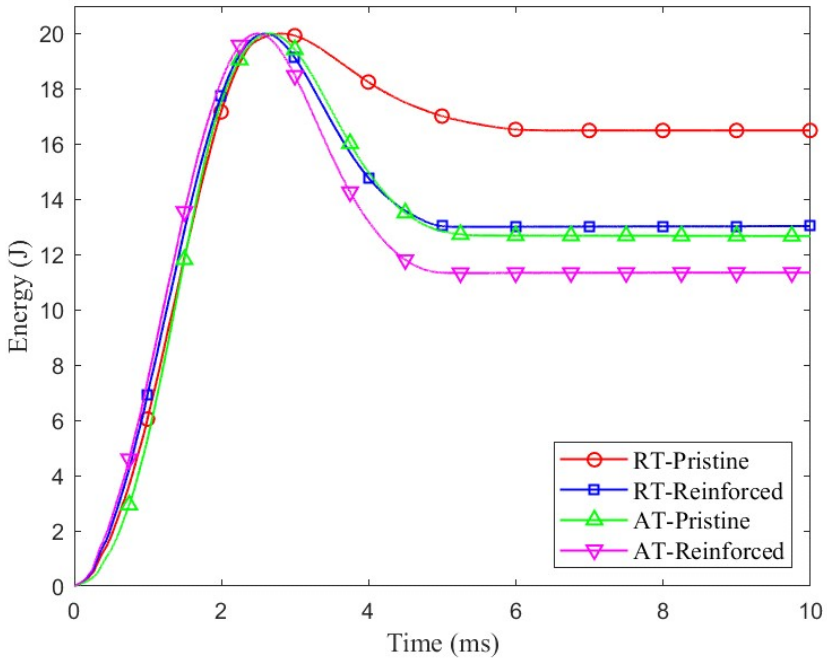

Figure 3.11: Representative energy-time graphs of pristine and reinforced composites subjected to 20 J at RT and AT.

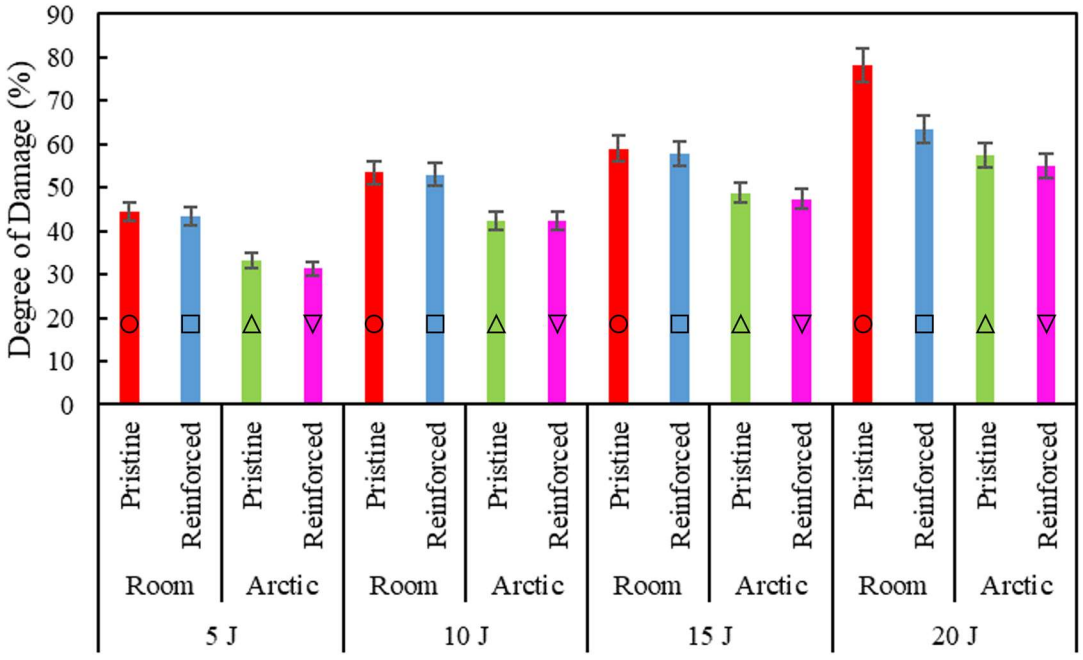

Figure 3.12: Average degree of damage for all the reinforced and pristine samples tested at both temperatures (RT and AT) and at all impacted energies (5, 10, 15, and 20 J).

Figure 3.11 shows the representative energy-time graphs of pristine (non-reinforced) and Kevlar® pulp reinforced specimens subjected to impact energy of 20 J at RT and AT. The sample that absorbed less energy was the AT-Reinforced. This lesser magnitude of damage is represented by the lower value of the plateau region, signifying the laminate absorbed less energy through deformation or failure mechanisms. This is attributed to the increase in stiffness of the laminate due to low temperatures and the Kevlar® pulp reinforcement. On the other hand, the RT-Pristine sample absorbed the most energy of all the samples. The drastic increase in absorbed energy corresponds to the drop in load observed in the force-time (Figure 3.5) and force-displacement (Figure 3.7) graphs due to fiber breakage at the back face of the laminate. The DoD for the pristine and reinforced samples tested at all the impacted energies at both temperatures is presented in Figure 3.12. As the impact energy increased, the DoD increased for all the samples, signifying an increase in damage. The RT-Pristine samples experienced the higher DoD of all the samples at their respective impact energy. All the samples tested at AT (reinforced and pristine) had lower DoD than their RT counterparts (reinforced and pristine). The reinforced specimens had lower DoD than their pristine counterparts at both temperatures.

Arctic Temperature Effect on the CFRP Composites

The two toughening mechanisms of CFRP laminates exposed to AT are: 1) the coefficient of thermal expansion (CTE) mismatch between the fiber and the matrix and 2) the increased intermolecular bond forces of the matrix. As the temperature drops, the CTE mismatch between the fiber and matrix increases the laminate's interfacial shear strength. As a result, the laminates' tensile strengths increase the laminates' rigidity [379]. The intermolecular bond forces of the matrix increase at low temperatures [380], [381]. Therefore, the laminates became more rigid but brittle at AT [325], [382]. Due to the increase in rigidity and stiffness of the laminates at low temperatures, the samples experienced higher bending stiffness and peak forces while exhibiting

a lower DoD and displacement than their RT counterparts. For this reason, less damage was observed for all the samples tested at AT.

Kevlar® Pulp Reinforcement Effect on CFRP Composites

Kevlar® pulp has been shown to have the potential to increase the impact damage tolerance of composite materials by strengthening their interfacial resin-rich and suppressing delamination. Although interlaminar reinforcements can increase the fracture toughness of composites, it is well known that any increase in thickness can drastically reduce the volume fraction and in-plane strength of the composite [383]–[385]. The Kevlar® pulp reinforced resin-rich regions had an average increase of approximately 8.75 μm as compared to the pristine samples. This is attributed to the high curing pressure (2 MPa) used during manufacturing. Kevlar® pulp is a combination of microfibers and nanofibers that, after being mixed with the resin, are randomly and evenly distributed between the carbon fiber layers. When the laminate is subjected to compression in the manufacturing process, the fibers are pushed into the gaps between the woven layers and are intertwined with the carbon fiber bundles [373]. During an LVI event, the Kevlar® microfibers are pulled out, split, or broken, creating a fiber bridging effect that suppresses delamination growth [372], [373]. Due to the increase in stiffness and damage tolerance, the reinforced laminates exhibited lesser DoD and displacements and higher peak forces and bending stiffness than their pristine counterparts at all impact energies and temperature conditions.

Damage Mechanisms

Figures 3.13 and 3.14 show the impacted face (front) and back face (back) of the reinforced and pristine laminates subjected to 5 and 20 J at RT and AT. All the samples impacted at 5, 10, and 15 J exhibited similar failure mechanisms. For this reason, the BVID of the specimens impacted at 5 J and 20 J are presented. With a brief description of the damage mechanisms observed within each representative specimen.

Pristine sample impacted with 5 J at room temperature: Front face damage was observed at the impact site in the form of matrix cracking in a cross-pattern. The cracking extended outwards from the center of the impact site up to 14 mm. There was no observed back face damage.

Reinforced sample impacted with 5J at room temperature: Front face damage was observed at the impact site in the form of matrix cracking in a cross-pattern. The cracking extended outwards from the center of the impact site up to 10 mm. There was no observed damage on the back face.

Pristine sample impacted with 5 J at arctic temperature: Front face damage was observed at the impact site in the form of matrix cracking primarily in a circular pattern coinciding with the location of the striker impact. The back face observed no damage.

Reinforced sample impacted with 5 J at arctic temperature: There was no observed visible damage on the front face, nor the back face.

Pristine sample impacted with 20 J at room temperature: Front face damage was observed at the impact site in the forms of matrix cracking and fiber breakage. Matrix cracking coincided primarily with the location of the striker impact. Fiber breakage and matrix cracking continued through to the back face as the striker began to perforate the laminate.

Reinforced sample impacted with 20 J at room temperature: Front face damage was observed at the impact site primarily consisting of matrix cracking in a large cross-pattern and minimal fiber breakage at the center of the impact site. The matrix cracking extended outwards from the impact site up to approximately 23 mm. The back face observed minimal matrix cracking in a circular pattern approximately 15 mm in diameter.

Pristine sample impacted with 20 J at arctic temperature: Front face damage was observed at the impact site as matrix cracking in a cross pattern, the largest cracking extended approximately 10 mm from the center of the impact site. The back face observed matrix cracking in a circular pattern with an overall diameter approximately 11 mm.

Reinforced sample impacted with 20 J at arctic temperature: Front face damage was minimal with a matrix crack approximately 3 mm long at the center of the impact indentation. The back side observed matrix cracking in a circular pattern approximately 10 mm in diameter.

From the analysis of damage mechanisms within each representative specimen, several comparisons can be made. At room temperature, reinforced specimens saw smaller areas of matrix cracking at low energies, and an increased presence of matrix cracking at higher energies, however fiber breakage to the degree seen by pristine samples never occurred in reinforced samples. The increased matrix cracking as opposed to fiber breakage and perforation can be attributed to the microfiber's interlinking and fiber bridging. The presence of the Kevlar® pulp resulted in less damage due to the strengthening of the matrix through inter-ply fiber bridging mitigating delamination and crack propagation [374].

Regarding temperature, the specimens impacted with low and high energies within a room temperature environment observed more damage. This was illustrated by the increased matrix cracking and penetration observed within the laminates. Specimens impacted at arctic temperatures observed smaller matrix cracking, and there was never penetration of the laminate. The increased impact resistance within arctic test specimens is correlated to the increase in rigidity of the matrix resulting from the lower temperatures hindering polymer chain mobility [113].

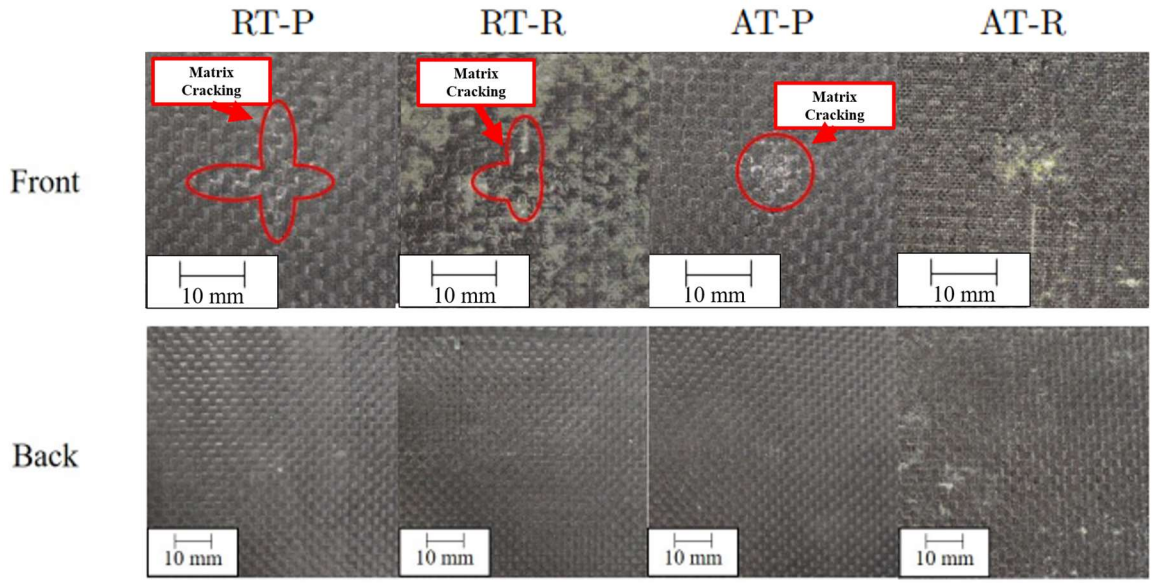

Figure 3.13: Representative BVID zones for Pristine (P) and Reinforced (R) specimens impacted at 5 J

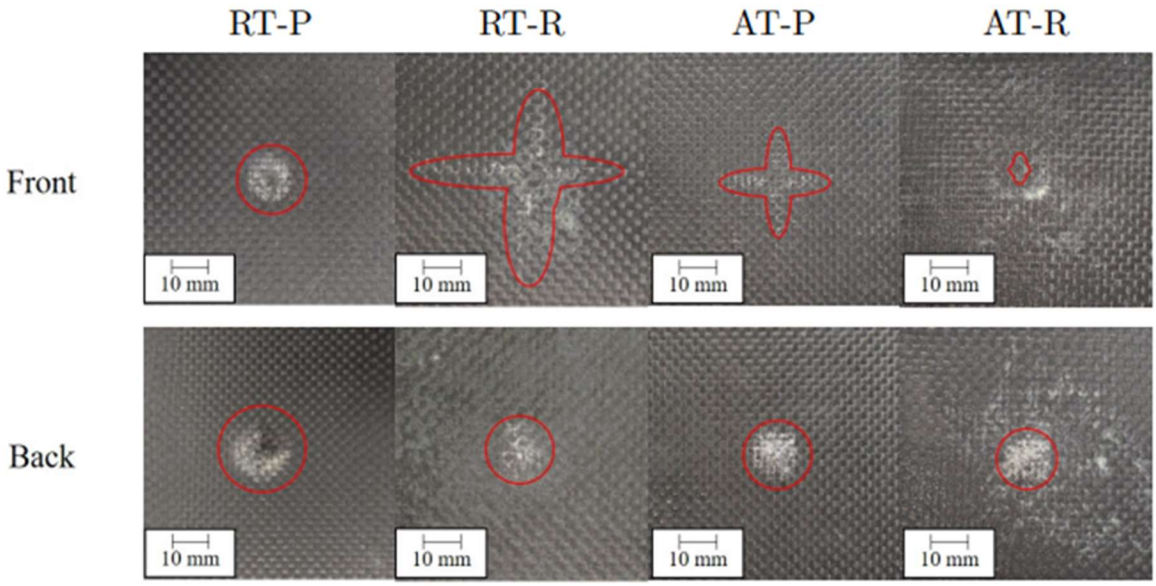

Figure 3.14: Representative BVID zones for Pristine (P) and Reinforced (R) specimens impacted at 20 J

CONCLUSION

This study investigates the feasibility of Kevlar® pulp as an interlaminar reinforcement for CFRP composites subjected to LVI at RT and AT for naval applications. The impacted responses and BVID were investigated. The conclusions are as follow:

- Temperature influence: Due to the increase in rigidity and stiffness of the laminates at AT, the samples experienced higher bending stiffness and peak forces while exhibiting a lower DoD and displacement than their RT counterparts. For this reason, less damage was observed for all the samples tested at AT. This was attributed to the polymer chain mobility being hindered by the lower temperatures, resulting in a stiffer system [113].
- Kevlar® pulp interlaminar reinforcement influence: Due to the increase in stiffness and damage mitigation of the laminates with Kevlar® pulp interlaminar reinforcement, the reinforced laminates exhibited lesser DoD and displacements and higher peak forces and bending stiffness than their pristine counterparts at all impact energies and temperature conditions. This was attributed to the microfiber presence strengthening the matrix through inter-ply fiber bridging mitigating delamination and crack propagation [374].

- Damage mechanisms, reinforcement: Specimens reinforced with Kevlar® Pulp observed a decrease in matrix cracking size at room temperature and an increase in matrix cracking instead of perforation at arctic temperature when compared to pristine samples.
- Damage mechanisms, temperature: Specimens impacted at arctic temperatures observed a decrease in overall damage mechanisms. This is attributed to the lower temperatures increasing the stiffness of the polymer matrix as polymer mobility is hindered.

Kevlar® pulp has the potential to be used as an interlaminar reinforcement for AT applications. AT and Kevlar® pulp enhanced the impact damage tolerance of plain weave woven carbon fiber/vinyl-ester laminates during LVI scenarios primarily due to the increase in rigidity and stiffness of the matrix. In addition, reinforced laminates did not have a significantly increase in their thickness when the interlaminar reinforcement was added. Therefore, the composite structures' in-plane strengths and volume fraction were not affected. This interlaminar reinforcement also has the potential that it could be easily incorporated into the large-scale production of composites.

Chapter 4: Vertically Aligned Carbon Nanotube Interlaminar Reinforcement (Brief Overview)

INTRODUCTION

Fiber-reinforced resin matrix composites find widespread application in aerospace, automotive, marine, medicine, energy, and other industries due to their unique combination of high specific strength, specific stiffness, and lightweight characteristics [386]–[393]. Typically, CF-reinforced composite laminates comprise plies with varied directions, with each ply featuring unidirectional continuous fibers, woven fabric, or prepreg, all incorporating CFs as the reinforcement material. Widely employed in aerospace [394], [395], land transportation [396], and marine industries [397], these laminates have become commonplace in secondary structures for aerospace applications. [398]–[403]. However, the mechanical performance of CF-reinforced composite laminates has encountered limitations, particularly concerning interlaminar properties.

Many existing laminates lack reinforcement throughout the overall thickness, rendering them susceptible to early-stage delamination, thereby impacting their structural integrity [404]. Various damage modes, including fiber failure, fiber/matrix interfacial debonding, matrix cracking, fiber pull-out, and delamination, manifest during this process [405]. Fiber-reinforced polymer composites exhibit superior in-plane mechanical performance, but their out-of-plane properties necessitate further investigation [349], [406], [407]. Traditional methods to mitigate delamination, such as stitching [392], weaving [393], and Z-pinning [408] have shown promise in bolstering delamination resistance, however, they often introduce challenges like increased weight, reduced cost-effectiveness, potentially damaging fibers compromising in-plane properties [409]–[411].

To address this, incorporating nano-constituents within the resin or at interlayers has been explored as a means of achieving more continuous through-thickness reinforcement [412]–[415]. Additionally, modifying composite interfaces through fiber surface treatments, such as sizing, coating nano-materials, chemical grafting, oxidation treatment, and plasma treatment, proves

effective. Recently, nano-constituents, including carbon nanotubes, graphene, and nano silica, have been considered to enhance mechanical properties [287]–[302]. However, diverse research conclusions arise from variations in dispersion, filling fraction, functionalization methods, and agglomeration control, posing a significant challenge [411], [432].

The emergence of carbon nanotubes (CNTs) introduces exciting prospects for improving the interlaminar mechanical performance of carbon fiber-based laminate composites. Extensive studies [398], [433] have highlighted the outstanding mechanical, electrical, and thermal properties of CNTs, positioning them as potential "super fibers" for the future. Furthermore, the chiral nature of CNTs allows for covalent and non-covalent modifications with various chemical groups, enhancing biocompatibility and making them suitable for multi-scale composite materials [400], [434]. Recent research [402], [403], [435], [436] has confirmed the adaptability of CNTs to polymer matrices and their positive impact on material performance. Consequently, scholars [335], [401], [437]–[439] have integrated CNTs into composite laminates to enhance interlaminar mechanical properties. For instance, Yanan Su [401] reported a 42.9% increase in interlaminar shear strength (ILSS) by incorporating CNTs into the interlaminar region, while Thakre [440] demonstrated a 6.5% enhancement in mode-I interlaminar fracture toughness with pristine single-wall CNTs (P-SWCNT). Despite these advantages, challenges arise from the spatial distribution of nanotubes, impacting the final properties due to inherent aggregation and anisotropy.

Several studies have examined the incorporation of vertically aligned carbon nanotubes (VACNTs) at the interlayer and their impact on composite mechanical properties [341], [432], [441]–[445]. Garcia et al. [441] demonstrated an increase in toughness due to VACNTs introduction in interplies. Veedu et al. [442] reported a significant increase in mode I and mode II toughness by synthesizing CNTs directly on SiC fuzzy fibers. Falzon et al. [443] observed improved interlaminar fracture toughness for nano-engineered composites, attributing it to VACNTs-resin adhesion. Dynamic mechanical properties, such as damping ratio and enhancement, were reported to increase substantially in nano-reinforced composites [432], [442].

Incorporating randomly oriented CNTs into composite matrices, while avoiding cluster formation and agglomeration, has been challenging [445]–[450]. Few studies provide comprehensive manufacturing instructions for nano-engineered composites that preserve the initially vertically aligned state of VACNTs. Garcia suggested several resin-VACNTs incorporation methods, with capillarity proving effective [451]. Capillary rise studies by Beard et al. [452] demonstrated partial and heterogeneous resin rise in VACNTs forests [Beard2015]. However, coalescence of VACNTs due to surface tension is commonly observed.

After impregnation, the challenge lies in separating VACNTs from their growth substrate before consolidating a hybrid composite laminate. Wardle et al. [453] described a separation step using a metallic roller, limiting the surface by the lateral aspect of the cylinder. Falzon et al. [454] proposed impregnating resin into VACNTs forest on the prepreg surface before removal, optimizing transfer efficiency by considering parameters like pressure, temperature, and time.

This paper undertakes a thorough examination of various VACNT introduction methods into carbon fiber-reinforced composite laminates. It delves into techniques for controlling crucial parameters like dispersion, distribution, and orientation of VACNTs in laminates. The influence of VACNT morphology and spatial distribution on interlaminar mechanical performance is scrutinized, providing valuable insights for laminate design. The paper also discusses and analyzes the influence mechanism of VACNTs on interlaminar properties, shedding light on intentional processing and control strategies. Finally, the challenges and opportunities in carbon fiber-reinforced composite laminates filled with VACNT fillers are outlined, offering a roadmap for both practical engineering production and the guidance of future researchers entering the field.

SYNTHESIS AND GROWTH OF VACNTS

The synthesis and growth of vertically aligned carbon nanotubes (VACNTs) represent a critical phase in harnessing their exceptional properties for interlaminar reinforcement in CFRP composites. Several methodologies exist for the synthesis of VACNTs, each with distinct

advantages and challenges. This section will delve into various methods employed for synthesizing VACNTs, the key parameters influencing the growth process, and the current landscape of challenges and recent advancements in VACNT synthesis.

Arc Discharge

Arc discharge is a well-established method for the synthesis of vertically aligned carbon nanotubes (VACNTs) and involves the application of a high electrical current between two graphite electrodes in an inert gas atmosphere. The intense heat generated by the electric arc vaporizes the graphite electrodes, creating a plasma of carbon vapor, which drifts toward the cathode. Upon reaching the cathode, the carbon cools, resulting in the formation of CNTs [455], [456]. Achieving vertical alignment in this method requires a vertical electric field between the cathode and anode, inducing growth normal to the substrate [457], [458]. Researchers manipulate primarily two parameters arc current and gas environment to tailor the properties of the nanotubes [459].

Higher arc currents result in an increased number of electrons striking the anode, leading to more sputtering of carbon precursors. The applied current generates resistive heating, raising the temperature. This elevated temperature causes the carbon precursors in the anode to sublimate, forming carbon vapors that nucleate at the cathode, ultimately resulting in the formation of nanotubes. The optimal current has been a heated debate, as studies have shown various amplitudes ranging from 1-20A [460]–[464] to above 700A [465]. While increasing the current increases the yield [466], [467], it does not improve the structure [468] and results in a reduced amount of SWNT [469].

In the arc chamber used for nanotube growth, pressurized gases such as nitrogen, hydrogen, helium, or argon are employed. Hydrogen, known for its high thermal conductivity, is considered the most efficient quencher for nanotube growth. Studies by Zhao and Ando [zhao1998] indicate that hydrogen promotes CNT growth and reduces carbonaceous materials by

forming hydrocarbons. Li et al. [470] observed that hydrogen leads to a cleaner CNT surface by selectively etching amorphous carbon impurities. However, challenges arise with pure hydrogen, as Zhao [471] suggests it is unfavorable for mass production of single-walled nanotubes (SWNT) due to plasma instability. Tang et al. [472] noted that rapid hydrogen introduction prevents nanotube ends from closing. To address this, hydrogen is often mixed with a noble gas like argon or helium to stabilize the plasma. Liu et al. [473] found that switching from hydrogen to helium promotes SWNT growth. Shi et al. [474] observed that a helium atmosphere strongly influences SWNT yield. Control over nanotube diameter is achieved by altering the composition of argon–helium gas ratios, as demonstrated by Farhat et al. [475].

By carefully adjusting these parameters, researchers can tailor the arc discharge process to produce CNTs with desired characteristics, such as high purity, specific chirality, and controlled diameter. However, while arc discharge is effective, challenges such as impurity incorporation and limited control over nanotube alignment persist. Nevertheless, ongoing advancements in process optimization and catalyst engineering continue to enhance the reproducibility and scalability of arc discharge for synthesizing vertically aligned carbon nanotubes.

Laser Ablation

Laser ablation is a method employed for the synthesis of vertically aligned carbon nanotubes (VACNTs). In this technique, a high-power laser is directed onto a target material containing a carbon source, usually a metal catalyst, within a controlled gas environment [476]. The intense laser energy vaporizes the target material, and carbon species subsequently condense and form nanotubes on a substrate [477]. Laser ablation offers precise control overgrowth conditions, allowing for the production of VACNTs with well-defined structures. Parameters such as laser power and wavelength are systematically optimized to enhance the uniformity and quality of the resulting nanotubes [478]. Growth and diameter distribution of CNT tubes can be tailored by altering the laser power, where an increase in power results in an increase in growth and

diameter [479] of the nanotubes. Tailoring the laser wavelength with respect to fluence (energy delivered per unit area) exists as another form to customize the diameter of CNT. Longer wavelengths have been reported to have a wider range of acceptable fluence coupling to develop satisfactory CNTs and produced more abundance in wider diameter nanotubes [480].

Chemical Vapor Deposition

In contrast, Chemical Vapor Deposition (CVD), despite producing lower crystallinity than arc discharge, is more popular for growing VACNTs due to its advantages in cost, yield, purity, structural control, and architecture [456], [481], [482]. Three key components are involved in CVD-based VACNT synthesis: a hydrocarbon, a catalyst, and a catalyst support. In this process, hydrocarbon vapor passes through a high-temperature (600–1200 °C) tubular reactor containing molten catalyst material. At this elevated temperature, the hydrocarbon thermally decomposes, and VACNTs grow on the catalyst. The growth mechanism has been extensively studied, with models like the "tip-growth model" [483] proposing volume diffusion-based growth, where the hydrocarbon decomposes, establishing a temperature gradient across the catalyst nanoparticle, and carbon diffuses down, initiating VACNT growth from the base. Alternatively, the "base-growth model" [481] occurs when strong catalyst–substrate interaction prevents VACNT precipitation from pushing the metal particle up, resulting in growth from the base. Advancements in in situ technologies led to the exploration of a surface diffusion growth mechanism. In this model, catalyst nanoparticles form at elevated temperatures, and carbon binds to step edges, initiating VACNT growth on the surface [484]. Recently, studies [485] suggest VACNT nucleation is initiated by carbon cap formation, where a graphene embryo forms between opposite step-edges of the catalyst nanoparticle, eventually leading to curved carbon cap formation and VACNT wall generation.

Plasma Enhanced Chemical Vapor Deposition

Various CVD methods have been developed to tune VACNT physical characteristics, including diameter, number of concentric tubes, and length. Plasma-enhanced CVD (PECVD) is considered the most reliable and controlled method among these [456]. PECVD is similar to traditional CVD but employs high-energy plasma to decompose the carbon precursor, offering higher selectivity and tunability by controlling the amount of ionized carbon species supplied to the catalyst. PECVD also provides high alignment controllability by managing the electric field [486], [487], and its use has demonstrated tunable chirality and growth rate of CNTs, emphasizing its controllability [488], [489]. This controllability is developed using a capacitively coupled radio frequency (cc rf) source, in which one of the electrodes is coupled to a rf power supply [490]. This results in a self-bias phenomenon, where positive ions are continuously accelerated to the electrode area [491]. Using this interaction allows researchers to not only align nanotubes [492]–[495], but they can also be grown free standing [496]–[498], as well as on surfaces that are curved and tilted [494]. Growth size and diameter of CNTs can also be tailored using PECVD. By exposing catalyst nanoparticles to plasma through a pretreatment, the plasma prevents agglomeration of the nanoparticles during CNT growth [499]. This in turn results in smaller diameter CNTs as this prevents the formation of larger particles.

Parameters Affecting the Growth Process

With the vast applications for VACNTs, the desired sizes change drastically, VACNT lengths observed from literature ranged from 5 μm to 2.6 mm [500]–[506]. Additionally, the diameter of VACNTs can also vary depending on the job application, previous studies have had diameters ranging from 7-nm to 43 nm [500]–[506].

Achieving precise control over the growth of VACNTs demands a nuanced understanding of the myriad parameters influencing the synthesis process. Catalyst properties, including size, composition, and distribution, play a pivotal role in determining nanotube characteristics.

Substrate morphology and temperature during growth are equally critical, impacting the alignment, density, and diameter of the resulting nanotubes [507]. The morphology of the substrate and the temperature conditions during the growth process play pivotal roles in determining the characteristics of the resulting nanotubes, encompassing factors such as alignment, density, and diameter [500].

The substrate, serving as the foundation for nanotube growth, provides a template that influences the orientation and arrangement of the nanotubes. Substrate properties, including surface roughness, crystal structure, and catalyst interaction, directly impact the nucleation and growth of carbon nanotubes [508]. For instance, a well-structured and catalytically active substrate can promote the uniform growth and alignment of nanotubes [508], contributing to enhanced structural integrity and desired properties.

Simultaneously, growth temperature is a critical parameter influencing the kinetics and energetics of the nanotube formation process. The choice of growth temperature significantly affects the diameter distribution, crystallinity, and overall quality of the nanotubes [509]. Higher growth temperatures can lead to increased carbon diffusion rates, promoting faster growth but potentially resulting in larger diameter nanotubes [510]. Conversely, lower temperatures may favor the formation of smaller diameter nanotubes but may require longer growth durations [511].

The interplay between catalyst and growth temperature further underscores the intricacies of nanotube synthesis. The catalyst acts as a facilitator in the growth process, influencing nucleation and guiding the direction of nanotube growth. Optimal catalyst–substrate interactions and growth temperature conditions are essential for achieving desired nanotube properties, such as chirality and structural uniformity.

In summary, substrate morphology and growth temperature are interrelated and critical parameters in carbon nanotube synthesis. Their combined influence determines the structural characteristics of the nanotubes, and a nuanced understanding of catalyst and growth temperature effects is imperative for tailoring nanotube properties to meet specific application requirements. Ongoing research continues to explore the synergies between substrate morphology, growth

temperature, and catalyst effects to advance the precision and efficiency of carbon nanotube synthesis processes. As such, the effects of catalyst and growth temperature effects are discussed.

Effect of Catalyst

In the synthesis process of VACNTs, catalyst selection stands out as a critical factor determining the successful preparation of these nanotubes. The catalyst assumes a pivotal role in shaping the morphology and structure of the resulting cracking products, serving as both the active center for carbon source decomposition and the focal point for carbon deposition [512]. Notably, transition metals, including Fe, Co, Ni, emerge as highly suitable catalysts for this purpose [513]. The distinctive high carbon solubility exhibited by these transition metals facilitates the formation of specific carbon structures, with carbon atoms benefiting from an elevated diffusion rate within this category of metals. It is this heightened diffusion rate that enables the nucleation and growth of VACNTs. Additionally, the strategic use of two-component or multicomponent metal catalysts presents an effective approach, capitalizing on the collective advantages of individual elements to attain optimal outcomes.

Effect of Growth Temperature

In the process of synthesizing VACNTs through CVD, the temperature plays a pivotal role in influencing both the carbon source cracking within the reaction chamber and the structure of the catalyst nanoparticles. Specifically, the structure and morphology of the resulting VACNTs exhibit a direct correlation with the growth temperature. The connection between temperature and growth rate [514] underscores the significance of temperature in determining the length of VACNTs. Lower growth temperatures contribute to incomplete carbon source decomposition and reduced catalyst activity, proving unfavorable for VACNT growth. As the temperature rises, the catalyst cracking and carbon atom activity intensifies, resulting in an augmented growth rate of VACNTs. However, an excessive increase in temperature eventually leads to elevated catalyst cleavage,

causing catalyst particle poisoning [515]. This critical juncture results in a loss of catalyst activity, consequently influencing the growth rate of VACNTs.

INTEGRATION METHODS FOR FRPC MANUFACTURING

The integration of vertically aligned carbon nanotubes (VACNTs) into fiber-reinforced polymer composites (FRPCs) involves strategic implementation methods during the manufacturing process to harness the enhanced properties offered by these nanotubes. Several distinct methods exist, each with their own benefits and drawbacks.

Prepreg impregnation and lay-up techniques

Prepreg impregnation and layup techniques represent a fundamental stage in integrating vertically aligned carbon nanotubes (VACNTs) into fiber-reinforced polymer composites (FRPCs). During prepreg manufacturing, VACNTs are dispersed within the resin matrix before impregnation onto the reinforcing fibers [516]. This process ensures a homogenous distribution of nanotubes, promoting consistent interlaminar reinforcement throughout the composite structure. The prepreg sheets, consisting of resin-infused fibers with embedded VACNTs, are then layered during the layup process to construct the desired composite structure. Precision in layup is crucial for controlling the alignment and distribution of VACNTs between individual laminae, directly influencing the enhancement of interlaminar properties. Effective impregnation and layup techniques are vital for achieving optimal mechanical and interlaminar performance in the resulting FRPCs [517]. Challenges with VACNT orientation during impregnation exist due to complexities with the aggregation of nanoparticles, viscosity control of dispersion, dispersion flowability through the reinforced materials, and filtration effects during the infusion into the fibers [518], .

VACNTS as Interleaves between Composite Laminae

In this approach, VACNT layers are strategically inserted between individual layers of reinforcing fibers during the layup process. The unique morphology and alignment of VACNTs offer the potential for targeted reinforcement in the interlaminar regions, addressing inherent weaknesses associated with delamination in FRPCs. The intimate contact between the VACNT interleave and adjacent laminae enhances load transfer mechanisms, thereby improving interlaminar strength and toughness [343]. Achieving proper alignment and uniform dispersion of VACNT interleaves is critical for ensuring consistent and dependable interlaminar reinforcement throughout the composite structure [519]. This method displays promise in overcoming interlaminar challenges in FRPCs, presenting an avenue for tailoring the interlaminar properties by strategically placing VACNTs between composite laminae during the manufacturing process.

Transfer Printing

An emerging method for integrating vertically aligned carbon nanotubes (VACNTs) into fiber-reinforced polymer composites (FRPCs) is transfer printing. This technique involves the controlled transfer of VACNTs from a growth substrate onto the surface of the composite during its fabrication. In this process, the aligned nanotubes are grown on a sacrificial substrate and subsequently transferred onto the resin-infused fibers or composite structure [520]. Transfer printing offers a precise and scalable approach, allowing for the strategic placement of VACNTs within the FRPC architecture [521]. This method displays potential advantages in achieving targeted interlaminar reinforcement by controlling the nanotube alignment and distribution [522].

CHARACTERIZATION TECHNIQUES FOR VACNTS IN CFRP COMPOSITES

Assessing the alignment, distribution, and interactions of vertically aligned carbon nanotubes (VACNTs) within carbon fiber reinforced polymer (CFRP) composites demands a

diverse array of characterization techniques. This section will delve into analytical methods employed for evaluating VACNT structures, morphology, and properties.

Structural Analysis

Raman Spectroscopy

Raman spectroscopy serves as a powerful analytical tool for characterizing vertically aligned carbon nanotubes (VACNTs) due to its ability to provide detailed information about the structural and vibrational properties of these nanomaterials [523]. In Raman spectroscopy, laser light is incident on the sample, and the scattered light is analyzed to reveal vibrational modes unique to the carbon-based structures of nanotubes. The distinctive G-band (graphitic) and D-band (disorder-induced) peaks in the Raman spectrum offer insights into the graphitic nature, defects, and alignment of VACNTs [524]. Additionally, the radial breathing mode (RBM) provides information about the nanotube diameter distribution [525].

Raman spectroscopy is invaluable in assessing the quality and uniformity of VACNTs, aiding researchers in optimizing synthesis techniques. Through this technique, researchers can monitor structural changes, assess the degree of functionalization, and ensure the desired characteristics for specific applications. Moreover, Raman spectroscopy plays a crucial role in quality control during the production of VACNTs, providing a non-destructive and rapid method for characterizing these vertically aligned structures.

Transmission Electron Microscope

Transmission Electron Microscopy (TEM) functions as a technique for elucidating the intricate structural details of vertically aligned carbon nanotubes (VACNTs) at the nanoscale. With its high spatial resolution, TEM enables researchers to investigate the morphology, alignment, and crystallinity of individual nanotubes. In TEM analysis, a beam of electrons passes through the sample, forming high-resolution images that provide valuable insights into the nanotube

dimensions, wall structure, and the presence of defects [526]. The technique also facilitates the study of VACNT interactions with catalyst particles, providing insights into the growth mechanisms [527]. By combining TEM with other characterization methods, such as selected area electron diffraction (SAED), researchers gain a comprehensive understanding of the crystalline structure and orientation of VACNTs [528].

X-Ray Diffraction

X-ray Diffraction (XRD) serves as a fundamental technique for characterizing the crystalline structure of vertically aligned carbon nanotubes (VACNTs). By exposing the nanotube sample to X-rays, the resulting diffracted patterns provide valuable information about the nanotube orientation, crystallographic phases, and interlayer spacing [529]. In XRD analysis, the diffraction peaks correspond to the arrangement of carbon atoms in the nanotube lattice. The identification and intensity of these peaks aid in determining the crystallinity and alignment of VACNTs [530]. The radial diffraction pattern often reveals information about the nanotube diameter distribution, offering insights into the uniformity of the synthesized nanotubes. Additionally, XRD complements other characterization techniques, providing a holistic understanding of the nanotube structure when combined with methods such as Raman spectroscopy and electron microscopy [531].

Morphological and Surface Analysis

Scanning Electron Microscope

Scanning Electron Microscopy (SEM) is a pivotal tool for investigating the surface morphology and structural characteristics of vertically aligned carbon nanotubes (VACNTs) at a micro to nanoscale resolution. In SEM analysis, a focused beam of electrons scans the sample's surface, generating high-resolution, three-dimensional images that offer valuable insights into the topography of VACNTs. SEM allows researchers to visualize the overall morphology of VACNT

arrays, providing information on the length, density, and alignment of individual nanotubes [532]. Furthermore, SEM is valuable for investigating the impact of growth parameters on the macroscopic structure of VACNTs [533].

Atomic Force Microscopy

Atomic Force Microscopy (AFM) is a highly valuable technique for characterizing the topography, surface roughness, and mechanical properties of vertically aligned carbon nanotubes (VACNTs) with exceptional spatial resolution. In AFM analysis, a sharp tip mounted on a cantilever scans the surface of the sample in a non-destructive manner, providing detailed insights into the nanoscale features of the nanotube arrays [534]. AFM allows researchers to visualize the height profiles of individual VACNTs, offering information on their length and diameter distribution [535]. Additionally, the technique provides valuable data on the surface roughness of VACNT films or arrays, aiding in the assessment of the overall quality and uniformity [532]. The ability of AFM to generate 3D images further enhances the understanding of the nanotube morphology [532]. One of the notable strengths of AFM lies in its capacity to measure the mechanical properties of VACNTs at the nanoscale. By applying force with the AFM tip, researchers can obtain information about the nanotube's elasticity, stiffness, and adhesion properties [536]. This mechanical characterization is crucial for applications where the mechanical behavior of VACNTs plays a pivotal role, such as in composite materials or nanoelectromechanical systems.

INTERLAMINAR REINFORCEMENT MECHANISMS OF VACNTS

The strategic integration of vertically aligned carbon nanotubes (VACNTs) within carbon fiber reinforced polymer (CFRP) composites introduces sophisticated interlaminar reinforcement mechanisms. This section will delve into the intricate interactions between VACNTs and the CFRP

matrix, highlighting their role in enhancing interlaminar shear strength (ILSS), contributing to fracture toughness, impact resistance, and influencing other key properties.

Interaction between VACNTs and CFRP Matrix

The successful integration of VACNTs into CFRP composites hinges on establishing strong and effective interactions between the nanotubes and the polymer matrix. The controlled vertical alignment of VACNTs facilitates direct load transfer pathways across the interlaminar regions. Additionally, the surface chemistry and functionalization of VACNTs play a pivotal role in promoting adhesion and compatibility with the surrounding polymer matrix [537]. These interactions create a seamless interface between the reinforcing nanotubes and the CFRP matrix, ensuring optimal stress transfer across layers and mitigating the risks of delamination. The tailored interfacial characteristics foster a synergistic relationship, enhancing the overall mechanical performance of the composite.

Enhancement of Interlaminar Shear Strength (ILSS)

A primary objective of incorporating VACNTs into CFRP composites is the augmentation of interlaminar shear strength (ILSS). The vertically aligned orientation of nanotubes creates an effective bridging mechanism between adjacent layers, significantly reducing the propensity for delamination. The intrinsic mechanical properties of VACNTs, such as high tensile strength and stiffness, synergize with the CFRP matrix to bolster ILSS. As a result, the composite exhibits enhanced resistance to interlaminar shear forces, crucial for applications where mechanical reliability and structural integrity are paramount.

Lee et al. [538] studied the effects of reinforcing HexPly IM7/8552 unidirectional plies reinforced with buckling patterned VACNTs. The hierarchical nano- and micro-engineered interlaminar reinforcement integration involved (1) inducing buckling in VACNT arrays to harness

energy dissipation of the wavy nanofibers, particularly during processes like pulling out, and (2) patterning VACNT arrays to enable a higher volume fraction of CNTs. The test methods involved short beam shear tests, which are essential for evaluating interlaminar shear strength and fatigue life. The impact of the hierarchical interlaminar reinforcements was substantial, altering the damage modes from monotonic and straight cracks to a more diffusive postmortem set of cracks. The integration of buckled and patterned VACNTs resulted in a significant enhancement, showing approximately a 7% increase in static interlaminar shear strength and an impressive 224% increase in fatigue life under short beam shear tests, compared to the non-reinforced specimens.

Conway et al. [340] investigated enhancing the mechanical properties of unidirectional pre-impregnated carbon fiber composite IM7/8552, which is susceptible to delamination under various loading conditions. Vertically aligned carbon nanotube (VACNT) forests were incorporated into the composite by transferring VACNTs to the surface of each prepreg ply before layup. VACNTs used were produced using a metallic substrate and a continuous chemical vapor deposition (CVD) process. Testing included short beam strength (SBS and short beam fatigue. VACNT reinforcement of the interlaminar region exhibited increased composite strength. The short beam static strength testing showed a dependence on layup, with a 2.0% increase in strength for the unidirectional (UD) layup. Fatigue testing indicated a substantial increase (2X to 30X) in short beam cycles to failure at tested stress levels, suggesting that the presence of VACNTs at interfaces positively impacts fatigue life, particularly in an interface-dominated scenario.

Garcia et al. [441] presented a hybrid composite architecture incorporating carbon nanotubes (CNTs), advanced fibers, and a matrix, displaying a comprehensive process from CNT synthesis and characterization to standard mechanical and electrical laminate tests. The approach involves the direct growth of aligned CNTs on the surface of advanced fibers in a woven fabric, resulting in a significant enhancement in multifunctional laminate performance. The study demonstrates a 69% increase in interlaminar shear strength compared to the unreinforced laminate. This enhancement surpasses existing interface reinforcement techniques, such as stitching which

typically shows a maximum increase of approximately 30% [539] and unaligned CNTs which showed no improvement [540]

Song et al. [541] focused on the development of multiscale laminated composite materials by incorporating carbon nanotube (CNT) materials into microfiber laminated composites. In this study, multiwalled carbon nanotube (MWCNT) arrays are strategically integrated between carbon fabric plies of laminated composites, serving as a bridge to interlock adjacent carbon fabric plies. Aligned CNT arrays play a crucial role in interlocking adjacent carbon fabric prepreg plies, facilitating increased load transfer between the CNT array, matrix, and carbon fiber interphase. The interlocking effect created a crack bridging mechanism, delaying crack propagation, contributing to improvements in both in-plane and interlaminar shear properties of the CNT array-reinforced laminated multiscale composite.

Contribution to Material Properties

VACNTs play a pivotal role in enhancing the fracture toughness and impact resistance of CFRP composites. The controlled alignment of nanotubes within the matrix acts as a barrier against crack propagation, absorbing and dissipating energy during impact events. This energy dissipation mechanism minimizes the risk of catastrophic failures and improves the composite's ability to withstand dynamic loading conditions. This dynamic contribution to fracture toughness and impact resistance positions VACNT-reinforced CFRP composites as robust materials for applications in aerospace, automotive, and sporting equipment.

Mode I Fracture Toughness

Worboy's [343] investigation on mode I fracture toughness in Vertically Aligned Carbon Nanotubes (VACNTs) reinforcement at the interlaminar region resulted in a predominantly intralaminar delamination fracture mode. In their study, they reported an increase in toughness between 10-20% coincided with the increased toughness within the intralaminar region compared to the interlaminar region observed in other studies [542], [543]. This intralaminar fracture

behavior aligned with data reported by Ni and Wardle [336], demonstrating that VACNTs cause the crack to bifurcate into the intralaminar region. While previous work on AS4/8552 indicated a reduction in Mode I fracture toughness with VACNTs [336], this study suggests an increase equivalent to the difference between interlaminar and intralaminar fracture toughness of the host laminate. Reinforcing the interlaminar region with VACNTs appears to elevate the localized interlaminar fracture toughness beyond that of intralaminar toughness, causing the crack to bifurcate into the now weaker intralaminar region. During failure analysis despite the majority of the fractured VACNT specimens showing intralaminar delamination, some nanotube rupture was observed. This additional fracture mechanism occurred during the crack transition between adjacent plies, contributing to a local increase in the fracture toughness of the Carbon Fiber Reinforced Polymer (CFRP) laminate. However, due to its infrequent occurrence in the tested specimens, nanotube rupture will lead to greater variability between sample results. No evidence of other interlaminar fracture mechanisms, such as nanotube pull-out, was observed in any of the specimens.

Le et al. [544] explored the incorporation of vertically aligned carbon nanotube forests (VACNTs) at composite interfaces to enhance interface toughness. In their study they conducted mode I (Double Cantilever Beam –DCB) fracture tests on 40 ply composite samples with VACNT reinforcement placed on the mid-ply interface. After testing, microscopic analysis was performed on both reference and VACNT reinforced composites to understand fracture behavior and toughness. VACNT reinforced DCB samples exhibited intralaminar crack paths located within the unidirectional carbon fiber plies as opposed to the interlaminar crack paths observed in non-reinforced samples. Due to the crack propagating intralaminarly into the non-reinforced plies, no changes were observed between reinforced and non-reinforced samples.

Garcia et al. [441] manufactured mode I test specimens by reinforcing unidirectional carbon tape composites with VACNT reinforcement applied to each interface using transfer-printing. After testing, specimens were examined under SEM to identify failure mechanisms. Fractographic analysis revealed *z*-direction oriented CNTs on both crack faces, suggesting

large-scale bridging of the crack by the (aligned) CNTs. Both CNT bridging and interlayer toughening were reported as possible reinforcing mechanisms, with direct evidence supporting CNT bridging. Due to these mechanisms aiding in crack mitigation, VACNT reinforced specimens observed an increase in fracture toughness 1.5x – 2.5x that of non-reinforced specimens.

While there have been conflicting responses reported in literature on vertically aligned carbon nanotube reinforcement's influence on mode I fracture toughness, this can be attributed to the location of inter-ply reinforcement. In tests which reported little to no enhancement, the VACNTs were located only on the mid-ply interface and observed intralaminar failure. Whereas, in the reports showing enhanced toughness, large-scale inter-ply bridging was observed by the VACNTs. This helps highlight the strengthening brought about the VACNTs, where failure will jump to a non-reinforced interface as a path of least resistance.

Mode II Fracture Toughness

Worboy's [343] continued investigation on mode II fracture toughness from their mode I setup (single interleaved VACNT layer at the mid-plane interface), illustrated the effects reinforcement had on fracture toughness and failure methods. Fractographic analysis performed using SEM after testing highlighted intralaminar crack propagation within the reinforced and non-reinforced specimens. In the VACNT interleaved specimens, nanotube pull-out was observed, however, the phenomenon was reported infrequently. Failure was primarily characterized by fiber pull-out, displaying numerous bare fibers and well-defined resin channels, surrounded by cusps. The clean appearance of the fiber surface and the presence of channels left by debonded fibers indicated that the crack propagated across the fiber-matrix interface [545]. It was also observed that in the reinforced specimens, the intralaminar crack propagation followed the topography of the nanotubes and the resin pockets formed around their non-uniform dispersion, highlighting an

increase in local stiffness of the interlaminar region caused by the nanotubes. Despite similar failure mechanisms as non-reinforced samples, VACNT specimens observed an increase in mode II fracture toughness by 8-10%.

In combination with the mode I test highlighted previously, Le et al. [544] performed mode II tests with the same material system. During the mode II toughness test, the shearing stress between the through-thickness lead to the deformation of the resin between the 20th and 21st ply, resulting in the formation of cusps. Resin cusps are observed in both reinforced and non-reinforced samples, attributed to high local strain levels of the resin. The non-reinforced mode II sample showed a higher cusp area density compared to the reinforced mode II sample, with larger cusps on average. These differences are associated with variations in the size of the resin volumes in the two composite types after consolidation. In reinforced composites, the presence of VACNTs reduces the volumes of deformable resin at the fracture interface. Consequently, the size and density of cusps decrease at the observed interface. Experimental data also illustrated a decrease in mode II fracture toughness within the reinforced specimens as well as unstable crack initiation and growth.

In the mode II tests performed by Garcia et al. [441], they did not report visual inspection or fractographic analysis of the mode II specimens. Due to the presence of reinforcement in all interfaces however, the increase to fracture toughness within VACNT specimens was 3x that of non-reinforced specimens. This was reportedly greater than other reinforcement studies using stitching [539], [546] and z-fiber reinforcement [539], [547]. Additionally, they stated the potential to greatly increase the mode II fracture toughness by increasing the volume fraction density of VACNT forests.

Similar to mode I fracture energy toughness, it is apparent from past studies that specifically reinforcing the mid-plane interface with VACNT forests minimal improvements are observed. This is attributed to the crack propagation bifurcating upon reaching the reinforced interface and jumping layers. By ensuring full reinforcement of the VACNT forests throughout

the laminate however, an increase in fracture toughness can reach at least 3x that of non-reinforced laminates and potentially even more.

Impact

Conway et al. [Conway2017] studied the reinforcement effects vertically aligned carbon nanotubes (VACNTs) had on three prepreg systems: Newport 34-700/NCT301, Tencate IM7/TC350-1, and Hexcel IM7/8552. Specimens were manufactured with VACNT reinforcement being applied to each ply interface during layup. Impact tests were performed according to ASTM D7136 using an impact energy range of 27-29 J to strike each laminate once. After impact tests, specimens were removed to perform C-Scan imagery to highlight damage mechanisms. Post inspection, specimens were then used according to ASTM D7317 for compression after impact (CAI) testing. It was reported that VACNT-reinforced samples exhibited a reduction of size and severity in impact damage and residual strengths 11–16% higher on average than the control group, without significantly increasing the weight or thickness of the composite.

While specific studies relating VACNT interlaminar reinforcement to impact damage mitigation are limited, inferences can be made from previous studies in conjunction with unaligned carbon nanotube's reinforcement effects. Unaligned carbon nanotube interlaminate reinforcement has been seen to improve interlaminar shear strength, damping, and impact toughness due to the remarkable CNT reinforcement and rich interfaces of the CNT composites [442], [548]–[551]. The increase in performance observed from vertically aligning carbon nanotubes regarding fracture toughness, in conjunction with the increase in impact performance of unaligned CNTs, future investigation is warranted.

Effect on Other Properties

Beyond ILSS, fracture toughness, fracture toughness, and impact resistance, the incorporation of VACNTs influences various other mechanical properties of CFRP composites.

The nanotubes' exceptional mechanical characteristics contribute to improvements in tensile properties [343], [552]–[557], flexural properties [47], [343], [541], [552], [555], [558]–[560], hardness [553]. The synergistic effects of VACNTs on these properties result in a composite material with an enhanced overall mechanical profile.

Additionally, the enhanced thermal and electrical conductivity [561]–[571] of VACNTs introduce multifunctionality to CFRP composites. The controlled integration of VACNTs allows for tailoring the thermal and electrical properties of the composite, expanding its utility in applications where heat dissipation or electrical conductivity is critical.

ADVANTAGES OF VERTICALLY ALIGNED CARBON NANOTUBES (VACNTS)

Vertically aligned carbon nanotubes (VACNTs) share inherent properties with randomly oriented CNTs, yet their perpendicular orientation imparts mechanical and electrical benefits.

Mechanical Advantages

The distinctive vertical aspect ratio of VACNTs opens various unique applications [572], [573]. While maintaining high tensile strength, VACNTs exhibit deflection under pressure, with a Poisson’s ratio of 0.19 and Young’s modulus ranging from 1 to 10 MPa [574]–[578]. Additionally, their normal orientation facilitates easy access to VACNT tips. The uniform spatial arrangement and absence of overlapping, as discussed earlier, contribute to the creation of densely packed structures [579], [580]. The vertical alignment of these nanotubes facilitates load transfer between layers in composite materials, contributing to enhanced interlaminar shear strength (ILSS) and overall mechanical reinforcement. This mechanical robustness positions VACNTs as ideal candidates for fortifying the interlaminar regions of CFRP composites, mitigating the risks associated with delamination and enhancing the composite's load-bearing capabilities.

Electrical Conductivity

The superior electron transfer rate of VACNT tips, demonstrated in various studies [581]–[585], is attributed to their unique chemical structure. Fayazfar et al. [581] conducted a direct comparison of the electrocatalytic activity between randomly oriented CNT and VACNT through cyclic voltammetry, finding greater activity in VACNT. This, coupled with their increased surface area and uniformity, positions VACNTs as excellent electrodes. Additionally, VACNTs have been shown to generate electric fields with low potentials, a feature that can be harnessed for inducing polarization [586]. Consequently, VACNTs, with their enhanced electrochemical properties, find widespread use in various electrochemical sensor applications when compared to randomly oriented CNTs, offering opportunities for multifunctional applications.

In scenarios where electrical conductivity is a critical requirement, such as in certain aerospace applications or structural health monitoring systems, the incorporation of VACNTs provides a dual benefit of mechanical reinforcement and improved electrical performance.

Thermal Properties

The introduction of Carbon Nanotubes (CNTs) into polymer matrices can significantly enhance the thermal properties of the resulting composites. This improvement is attributed to the constraint effect exerted by CNTs on polymer segments and chains. For instance, when 1 wt.% CNTs are added to epoxy with a surfactant, the glass transition temperature increases from 63 to 88 °C, displaying the positive impact on thermal endurance [587]. Similarly, the incorporation of 1 wt.% well-dispersed Single-Walled CNTs (SWCNTs) raises the glass transition temperature of PMMA by approximately 40 °C [588]. CNTs, acting as nucleation sites, promote polymer crystallization, leading to an increase in the melting temperature [589]. Studies by Kashiwagi et al. [590] indicate a roughly 12 °C increase in the thermal decomposition temperature of polypropylene (PP) with 2 vol.% Multi-Walled CNTs (MWCNTs), effectively rendering the composite as fire-retardant as PP/PP-g-MA/clay.

Additionally, the inclusion of CNTs enhances the thermal transport properties of polymer composites due to the remarkable thermal conductivity of CNTs. This opens avenues for applications such as printed circuit boards, connectors, thermal interface materials, heat sinks, lids, housings, and high-performance thermal management across various structures. Biercuk et al. [591] observed a 70% increase in thermal conductivity at 40 K and a 125% increase at room temperature with 1 wt.% un-purified SWCNTs in epoxy. Choi et al. [592] reported a thermal conductivity increase of up to 300% in epoxy with 3 wt.% SWCNTs. Notably, the alignment of Multi-Walled CNTs (MWCNTs) under a 25T magnetic field has been found to further enhance thermal conductivity by 10% compared to epoxy/MWCNT nanocomposites without an applied magnetic field [592].

CHALLENGES AND OPPORTUNITIES

This brief review highlighted the field of incorporating vertically aligned carbon nanotubes (VACNTs) into carbon fiber reinforced polymer (CFRP) composites and their challenges. This section addresses the remaining challenges and potential venues of research to overcome them.

Dispersion and Stability

Achieving and maintaining a uniform dispersion of VACNTs within the polymer matrix remains a primary challenge. Agglomeration tendencies and long-term stability issues pose hurdles in ensuring consistent performance over the lifespan of the composite material. Future studies can aim to overcome this problem through methods such as transfer printing. By focusing on optimizing VACNT synthesis parameters on a consistent substrate, the influence of fiber systems is avoided. After valid methods have been observed to create uniform VACNT substrates, the VACNT forests can then be transferred to the composite system using the lay-up or interleaving method.

Scalability

While VACNT-reinforced CFRP composites exhibit remarkable properties, achieving scalability in production processes remains a challenge. Developing cost-effective manufacturing methods that can be readily implemented on an industrial scale is essential for widespread adoption. Investigations performed on dip immersion and transfer printing are already being conducted. Both methods allow for larger scale composites to be developed as they do not require specific small-scale synthesis onto the fibers.

Interfacial Engineering

Optimizing the interfacial interaction between VACNTs and the CFRP matrix is crucial for maximizing the material's potential. Challenges persist in achieving strong adhesion and load transfer across the interlaminar regions. Interfacial engineering strategies, including tailored surface functionalization and advanced bonding techniques, are areas of ongoing research to address these challenges.

Conflicting Reports Regarding VACNT Interlaminar Reinforcement

As highlighted previously in the review, the influence VACNT reinforcement has on mechanical properties observed conflicting conclusions. This is a result from not only a lack of studies performed, but differences regarding reinforced interfaces. Specifically, during fracture toughness tests, intralaminar damage was the dominant failure mode resulting from the cracks propagating to the non-reinforced region. As a result, the recorded fracture toughness saw minimal improvement by the VACNT reinforcement. However, in tests performed with reinforcement throughout the entire composite, fracture toughness tripled for mode II tests. To combat these conflicting reports, future studies should contemplate reinforcing the entire laminate depending on their test case to ensure VACNT reinforcement is influencing the test properly.

CONCLUSION

In summary, the integration of vertically aligned carbon nanotubes (VACNTs) into carbon fiber reinforced polymer (CFRP) composites represents a transformative approach to enhancing interlaminar reinforcement. Through a comprehensive exploration of synthesis, integration methods, characterization techniques, interlaminar reinforcement mechanisms, advantages of vertically aligned carbon nanotubes, and challenges, several key findings have emerged.

Key Findings:

- Interlaminar Reinforcement Mechanisms: VACNTs strategically improve interlaminar shear strength (ILSS), fracture toughness, impact resistance, and other mechanical properties, mitigating delamination risks in composite structures.
- Thermal and Electrical Conductivity: The one-dimensional structure of VACNTs imparts excellent thermal and electrical conductivity to CFRP composites, opening new possibilities for multifunctional applications.
- Challenges in Dispersion and Scalability: Challenges remain in achieving uniform dispersion and scalability of VACNTs in production processes, necessitating innovative approaches for stable dispersion and cost-effective manufacturing.
- Significance of VACNTs in Interlaminar Reinforcement: The significance of VACNTs in interlaminar reinforcement cannot be overstated. The controlled vertical alignment of these nanotubes facilitates direct load transfer pathways across layers, preventing delamination and enhancing the overall structural integrity of CFRP composites. The exceptional mechanical properties, coupled with unique thermal and electrical conductivity, position VACNTs as a versatile and impactful reinforcement material.

As the field continues to evolve, several avenues for future research directions emerge:

- Dispersion and Stability: Further research is needed to develop advanced dispersion techniques and surface functionalization methods to address challenges related to the uniform dispersion and long-term stability of VACNTs in CFRP composites.

- Scalability and Cost-Effectiveness: Future research should focus on refining manufacturing processes to achieve scalability and cost-effectiveness, enabling the widespread adoption of VACNT-reinforced CFRP materials in various industries.
- In-Situ Monitoring and Control: Advancements in in-situ monitoring and control mechanisms during the manufacturing process can enhance the reproducibility and reliability of VACNT-reinforced CFRP composites.
- Tailored Applications: Research efforts should be directed toward understanding the specific requirements of diverse applications, enabling the customization of VACNT-reinforced materials for optimal performance in various industries.

In conclusion, the integration of VACNTs into CFRP composites holds immense promise for revolutionizing material performance and expanding the application horizons in aerospace, automotive, sports, and structural engineering. Addressing the remaining challenges and pursuing innovative research directions will undoubtedly unlock the full potential of VACNT-reinforced CFRP materials in the years to come.

Chapter 5: Contributions to the Scientific Community

INTRODUCTION

Composite structures have experienced an increase presence throughout sectors such as naval transportation, green energy, and aerospace due to their light weight, fatigue resistance, job tailorable customizations, and high bending-to-stiffness ratios. With the demand for composite structures increasing, the need for advancing composite technologies is more prevalent than ever.

In this report, methods for enhancing current composite technologies were performed by focusing on the constituent materials related to sandwich composites structures focusing on new core materials, uncertainty quantification on resin matrix systems, and interlaminar reinforcement.

CORE MATERIALS

Background

In chapter 1, the limitations to current core materials for arctic naval transportation were highlighted. Wooden and cork cores decrease in mechanical properties when water moisture is present, and foam cores observe catastrophic failure mechanisms through crushing mechanisms resulting from the embrittlement of arctic temperatures. In newer core technologies, there has been an increased focus on geometric-based cores, allowing application of new materials with enhanced tailorable properties.

Focus

The focus in this chapter investigated the quasi-static properties and failure mechanisms of Durable resin at room and arctic temperature environments. Durable resin is a photoreactive resin by Formlabs and manufactured using stereolithography additive manufacturing. This material would be able to implement the newer core geometric designs which require high precision during manufacturing to enhance their mechanical properties while reducing the net weight of the core.

Methodology

Experimental tests were performed on specimens manufactured from Durable resin to identify mechanical properties associated with tensile, compressive, and flexural load cases at room and arctic temperatures. Failure mechanisms were identified after testing to compare the influence arctic temperatures had on the material system, and computational finite-element analysis models were developed to represent the quasi-static experiments.

Results and Discussion

Experimental tests illustrated an increase in mechanical strengths and moduli of the Durable resin specimens at arctic temperatures with a decrease in ultimate strain. As the temperature decreases, the polymer chains within the material experience hindered mobility resulting in a stiffer material system. Failure mechanisms observed after testing reaffirmed this, with arctic temperature tests resulting in brittle failure while room temperature tests experienced ductile failure. Computational models were able to accurately represent the quasi-static experiments within the linear-elastic region for each test at room and arctic temperature.

Contributions

Quasi-static tests performed at room and arctic temperatures highlighted an increase in mechanical properties at arctic temperatures without the severe crushing illustrated with traditional core materials such as foams. In combination with the material being used in additive manufacturing, further studies can be performed to investigate the core geometry effects using Durable resin. Lattice structure geometries can be implemented and studied to develop new job tailorable cores intended for room to arctic temperature environments with the new knowledge of the influence temperature has on the material system.

UNCERTAINTY QUANTIFICATION OF MATRIX SYSTEM

Background

In chapter 2, the development of uncertainty within composite structures during manufacturing and testing is highlighted. As a composite system is manufactured, uncertainties develop from the micro-scale to macro-scale resulting in a common basis of designers to either over-design their components for safety or risk failure due to differences from their predictions and real-life application. Over the years researchers have investigated methods to quantify the uncertainties in composite systems and increase the predictive capabilities used during the design process. The methods used for quantification is designed by the scale of system, where structural studies for example, tend to focus only on the macro-scale uncertainties involved and use the differences observed in post-manufactured specimens as their starting point. While there have been efforts to use micro-scale to meso-scale studies for uncertainty quantification, they involved the fiber system already within the matrix and not the constituents by themselves. Similar to the macro-scale system resulting in not quantifying the meso-scale, this also results in losing the quantification of uncertainties developed specifically by the constituent materials.

Focus

In this study, an exploratory study was performed to quantify the uncertainties developed specifically by a vinyl-ester resin matrix system as it undergoes the manufacturing process. Narrowing the scope of view to a single constituent system to analyze the effects uncertainty has on impact damage will highlight the degree of influence that has been neglected and if it has relevance in larger scale studies.

Methodology

The exploratory study utilized several key steps towards uncertainty quantification of the vinyl-ester specimens. First, uncertainties within the system were categorized as either aleatoric, epistemic, or prejudicial to aid in defining how the test methods were developed. Defined variables for testing included resin-to-hardener mixture ratio and the time of curing of the specimen before testing. The two independent variables were categorically altered to record and analyze their influences they had by themselves and together on the degree of impact damage within the system. To isolate the individual influences of the variables, local analyses were performed using a polynomial regression method to define their isolated trends. Uncertainty quantification to incorporate both variables on a global scale involved a multi-linear regression method coupled with a sensitivity analysis portrayed previously by researchers.

Results and Discussion

From the experimental tests, notable trends exhibited by the independent variables were observed to have influence on the degree of impact damage within the specimen. On the local scale, specimens manufactured with a deviation from the baseline resin-to-hardener mixture ratio experienced an increase in the degree of damage. The increase in damage was attributed to the lower end hardener-to-resin mixture resulting in excess resin caused by an incomplete chemical reaction, whereas the specimens with higher hardener concentrations would result in excess hardener for the same reason. Local trends regarding the cure time before testing illustrated a decrease in the degree of damage as the time before testing increased. This was attributed to the specimens having a higher chance of reaching full chemical cure and resting of the polymer chains as the time increased. From the global uncertainty quantification and sensitivity analysis, the theoretical model was able to encompass all of the experimental data within the predictive region. It was observed that within the performed tests, the hardener-to-resin ratio held a higher influence on the degree of impact damage illustrated by the higher coefficient in the global trend equation.

While both variables were tracked and predicted, there still existed an approximately 14% variance in the degree of damage resultant from the inevitable uncertainties, categorized as "miscellaneous".

Contributions

Through the investigation of this study, it was shown that even on a single constituent scale using a vinyl-ester matrix system, uncertainties play a key role in performance deviation. This highlights the impact that neglecting smaller-scale systems carries when developing macro-scale analyses. Due to this studies' exploratory nature, there exists improvements which can be made in the future to increase predictive capabilities which can then be up-scaled for future models. Studies involving more independent variables will help understand and define the contributors within the 14% "miscellaneous" variable. Future studies can also utilize a higher number of samples to incorporate more complex numerical methods which can take 5000 samples or more to develop.

INTERLAMINAR REINFORCEMENT

Background

In chapters 3 and 4, the importance of interlaminar reinforcement techniques is addressed. In composite structures, where a majority of the system strength comes from the fiber system used, the interlaminar region which is devoid of fibers poses concern as the weakest area. Within this region, low-velocity impact events can result in barely visible impact damage in the form of matrix cracking and delamination. This damage can cause significant reduction in mechanical properties without any visible identifiers and lead to onset catastrophic failure. Previous attempts to enhance the interlaminar region can be categorized into two main types, 3-D reinforcement, and 2-D reinforcement. 3-D reinforcement penetrates the fibers to increase the through-thickness properties but results in weakening the in-plane properties due to resin pockets and fiber breakage. 2-D

reinforcement acts by applying reinforcement explicitly to the interlaminar region, but can result in an increase of resin pockets, increased fiber pullout, and difficulties to apply in a commercial setting. Investigation into new forms of application for 2-D reinforcement is crucial to enhancing the damage tolerance of composite structures which can then be applied on a commercial scale.

Focus

Chapter 3 investigates the use of Kevlar® pulp interlaminar reinforcement to enhance impact damage mitigation for room and arctic temperature environments. Kevlar® pulp exists in the form of microfibers which can be mixed into a resin matrix system for toughening. The toughened resin matrix can then be applied during the hand-layup method without any modification. During impact events, the Kevlar® pulp microfibers can aid damage mitigation by cross-linking within the matrix and inter-ply fiber bridging.

Chapter 4 investigates the potential use of vertically aligned carbon nanotubes and their application for future studies. Carbon nanotube interlaminar reinforcement in the past has been shown to enhance the mechanical and conductive properties of composite structures but relies heavily on the nanotube forest geometry. During synthesis and application, the forest geometries can be affected by altering the composite properties in unintended fashions. To optimize carbon nanotubes, newer methods are being developed to design vertically explicit forests which increase the potential of through-thickness mechanical performance enhancement using inter-ply bridging.

Methodology

Kevlar® pulp interlaminar reinforcement was investigated under impact loads at room and arctic temperatures to determine its influence on damage mitigation. Pristine and reinforced specimens were manufactured using woven carbon fiber and a vinyl-ester resin matrix system. Arctic specimens were conditioned at -60 °C prior to testing and utilized an environmental chamber equipped with liquid nitrogen to maintain the arctic temperature during testing. Impact

events followed ASTM standards with four different sets of impact energies, 5 J, 10 J, 15 J, and 20 J to investigate the influence temperature and reinforcement had on degree of degree of damage, peak force, and bending stiffness of the specimens. After testing, specimens were then examined for visible damage for comparison.

An extensive literature review was performed to encompass the development of vertically aligned carbon nanotubes over the years. The review focuses on the different methods of synthesis and growth of the VACNTs, properties of the nanotubes, interlaminar reinforcement mechanisms, processing techniques, characterization techniques, and current applications.

Results and Discussion

Specimens reinforced with Kevlar® pulp illustrated a reduction in the degree of damage, an increase to peak forces, and an increase to bending stiffness when compared to pristine samples. This was attributed to the inter-ply bridging aided by the micro-fibers present in the interlaminar region and reaffirmed by the smaller area of impact damage observed after testing. Arctic temperature specimens also observed a reduction in the degree of damage with an increase to peak force and bending stiffness when compared to room temperature specimens. This was attributed to the stiffening of the matrix caused by hindered chain mobility and coincided with smaller areas of impact damage observed after testing.

Contributions

Through the investigations made towards interlaminar reinforcement, two potential materials have shown great potential. Kevlar® pulp exists as a cheap material choice which can be applied with minimal effort to increase through-thickness properties of composite structures at room and arctic temperatures. Vertically aligned carbon nanotubes look to optimize the performance capabilities of carbon nanotubes within composite structures. Newer technologies are

being developed which aim to enhance the application of VACNTs from the lab synthesis setting to larger scale commercial applications.

Both materials have shown potential regarding interlaminar reinforcement of composite structures. Future studies of Kevlar® pulp can investigate the influence of increased presence within matrix systems and how it affects the microstructure within the composite system. By defining optimal manufacturing methods, Kevlar® pulp can aid in selective reinforcement for future applications without any drawbacks. VACNT interlaminar reinforcement studies can be performed on different composite systems to define the viability of transference vs synthesis, analyzing the effects fracture toughness, tensile, compressive, and impact performance. For both materials, additional implementation of visualization through SEM and micro-XRCT scanning can aid in understanding how the reinforcement interacts with the composite systems under loading.

CONCLUDING REMARKS

Investigation of constituent materials and techniques applied in this report have helped to define future venues of study to enhance composite structures as a whole. Quasi-static experimentation on Durable resin has defined a new material which can be applied to geometric studies for sandwich composite cores. Uncertainty quantification on vinyl-ester resin matrix systems highlighted the issues associated by ignoring constituent material uncertainties, while illustrating the need for future study. Investigation into Kevlar® pulp and vertically aligned carbon nanotubes has portrayed two forms of interlaminar reinforcement which can increase overall composite structure performance with minimal drawbacks.

References

[1] A. Banik, C. Zhang, M. H. Khan, M. Wilson, and K. T. Tan, "Low-velocity ice impact response and damage phenomena on steel and CFRP sandwich composite," *Int J Impact Eng*, vol. 162, p. 104134, Apr. 2022, doi: 10.1016/j.ijimpeng.2021.104134.

[2] U. S. U. Navy, "Arctic Roadmap 2014-2030," 2014.

[3] P. A. Berkman *et al.*, "Satellite Record of Pan-Arctic Maritime Ship Traffic Maritime ship traffic data across jurisdictions in the Arctic Ocean," pp. 1–9, 2022.

[4] Y. Y. Choi and M. H. Kim, "Corrosion behaviour of welded low-carbon steel in the Arctic marine environment," *RSC Adv*, vol. 8, no. 53, pp. 30155–30162, 2018, doi: 10.1039/C8RA05371E.

[5] V. Novac, E. Rusu, F. Onea, and G. Stăvărache, "Sea ice impact on naval operations," *J Phys Conf Ser*, vol. 1781, no. 1, p. 012041, Feb. 2021, doi: 10.1088/1742-6596/1781/1/012041.

[6] K. J. Kim, J. H. Lee, D. K. Park, B. G. Jung, X. Han, and J. K. Paik, "An experimental and numerical study on nonlinear impact responses of steel-plated structures in an Arctic environment," *Int J Impact Eng*, vol. 93, pp. 99–115, Jul. 2016, doi: 10.1016/j.ijimpeng.2016.02.013.

[7] L.-H. Larsen *et al.*, "Technological and environmental challenges of Arctic shipping—a case study of a fictional voyage in the Arctic," *Polar Res*, vol. 35, no. 1, p. 27977, Jan. 2016, doi: 10.3402/polar.v35.27977.

[8] S. K. Mazumdar, *Composites manufacturing: Materials, product, and process engineering*. 2001.

[9] D. Zenkert, "The Handbook of Sandwich Construction," 1997.

[10] S. Goswami and W. Becker, "The effect of facesheet/core delamination in sandwich structures under transverse loading," *Compos Struct*, vol. 54, no. 4, pp. 515–521, Dec. 2001, doi: 10.1016/S0263-8223(01)00124-6.

[11] C. Atas and C. Sevim, "On the impact response of sandwich composites with cores of balsa wood and PVC foam," *Compos Struct*, vol. 93, no. 1, 2010, doi: 10.1016/j.compstruct.2010.06.018.

[12] J. Dai and H. T. Hahn, "Flexural behavior of sandwich beams fabricated by vacuum-assisted resin transfer molding," *Compos Struct*, vol. 61, no. 3, 2003, doi: 10.1016/S0263-8223(03)00040-0.

[13] A. Denay, S. Castagnet, A. Roy, G. Alise, and N. Thenard, "Compression behavior of glass-fiber-reinforced and pure polyurethane foams at negative temperatures down to cryogenic ones," vol. 49, no. 3, 2013.

[14] A. Da Silva and S. Kyriakides, "Compressive response and failure of balsa wood," *Int J Solids Struct*, vol. 44, no. 25–26, 2007, doi: 10.1016/j.ijsolstr.2007.07.003.

[15] T. Goodrich, N. Nawaz, S. Feih, B. Y. Lattimer, and A. P. Mouritz, "High-temperature mechanical properties and thermal recovery of balsa wood," *Journal of Wood Science*, vol. 56, no. 6, 2010, doi: 10.1007/s10086-010-1125-2.

[16] R. L. Sadler, M. Sharpe, R. Panduranga, and K. Shivakumar, "Water immersion effect on swelling and compression properties of Eco-Core, PVC foam and balsa wood," *Compos Struct*, vol. 90, no. 3, 2009, doi: 10.1016/j.compstruct.2009.03.016.

[17] J. Galos, R. Das, M. P. Sutcliffe, and A. P. Mouritz, "Materials & Design Review of balsa core sandwich composite structures," vol. 221, 2022.

[18] E. A. Toubia, S. Emami, and D. Klosterman, “Degradation mechanisms of balsa wood and PVC foam sandwich core composites due to freeze/thaw exposure in saline solution,” *Journal of Sandwich Structures and Materials*, vol. 21, no. 3, 2019, doi: 10.1177/1099636217706895.
[19] O. E. Özkan, “Effects of cryogenic temperature on some mechanical properties of beech (Fagus orientalis Lipsky) wood,” *European Journal of Wood and Wood Products*, vol. 79, no. 2, pp. 417–421, 2021, doi: 10.1007/s00107-020-01639-1.
[20] L. Zhao, J. Jiang, J. Lu, and T. Zhan, “Flexural property of wood in low temperature environment,” *Cold Reg Sci Technol*, vol. 116, pp. 65–69, Aug. 2015, doi: 10.1016/J.COLDREGIONS.2015.04.001.
[21] J. Jiang, J. Lu, Y. Zhou, Y. Zhao, and L. Zhao, “Compression Strength and Modulus of Elasticity Parallel to the Grain of Oak Wood at Ultra-low and High Temperatures,” vol. 9, no. 1968, pp. 3571–3579, 2014.
[22] N. Ayrilmis, U. Buyuksari, and N. As, “Bending strength and modulus of elasticity of wood-based panels at cold and moderate temperatures,” *Cold Reg Sci Technol*, vol. 63, no. 1–2, pp. 40–43, 2010.
[23] O. Eichi, N. Misato, and T. Bunichiro, “Mechanical Relaxation Processes of Wood in the Low-Temperature Range,” *J Appl Polym Sci*, vol. 81, no. 13, pp. 3338–3347, 2001.
[24] M. B. Szmutku, M. Campean, and M. Porojan, “Strength reduction of spruce wood through slow freezing,” pp. 205–210, 2013, doi: 10.1007/s00107-013-0667-6.
[25] J. Jiang, J. Lu, Y. Zhou, Y. Zhao, and L. Zhao, “Compression Strength and Modulus of Elasticity Parallel to the Grain of Oak Wood at Ultra-low and High Temperatures,” vol. 9, no. 1968, pp. 3571–3579, 2014.
[26] N. Ayrilmis, U. Buyuksari, and N. As, “Bending strength and modulus of elasticity of wood-based panels at cold and moderate temperatures,” *Cold Reg Sci Technol*, vol. 63, no. 1–2, pp. 40–43, 2010.
[27] O. E. Özkan, “Effects of cryogenic temperature on some mechanical properties of beech (Fagus orientalis Lipsky) wood,” *European Journal of Wood and Wood Products*, vol. 79, no. 2, pp. 417–421, 2021, doi: 10.1007/s00107-020-01639-1.
[28] R. L. Sadler, M. Sharpe, R. Panduranga, and K. Shivakumar, “Water immersion effect on swelling and compression properties of Eco-Core, PVC foam and balsa wood,” *Compos Struct*, vol. 90, no. 3, 2009, doi: 10.1016/j.compstruct.2009.03.016.
[29] T. X. Ptak, “International Journal of Impact Engineering Assessing impact velocity and temperature effects on crashworthiness properties of cork material,” vol. 106, pp. 238–248, 2017.
[30] S. Prabhakaran, “Experimental study on thermal and morphological analyses of green composite sandwich made of flax and agglomerated cork,” *J Therm Anal Calorim*, vol. 139, no. 5, pp. 3003–3012, 2020, doi: 10.1007/s10973-019-08691-x.
[31] C. Sergi, F. Sarasini, P. Russo, L. Vitiello, and E. Barbero, “Effect of temperature on the low-velocity impact response of environmentally friendly cork sandwich structures,” vol. 24, no. 2, 2022.
[32] A. Review, “The Compressive Behavior and Crashworthiness of Cork : A Review,” 2022.
[33] M. Aowad, A. Banik, C. Zhang, I. Kaiser, M. H. Khan, and A. Clecia, “Flexural behavior and microstructural material properties of sandwich foam core under arctic temperature conditions,” 2023.

[34] G.-H. Kang *et al.*, “Manufacturing, thermoforming, and recycling of glass fiber/PET/Pet foam sandwich composites: DOE analysis of recycled materials,” *Polym Compos*, vol. 43, no. 12, pp. 8807–8817, 2022.
[35] H. Shen and S. Nutt, “Mechanical characterization of short fiber reinforced phenolic foam,” *Compos Part A Appl Sci Manuf*, vol. 34, no. 9, 2003, doi: 10.1016/S1359-835X(03)00136-2.
[36] S. B. Park, C. S. Lee, S. W. Choi, J. H. Kim, C. S. Bang, and J. M. Lee, “Polymeric foams for cryogenic temperature application: Temperature range for non-recovery and brittle-fracture of microstructure,” *Compos Struct*, vol. 136, 2016, doi: 10.1016/j.compstruct.2015.10.002.
[37] S. M. Soni, R. F. Gibson, and E. O. Ayorinde, “SCIENCE AND The influence of subzero temperatures on fatigue behavior of composite sandwich structures,” vol. 69, pp. 829–838, 2009, doi: 10.1016/j.compscitech.2008.02.007.
[38] V. N. Pilipchuk, R. A. Ibrahim, and I. Grace, “Low temperature brittle debond damage under normal compression of sandwich plates : Analytical modeling and experimental validation,” vol. 98, pp. 24–33, 2013.
[39] C. Y. Tan and H. M. Akil, “Impact response of fiber metal laminate sandwich composite structure with polypropylene honeycomb core,” *Compos B Eng*, vol. 43, no. 3, 2012, doi: 10.1016/j.compositesb.2011.08.036.
[40] E. Linul, C. Vălean, and P. A. Linul, “Compressive behavior of aluminum microfibers reinforced semi-rigid polyurethane foams,” *Polymers (Basel)*, vol. 10, no. 12, 2018, doi: 10.3390/polym10121298.
[41] J. V Mane *et al.*, “Mechanical Property Evaluation of Polyurethane Foam under Quasi-static and Dynamic Strain Rates- An Experimental Study,” vol. 173, pp. 726–731, 2017, doi: 10.1016/j.proeng.2016.12.160.
[42] M. Mohamed, S. Anandan, Z. Huo, V. Birman, J. Volz, and K. Chandrashekhara, “Manufacturing and characterization of polyurethane based sandwich composite structures,” *Compos Struct*, vol. 123, 2015, doi: 10.1016/j.compstruct.2014.12.042.
[43] M. C. Saha, H. Mahfuz, U. K. Chakravarty, M. Uddin, M. E. Kabir, and S. Jeelani, “Effect of density, microstructure, and strain rate on compression behavior of polymeric foams,” *Materials Science and Engineering: A*, vol. 406, no. 1–2, 2005, doi: 10.1016/j.msea.2005.07.006.
[44] M. C. Saha, Md. E. Kabir, and S. Jeelani, “Enhancement in thermal and mechanical properties of polyurethane foam infused with nanoparticles,” *Materials Science and Engineering: A*, vol. 479, no. 1–2, pp. 213–222, Apr. 2008, doi: 10.1016/j.msea.2007.06.060.
[45] A. P. Sartori *et al.*, “Development and characterization of sandwich panels for thermal insulation in a cold storage chamber,” *Journal of Cellular Plastics*, vol. 59, no. 3, pp. 215–230, May 2023, doi: 10.1177/0021955X231162799.
[46] M. Thirumal, D. Khastgir, N. K. Singha, B. S. Manjunath, and Y. P. Naik, “Effect of foam density on the properties of water blown rigid polyurethane foam,” *J Appl Polym Sci*, vol. 108, no. 3, 2008, doi: 10.1002/app.27712.
[47] D. Whisler and H. Kim, “Experimental and simulated high strain dynamic loading of polyurethane foam,” *Polym Test*, vol. 41, 2015, doi: 10.1016/j.polymertesting.2014.12.004.

[48] J. M. Arvidson and L. Sparks, “Low temperature mechanical properties of a polyurethane foam,” Gaithersburg, MD, 1981. doi: 10.6028/NBS.IR.81-1654.
[49] T. C. Cotgreave and J. B. Shortall, “The mechanism of reinforcement of polyurethane foam by high-modulus chopped fibres,” *J Mater Sci*, vol. 12, no. 4, pp. 708–717, Apr. 1977, doi: 10.1007/BF00548161.
[50] A. Demharter, “Polyurethane rigid foam, a proven thermal insulating material for applications between +130°C and −196°C,” *Cryogenics (Guildf)*, vol. 38, no. 1, pp. 113–117, Jan. 1998, doi: 10.1016/S0011-2275(97)00120-3.
[51] J.-H. Kim, S.-K. Kim, S. Park, K. Hyun Park, and J.-M. Lee, “Low-temperature Mechanical Behavior of Reinforced Polyurethane Foam,” *International Journal of Mechanical Engineering*, vol. 2, pp. 15–18, 2017.
[52] E. Linul, L. Marşavina, C. Vălean, and R. Bănică, “Static and dynamic mode I fracture toughness of rigid PUR foams under room and cryogenic temperatures,” *Eng Fract Mech*, vol. 225, 2020, doi: 10.1016/j.engfracmech.2018.12.007.
[53] U. Stirna, I. Beverte, V. Yakushin, and U. Cabulis, “Mechanical properties of rigid polyurethane foams at room and cryogenic temperatures,” *Journal of Cellular Plastics*, vol. 47, no. 4, pp. 337–355, Jul. 2011, doi: 10.1177/0021955X11398381.
[54] V. A. Yakushin, N. P. Zhmud, and U. K. Stirna, “Mechanics of Composite Materials, Vol. 38, No. 3, 2002,” *Mechanics of Composite Materials*, vol. 38, no. 3, pp. 273–280, 2002, doi: https://ui.adsabs.harvard.edu/link_gateway/2002MCM....38..273Y/doi:10.1023/A:1016043519788.
[55] V. Yakushin, U. Cabulis, and I. Sevastyanova, “Effect of Filler Type on the Properties of Rigid Polyurethane Foams at a Cryogenic Temperature,” *Mechanics of Composite Materials*, vol. 51, no. 4, pp. 447–454, Sep. 2015, doi: 10.1007/s11029-015-9516-5.
[56] Y. H. Yu, I. Choi, S. Nam, and D. G. Lee, “Cryogenic characteristics of chopped glass fiber reinforced polyurethane foam,” vol. 107, pp. 476–481, 2014.
[57] J. A. Elliott *et al.*, “In-situ deformation of an open-cell flexible polyurethane foam characterised by 3D computed microtomography,” *J Mater Sci*, vol. 37, no. 8, 2002, doi: 10.1023/A:1014920902712.
[58] D. Feng and F. Aymerich, “E ff ect of core density on the low-velocity impact response of foam-based sandwich composites,” vol. 239, no. January, 2020.
[59] M. F. Funari, S. Spadea, F. Fabbrocino, and P. Lonetti, “On the elastic properties of PVC foam,” *Procedia Structural Integrity*, vol. 28, no. 2019, pp. 1503–1510, 2020, doi: 10.1016/j.prostr.2020.10.123.
[60] K. Kanny, H. Mahfuz, T. Thomas, and S. Jeelani, “Temperature effects on the fatigue behavior of foam core sandwich structures,” *Polymers and Polymer Composites*, vol. 12, no. 7, 2004, doi: 10.1177/096739110401200702.
[61] H. P. S. A. Khalil, M. A. Tehrani, Y. Davoudpour, A. H. Bhat, M. Jawaid, and A. Hassan, “Natural fiber reinforced poly(vinyl chloride) composites: A review,” *Journal of Reinforced Plastics and Composites*, vol. 32, no. 5. 2013. doi: 10.1177/0731684412458553.
[62] G. M. Viana and L. A. Carlsson, “Mechanical Properties and Fracture Characterization of Cross-Linked PVC Foams,” *Journal of Sandwich Structures & Materials*, vol. 4, no. 2, 2002, doi: 10.1177/1099636202004002227.

[63] A. G. Castellanos and P. Prabhakar, “Elucidating the mechanisms of damage in foam core sandwich composites under impact loading and low temperatures,” *Journal of Sandwich Structures and Materials*, vol. 24, no. 1, 2022, doi: 10.1177/1099636221993848.
[64] M. Elamin, B. Li, and K. T. Tan, “Impact damage of composite sandwich structures in arctic condition,” vol. 192, no. October 2017, pp. 422–433, 2018.
[65] A. Farshidi, C. Berggreen, and L. A. Carlsson, “Low temperature mixed-mode debond fracture and fatigue characterisation of foam core sandwich,” *Journal of Sandwich Structures & Materials*, vol. 22, no. 4, pp. 1039–1054, May 2020, doi: 10.1177/1099636218779420.
[66] M. S. H. Fatt and A. R. Vedire, “Mechanical properties of marine polymer foams in the arctic environment,” vol. 86, no. May, 2022.
[67] C. D. Garcia, “Behavior of Sandwich Composite Cores under Extreme Conditions Master s Program in Mechanical Engineering,” The University of Texas at El Paso, 2017.
[68] M. H. Khan, B. Li, and K. T. Tan, “Impact performance and bending behavior of carbon-fiber foam-core sandwich composite structures in cold arctic temperature,” *Journal of Composites Science*, vol. 4, no. 3, 2020, doi: 10.3390/jcs4030133.
[69] D.-H. Kim *et al.*, “Evaluation of PVC-Type Insulation Foam Material for Cryogenic Applications,” *Polymers (Basel)*, vol. 15, no. 6, p. 1401, Mar. 2023, doi: 10.3390/polym15061401.
[70] I. Papa, D. Mocerino, V. Pagliarulo, M. Rippa, and A. Langella, “Damage evolution in sandwich components at different extreme temperatures,” *J Compos Mater*, vol. 55, no. 30, pp. 4459–4468, Dec. 2021, doi: 10.1177/00219983211041758.
[71] A. K. Singh and B. D. Davidson, “Effects of temperature, seawater and impact on the strength, stiffness, and life of sandwich composites,” *Journal of Reinforced Plastics and Composites*, vol. 30, no. 3, pp. 269–277, Feb. 2011, doi: 10.1177/0731684410393053.
[72] A. Siriruk, D. Penumadu, and A. Sharma, “Effects of Seawater and Low Temperatures on Polymeric Foam Core Material,” *Exp Mech*, vol. 52, no. 1, pp. 25–36, Jan. 2012, doi: 10.1007/s11340-011-9564-2.
[73] K. T. Tan, “Behavior of Composite Materials and Structures in Low Temperature Arctic Conditions,” in *Advances in Thick Section Composite and Sandwich Structures*, Cham: Springer International Publishing, 2020, pp. 605–624. doi: 10.1007/978-3-030-31065-3_21.
[74] W. Xiao, Y. Hu, and Y. Li, “Ice impact response and energy dissipation characteristics of PVC foam core sandwich plates : Experimental and numerical study,” vol. 89, no. November 2022, 2023.
[75] P. Yang, S. S. Shams, A. Slay, B. Brokate, and R. Elhajjar, “Evaluation of temperature effects on low velocity impact damage in composite sandwich panels with polymeric foam cores,” *Compos Struct*, vol. 129, 2015, doi: 10.1016/j.compstruct.2015.03.065.
[76] E. Lamanna, N. Gupta, P. Cappa, O. M. Strbik, and K. Cho, “Evaluation of the dynamic properties of an aluminum syntactic foam core sandwich,” *J Alloys Compd*, vol. 695, 2017, doi: 10.1016/j.jallcom.2016.11.361.
[77] Z. Zhang, L. Huang, B. Li, T. Chen, and Q. Zhang, “Design of a novel multi-walled tube-reinforced aluminum foam for energy absorption,” vol. 276, no. November 2020, 2021.
[78] C. M. Cady, G. T. G. Iii, C. Liu, M. L. Lovato, and T. Mukai, “Compressive properties of a closed-cell aluminum foam as a function of strain rate and temperature,” vol. 525, pp. 1–6, 2009, doi: 10.1016/j.msea.2009.07.007.

[79] P. Breunig *et al.*, “Dynamic impact behavior of syntactic foam core sandwich composites,” *J Compos Mater*, vol. 54, no. 4, 2020, doi: 10.1177/0021998319885000.
[80] C. D. Garcia, K. Shahapurkar, M. Doddamani, G. C. M. Kumar, and P. Prabhakar, “Effect of arctic environment on flexural behavior of fly ash cenosphere reinforced epoxy syntactic foams,” *Compos B Eng*, vol. 151, 2018, doi: 10.1016/j.compositesb.2018.06.035.
[81] K. Shahapurkar, C. D. Garcia, M. Doddamani, G. C. Mohan Kumar, and P. Prabhakar, “Compressive behavior of cenosphere/epoxy syntactic foams in arctic conditions,” *Compos B Eng*, vol. 135, no. October 2017, pp. 253–262, Feb. 2018, doi: 10.1016/j.compositesb.2017.10.006.
[82] C. Swetha and R. Kumar, “Quasi-static uni-axial compression behaviour of hollow glass microspheres/epoxy based syntactic foams,” *Mater Des*, vol. 32, no. 8–9, 2011, doi: 10.1016/j.matdes.2011.04.058.
[83] S. W. Lee and A. Anthology, *Advances in Thick Section Composite and Sandwich Structures*. Cham: Springer International Publishing, 2020. doi: 10.1007/978-3-030-31065-3.
[84] V. C. Shunmugasamy, “Viscoelastic properties of hollow glass particle filled vinyl ester matrix syntactic foams : effect of temperature and loading frequency,” pp. 1685–1701, 2013, doi: 10.1007/s10853-012-6927-8.
[85] W. Ahmed, S. Ahmed, F. Alnajjar, and E. Zaneldin, “Mechanical performance of three-dimensional printed sandwich composite with a high-flexible core,” *Proceedings of the Institution of Mechanical Engineers, Part L: Journal of Materials: Design and Applications*, vol. 235, no. 6, pp. 1382–1400, Jun. 2021, doi: 10.1177/14644207211011729.
[86] D. Lee, H.-J. Kwon, S. Yang, and M.-S. Kim, “Fabrication, testing, and analysis of sandwich structure with composite skin and additive manufactured core,” *Journal of Reinforced Plastics and Composites*, vol. 40, no. 17–18, pp. 654–664, Sep. 2021, doi: 10.1177/0731684421995883.
[87] Y. Bai, K. Yu, J. Zhao, and R. Zhao, “Experimental and simulation investigation of temperature e ff ects on modal characteristics of composite honeycomb structure,” vol. 201, no. February, pp. 816–827, 2018.
[88] C. C. Foo, G. B. Chai, and L. K. Seah, “Mechanical properties of Nomex material and Nomex honeycomb structure,” *Compos Struct*, vol. 80, no. 4, 2007, doi: 10.1016/j.compstruct.2006.07.010.
[89] Y. Liu, W. Liu, W. Gao, L. Zhang, and E. Zhang, “Mechanical responses of a composite sandwich structure with Nomex honeycomb core,” *Journal of Reinforced Plastics and Composites*, vol. 38, no. 13, 2019, doi: 10.1177/0731684419836492.
[90] M. C. Taylor and M. C. Taylor, “DAMAGE TOLERANCE OF COMPOSITE HONEYCOMB SANDWICH PANELS,” 1989.
[91] M. Jean-st-laurent, M. Dano, and M. Potvin, “Compression after impact behavior of carbon / epoxy composite sandwich panels with Nomex honeycomb core subjected to low velocity impacts at extreme cold temperatures,” vol. 261, no. December 2020, pp. 1–11, 2021.
[92] A. Salehi-khojin and M. Mahinfalah, “Temperature effects on Kevlar / hybrid and carbon fiber composite sandwiches under impact loading,” vol. 78, pp. 197–206, 2007, doi: 10.1016/j.compstruct.2005.09.005.

[93] S. Fischer, K. Drechsler, S. Kilchert, and A. Johnson, “Mechanical tests for foldcore base material properties,” *Compos Part A Appl Sci Manuf*, vol. 40, no. 12, 2009, doi: 10.1016/j.compositesa.2009.03.005.
[94] N. Aliheidari, R. Tripuraneni, C. Hohimer, J. Christ, A. Ameli, and S. Nadimpalli, “The impact of nozzle and bed temperatures on the fracture resistance of FDM printed materials,” in *Behavior and Mechanics of Multifunctional Materials and Composites 2017*, 2017. doi: 10.1117/12.2260105.
[95] J. T. Cantrell *et al.*, “Experimental characterization of the mechanical properties of 3D-printed ABS and polycarbonate parts,” *Rapid Prototyp J*, vol. 23, no. 4, 2017, doi: 10.1108/RPJ-03-2016-0042.
[96] M. R. Khosravani, A. Zolfagharian, M. Jennings, and T. Reinicke, “Structural performance of 3D-printed composites under various loads and environmental conditions,” *Polym Test*, vol. 91, no. April, p. 106770, Nov. 2020, doi: 10.1016/j.polymertesting.2020.106770.
[97] T. Li and L. Wang, “Bending behavior of sandwich composite structures with tunable 3D-printed core materials,” *Compos Struct*, vol. 175, 2017, doi: 10.1016/j.compstruct.2017.05.001.
[98] X. Li, F. Cong, Y. Zhang, Z. Qin, S. Wang, and J. He, “Effect of high-low temperature on the compressive and shear performances of composite sandwich panels with pyramidal lattice truss cores,” vol. 292, no. April, 2022.
[99] R. Nam, M. Jakubinek, H. Niknam, M. Rahmat, B. Ashrafi, and H. E. Naguib, “Materials & Design 3D printed octet plate-lattices for tunable energy absorption,” vol. 228, pp. 1–12, 2023.
[100] M. D. Erickson, A. R. Kallmeyer, and K. G. Kellogg, “Effect of Temperature on the Low-velocity Impact Behavior of Composite Sandwich Panels,” *Journal of Sandwich Structures & Materials*, vol. 7, no. 3, pp. 245–264, May 2005, doi: 10.1177/1099636205048636.
[101] S. A. M. Ghannadpour, M. Mahmoudi, and K. H. Nedjad, “Structural behavior of 3D-printed sandwich beams with strut-based lattice core : Experimental and numerical study,” vol. 281, no. October 2021, 2022.
[102] F. Yıldırım, A. C. Tatar, V. Eskizeybek, A. Avcı, and M. Aydın, “Impact response of nanoparticle reinforced 3D woven spacer/epoxy composites at cryogenic temperatures,” *J Compos Mater*, vol. 55, no. 28, pp. 4231–4244, Dec. 2021, doi: 10.1177/00219983211037052.
[103] S. Li, R. Hu, J. Cheng, and Y. Hu, “Compressive effect of jute fiber corrugated lattice sandwich structure,” *Journal of Reinforced Plastics and Composites*, vol. 39, no. 5–6, pp. 209–218, Mar. 2020, doi: 10.1177/0731684419881785.
[104] V. Kallannavar and S. Kattimani, “Thin-Walled Structures Effect of temperature and porosity on free vibration characteristics of a doubly-curved skew laminated sandwich composite structures with 3D printed PLA core,” vol. 182, no. October 2022, 2023.
[105] J. Bru, M. Leite, A. R. Ribeiro, L. Reis, A. M. Deus, and M. Fátima Vaz, “Bioinspired structures for core sandwich composites produced by fused deposition modelling,” *Proceedings of the Institution of Mechanical Engineers, Part L: Journal of Materials: Design and Applications*, vol. 234, no. 3, 2020, doi: 10.1177/1464420719886906.

[106] M. J. Khoshgoftar, A. Barkhordari, M. Limuti, F. Buccino, L. Vergani, and M. J. Mirzaali, "Bending analysis of sandwich panel composite with a re - entrant lattice core using zig - zag theory," *Sci Rep*, pp. 1–12, 2022, doi: 10.1038/s41598-022-19930-x.
[107] J. Smardzewski and K. Witold, "Response of wood-based sandwich beams with three-dimensional lattice core," vol. 216, no. November 2018, pp. 340–349, 2019.
[108] R. N. Manjunath, V. Khatkar, and B. K. Behera, "Influence of augmented tuning of core architecture in 3D woven sandwich structures on flexural and compression properties of their composites," *Advanced Composite Materials*, vol. 29, no. 4, 2020, doi: 10.1080/09243046.2019.1680925.
[109] J. Xiong *et al.*, "Advanced Micro-Lattice Materials," *Adv Eng Mater*, vol. 17, no. 9, pp. 1253–1264, Sep. 2015, doi: 10.1002/adem.201400471.
[110] A. Bakhtiyari, M. Baghani, M. A. Maleki-bigdeli, and S. Sohrabpour, "European Journal of Mechanics / A Solids Analytical and numerical solution for multiple shape memory effect of smart corrugated-core sandwich panels with different patterns," vol. 100, no. April, 2023.
[111] H. Mei *et al.*, "3D-printed SiC lattices integrated with lightweight quartz fiber / silica aerogel sandwich structure for thermal protection system," vol. 454, no. November 2022, 2023.
[112] K. Wei, R. He, X. Cheng, Y. Pei, R. Zhang, and D. Fang, "Fabrication and heat transfer characteristics of C / SiC pyramidal core lattice sandwich panel," vol. 81, pp. 10–17, 2015.
[113] C. Li, H. Shen, and J. Yang, "Low-velocity impact response of cylindrical sandwich shells with auxetic 3D double-V meta-lattice core and FG GRC facesheets," vol. 262, no. April, 2022.
[114] X. Wei, J. Xiong, J. Wang, and W. Xu, "New advances in fiber-reinforced composite honeycomb materials," *Sci China Technol Sci*, vol. 63, no. 8, pp. 1348–1370, Aug. 2020, doi: 10.1007/s11431-020-1650-9.
[115] B. L. Buitrago, C. Santiuste, S. Sánchez-Sáez, E. Barbero, and C. Navarro, "Modelling of composite sandwich structures with honeycomb core subjected to high-velocity impact," *Compos Struct*, vol. 92, no. 9, pp. 2090–2096, Aug. 2010, doi: 10.1016/j.compstruct.2009.10.013.
[116] Z. Sun, S. Shi, X. Guo, X. Hu, and H. Chen, "On compressive properties of composite sandwich structures with grid reinforced honeycomb core," *Compos B Eng*, vol. 94, pp. 245–252, Jun. 2016, doi: 10.1016/j.compositesb.2016.03.054.
[117] E. Zaini, M. Azaman, M. Jamali, and K. Ismail, "Synthesis and characterization of natural fiber reinforced polymer composites as core for honeycomb core structure: A review," *Journal of Sandwich Structures & Materials*, vol. 22, no. 3, pp. 525–550, Mar. 2020, doi: 10.1177/1099636218758589.
[118] K. Finnegan, G. Kooistra, H. N. G. Wadley, and V. S. Deshpande, "The compressive response of carbon fiber composite pyramidal truss sandwich cores," *International Journal of Materials Research*, vol. 98, no. 12, pp. 1264–1272, Dec. 2007, doi: 10.3139/146.101594.
[119] J. Xiong, L. Ma, L. Wu, J. Liu, and A. Vaziri, "Mechanical behavior and failure of composite pyramidal truss core sandwich columns," *Compos B Eng*, vol. 42, no. 4, pp. 938–945, Jun. 2011, doi: 10.1016/j.compositesb.2010.12.021.

[120] Y. Sun and L. Gao, “Structural responses of all-composite improved-pyramidal truss sandwich cores,” *Mater Des*, vol. 43, pp. 50–58, Jan. 2013, doi: 10.1016/j.matdes.2012.06.033.
[121] L. Gao, Y. Sun, L. Cong, and P. Chen, “Mechanical behaviours of composite sandwich panel with strengthened pyramidal truss cores,” *Compos Struct*, vol. 105, pp. 149–152, Nov. 2013, doi: 10.1016/j.compstruct.2013.05.015.
[122] X. Li, F. Cong, Y. Zhang, Z. Qin, S. Wang, and J. He, “Effect of high-low temperature on the compressive and shear performances of composite sandwich panels with pyramidal lattice truss cores,” *Compos Struct*, vol. 292, p. 115675, Jul. 2022, doi: 10.1016/j.compstruct.2022.115675.
[123] H.-L. Fan, T. Zeng, D.-N. Fang, and W. Yang, “Mechanics of advanced fiber reinforced lattice composites,” *Acta Mechanica Sinica*, vol. 26, no. 6, pp. 825–835, Dec. 2010, doi: 10.1007/s10409-010-0390-z.
[124] M. Mir, M. N. Ali, J. Sami, and U. Ansari, “Review of Mechanics and Applications of Auxetic Structures,” *Advances in Materials Science and Engineering*, vol. 2014, pp. 1–17, 2014, doi: 10.1155/2014/753496.
[125] W. Yang, Z.-M. Li, W. Shi, B.-H. Xie, and M.-B. Yang, “Review on auxetic materials,” *J Mater Sci*, vol. 39, no. 10, pp. 3269–3279, May 2004, doi: 10.1023/B:JMSC.0000026928.93231.e0.
[126] S. Shukla and B. K. Behera, “Auxetic fibrous structures and their composites: A review,” *Compos Struct*, vol. 290, p. 115530, Jun. 2022, doi: 10.1016/j.compstruct.2022.115530.
[127] C. Li, H. Shen, and H. Wang, “Postbuckling behavior of sandwich plates with functionally graded auxetic 3D lattice core,” vol. 237, no. January, 2020.
[128] J. Zhang, G. Lu, and Z. You, “Large deformation and energy absorption of additively manufactured auxetic materials and structures: A review,” *Compos B Eng*, vol. 201, p. 108340, Nov. 2020, doi: 10.1016/j.compositesb.2020.108340.
[129] N. D. Duc, K. Seung-Eock, N. D. Tuan, P. Tran, and N. D. Khoa, “New approach to study nonlinear dynamic response and vibration of sandwich composite cylindrical panels with auxetic honeycomb core layer,” *Aerosp Sci Technol*, vol. 70, pp. 396–404, Nov. 2017, doi: 10.1016/j.ast.2017.08.023.
[130] C. Li, H. Shen, and J. Yang, “Low-velocity impact response of cylindrical sandwich shells with auxetic 3D double-V meta-lattice core and FG GRC facesheets,” vol. 262, no. April, 2022.
[131] B. Vijaya Ramnath, K. Alagarraja, and C. Elanchezhian, “Review on Sandwich Composite and their Applications,” *Mater Today Proc*, vol. 16, pp. 859–864, 2019, doi: 10.1016/j.matpr.2019.05.169.
[132] K. KanthaRao, K. JayathirthaRao, A. G. Sarwade, and B. MadhavaVarma, “Bending behaviour of aluminium honey comb sandwich panels,” *Int J Eng Adv Technol*, vol. 1, no. 4, pp. 268–272, 2012.
[133] J. Yang, J. Xiong, L. Ma, B. Wang, G. Zhang, and L. Wu, “Vibration and damping characteristics of hybrid carbon fiber composite pyramidal truss sandwich panels with viscoelastic layers,” *Compos Struct*, vol. 106, pp. 570–580, Dec. 2013, doi: 10.1016/j.compstruct.2013.07.015.
[134] H. Fan, L. Yang, F. Sun, and D. Fang, “Composites : Part A Compression and bending performances of carbon fiber reinforced lattice-core sandwich composites,” vol. 52, pp. 118–125, 2013.

[135] B. Wang, L. Wu, L. Ma, Y. Sun, and S. Du, "Mechanical behavior of the sandwich structures with carbon fiber-reinforced pyramidal lattice truss core," *Materials & Design (1980-2015)*, vol. 31, no. 5, pp. 2659–2663, May 2010, doi: 10.1016/j.matdes.2009.11.061.
[136] J. Xiong, A. Vaziri, L. Ma, J. Papadopoulos, and L. Wu, "Compression and impact testing of two-layer composite pyramidal-core sandwich panels," *Compos Struct*, vol. 94, no. 2, 2012, doi: 10.1016/j.compstruct.2011.09.018.
[137] J. Xiong, L. Ma, L. Wu, B. Wang, and A. Vaziri, "Fabrication and crushing behavior of low density carbon fiber composite pyramidal truss structures," *Compos Struct*, vol. 92, no. 11, pp. 2695–2702, Oct. 2010, doi: 10.1016/j.compstruct.2010.03.010.
[138] S. Heimbs, J. Cichosz, M. Klaus, S. Kilchert, and A. F. Johnson, "Sandwich structures with textile-reinforced composite foldcores under impact loads," *Compos Struct*, vol. 92, no. 6, pp. 1485–1497, May 2010, doi: 10.1016/j.compstruct.2009.11.001.
[139] T. Wang, L. Wang, Z. Ma, and G. M. Hulbert, "Elastic analysis of auxetic cellular structure consisting of re-entrant hexagonal cells using a strain-based expansion homogenization method," *Mater Des*, vol. 160, pp. 284–293, Dec. 2018, doi: 10.1016/j.matdes.2018.09.013.
[140] V. H. Carneiro, N. Peixinho, and J. Meireles, "Significance of cell number on the bulk elastic properties of auxetic reentrant lattices," *Science and Technology of Materials*, vol. 30, no. 1, pp. 8–12, Jan. 2018, doi: 10.1016/j.stmat.2018.01.003.
[141] D.-L. Shi, X.-Q. Feng, Y. Y. Huang, K.-C. Hwang, and H. Gao, "The Effect of Nanotube Waviness and Agglomeration on the Elastic Property of Carbon Nanotube-Reinforced Composites," *J Eng Mater Technol*, vol. 126, no. 3, pp. 250–257, Jul. 2004, doi: 10.1115/1.1751182.
[142] M. Shruti, N. Sri Hemanth, N. D. Badgayan, and S. K. Sahu, "Compressive behavior of auxetic structural metamaterial for lightweight construction using ANSYS static structural analysis," *Mater Today Proc*, vol. 38, pp. 12–17, 2021, doi: 10.1016/j.matpr.2020.05.410.
[143] V. Amaya-Amaya, M. de Icaza-Herrera, A. L. Martínez-Hernández, G. Martínez-Barrera, and C. Velasco-Santos, "Experimental approximation of the sound absorption coefficient ($\propto$) for 3D printed reentrant auxetic structures of poly lactic acid reinforced with chicken keratin materials," *Mater Lett*, vol. 283, p. 128757, Jan. 2021, doi: 10.1016/j.matlet.2020.128757.
[144] V. Gupta, B. Bhattacharya, and S. Adhikari, "Energy Absorption of Hourglass Shaped Lattice Metastructures," *Exp Mech*, vol. 62, no. 6, pp. 943–952, Jul. 2022, doi: 10.1007/s11340-022-00840-y.
[145] D. Mousanezhad *et al.*, "Hierarchical honeycomb auxetic metamaterials," *Sci Rep*, vol. 5, no. 1, p. 18306, Dec. 2015, doi: 10.1038/srep18306.
[146] H. Mitschke *et al.*, "Finding Auxetic Frameworks in Periodic Tessellations," *Advanced Materials*, vol. 23, no. 22–23, pp. 2669–2674, Jun. 2011, doi: 10.1002/adma.201100268.
[147] M. Taylor, L. Francesconi, M. Gerendás, A. Shanian, C. Carson, and K. Bertoldi, "Low Porosity Metallic Periodic Structures with Negative Poisson's Ratio," *Advanced Materials*, vol. 26, no. 15, pp. 2365–2370, Apr. 2014, doi: 10.1002/adma.201304464.
[148] J. Schwerdtfeger *et al.*, "Design of Auxetic Structures via Mathematical Optimization," *Advanced Materials*, vol. 23, no. 22–23, pp. 2650–2654, Jun. 2011, doi: 10.1002/adma.201004090.

[149] R. Lakes, “Advances in negative Poisson’s ratio materials,” *Advanced Materials*, vol. 5, no. 4, pp. 293–296, Apr. 1993, doi: 10.1002/adma.19930050416.
[150] L. Liu, P. Kamm, F. García-Moreno, J. Banhart, and D. Pasini, “Elastic and failure response of imperfect three-dimensional metallic lattices: the role of geometric defects induced by Selective Laser Melting,” *J Mech Phys Solids*, vol. 107, 2017, doi: 10.1016/j.jmps.2017.07.003.
[151] A. R. Torrado and D. A. Roberson, “Failure Analysis and Anisotropy Evaluation of 3D-Printed Tensile Test Specimens of Different Geometries and Print Raster Patterns,” *Journal of Failure Analysis and Prevention*, vol. 16, no. 1, 2016, doi: 10.1007/s11668-016-0067-4.
[152] “formlabs.” Accessed: Nov. 01, 2023. [Online]. Available: https://formlabs.com/
[153] ASTM International, “ASTM D638-14 Standard Test Method for Tensile Properties of Plastics,” 2014 doi: 10.1520/D0638-14.1.
[154] E. F. de Castro, G. Nima, F. A. Rueggeberg, and M. Giannini, “Effect of build orientation in accuracy, flexural modulus, flexural strength, and microhardness of 3D-Printed resins for provisional restorations,” *J Mech Behav Biomed Mater*, vol. 136, no. June, 2022, doi: 10.1016/j.jmbbm.2022.105479.
[155] M. Shirinbayan *et al.*, “Effect of build orientation and post-curing of (meth)acrylate-based photocurable resin fabricated by stereolithography on the mechanical behavior from quasi-static to high strain rate loadings,” *The International Journal of Advanced Manufacturing Technology*, vol. 123, no. 5–6, pp. 1877–1887, Nov. 2022, doi: 10.1007/s00170-022-10336-7.
[156] N. Zirak, M. Shirinbayan, K. Benfriha, M. Deligant, and A. Tcharkhtchi, “Stereolithography of (meth)acrylate-based photocurable resin: Thermal and mechanical properties,” *J Appl Polym Sci*, vol. 139, no. 22, Jun. 2022, doi: 10.1002/app.52248.
[157] Y. A. Al-Dulaijan *et al.*, “Effect of Printing Orientation and Postcuring Time on the Flexural Strength of 3D-Printed Resins,” *Journal of Prosthodontics*, vol. 32, no. S1, pp. 45–52, Apr. 2023, doi: 10.1111/jopr.13572.
[158] R. L. Sælen, O. S. Hopperstad, and A. H. Clausen, “Mechanical behaviour and constitutive modelling of an additively manufactured stereolithography polymer,” *Mechanics of Materials*, vol. 185, no. July, p. 104777, Oct. 2023, doi: 10.1016/j.mechmat.2023.104777.
[159] J. Martín-Montal, J. Pernas-Sánchez, and D. Varas, “Experimental characterization framework for SLA additive manufacturing materials,” *Polymers (Basel)*, vol. 13, no. 7, 2021, doi: 10.3390/polym13071147.
[160] ASTM INTERNATIONAL, “Standard Test Methods for Flexural Properties of Unreinforced and Reinforced Plastics and Electrical Insulating Materials. D790,” *Annual Book of ASTM Standards*, pp. 1–12, 2017, doi: 10.1520/D0790-17.2.
[161] ASTM INTERNATIONAL, “Standard test method for compressive properties of rigid plastics D695,” *Annual Book of ASTM Standards*, vol. 08, pp. 1–7, 2023, doi: 10.1520/D0695-23.2.
[162] J. T. Cantrell *et al.*, “Experimental characterization of the mechanical properties of 3D-printed ABS and polycarbonate parts,” *Rapid Prototyp J*, vol. 23, no. 4, 2017, doi: 10.1108/RPJ-03-2016-0042.

[163] J. Martín-Montal, J. Pernas-Sánchez, and D. Varas, "Experimental characterization framework for SLA additive manufacturing materials," *Polymers (Basel)*, vol. 13, no. 7, 2021, doi: 10.3390/polym13071147.
[164] D. V. W. M. de Vries, "Characterization of polymeric foams," 2009.
[165] M. S. H. Fatt and A. R. Vedire, "Mechanical properties of marine polymer foams in the arctic environment," vol. 86, no. May, 2022.
[166] A. Galeski, "Strength and toughness of crystalline polymer systems," *Prog Polym Sci*, vol. 28, no. 12, pp. 1643–1699, Dec. 2003, doi: 10.1016/j.progpolymsci.2003.09.003.
[167] J. A. Jansen, "Ductile-to-brittle transition of plastic materials: failure analysis of polymers often shows that the part failed after the material changed from a ductile to a brittle microstructure," *Advanced Materials & Processes*, vol. 164, no. 2, 2006.
[168] E. Lucon, "Influence of Shear Lip Symmetry on the Fracture Behavior of Charpy Specimens," *J Test Eval*, vol. 47, no. 2, p. 20180403, Mar. 2019, doi: 10.1520/JTE20180403.
[169] J. R. Matthews, "On the relationship between shear lip, shear index and energy in dynamic tear specimens," *Eng Fract Mech*, vol. 54, no. 1, pp. 11–23, May 1996, doi: 10.1016/0013-7944(95)00258-8.
[170] H. R. Brown, "A model for brittle-ductile transitions in polymers," *J Mater Sci*, vol. 17, no. 2, pp. 469–476, Feb. 1982, doi: 10.1007/BF00591482.
[171] R. Afrin, S. Kasas, T. Gmur, and G. Dietler, "Polymer chain mechanics," in *The World of Nano-Biomechanics*, I. Atsushi, Ed., Elsevier, 2008, pp. 69–87. doi: 10.1016/B978-044452777-6.50006-1.
[172] D. V. W. M. de Vries, "Characterization of polymeric foams," 2009.
[173] A. H. V. 8: M. T. and Evaluation, Ed., *ASM Handbook Volume 8: Mechanical Testing and Evaluation*. ASM International.
[174] M. Jerabek, Z. Major, and R. W. Lang, "Uniaxial compression testing of polymeric materials," *Polym Test*, vol. 29, no. 3, pp. 302–309, May 2010, doi: 10.1016/j.polymertesting.2009.12.003.
[175] M. Hassani Niaki, A. Fereidoon, and M. Ghorbanzadeh Ahangari, "Mechanical properties of epoxy/basalt polymer concrete: Experimental and analytical study," *Structural Concrete*, vol. 19, no. 2, pp. 366–373, Apr. 2018, doi: 10.1002/suco.201700003.
[176] J. Chevalier, X. P. Morelle, C. Bailly, P. P. Camanho, T. Pardoen, and F. Lani, "Micro-mechanics based pressure dependent failure model for highly cross-linked epoxy resins," *Eng Fract Mech*, vol. 158, pp. 1–12, Jun. 2016, doi: 10.1016/j.engfracmech.2016.02.039.
[177] W. Yu, G. Wu, B. An, and P. Wang, "Experimental Study on the Brittle-Ductile Response of a Heterogeneous Soft Coal Rock Mass under Multifactor Coupling," *Geofluids*, vol. 2019, 2019, doi: 10.1155/2019/5316149.
[178] H. Horii and S. Nemat-Nasser, "Compression-induced microcrack growth in brittle solids: Axial splitting and shear failure," *J Geophys Res Solid Earth*, vol. 90, no. B4, pp. 3105–3125, Mar. 1985, doi: 10.1029/JB090iB04p03105.
[179] S. Salehin, "Investigation into engineering parameters of marls from Seydoon dam in Iran," *Journal of Rock Mechanics and Geotechnical Engineering*, vol. 9, no. 5, pp. 912–923, Oct. 2017, doi: 10.1016/j.jrmge.2017.05.002.
[180] X. P. Zhou, Y. J. Lian, L. N. Y. Wong, and F. Berto, "Understanding the fracture behavior of brittle and ductile multi-flawed rocks by uniaxial loading by digital image correlation,"

Eng Fract Mech, vol. 199, pp. 438–460, Aug. 2018, doi: 10.1016/j.engfracmech.2018.06.007.
[181] R. Afrin, S. Kasas, T. Gmur, and G. Dietler, "Polymer chain mechanics," in *The World of Nano-Biomechanics*, I. Atsushi, Ed., Elsevier, 2008, pp. 69–87. doi: 10.1016/B978-044452777-6.50006-1.
[182] R. Karakuzu, E. Erbil, and M. Aktas, "Impact characterization of glass/epoxy composite plates: An experimental and numerical study," *Compos B Eng*, vol. 41, no. 5, pp. 388–395, 2010, doi: 10.1016/j.compositesb.2010.02.003.
[183] L. L. Sobrinho, M. Ferreira, and F. L. Bastian, "The effects of water absorption on an ester vinyl resin system," *Materials Research*, vol. 12, no. 3, pp. 353–361, 2009, doi: 10.1590/s1516-14392009000300017.
[184] A. W. Signor, M. R. VanLandingham, and J. W. Chin, "Effects of ultraviolet radiation exposure on vinyl ester resins: Characterization of chemical, physical and mechanical damage," *Polym Degrad Stab*, vol. 79, no. 2, pp. 359–368, 2003, doi: 10.1016/S0141-3910(02)00300-2.
[185] V. Lunetto, M. Galati, L. Settineri, and L. Iuliano, "Sustainability in the manufacturing of composite materials: A literature review and directions for future research," *J Manuf Process*, vol. 85, no. December 2022, pp. 858–874, 2023, doi: 10.1016/j.jmapro.2022.12.020.
[186] M. Elkington, D. Bloom, C. Ward, A. Chatzimichali, and K. Potter, "Hand layup: understanding the manual process," *Advanced Manufacturing: Polymer and Composites Science*, vol. 1, no. 3, pp. 138–151, 2015, doi: 10.1080/20550340.2015.1114801.
[187] V. R. Tamakuwala, "Manufacturing of fiber reinforced polymer by using VARTM process: A review," *Mater Today Proc*, vol. 44, pp. 987–993, 2021, doi: 10.1016/j.matpr.2020.11.102.
[188] D. Abliz, Y. Duan, L. Steuernagel, L. Xie, D. Li, and G. Ziegmann, "Curing Methods for Advanced Polymer Composites - A Review," *Polymers and Polymer Composites*, vol. 21, no. 6, pp. 341–348, Jul. 2013, doi: 10.1177/096739111302100602.
[189] O. A. Ekuase, N. Anjum, V. O. Eze, and O. I. Okoli, "A Review on the Out-of-Autoclave Process for Composite Manufacturing," *Journal of Composites Science*, vol. 6, no. 6, 2022, doi: 10.3390/jcs6060172.
[190] M. Azeem *et al.*, "Application of Filament Winding Technology in Composite Pressure Vessels and Challenges: A Review," *J Energy Storage*, vol. 49, no. October 2021, 2022, doi: 10.1016/j.est.2021.103468.
[191] P. K. Karsh, T. Mukhopadhyay, and S. Dey, "Stochastic low-velocity impact on functionally graded plates: Probabilistic and non-probabilistic uncertainty quantification," *Compos B Eng*, vol. 159, no. July 2018, pp. 461–480, 2019, doi: 10.1016/j.compositesb.2018.09.066.
[192] M. W. Long and J. D. Narciso, *Probabilistic design methodology for composite aircraft structures*. Office of Aviation Research, US Federal Aviation Administration, 1999.
[193] M. Park and M. V. Tretyakov, "Stochastic resin transfer molding process," *SIAM-ASA Journal on Uncertainty Quantification*, vol. 5, no. 1, pp. 1110–1135, 2017, doi: 10.1137/16M1096578.
[194] R. C. Smith, *Uncertainty Quantification: Theory, Implementation, and Applications (Computational Science and Engineering)*. Society for Industrial and Applied Mathematics, 2014.

[195] S. Dey and K. K. Gupta, “Uncertainty Quantification—An Eternal Future of Engineering and Technology,” in *Engineering Pedagogy*, Singapore: Springer Nature Singapore, 2023, pp. 145–155. doi: 10.1007/978-981-19-8016-9_11.
[196] G. Li, L. Yang, C.-G. Lee, X. Wang, and M. Rong, “A Bayesian Deep Learning RUL Framework Integrating Epistemic and Aleatoric Uncertainties,” *IEEE Transactions on Industrial Electronics*, vol. 68, no. 9, pp. 8829–8841, Sep. 2021, doi: 10.1109/TIE.2020.3009593.
[197] G. Terejanu, P. Singla, T. Singh, and P. D. Scott, “Approximate propagation of both epistemic and aleatory uncertainty through dynamic systems,” in *2010 13th International Conference on Information Fusion*, IEEE, Jul. 2010, pp. 1–8. doi: 10.1109/ICIF.2010.5711831.
[198] M. Hanss and S. Turrin, “A fuzzy-based approach to comprehensive modeling and analysis of systems with epistemic uncertainties,” *Structural Safety*, vol. 32, no. 6, pp. 433–441, Nov. 2010, doi: 10.1016/j.strusafe.2010.06.003.
[199] P. Baraldi, M. Compare, and E. Zio, “Component Ranking by Birnbaum Importance in Presence of Epistemic Uncertainty in Failure Event Probabilities,” *IEEE Trans Reliab*, vol. 62, no. 1, pp. 37–48, Mar. 2013, doi: 10.1109/TR.2013.2240885.
[200] C. Wang, H. Fan, and T. Wu, “Novel rough set theory-based method for epistemic uncertainty modeling, analysis and applications,” *Appl Math Model*, vol. 113, pp. 456–474, Jan. 2023, doi: 10.1016/j.apm.2022.09.002.
[201] L. Yang and A. Rauzy, “Epistemic space of degradation processes,” *Journal of Applied Non-Classical Logics*, vol. 31, no. 1, pp. 1–25, Jan. 2021, doi: 10.1080/11663081.2020.1850047.
[202] A. Díaz-Curbelo, R. A. Espin Andrade, and Á. M. Gento Municio, “The Role of Fuzzy Logic to Dealing with Epistemic Uncertainty in Supply Chain Risk Assessment: Review Standpoints,” *International Journal of Fuzzy Systems*, vol. 22, no. 8, pp. 2769–2791, Nov. 2020, doi: 10.1007/s40815-020-00846-5.
[203] S. Adhikari, “Models, Verification, Validation, Identification and Stochastic Eigenvalue Problems,” in *Mechanical Vibration: Where do we Stand?*, Vienna: Springer Vienna, pp. 321–388. doi: 10.1007/978-3-211-70963-4_14.
[204] S. Dey, T. Mukhopadhyay, S. K. Sahu, G. Li, H. Rabitz, and S. Adhikari, “Thermal uncertainty quantification in frequency responses of laminated composite plates,” *Compos B Eng*, vol. 80, pp. 186–197, 2015, doi: 10.1016/j.compositesb.2015.06.006.
[205] J. N. Reddy, *Mechanics of Laminated Composite Plates and Shells Theory and Analysis*, 2nd ed. 2003. doi: 10.1201/b12409.
[206] A. Chakrabarti, A. H. Sheikh, M. Griffith, and D. J. Oehlers, “Dynamic Response of Composite Beams with Partial Shear Interaction Using a Higher-Order Beam Theory,” *Journal of Structural Engineering*, vol. 139, no. 1, pp. 47–56, Jan. 2013, doi: 10.1061/(ASCE)ST.1943-541X.0000603.
[207] A. Mandal, C. Ray, and S. Haldar, “Free vibration analysis of laminated composite skew plates with cut-out,” *Archive of Applied Mechanics*, vol. 87, no. 9, pp. 1511–1523, 2017, doi: 10.1007/s00419-017-1267-4.
[208] D. J. Lekou and T. P. Philippidis, “Mechanical property variability in FRP laminates and its effect on failure prediction,” *Compos B Eng*, vol. 39, no. 7–8, pp. 1247–1256, 2008, doi: 10.1016/j.compositesb.2008.01.004.

[209] US Department of Defense, “Composite Materials Handbook Volume 1: Polymer Matrix Composites - Guidelines for Characterisation of Structural Materials,” *Composite Materials Handbook Series*, vol. 1, no. June, pp. 1–586, 2002.
[210] M. C. Shiao, S. N. Singhal, and C. C. Chamis, “A method for the probabilistic design assessment of composite structures,” *Journal of Structural Engineering*, vol. 39, no. 06, 1994.
[211] M. W. Long and J. D. Narciso, *Probabilistic design methodology for composite aircraft structures*. Office of Aviation Research, US Federal Aviation Administration, 1999.
[212] F. vom Lehn, L. Cai, and H. Pitsch, “Sensitivity analysis, uncertainty quantification, and optimization for thermochemical properties in chemical kinetic combustion models,” *Proceedings of the Combustion Institute*, vol. 37, no. 1, pp. 771–779, 2019, doi: 10.1016/j.proci.2018.06.188.
[213] R. Butler *et al.*, “Uncertainty quantification of composite structures with defects using multilevel monte carlo simulations,” *17th AIAA Non-Deterministic Approaches Conference*, no. January, pp. 1–18, 2015, doi: 10.2514/6.2015-1598.
[214] C. Scarth, J. E. Cooper, P. M. Weaver, and G. H. C. Silva, “Uncertainty quantification of aeroelastic stability of composite plate wings using lamination parameters,” *Compos Struct*, vol. 116, no. 1, pp. 84–93, 2014, doi: 10.1016/j.compstruct.2014.05.007.
[215] S. Dey, T. Mukhopadhyay, S. K. Sahu, G. Li, H. Rabitz, and S. Adhikari, “Thermal uncertainty quantification in frequency responses of laminated composite plates,” *Compos B Eng*, vol. 80, pp. 186–197, 2015, doi: 10.1016/j.compositesb.2015.06.006.
[216] S. Dey, T. Mukhopadhyay, A. Spickenheuer, U. Gohs, and S. Adhikari, “Uncertainty quantification in natural frequency of composite plates - An artificial neural network based approach,” *Advanced Composites Letters*, vol. 25, no. 2, pp. 43–48, 2016, doi: 10.1177/096369351602500203.
[217] P. Sasikumar, R. Suresh, and S. Gupta, “Stochastic model order reduction in uncertainty quantification of composite structures,” *Compos Struct*, vol. 128, pp. 21–34, Sep. 2015, doi: 10.1016/j.compstruct.2015.03.045.
[218] X. Peng, T. Ye, J. Li, H. Wu, S. Jiang, and G. Chen, “Multi-scale uncertainty quantification of composite laminated plate considering random and interval variables with data driven PCE method,” *Mechanics of Advanced Materials and Structures*, vol. 28, no. 23, pp. 2429–2439, 2021, doi: 10.1080/15376494.2020.1741749.
[219] N. Sharma, M. Nishad, D. K. Maiti, M. R. Sunny, and B. N. Singh, “Uncertainty quantification in buckling strength of variable stiffness laminated composite plate under thermal loading,” *Compos Struct*, vol. 275, p. 114486, Nov. 2021, doi: 10.1016/j.compstruct.2021.114486.
[220] K. Sepahvand, M. Scheffler, and S. Marburg, “Uncertainty quantification in natural frequencies and radiated acoustic power of composite plates: Analytical and experimental investigation,” *Applied Acoustics*, vol. 87, pp. 23–29, 2015, doi: 10.1016/j.apacoust.2014.06.008.
[221] Q. Yang, C. Xu, G. Cheng, S. Meng, and W. Xie, “Uncertainty quantification method for mechanical behavior of C/SiC composite and its experimental validation,” *Compos Struct*, vol. 230, no. July, 2019, doi: 10.1016/j.compstruct.2019.111516.
[222] A. H. Seno and M. F. Aliabadi, “Uncertainty quantification for impact location and force estimation in composite structures,” *Struct Health Monit*, vol. 21, no. 3, pp. 1061–1075, 2022, doi: 10.1177/14759217211020255.

[223] P. Acar and V. Sundararaghavan, “Uncertainty quantification and stochastic optimization for spatially varying composite fiber paths,” *AIAA Scitech 2019 Forum*, no. January, 2019, doi: 10.2514/6.2019-0969.
[224] O. P. Le Maître and O. M. Knio, *Spectral Methods for Uncertainty Quantification*. in Scientific Computation. Dordrecht: Springer Netherlands, 2010. doi: 10.1007/978-90-481-3520-2.
[225] L. Mathelin, M. Y. Hussaini, and T. A. Zang, “Stochastic approaches to uncertainty quantification in CFD simulations,” *Numer Algorithms*, vol. 38, no. 1–3, pp. 209–236, Mar. 2005, doi: 10.1007/BF02810624.
[226] R. J. Furnstahl, D. R. Phillips, and S. Wesolowski, “A recipe for EFT uncertainty quantification in nuclear physics,” *Journal of Physics G: Nuclear and Particle Physics*, vol. 42, no. 3, p. 034028, Mar. 2015, doi: 10.1088/0954-3899/42/3/034028.
[227] T. Schultz, L. Schlaffke, B. Schölkopf, and T. Schmidt-Wilcke, “HiFiVE: A Hilbert Space Embedding of Fiber Variability Estimates for Uncertainty Modeling and Visualization,” *Computer Graphics Forum*, vol. 32, no. 3pt1, pp. 121–130, Jun. 2013, doi: 10.1111/cgf.12099.
[228] M. Witte, S. Jaspers, H. Wenck, M. Rübhausen, and F. Fischer, “Noise reduction and quantification of fiber orientations in greyscale images,” *PLoS One*, vol. 15, no. 1, p. e0227534, Jan. 2020, doi: 10.1371/journal.pone.0227534.
[229] S. Mahesh and A. Mishra, “Strength distribution of Ti/SiC metal-matrix composites under monotonic loading,” *Eng Fract Mech*, vol. 194, pp. 86–104, May 2018, doi: 10.1016/j.engfracmech.2018.03.015.
[230] B. Liu, N. Vu-Bac, X. Zhuang, X. Fu, and T. Rabczuk, “Stochastic full-range multiscale modeling of thermal conductivity of Polymeric carbon nanotubes composites: A machine learning approach,” *Compos Struct*, vol. 289, p. 115393, Jun. 2022, doi: 10.1016/j.compstruct.2022.115393.
[231] J.-A. Tröger and S. Hartmann, “Parameter identification and uncertainty quantification of the thermal conductivity tensor for transversely isotropic composite materials,” *PAMM*, vol. 22, no. 1, Mar. 2023, doi: 10.1002/pamm.202200026.
[232] P. D. Spanos and A. Kontsos, “A multiscale Monte Carlo finite element method for determining mechanical properties of polymer nanocomposites,” *Probabilistic Engineering Mechanics*, vol. 23, no. 4, pp. 456–470, Oct. 2008, doi: 10.1016/j.probengmech.2007.09.002.
[233] N. Vu-Bac, R. Rafiee, X. Zhuang, T. Lahmer, and T. Rabczuk, “Uncertainty quantification for multiscale modeling of polymer nanocomposites with correlated parameters,” *Compos B Eng*, vol. 68, pp. 446–464, Jan. 2015, doi: 10.1016/j.compositesb.2014.09.008.
[234] T. Mukhopadhyay, S. Chakraborty, S. Dey, S. Adhikari, and R. Chowdhury, “A Critical Assessment of Kriging Model Variants for High-Fidelity Uncertainty Quantification in Dynamics of composite Shells,” *Archives of Computational Methods in Engineering*, vol. 24, no. 3, pp. 495–518, Jul. 2017, doi: 10.1007/s11831-016-9178-z.
[235] S. Naskar, T. Mukhopadhyay, and S. Sriramula, “Spatially varying fuzzy multi-scale uncertainty propagation in unidirectional fibre reinforced composites,” *Compos Struct*, vol. 209, pp. 940–967, Feb. 2019, doi: 10.1016/j.compstruct.2018.09.090.

[236] S. Koley, P. M. Mohite, and C. S. Upadhyay, “A micromechanical study and uncertainty quantification for effective properties of unidirectional fibre reinforced composites,” *Compos Struct*, vol. 225, p. 111141, Oct. 2019, doi: 10.1016/j.compstruct.2019.111141.
[237] B. Shi and Z. Deng, “An efficient reliability method for composite laminates with high-dimensional uncertainty variables,” *Acta Mech*, vol. 232, no. 9, pp. 3509–3527, Sep. 2021, doi: 10.1007/s00707-021-03008-2.
[238] K. D. Potter, M. Campbell, C. Langer, and M. R. Wisnom, “The generation of geometrical deformations due to tool/part interaction in the manufacture of composite components,” *Compos Part A Appl Sci Manuf*, vol. 36, no. 2 SPEC. ISS., pp. 301–308, 2005, doi: 10.1016/j.compositesa.2004.06.002.
[239] K. Potter, C. Langer, B. Hodgkiss, and S. Lamb, “Sources of variability in uncured aerospace grade unidirectional carbon fibre epoxy preimpregnate,” *Compos Part A Appl Sci Manuf*, vol. 38, no. 3, pp. 905–916, 2007, doi: 10.1016/j.compositesa.2006.07.010.
[240] K. Potter, B. Khan, M. Wisnom, T. Bell, and J. Stevens, “Variability, fibre waviness and misalignment in the determination of the properties of composite materials and structures,” *Compos Part A Appl Sci Manuf*, vol. 39, no. 9, pp. 1343–1354, 2008, doi: 10.1016/j.compositesa.2008.04.016.
[241] G. Fernlund *et al.*, “Experimental and numerical study of the effect of cure cycle, tool surface, geometry, and lay-up on the dimensional fidelity of autoclave-processed composite parts,” *Compos Part A Appl Sci Manuf*, vol. 33, no. 3, pp. 341–351, 2002, doi: 10.1016/S1359-835X(01)00123-3.
[242] M. Olave, A. Vanaerschot, S. V. Lomov, and D. Vandepitte, “Internal geometry variability of two woven composites and related variability of the stiffness,” *Polym Compos*, vol. 33, no. 8, pp. 1335–1350, Aug. 2012, doi: 10.1002/pc.22260.
[243] W. Chen and D. Zhang, “Improved prediction of residual stress induced warpage in thermoset composites using a multiscale thermo-viscoelastic processing model,” *Compos Part A Appl Sci Manuf*, vol. 126, p. 105575, Nov. 2019, doi: 10.1016/j.compositesa.2019.105575.
[244] K. Zhou, R. Enos, D. Zhang, and J. Tang, “Uncertainty analysis of curing-induced dimensional variability of composite structures utilizing physics-guided Gaussian process meta-modeling,” *Compos Struct*, vol. 280, p. 114816, Jan. 2022, doi: 10.1016/j.compstruct.2021.114816.
[245] B. Markicevic, D. Heider, S. G. Advani, and S. Walsh, “Stochastic modeling of preform heterogeneity to address dry spots formation in the VARTM Process,” *Compos Part A Appl Sci Manuf*, vol. 36, no. 6, pp. 851–858, Jun. 2005, doi: 10.1016/j.compositesa.2004.09.002.
[246] C. Zhu, P. Zhu, and Z. Liu, “Uncertainty analysis of mechanical properties of plain woven carbon fiber reinforced composite via stochastic constitutive modeling,” *Compos Struct*, vol. 207, pp. 684–700, Jan. 2019, doi: 10.1016/j.compstruct.2018.09.089.
[247] M. Ostoja-Starzewski, “Material spatial randomness: From statistical to representative volume element,” *Probabilistic Engineering Mechanics*, vol. 21, no. 2, pp. 112–132, 2006, doi: 10.1016/j.probengmech.2005.07.007.
[248] S. Ghosh, Z. Nowak, and L. Kyunghoon, “Quantitative characterization and modeling of composite microstructures by Voronoi cells,” *Acta Mater*, vol. 45, no. 6, pp. 2215–2234, 1997, doi: 10.1016/S1359-6454(96)00365-5.

[249] E. Car, F. Zalamea, S. Oller, J. Miquel, and E. Oñate, “Numerical simulation of fiber reinforced composite materials - Two procedures,” *Int J Solids Struct*, vol. 39, no. 7, pp. 1967–1986, 2002, doi: 10.1016/S0020-7683(01)00240-2.
[250] L. L. Graham-Brady, E. F. Siragy, and S. C. Baxter, “Analysis of Heterogeneous Composites Based on Moving-Window Techniques,” *J Eng Mech*, vol. 129, no. 9, pp. 1054–1064, 2003, doi: 10.1061/(asce)0733-9399(2003)129:9(1054).
[251] T. Huang *et al.*, “Stochastic nonlinear analysis of unidirectional fiber composites using image-based microstructural uncertainty quantification,” *Compos Struct*, vol. 260, p. 113470, Mar. 2021, doi: 10.1016/j.compstruct.2020.113470.
[252] R. Bostanabad *et al.*, “Uncertainty quantification in multiscale simulation of woven fiber composites,” *Comput Methods Appl Mech Eng*, vol. 338, pp. 506–532, 2018, doi: 10.1016/j.cma.2018.04.024.
[253] R. Bostanabad *et al.*, “Uncertainty quantification in multiscale simulation of woven fiber composites,” *Comput Methods Appl Mech Eng*, vol. 338, pp. 506–532, 2018, doi: 10.1016/j.cma.2018.04.024.
[254] N. K. Balasubramani, B. Zhang, N. T. Chowdhury, A. Mukkavilli, M. Suter, and G. M. Pearce, “Micro-mechanical analysis on random RVE size and shape in multiscale finite element modelling of unidirectional FRP composites,” *Compos Struct*, vol. 282, p. 115081, Feb. 2022, doi: 10.1016/j.compstruct.2021.115081.
[255] G. Bechtold and L. Ye, “Influence of fibre distribution on the transverse flow permeability in fibre bundles,” *Compos Sci Technol*, vol. 63, no. 14, pp. 2069–2079, Nov. 2003, doi: 10.1016/S0266-3538(03)00112-X.
[256] E. J. Pitz and K. V. Pochiraju, “Quantifying Uncertainty of Damage in Composites Using a Quasi Monte Carlo Technique,” *J Verif Valid Uncertain Quantif*, vol. 7, no. 1, Mar. 2022, doi: 10.1115/1.4052895.
[257] D. Kumar, Y. Koutsawa, G. Rauchs, M. Marchi, C. Kavka, and S. Belouettar, “Efficient uncertainty quantification and management in the early stage design of composite applications,” *Compos Struct*, vol. 251, p. 112538, Nov. 2020, doi: 10.1016/j.compstruct.2020.112538.
[258] K. Kobayashi *et al.*, “Data-Driven Multiscale Modeling and Robust Optimization of Composite Structure with Uncertainty Quantification,” in *Handbook of Smart Energy Systems*, Cham: Springer International Publishing, 2023, pp. 1–11. doi: 10.1007/978-3-030-72322-4_207-1.
[259] H. Wang, L. Chen, F. Ye, and L. Chen, “Global sensitivity analysis for fiber reinforced composite fiber path based on D-MORPH-HDMR algorithm,” *Structural and Multidisciplinary Optimization*, vol. 56, no. 3, pp. 697–712, 2017, doi: 10.1007/s00158-017-1681-9.
[260] M. Thapa, A. Paudel, S. B. Mulani, and R. W. Walters, “Uncertainty quantification and global sensitivity analysis for progressive failure of fiber-reinforced composites,” *Structural and Multidisciplinary Optimization*, vol. 63, no. 1, pp. 245–265, 2021, doi: 10.1007/s00158-020-02690-5.
[261] M. J. Bogdanor, S. Mahadevan, and C. Oskay, “Uncertainty quantification in damage modeling of heterogeneous materials,” *Int J Multiscale Comput Eng*, vol. 11, no. 3, pp. 289–307, 2013, doi: 10.1615/IntJMultCompEng.2013005821.
[262] R. M. Heiberger and E. Neuwirth, “Polynomial Regression,” in *R Through Excel*, New York, NY: Springer New York, 2009, pp. 269–284. doi: 10.1007/978-1-4419-0052-4_11.

[263] L. R. Shanock, B. E. Baran, W. A. Gentry, S. C. Pattison, and E. D. Heggestad, “Erratum to: Polynomial Regression with Response Surface Analysis: A Powerful Approach for Examining Moderation and Overcoming Limitations of Difference Scores,” *J Bus Psychol*, vol. 29, no. 1, pp. 161–161, Mar. 2014, doi: 10.1007/s10869-013-9317-6.
[264] H. Wang, L. Chen, F. Ye, and L. Chen, “Global sensitivity analysis for fiber reinforced composite fiber path based on D-MORPH-HDMR algorithm,” *Structural and Multidisciplinary Optimization*, vol. 56, no. 3, pp. 697–712, 2017, doi: 10.1007/s00158-017-1681-9.
[265] M. Thapa, A. Paudel, S. B. Mulani, and R. W. Walters, “Uncertainty quantification and global sensitivity analysis for progressive failure of fiber-reinforced composites,” *Structural and Multidisciplinary Optimization*, vol. 63, no. 1, pp. 245–265, 2021, doi: 10.1007/s00158-020-02690-5.
[266] G. T. Knofczynski and D. Mundfrom, “Sample Sizes When Using Multiple Linear Regression for Prediction,” *Educ Psychol Meas*, vol. 68, no. 3, pp. 431–442, Jun. 2008, doi: 10.1177/0013164407310131.
[267] K. A. Marill, “*Advanced Statistics:* Linear Regression, Part II: Multiple Linear Regression,” *Academic Emergency Medicine*, vol. 11, no. 1, pp. 94–102, Jan. 2004, doi: 10.1197/j.aem.2003.09.006.
[268] Ya Su, Xinbo Gao, Xuelong Li, and Dacheng Tao, “Multivariate Multilinear Regression,” *IEEE Transactions on Systems, Man, and Cybernetics, Part B (Cybernetics)*, vol. 42, no. 6, pp. 1560–1573, Dec. 2012, doi: 10.1109/TSMCB.2012.2195171.
[269] G. Lin, D. W. Engel, and P. W. Eslinger, “Survey and Evaluate Uncertainty Quantification Methodologies,” Richland, WA (United States), Feb. 2012. doi: 10.2172/1035732.
[270] “Fibreglast.” Accessed: Nov. 01, 2023. [Online]. Available: https://www.fibreglast.com/
[271] R. Lima and R. Sampaio, “What is uncertainty quantification?,” *Journal of the Brazilian Society of Mechanical Sciences and Engineering*, vol. 40, no. 3, p. 155, Mar. 2018, doi: 10.1007/s40430-018-1079-7.
[272] X. Hu, G. Fang, J. Yang, L. Zhao, and Y. Ge, “Simplified models for uncertainty quantification of extreme events using Monte Carlo technique,” *Reliab Eng Syst Saf*, vol. 230, p. 108935, Feb. 2023, doi: 10.1016/j.ress.2022.108935.
[273] R. R. P. Kuppusamy, A. Zade, and K. Kumar, “Time-temperature-cure process window of epoxy-vinyl ester resin for applications in liquid composite moulding processes,” *Mater Today Proc*, vol. 39, pp. 1407–1411, 2021, doi: 10.1016/j.matpr.2020.05.048.
[274] C. Czaderski, E. Martinelli, J. Michels, and M. Motavalli, “Effect of curing conditions on strength development in an epoxy resin for structural strengthening,” *Compos B Eng*, vol. 43, no. 2, pp. 398–410, Mar. 2012, doi: 10.1016/j.compositesb.2011.07.006.
[275] A. L. Nazareth da Silva, S. C. S. Teixeira, A. C. C. Widal, and F. M. B. Coutinho, “Mechanical properties of polymer composites based on commercial epoxy vinyl ester resin and glass fiber,” *Polym Test*, vol. 20, no. 8, pp. 895–899, 2001, doi: 10.1016/S0142-9418(01)00018-6.
[276] I. A. Moujdin, H. S. Totah, H. A. Abulkhair, A. O. Alsaiari, A. A. Shaiban, and H. A. Organji, “Development of Low Shrinkage Curing Techniques for Unsaturated Polyester and Vinyl Ester Reinforced Composites,” *Materials*, vol. 15, no. 9, p. 2972, Apr. 2022, doi: 10.3390/ma15092972.

[277] E. J. Molenaar, “Arctic marine shipping: overview of the international legal framework, gaps, and options,” *J Transnatl Law Policy*, vol. 18, no. 2, 2009.
[278] D. Chen, Q. Luo, M. Meng, Q. Li, and G. Sun, “Low velocity impact behavior of interlayer hybrid composite laminates with carbon/glass/basalt fibres,” *Compos B Eng*, vol. 176, p. 107191, Nov. 2019, doi: 10.1016/j.compositesb.2019.107191.
[279] K. Liu, J. L. Liu, and Z. Wang, “A damage threshold prediction model of CFRP panel by hail impact based on delamination mechanism,” *Eng Fract Mech*, vol. 239, p. 107282, Nov. 2020, doi: 10.1016/j.engfracmech.2020.107282.
[280] J. Körbelin, M. Derra, and B. Fiedler, “Influence of temperature and impact energy on low velocity impact damage severity in CFRP,” *Compos Part A Appl Sci Manuf*, vol. 115, pp. 76–87, Dec. 2018, doi: 10.1016/j.compositesa.2018.09.010.
[281] D. Zhang, Y. Sun, L. Chen, and N. Pan, “A comparative study on low-velocity impact response of fabric composite laminates,” *Mater Des*, vol. 50, pp. 750–756, Sep. 2013, doi: 10.1016/j.matdes.2013.03.044.
[282] M. Kara, M. Kırıcı, A. C. Tatar, and A. Avcı, “Impact behavior of carbon fiber/epoxy composite tubes reinforced with multi-walled carbon nanotubes at cryogenic environment,” *Compos B Eng*, vol. 145, pp. 145–154, Jul. 2018, doi: 10.1016/j.compositesb.2018.03.027.
[283] Y. Hu *et al.*, “Comparison of impact resistance of carbon fibre composites with multiple ultra-thin CNT, aramid pulp, PBO and graphene interlayers,” *Compos Part A Appl Sci Manuf*, vol. 155, p. 106815, Apr. 2022, doi: 10.1016/j.compositesa.2022.106815.
[284] J. Körbelin, C. Dreiner, and B. Fiedler, “Impact of temperature on LVI-damage and tensile and compressive residual strength of CFRP,” *Composites Part C: Open Access*, vol. 3, p. 100074, Nov. 2020, doi: 10.1016/j.jcomc.2020.100074.
[285] W. J. Cantwell and J. Morton, “The impact resistance of composite materials — a review,” *Composites*, vol. 22, no. 5, pp. 347–362, Sep. 1991, doi: 10.1016/0010-4361(91)90549-V.
[286] S. I. B. Syed Abdullah, “Low Velocity Impact Testing on Laminated Composites,” 2021, pp. 1–17. doi: 10.1007/978-981-16-1323-4_1.
[287] Y. Li, W. Zhang, Z. Yang, J. Zhang, and S. Tao, “Low-velocity impact damage characterization of carbon fiber reinforced polymer (CFRP) using infrared thermography,” *Infrared Phys Technol*, vol. 76, pp. 91–102, May 2016, doi: 10.1016/j.infrared.2016.01.019.
[288] Y. Tie, Y. Hou, C. Li, X. Zhou, T. Sapanathan, and M. Rachik, “An insight into the low-velocity impact behavior of patch-repaired CFRP laminates using numerical and experimental approaches,” *Compos Struct*, vol. 190, pp. 179–188, Apr. 2018, doi: 10.1016/j.compstruct.2018.01.075.
[289] Y. Hou, Y. Tie, C. Li, T. Sapanathan, and M. Rachik, “Low-velocity impact behaviors of repaired CFRP laminates: Effect of impact location and external patch configurations,” *Compos B Eng*, vol. 163, pp. 669–680, Apr. 2019, doi: 10.1016/j.compositesb.2018.12.153.
[290] Z. Xu, F. Yang, Z. W. Guan, and W. J. Cantwell, “An experimental and numerical study on scaling effects in the low velocity impact response of CFRP laminates,” *Compos Struct*, vol. 154, pp. 69–78, Oct. 2016, doi: 10.1016/j.compstruct.2016.07.029.

[291] F. Ahmad, J.-W. Hong, H. S. Choi, and M. K. Park, “Hygro effects on the low-velocity impact behavior of unidirectional CFRP composite plates for aircraft applications,” *Compos Struct*, vol. 135, pp. 276–285, Jan. 2016, doi: 10.1016/j.compstruct.2015.09.040.
[292] V. Prentzias and G. J. Tsamasphyros, “Simulation of Low Velocity Impact on CFRP Aerospace Structures: Simplified Approaches, Numerical and Experimental Results,” *Applied Composite Materials*, vol. 26, no. 3, pp. 835–856, Jun. 2019, doi: 10.1007/s10443-018-9752-7.
[293] M. E. Kazemi *et al.*, “Developing thermoplastic hybrid titanium composite laminates (HTCLS) at room temperature: Low-velocity impact analyses,” *Compos Part A Appl Sci Manuf*, vol. 149, p. 106552, Oct. 2021, doi: 10.1016/j.compositesa.2021.106552.
[294] S. Fakhreddini-Najafabadi, M. Torabi, and F. Taheri-Behrooz, “An experimental investigation on the low-velocity impact performance of the CFRP filled with nanoclay,” *Aerosp Sci Technol*, vol. 116, p. 106858, Sep. 2021, doi: 10.1016/j.ast.2021.106858.
[295] J. Körbelin, M. Derra, and B. Fiedler, “Influence of temperature and impact energy on low velocity impact damage severity in CFRP,” *Compos Part A Appl Sci Manuf*, vol. 115, pp. 76–87, Dec. 2018, doi: 10.1016/j.compositesa.2018.09.010.
[296] Q. Zhao, W. Wang, Y. Liu, Y. Hou, J. Li, and C. Li, “Multiscale modeling framework to predict the low-velocity impact and compression after impact behaviors of plain woven CFRP composites,” *Compos Struct*, vol. 299, p. 116090, Nov. 2022, doi: 10.1016/j.compstruct.2022.116090.
[297] Z. Xin, W. Xu, D. Liu, and J. Duan, “Research on Energy Absorption Characteristics of Bouligand Biomimetic Structure Based on CFRP Composite Materials,” *Sustainability*, vol. 15, no. 13, p. 9911, Jun. 2023, doi: 10.3390/su15139911.
[298] T. Berton, F. Najafi, and C. V. Singh, “Development and implementation of a multi-scale model for matrix micro-cracking prediction in composite structures subjected to low velocity impact,” *Compos B Eng*, vol. 168, pp. 140–151, Jul. 2019, doi: 10.1016/j.compositesb.2018.12.033.
[299] G. Wang *et al.*, “Real-time detection of barely visible defects on composite structures based on surface reconstruction,” *Compos Struct*, vol. 311, p. 116852, May 2023, doi: 10.1016/j.compstruct.2023.116852.
[300] S. A. Grammatikos, E. Z. Kordatos, T. E. Matikas, and A. S. Paipetis, “Low-velocity impact damage identification using a novel current injection thermographic technique,” T. E. Matikas, Ed., Apr. 2012, p. 83461A. doi: 10.1117/12.915494.
[301] H. Cai *et al.*, “Low-velocity impact response and post-impact assessment of self-healing composites with different stacking configurations of core–shell nanofibers,” *Polym Compos*, Nov. 2023, doi: 10.1002/pc.27925.
[302] K. Kaware, M. Kotambkar, A. Sontakkey, and N. Talekar, “Finite element analysis of CFRP composite under low velocity impact to improve the impact strength,” *International Journal of Crashworthiness*, vol. 28, no. 6, pp. 717–731, Nov. 2023, doi: 10.1080/13588265.2022.2123178.
[303] C. Hu, G. Huang, and C. Li, “Experimental and Numerical Study of Low-Velocity Impact and Tensile after Impact for CFRP Laminates Single-Lap Joints Adhesively Bonded Structure,” *Materials*, vol. 14, no. 4, p. 1016, Feb. 2021, doi: 10.3390/ma14041016.
[304] Y. S. Tarih, T. Coskun, A. Yar, Ö. Gundogdu, and Ö. S. Sahin, “The influences of low-velocity impact loading on the vibration responses of the carbon/glass fiber-reinforced

epoxy composites interleaved with various non-woven thermoplastic veils," *J Appl Polym Sci*, vol. 140, no. 15, Apr. 2023, doi: 10.1002/app.53728.
[305] V. Kostopoulos, A. Kotrotsos, A. Geitona, and S. Tsantzalis, "Low velocity impact response and post impact assessment of carbon fiber/epoxy composites modified with Diels-Alder based healing agent. A novel approach," *Compos Part A Appl Sci Manuf*, vol. 140, p. 106151, Jan. 2021, doi: 10.1016/j.compositesa.2020.106151.
[306] F. Schimmer, S. Ladewig, N. Motsch, J. M. Hausmann, and I. Ehrlich, "Comparison of Low-Velocity Impact Damage Behavior of Unidirectional Carbon Fiber-Reinforced Thermoset and Thermoplastic Composites," *Key Eng Mater*, vol. 809, pp. 9–14, Jun. 2019, doi: 10.4028/www.scientific.net/KEM.809.9.
[307] M. E. Kazemi *et al.*, "Investigating the roles of fiber, resin, and stacking sequence on the low-velocity impact response of novel hybrid thermoplastic composites," *Compos B Eng*, vol. 207, p. 108554, Feb. 2021, doi: 10.1016/j.compositesb.2020.108554.
[308] Z. Lei, C. Cheng, B. Yin, L. Tong, and Y. Wan, "Low-velocity impact responses and failure mechanisms of CFRP after fire exposure," *Composites Communications*, vol. 34, p. 101277, Oct. 2022, doi: 10.1016/j.coco.2022.101277.
[309] A. G. Castellanos, K. Cinar, I. Guven, and P. Prabhakar, "Low-Velocity Impact Response of Woven Carbon Composites in Arctic Conditions," *Journal of Dynamic Behavior of Materials*, vol. 4, no. 3, pp. 308–316, Sep. 2018, doi: 10.1007/s40870-018-0160-8.
[310] A. G. Castellanos and P. Prabhakar, "Durability and failure mechanics of woven carbon composites under repeated impact loading in Arctic conditions," *Multiscale and Multidisciplinary Modeling, Experiments and Design*, vol. 1, no. 3, pp. 157–170, Sep. 2018, doi: 10.1007/s41939-018-0024-x.
[311] P. Prabhakar, "Failure Mechanics of Low Velocity Dynamic Impact on Woven Polymeric Composites in Arctic Conditions," in *Advances in Thick Section Composite and Sandwich Structures*, Cham: Springer International Publishing, 2020, pp. 579–604. doi: 10.1007/978-3-030-31065-3_20.
[312] V. Giammaria *et al.*, "Low-velocity impact behaviour of biocomposite laminates reinforced by flax, basalt and hybrid fibres at various temperatures: Analytical, numerical and experimental results," *Compos Struct*, vol. 322, p. 117332, Oct. 2023, doi: 10.1016/j.compstruct.2023.117332.
[313] J. Körbelin, M. Derra, and B. Fiedler, "Influence of temperature and impact energy on low velocity impact damage severity in CFRP," *Compos Part A Appl Sci Manuf*, vol. 115, pp. 76–87, Dec. 2018, doi: 10.1016/j.compositesa.2018.09.010.
[314] S. Liu, P. Rawat, Z. Chen, and D. Zhu, "Low-velocity impact behavior of carbon woven laminates after exposure to varying temperatures," *Thin-Walled Structures*, vol. 179, p. 109636, Oct. 2022, doi: 10.1016/j.tws.2022.109636.
[315] G. Caprino, I. Crivelli Visconti, and A. Di Ilio, "Composite materials response under low-velocity impact," *Compos Struct*, vol. 2, no. 3, pp. 261–271, Jan. 1984, doi: 10.1016/0263-8223(84)90018-7.
[316] M. O. W. Richardson and M. J. Wisheart, "Review of low-velocity impact properties of composite materials," *Compos Part A Appl Sci Manuf*, vol. 27, no. 12, pp. 1123–1131, 1996, doi: 10.1016/1359-835X(96)00074-7.
[317] T.-W. Shyr and Y.-H. Pan, "Impact resistance and damage characteristics of composite laminates," *Compos Struct*, vol. 62, no. 2, pp. 193–203, Nov. 2003, doi: 10.1016/S0263-8223(03)00114-4.

[318] Y. Tie, Q. Zhang, Y. Hou, and C. Li, “Impact damage assessment in orthotropic CFRP laminates using nonlinear Lamb wave: Experimental and numerical investigations,” *Compos Struct*, vol. 236, p. 111869, Mar. 2020, doi: 10.1016/j.compstruct.2020.111869.
[319] F. Caputo, D. F. Gennaro, G. Lamanna, A. Lefons, and A. Riccio, “Numerical Procedures for Damage Mechanisms Analysis in CFRP Composites,” *Key Eng Mater*, vol. 569–570, pp. 111–118, Jul. 2013, doi: 10.4028/www.scientific.net/KEM.569-570.111.
[320] E. Abisset, F. Daghia, X. C. Sun, M. R. Wisnom, and S. R. Hallett, “Interaction of inter- and intralaminar damage in scaled quasi-static indentation tests: Part 1 – Experiments,” *Compos Struct*, vol. 136, pp. 712–726, Feb. 2016, doi: 10.1016/j.compstruct.2015.09.061.
[321] E. Fuoss, P. V. Straznicky, and C. Poon, “Effects of stacking sequence on the impact resistance in composite laminates — Part 1: parametric study,” *Compos Struct*, vol. 41, no. 1, pp. 67–77, Jan. 1998, doi: 10.1016/S0263-8223(98)00036-1.
[322] P. Kumar and B. Rai, “Delaminations of barely visible impact damage in CFRP laminates,” *Compos Struct*, vol. 23, no. 4, pp. 313–318, Jan. 1993, doi: 10.1016/0263-8223(93)90231-E.
[323] T. Gómez-del Río, R. Zaera, E. Barbero, and C. Navarro, “Damage in CFRPs due to low velocity impact at low temperature,” *Compos B Eng*, vol. 36, no. 1, pp. 41–50, Jan. 2005, doi: 10.1016/j.compositesb.2004.04.003.
[324] I. Papa, A. Langella, and V. Lopresto, “CFRP laminates under low-velocity impact conditions: Influence of matrix and temperature,” *Polym Eng Sci*, vol. 59, no. 12, pp. 2429–2437, Dec. 2019, doi: 10.1002/pen.25102.
[325] Z. Sápi and R. Butler, “Properties of cryogenic and low temperature composite materials – A review,” *Cryogenics (Guildf)*, vol. 111, p. 103190, Oct. 2020, doi: 10.1016/j.cryogenics.2020.103190.
[326] L. Francesconi and F. Aymerich, “Effect of Z-pinning on the impact resistance of composite laminates with different layups,” *Compos Part A Appl Sci Manuf*, vol. 114, pp. 136–148, Nov. 2018, doi: 10.1016/j.compositesa.2018.08.013.
[327] B. Liao *et al.*, “Effect of Z-pin inclined angle on the impact damage suppression effectiveness for cross-ply composite laminates,” *Compos Part A Appl Sci Manuf*, vol. 142, p. 106264, Mar. 2021, doi: 10.1016/j.compositesa.2020.106264.
[328] G. Kaya and E. Selver, “Impact resistance of Z-pin-reinforced sandwich composites,” *J Compos Mater*, vol. 53, no. 26–27, pp. 3681–3699, Nov. 2019, doi: 10.1177/0021998319845428.
[329] Vaidya UK, Duncan B, and Kopacz., “Affordable processing and characterization of multi-functional z-pin reinforced VARTM composites.,” *Proceedings of the 13th international conference on composite materials*, 2001.
[330] A. Knopp, E. Funck, A. Holtz, and G. Scharr, “Delamination and compression-after-impact properties of z-pinned composite laminates reinforced with circumferentially notched z-pins,” *Compos Struct*, vol. 285, no. December 2021, 2022, doi: 10.1016/j.compstruct.2022.115188.
[331] V. Kostopoulos, N. Sarantinos, and S. Tsantzalis, “Review of Through-the-Thickness Reinforced z-Pinned Composites,” 2020.
[332] S. Wang, M. Li, Z. Che, S. Wang, Y. Gu, and W. Zhang, “Balance interlaminar improvement and in-plane adverse impact of hexagonal semi-embedded fine Z-pin reinforced polymer composite,” *Journal of Materials Research and Technology*, vol. 22, no. 37, pp. 1297–1306, 2023, doi: 10.1016/j.jmrt.2022.12.009.

[333] X. Teng *et al.*, “Experimental study on the low-velocity impact and post-impact flexural properties of curved CFRP laminates reinforced by pre-hole Z-pinning (PHZ) technique,” *Mechanics of Advanced Materials and Structures*, vol. 30, no. 17, pp. 3479–3490, 2023, doi: 10.1080/15376494.2022.2077485.
[334] Y. He *et al.*, “A multi-layer resin film infusion process to control CNTs distribution and alignment for improving CFRP interlaminar fracture toughness,” *Compos Struct*, vol. 260, p. 113510, Mar. 2021, doi: 10.1016/j.compstruct.2020.113510.
[335] Y. Ou, C. González, and J. J. Vilatela, “Understanding interlaminar toughening of unidirectional CFRP laminates with carbon nanotube veils,” *Compos B Eng*, vol. 201, p. 108372, Nov. 2020, doi: 10.1016/j.compositesb.2020.108372.
[336] X. Ni *et al.*, “Static and fatigue interlaminar shear reinforcement in aligned carbon nanotube-reinforced hierarchical advanced composites,” *Compos Part A Appl Sci Manuf*, vol. 120, no. February, pp. 106–115, 2019, doi: 10.1016/j.compositesa.2019.02.023.
[337] J. Cheon and M. Kim, “Impact resistance and interlaminar shear strength enhancement of carbon fiber reinforced thermoplastic composites by introducing MWCNT-anchored carbon fiber,” *Compos B Eng*, vol. 217, 2021, doi: 10.1016/j.compositesb.2021.108872.
[338] W. Xin *et al.*, “Impact and post-impact properties of multiscale carbon fiber composites interleaved with carbon nanotube sheets,” *Compos B Eng*, vol. 183, no. November 2019, 2020, doi: 10.1016/j.compositesb.2019.107711.
[339] A. Nasirmanesh, A. K. Singh, D. Villaflor, and B. Blandford, “Effects of midplane carbon nanotube sheet interleave on the strength and impact damage resistance of carbon fiber reinforced polymer composites,” *Polym Compos*, vol. 43, no. 5, pp. 3085–3095, May 2022, doi: 10.1002/pc.26601.
[340] H. Conway and C. Gouldstone, “Vertically aligned carbon nanotubes as interlaminar reinforcement in carbon fiber composite laminates,” *AIAA Scitech 2019 Forum*, no. January, pp. 1–6, 2019, doi: 10.2514/6.2019-1764.
[341] A. T. Le, Q. Govignon, S. Rivallant, and T. Cutard, “Composite laminates reinforced by vertically aligned carbon nanotubes: Detailed manufacturing process, from nanotubes transfer to composite consolidation,” *J Compos Mater*, vol. 57, no. 27, pp. 4239–4253, 2023, doi: 10.1177/00219983231207441.
[342] J. Lee, L. H. Acauan, E. Kalfon-Cohen, S. S. Kessler, and B. L. Wardle, “Hierarchical Nano- and Micro-engineered Interlaminar Reinforcement of Advanced Aerospace Grade Composites with Carbon Nanotube Arrays,” in *AIAA Scitech 2021 Forum*, Reston, Virginia: American Institute of Aeronautics and Astronautics, Jan. 2021. doi: 10.2514/6.2021-0443.
[343] R. C. Worboys, “Suppressing Delamination Through Vertically Aligned Carbon Nanotubes (VACNT) Interleaves,” The University of Bristol, 2020.
[344] Z. Wu, L. Zhang, Z. Ying, J. Ke, and X. Hu, “Low-velocity impact performance of hybrid 3D carbon/glass woven orthogonal composite: Experiment and simulation,” *Compos B Eng*, vol. 196, p. 108098, Sep. 2020, doi: 10.1016/j.compositesb.2020.108098.
[345] W. Ao, W. Zhuang, B. Xing, Q. Zhou, and Y. Xia, “Finite element method of a progressive intralaminar and interlaminar damage model for woven fibre laminated composites under low velocity impact,” *Mater Des*, vol. 223, 2022, doi: 10.1016/j.matdes.2022.111256.

[346] M. Umair, M. Hussain, K. Shaker, and Y. Nawab, “Impact Performance of Three-dimensional Woven Composites with Novel Binding Yarn Patterns,” *Journal of Natural Fibers*, vol. 19, no. 16, pp. 14461–14476, 2022, doi: 10.1080/15440478.2022.2064399.
[347] Y. Liu, H. Xia, and Q. Q. Ni, “Experimental Investigation on Low-Velocity Impact Performance of 3D Woven Textile Composites,” *Applied Composite Materials*, vol. 29, no. 1, pp. 121–146, 2022, doi: 10.1007/s10443-021-10005-0.
[348] C.-H. Kim, H.-W. Sim, W.-J. An, J.-H. Kweon, and J.-H. Choi, “Impact characteristics of composite panel stitched by I-fiber process,” *Compos Part A Appl Sci Manuf*, vol. 127, p. 105644, Dec. 2019, doi: 10.1016/j.compositesa.2019.105644.
[349] D. A. Drake, R. W. Sullivan, A. E. Lovejoy, S. B. Clay, and D. C. Jegley, “Influence of stitching on the out-of-plane behavior of composite materials – A mechanistic review,” *J Compos Mater*, vol. 55, no. 23, pp. 3307–3321, 2021, doi: 10.1177/00219983211009290.
[350] J. Lai, Z. Peng, Z. Huang, M. Li, M. Mo, and B. Liu, “Effect of Stitching, Stitch Density, Stacking Sequences on Low-Velocity Edge Impact and Compression after Edge Impact (CAEI) Behavior of Stitched CFRP Laminates,” *Materials*, vol. 15, no. 24, 2022, doi: 10.3390/ma15248822.
[351] C. Cigliano, F. Donadio, V. Lopresto, I. Papa, V. Pagliarulo, and P. Russo, “Stitching Effect on Impact Behaviour of Composite Materials,” 2023, pp. 649–657. doi: 10.1007/978-3-031-07258-1_65.
[352] L. G. Blok, J. Kratz, D. Lukaszewicz, S. Hesse, C. Ward, and C. Kassapoglou, “Improvement of the in-plane crushing response of CFRP sandwich panels by through-thickness reinforcements,” *Compos Struct*, vol. 161, pp. 15–22, Feb. 2017, doi: 10.1016/j.compstruct.2016.11.034.
[353] K. K. Verma, G. Padmakara, K. M. Gaddikeri, S. Ramesh, S. Kumar, and S. Bose, “The key role of thread and needle selection towards ‘through-thickness reinforcement’ in tufted carbon fiber-epoxy laminates,” *Compos B Eng*, vol. 174, p. 106970, Oct. 2019, doi: 10.1016/j.compositesb.2019.106970.
[354] D. B. Bortoluzzi, G. F. Gomes, D. Hirayama, and A. C. Ancelotti, “Development of a 3D reinforcement by tufting in carbon fiber/epoxy composites,” *International Journal of Advanced Manufacturing Technology*, vol. 100, no. 5–8, pp. 1593–1605, 2019, doi: 10.1007/s00170-018-2764-5.
[355] C. Hui, C. Chen, X. Legrand, and P. Wang, “Investigation of the Interlaminar Shear Performance of Tufted Preforms and Composites under Mode II Loading Condition,” *Polymers (Basel)*, vol. 14, no. 4, pp. 1–13, 2022, doi: 10.3390/polym14040690.
[356] K. K. Verma, C. H. Viswarupachari, K. M. Gaddikeri, S. Ramesh, S. Kumar, and S. Bose, “Unfolding the effects of tuft density on compression after impact properties in unidirectional carbon/epoxy composite laminates,” *Compos Struct*, vol. 258, no. November 2020, 2021, doi: 10.1016/j.compstruct.2020.113378.
[357] L. Walker, M.-S. Sohn, and X.-Z. Hu, “Improving impact resistance of carbon-fibre composites through interlaminar reinforcement,” *Compos Part A Appl Sci Manuf*, vol. 33, no. 6, pp. 893–902, Jun. 2002, doi: 10.1016/S1359-835X(02)00010-6.
[358] C. Zhang, X. Zheng, K. Zhu, J. Peng, Z. Wang, and L. Lan, “Experimental investigation of low-velocity impact behavior and CAI on composite laminates by discrete interleaved toughening,” *Mechanics of Advanced Materials and Structures*, vol. 0, no. 0, pp. 1–12, 2022, doi: 10.1080/15376494.2022.2158504.

[359] A. Ramji, Y. Xu, M. Yasaee, M. Grasso, and P. Webb, “Influence of veil interleave distribution on the delamination resistance of cross-ply CFRP laminates under low velocity impact,” *Int J Impact Eng*, vol. 157, no. April, 2021, doi: 10.1016/j.ijimpeng.2021.103997.
[360] Y. C. Shin and S. M. Kim, “Enhancement of the interlaminar fracture toughness of a Carbon-Fiber-Reinforced polymer using interleaved carbon nanotube Buckypaper,” *Applied Sciences (Switzerland)*, vol. 11, no. 15, 2021, doi: 10.3390/app11156821.
[361] N. T. Kamar, M. M. Hossain, A. Khomenko, M. Haq, L. T. Drzal, and A. Loos, “Interlaminar reinforcement of glass fiber/epoxy composites with graphene nanoplatelets,” *Compos Part A Appl Sci Manuf*, vol. 70, pp. 82–92, Mar. 2015, doi: 10.1016/j.compositesa.2014.12.010.
[362] A. Elmarakbi *et al.*, “Effect of graphene nanoplatelets on the impact response of a carbon fibre reinforced composite,” *Mater Today Commun*, vol. 25, no. January, 2020, doi: 10.1016/j.mtcomm.2020.101530.
[363] K. Zafeiropoulou, C. Kostagiannakopoulou, G. Sotiriadis, and V. Kostopoulos, “A preliminary study of the influence of graphene nanoplatelet specific surface area on the interlaminar fracture properties of carbon fiber/epoxy composites,” *Polymers (Basel)*, vol. 12, no. 12, pp. 1–15, 2020, doi: 10.3390/polym12123060.
[364] W. Jarrett and F. Korkees, “Environmental impact investigation on the interlaminar properties of carbon fibre composites modified with graphene nanoparticles,” *Polymer (Guildf)*, vol. 252, no. January, 2022, doi: 10.1016/j.polymer.2022.124921.
[365] A. Namdev, A. Telang, and R. Purohit, “Effect of Graphene Nano Platelets on Mechanical and Physical Properties of Carbon Fibre/Epoxy Hybrid Composites,” *Advances in Materials and Processing Technologies*, vol. 8, no. sup3, pp. 1168–1181, 2022, doi: 10.1080/2374068X.2021.1939557.
[366] A. Castellanos, M. S. Islam, E. Tarango, Y. Lin, and P. Prabhakar, “Interlaminar reinforcement for enhancing low-velocity impact response of woven composites,” *Textile Research Journal*, vol. 88, no. 15, pp. 1710–1720, Aug. 2018, doi: 10.1177/0040517517708536.
[367] C. Yang, R. Han, M. Nie, and Q. Wang, “Interfacial reinforcement mechanism in poly(lactic acid)/natural fiber biocomposites featuring ZnO nanowires at the interface,” *Mater Des*, vol. 186, pp. 0–7, 2020, doi: 10.1016/j.matdes.2019.108332.
[368] X. Meng, J. Li, H. Cui, C. Zhang, Z. Tang, and Y. Li, “Dynamic shear failure behavior of the interfaces in carbon fiber/ZnO nanowire/epoxy resin hierarchical composites,” *Compos Sci Technol*, vol. 221, no. December 2021, pp. 1–10, 2022, doi: 10.1016/j.compscitech.2022.109284.
[369] J. Zhang and C. Teng, “Nondestructive growing nano-ZnO on aramid fibers to improve UV resistance and enhance interfacial strength in composites,” *Mater Des*, vol. 192, 2020, doi: 10.1016/j.matdes.2020.108774.
[370] A. P. Mouritz, “Design dilemma for Z-pinned composite structures,” *27th Congress of the International Council of the Aeronautical Sciences 2010, ICAS 2010*, vol. 3, pp. 1895–1905, 2010.
[371] Z. CHENG and J. XIONG, “Progressive damage behaviors of woven composite laminates subjected to LVI, TAI and CAI,” *Chinese Journal of Aeronautics*, vol. 33, no. 10, pp. 2807–2823, Oct. 2020, doi: 10.1016/j.cja.2019.12.015.

[372] Y. Hu, F. Cheng, Y. Ji, B. Yuan, and X. Hu, “Effect of aramid pulp on low temperature flexural properties of carbon fibre reinforced plastics,” *Compos Sci Technol*, vol. 192, p. 108095, May 2020, doi: 10.1016/j.compscitech.2020.108095.
[373] M. Ye, B. Yuan, Y. Hu, and X. Hu, “Compression-after-impact properties of carbon fiber composites with interlays of Aramid pulp micro-/ nanofibers,” *Polym Compos*, vol. 42, no. 9, pp. 4424–4433, Sep. 2021, doi: 10.1002/pc.26159.
[374] G. YANG *et al.*, “Constructing quasi-vertical fiber bridging behaviors of aramid pulp at interlayer of laminated basalt fiber reinforced polymer composites to improve flexural performances,” *Chinese Journal of Aeronautics*, 2023, doi: 10.1016/j.cja.2023.10.013.
[375] N. Alif, L. A. Carlsson, and L. Boogh, “The effect of weave pattern and crack propagation direction on mode I delamination resistance of woven glass and carbon composites,” *Compos B Eng*, vol. 29, no. 5, pp. 603–611, Sep. 1998, doi: 10.1016/S1359-8368(98)00014-6.
[376] A. I. D7136/D7136M - 20, “D7136: Standard test method for measuring the damage resistance of a fiber-reinforced polymer matrix composite to a drop-weight impact event,” *Annual Book of ASTM Standards*, vol. i, no. C, pp. 1–16, 2012, doi: 10.1520/D7136.
[377] S. Z. H. Shah *et al.*, “Performance comparison of resin-infused thermoplastic and thermoset 3D fabric composites under impact loading,” *Int J Mech Sci*, vol. 189, p. 105984, Jan. 2021, doi: 10.1016/j.ijmecsci.2020.105984.
[378] S. P. Subadra, P. Griskevicius, and S. Yousef, “Low velocity impact and pseudo-ductile behaviour of carbon/glass/epoxy and carbon/glass/PMMA hybrid composite laminates for aircraft application at service temperature,” *Polym Test*, vol. 89, p. 106711, Sep. 2020, doi: 10.1016/j.polymertesting.2020.106711.
[379] M.-G. Kim, S.-G. Kang, C.-G. Kim, and C.-W. Kong, “Tensile response of graphite/epoxy composites at low temperatures,” *Compos Struct*, vol. 79, no. 1, pp. 84–89, Jun. 2007, doi: 10.1016/j.compstruct.2005.11.031.
[380] I. M. Ward and J. Sweeney, *Mechanical Properties of Solid Polymers*. Wiley, 2012. doi: 10.1002/9781119967125.
[381] Q. Feng, J. Yang, Y. Liu, H. Xiao, and S. Fu, “Simultaneously Enhanced Cryogenic Tensile Strength, Ductility and Impact Resistance of Epoxy Resins by Polyethylene Glycol,” *J Mater Sci Technol*, vol. 30, no. 1, pp. 90–96, Jan. 2014, doi: 10.1016/j.jmst.2013.08.016.
[382] Y. He *et al.*, “Reinforced carbon fiber laminates with oriented carbon nanotube epoxy nanocomposites: Magnetic field assisted alignment and cryogenic temperature mechanical properties,” *J Colloid Interface Sci*, vol. 517, pp. 40–51, May 2018, doi: 10.1016/j.jcis.2018.01.087.
[383] J. Zhang, T. Lin, and X. Wang, “Electrospun nanofibre toughened carbon/epoxy composites: Effects of polyetherketone cardo (PEK-C) nanofibre diameter and interlayer thickness,” *Compos Sci Technol*, vol. 70, no. 11, pp. 1660–1666, Oct. 2010, doi: 10.1016/j.compscitech.2010.06.019.
[384] S. M. García-Rodríguez, J. Costa, K. E. Rankin, R. P. Boardman, V. Singery, and J. A. Mayugo, “Interleaving light veils to minimise the trade-off between mode-I interlaminar fracture toughness and in-plane properties,” *Compos Part A Appl Sci Manuf*, vol. 128, p. 105659, Jan. 2020, doi: 10.1016/j.compositesa.2019.105659.

[385] N. Sela and O. Ishai, “Interlaminar fracture toughness and toughening of laminated composite materials: a review,” *Composites*, vol. 20, no. 5, pp. 423–435, Sep. 1989, doi: 10.1016/0010-4361(89)90211-5.
[386] K. M. Liew, Z. X. Lei, and L. W. Zhang, “Mechanical analysis of functionally graded carbon nanotube reinforced composites: A review,” *Compos Struct*, vol. 120, pp. 90–97, Feb. 2015, doi: 10.1016/j.compstruct.2014.09.041.
[387] A. Kafi *et al.*, “Effect of surface functionality of PAN-based carbon fibres on the mechanical performance of carbon/epoxy composites,” *Compos Sci Technol*, vol. 94, pp. 89–95, Apr. 2014, doi: 10.1016/j.compscitech.2014.01.011.
[388] Y. Gu, M. Li, Z. Zhang, and Z. Sun, “Numerical Simulation and Experimental Study on Consolidation of Toughened Epoxy Resin Composite Laminates,” *J Compos Mater*, vol. 40, no. 24, pp. 2257–2277, Dec. 2006, doi: 10.1177/0021998306062319.
[389] M. A. Muflikhun, T. Yokozeki, and T. Aoki, “The strain performance of thin CFRP-SPCC hybrid laminates for automobile structures,” *Compos Struct*, vol. 220, pp. 11–18, Jul. 2019, doi: 10.1016/j.compstruct.2019.03.094.
[390] S. S. Wicks, W. Wang, M. R. Williams, and B. L. Wardle, “Multi-scale interlaminar fracture mechanisms in woven composite laminates reinforced with aligned carbon nanotubes,” *Compos Sci Technol*, vol. 100, pp. 128–135, Aug. 2014, doi: 10.1016/j.compscitech.2014.06.003.
[391] G. Xie, G. Zhou, and X. Bao, “Mechanical behaviour of advanced composite laminates embedded with carbon nanotubes: review,” J. Leng, A. K. Asundi, and W. Ecke, Eds., Jul. 2009, p. 74932E. doi: 10.1117/12.836060.
[392] A. P. Mouritz and B. N. Cox, “A mechanistic interpretation of the comparative in-plane mechanical properties of 3D woven, stitched and pinned composites,” *Compos Part A Appl Sci Manuf*, vol. 41, no. 6, pp. 709–728, Jun. 2010, doi: 10.1016/j.compositesa.2010.02.001.
[393] L. Lee, S. Rudov-Clark, A. P. Mouritz, M. K. Bannister, and I. Herszberg, “Effect of weaving damage on the tensile properties of three-dimensional woven composites,” *Compos Struct*, vol. 57, no. 1–4, pp. 405–413, Jul. 2002, doi: 10.1016/S0263-8223(02)00108-3.
[394] S.-S. Yao, F.-L. Jin, K. Y. Rhee, D. Hui, and S.-J. Park, “Recent advances in carbon-fiber-reinforced thermoplastic composites: A review,” *Compos B Eng*, vol. 142, pp. 241–250, Jun. 2018, doi: 10.1016/j.compositesb.2017.12.007.
[395] R. Khan, “Fiber bridging in composite laminates: A literature review,” *Compos Struct*, vol. 229, p. 111418, Dec. 2019, doi: 10.1016/j.compstruct.2019.111418.
[396] J. Zhang, V. S. Chevali, H. Wang, and C.-H. Wang, “Current status of carbon fibre and carbon fibre composites recycling,” *Compos B Eng*, vol. 193, p. 108053, Jul. 2020, doi: 10.1016/j.compositesb.2020.108053.
[397] N. Forintos and T. Czigany, “Multifunctional application of carbon fiber reinforced polymer composites: Electrical properties of the reinforcing carbon fibers – A short review,” *Compos B Eng*, vol. 162, pp. 331–343, Apr. 2019, doi: 10.1016/j.compositesb.2018.10.098.
[398] D. Nguyen Dinh and P. Nguyen, “The Dynamic Response and Vibration of Functionally Graded Carbon Nanotube-Reinforced Composite (FG-CNTRC) Truncated Conical Shells Resting on Elastic Foundations,” *Materials*, vol. 10, no. 10, p. 1194, Oct. 2017, doi: 10.3390/ma10101194.

[399] N. Li *et al.*, "Electromagnetic Interference (EMI) Shielding of Single-Walled Carbon Nanotube Epoxy Composites," *Nano Lett*, vol. 6, no. 6, pp. 1141–1145, Jun. 2006, doi: 10.1021/nl0602589.
[400] S. Kumar, W. Ahlawat, R. Kumar, and N. Dilbaghi, "Graphene, carbon nanotubes, zinc oxide and gold as elite nanomaterials for fabrication of biosensors for healthcare," *Biosens Bioelectron*, vol. 70, pp. 498–503, Aug. 2015, doi: 10.1016/j.bios.2015.03.062.
[401] Y. Su, F. Zhou, X. Wei, D. Jing, X. Zhang, and S. Zhang, "Enhanced mechanical and electrical properties of carbon fiber/poly(ether ether ketone) laminates via inserting carbon nanotubes interleaves," *J Appl Polym Sci*, vol. 137, no. 19, May 2020, doi: 10.1002/app.48658.
[402] F. Xu, H.-Y. Liu, and X. Du, "An Analytical Model of Interlaminar Fracture of Polymer Composite Reinforced by Carbon Fibres Grafted with Carbon Nanotubes," *Polymers (Basel)*, vol. 10, no. 6, p. 683, Jun. 2018, doi: 10.3390/polym10060683.
[403] J. Guo, Q. Zhang, L. Gao, W. Zhong, G. Sui, and X. Yang, "Significantly improved electrical and interlaminar mechanical properties of carbon fiber laminated composites by using special carbon nanotube pre-dispersion mixture," *Compos Part A Appl Sci Manuf*, vol. 95, pp. 294–303, Apr. 2017, doi: 10.1016/j.compositesa.2017.01.021.
[404] F. S. Wang, Y. Y. Ji, X. S. Yu, H. Chen, and Z. F. Yue, "Ablation damage assessment of aircraft carbon fiber/epoxy composite and its protection structures suffered from lightning strike," *Compos Struct*, vol. 145, pp. 226–241, Jun. 2016, doi: 10.1016/j.compstruct.2016.03.005.
[405] T. L. Anderson, *Fracture mechanics: fundamentals and applications.* CRC, 2017.
[406] M. Thor, M. G. R. Sause, and R. M. Hinterhölzl, "Mechanisms of Origin and Classification of Out-of-Plane Fiber Waviness in Composite Materials—A Review," *Journal of Composites Science*, vol. 4, no. 3, p. 130, Sep. 2020, doi: 10.3390/jcs4030130.
[407] W. T. Y. Tze, D. J. Gardner, C. P. Tripp, and S. C. O'Neill, "Cellulose fiber/polymer adhesion: effects of fiber/matrix interfacial chemistry on the micromechanics of the interphase," *J Adhes Sci Technol*, vol. 20, no. 15, pp. 1649–1668, Jan. 2006, doi: 10.1163/156856106779024427.
[408] H. Sam Huang and A. M. Waas, "Quasi-static mode II fracture tests and simulations of Z-pinned woven composites," *Eng Fract Mech*, vol. 126, pp. 155–165, Aug. 2014, doi: 10.1016/j.engfracmech.2014.05.002.
[409] C. Song, W. Fan, T. Liu, S. Wang, W. Song, and X. Gao, "A review on three-dimensional stitched composites and their research perspectives," *Compos Part A Appl Sci Manuf*, vol. 153, p. 106730, Feb. 2022, doi: 10.1016/j.compositesa.2021.106730.
[410] A. P. Mouritz, "Review of z-pinned composite laminates," *Compos Part A Appl Sci Manuf*, vol. 38, no. 12, pp. 2383–2397, Dec. 2007, doi: 10.1016/j.compositesa.2007.08.016.
[411] G. Lubineau and A. Rahaman, "A review of strategies for improving the degradation properties of laminated continuous-fiber/epoxy composites with carbon-based nanoreinforcements," *Carbon N Y*, vol. 50, no. 7, pp. 2377–2395, Jun. 2012, doi: 10.1016/j.carbon.2012.01.059.
[412] X. Cui, J. Liu, H. Liu, and G. Wu, "Enhanced interfacial strength and mechanical properties of carbon fiber composites by introducing functionalized silica nanoparticles into the interface," *J Adhes Sci Technol*, vol. 33, no. 5, pp. 479–492, Mar. 2019, doi: 10.1080/01694243.2018.1543634.

[413] S. R. Karnati, P. Agbo, and L. Zhang, “Applications of silica nanoparticles in glass/carbon fiber-reinforced epoxy nanocomposite,” *Composites Communications*, vol. 17, pp. 32–41, Feb. 2020, doi: 10.1016/j.coco.2019.11.003.
[414] M. R. Khosravani and K. Weinberg, “Characterization of sandwich composite T-joints under different ageing conditions,” *Compos Struct*, vol. 197, pp. 80–88, Aug. 2018, doi: 10.1016/j.compstruct.2018.05.043.
[415] A. Klingler, A. Bajpai, and B. Wetzel, “The effect of block copolymer and core-shell rubber hybrid toughening on morphology and fracture of epoxy-based fibre reinforced composites,” *Eng Fract Mech*, vol. 203, pp. 81–101, Nov. 2018, doi: 10.1016/j.engfracmech.2018.06.044.
[416] X. Zhang *et al.*, “Interfacial Microstructure and Properties of Carbon Fiber Composites Modified with Graphene Oxide,” *ACS Appl Mater Interfaces*, vol. 4, no. 3, pp. 1543–1552, Mar. 2012, doi: 10.1021/am201757v.
[417] S. Aldajah and Y. Haik, “Transverse strength enhancement of carbon fiber reinforced polymer composites by means of magnetically aligned carbon nanotubes,” *Mater Des*, vol. 34, pp. 379–383, Feb. 2012, doi: 10.1016/j.matdes.2011.07.013.
[418] N. Xu *et al.*, “A hybrid 1D/2D coating strategy with MXene and CNT towards the interfacial reinforcement of carbon fiber/poly(ether ether ketone) composite,” *Compos B Eng*, vol. 246, p. 110278, Nov. 2022, doi: 10.1016/j.compositesb.2022.110278.
[419] S. Imani Yengejeh, S. A. Kazemi, and A. Öchsner, “Carbon nanotubes as reinforcement in composites: A review of the analytical, numerical and experimental approaches,” *Comput Mater Sci*, vol. 136, pp. 85–101, Aug. 2017, doi: 10.1016/j.commatsci.2017.04.023.
[420] L. Sun *et al.*, “Mechanical properties of surface-functionalized SWCNT/epoxy composites,” *Carbon N Y*, vol. 46, no. 2, pp. 320–328, Feb. 2008, doi: 10.1016/j.carbon.2007.11.051.
[421] T. H. Hsieh, A. J. Kinloch, A. C. Taylor, and S. Sprenger, “The effect of silica nanoparticles and carbon nanotubes on the toughness of a thermosetting epoxy polymer,” *J Appl Polym Sci*, vol. 119, no. 4, pp. 2135–2142, Feb. 2011, doi: 10.1002/app.32937.
[422] F. H. Gojny, M. H. G. Wichmann, U. Köpke, B. Fiedler, and K. Schulte, “Carbon nanotube-reinforced epoxy-composites: enhanced stiffness and fracture toughness at low nanotube content,” *Compos Sci Technol*, vol. 64, no. 15, pp. 2363–2371, Nov. 2004, doi: 10.1016/j.compscitech.2004.04.002.
[423] F. GOJNY, M. WICHMANN, B. FIEDLER, and K. SCHULTE, “Influence of different carbon nanotubes on the mechanical properties of epoxy matrix composites – A comparative study,” *Compos Sci Technol*, vol. 65, no. 15–16, pp. 2300–2313, Dec. 2005, doi: 10.1016/j.compscitech.2005.04.021.
[424] M. R. Ayatollahi, S. Shadlou, and M. M. Shokrieh, “Fracture toughness of epoxy/multi-walled carbon nanotube nano-composites under bending and shear loading conditions,” *Mater Des*, vol. 32, no. 4, pp. 2115–2124, Apr. 2011, doi: 10.1016/j.matdes.2010.11.034.
[425] M. R. Ayatollahi, S. Shadlou, and M. M. Shokrieh, “Mixed mode brittle fracture in epoxy/multi-walled carbon nanotube nanocomposites,” *Eng Fract Mech*, vol. 78, no. 14, pp. 2620–2632, Sep. 2011, doi: 10.1016/j.engfracmech.2011.06.021.
[426] X. Zhao, Q. Zhang, D. Chen, and P. Lu, “Enhanced Mechanical Properties of Graphene-Based Poly(vinyl alcohol) Composites,” *Macromolecules*, vol. 43, no. 5, pp. 2357–2363, Mar. 2010, doi: 10.1021/ma902862u.

[427] Y. Chen, S. Zhou, H. Yang, and L. Wu, “Structure and properties of polyurethane/nanosilica composites,” *J Appl Polym Sci*, vol. 95, no. 5, pp. 1032–1039, Mar. 2005, doi: 10.1002/app.21180.
[428] D. M. Panaitescu, Z. Vuluga, C. Radovici, and C. Nicolae, “Morphological investigation of PP/nanosilica composites containing SEBS,” *Polym Test*, vol. 31, no. 2, pp. 355–365, Apr. 2012, doi: 10.1016/j.polymertesting.2011.12.010.
[429] M. M. A. Nikje and Z. M. Tehrani, “Thermal and mechanical properties of polyurethane rigid foam/modified nanosilica composite,” *Polym Eng Sci*, vol. 50, no. 3, pp. 468–473, Mar. 2010, doi: 10.1002/pen.21559.
[430] H. M. Saleh, F. A. El-Saied, T. A. Salaheldin, and A. A. Hezo, “Influence of severe climatic variability on the structural, mechanical and chemical stability of cement kiln dust-slag-nanosilica composite used for radwaste solidification,” *Constr Build Mater*, vol. 218, pp. 556–567, Sep. 2019, doi: 10.1016/j.conbuildmat.2019.05.145.
[431] S. A. Awad and E. M. Khalaf, “Investigation of improvement of properties of polypropylene modified by nano silica composites,” *Composites Communications*, vol. 12, pp. 59–63, Apr. 2019, doi: 10.1016/j.coco.2018.12.008.
[432] I. A. Kinloch, J. Suhr, J. Lou, R. J. Young, and P. M. Ajayan, “Composites with carbon nanotubes and graphene: An outlook,” *Science (1979)*, vol. 362, no. 6414, pp. 547–553, Nov. 2018, doi: 10.1126/science.aat7439.
[433] N. Li *et al.*, “Electromagnetic Interference (EMI) Shielding of Single-Walled Carbon Nanotube Epoxy Composites,” *Nano Lett*, vol. 6, no. 6, pp. 1141–1145, Jun. 2006, doi: 10.1021/nl0602589.
[434] S. Su *et al.*, “Continuous method for grafting CNTs on the surface of carbon fibers based on cobalt catalyst assisted by thiourea,” *J Mater Sci*, vol. 54, no. 19, pp. 12498–12508, Oct. 2019, doi: 10.1007/s10853-019-03827-8.
[435] W. Li *et al.*, “Simultaneous enhancement of electrical conductivity and interlaminar shear strength of CF /EP composites through MWCNTs doped thermoplastic polyurethane film interleaves,” *J Appl Polym Sci*, vol. 136, no. 39, Oct. 2019, doi: 10.1002/app.47988.
[436] H. Qian, E. S. Greenhalgh, M. S. P. Shaffer, and A. Bismarck, “Carbon nanotube-based hierarchical composites: a review,” *J Mater Chem*, vol. 20, no. 23, p. 4751, 2010, doi: 10.1039/c000041h.
[437] D. Sheth, S. Maiti, S. Patel, J. Kandasamy, M. R. Chandan, and A. Rahaman, “Enhancement of mechanical properties of carbon fiber reinforced epoxy matrix laminated composites with multiwalled carbon nanotubes,” *Fullerenes, Nanotubes and Carbon Nanostructures*, vol. 29, no. 4, pp. 288–294, Apr. 2021, doi: 10.1080/1536383X.2020.1839424.
[438] L. Shen, L. Liu, Y. Zhou, and Z. Wu, “Thickness effect of carbon nanotube interleaves on free-edge delamination and ultimate strength within a symmetric composite laminate,” *Compos Part A Appl Sci Manuf*, vol. 132, p. 105828, May 2020, doi: 10.1016/j.compositesa.2020.105828.
[439] E. Kalfon-Cohen *et al.*, “Synergetic effects of thin plies and aligned carbon nanotube interlaminar reinforcement in composite laminates,” *Compos Sci Technol*, vol. 166, pp. 160–168, Sep. 2018, doi: 10.1016/j.compscitech.2018.01.007.
[440] P. R. Thakre *et al.*, “Investigation of the effect of single wall carbon nanotubes on interlaminar fracture toughness of woven carbon fiber—epoxy composites,” *J Compos Mater*, vol. 45, no. 10, pp. 1091–1107, May 2011, doi: 10.1177/0021998310389088.

[441] E. J. Garcia, B. L. Wardle, and A. John Hart, "Joining prepreg composite interfaces with aligned carbon nanotubes," *Compos Part A Appl Sci Manuf*, vol. 39, no. 6, pp. 1065–1070, Jun. 2008, doi: 10.1016/j.compositesa.2008.03.011.
[442] V. P. Veedu *et al.*, "Multifunctional composites using reinforced laminae with carbon-nanotube forests," *Nat Mater*, vol. 5, no. 6, pp. 457–462, Jun. 2006, doi: 10.1038/nmat1650.
[443] B. G. Falzon, S. C. Hawkins, C. P. Huynh, R. Radjef, and C. Brown, "An investigation of Mode I and Mode II fracture toughness enhancement using aligned carbon nanotubes forests at the crack interface," *Compos Struct*, vol. 106, pp. 65–73, Dec. 2013, doi: 10.1016/j.compstruct.2013.05.051.
[444] X. Ni, C. Furtado, N. K. Fritz, R. Kopp, P. P. Camanho, and B. L. Wardle, "Interlaminar to intralaminar mode I and II crack bifurcation due to aligned carbon nanotube reinforcement of aerospace-grade advanced composites," *Compos Sci Technol*, vol. 190, p. 108014, Apr. 2020, doi: 10.1016/j.compscitech.2020.108014.
[445] R. Islam Rubel, Md. Hasan Ali, Md. Abu Jafor, and Md. Mahmodul Alam, "Carbon nanotubes agglomeration in reinforced composites: A review," *AIMS Mater Sci*, vol. 6, no. 5, pp. 756–780, 2019, doi: 10.3934/matersci.2019.5.756.
[446] M. A. Maghsoudlou, R. Barbaz Isfahani, S. Saber-Samandari, and M. Sadighi, "Effect of interphase, curvature and agglomeration of SWCNTs on mechanical properties of polymer-based nanocomposites: Experimental and numerical investigations," *Compos B Eng*, vol. 175, p. 107119, Oct. 2019, doi: 10.1016/j.compositesb.2019.107119.
[447] S. K. Smart, W. C. Ren, H. M. Cheng, G. Q. Lu, and D. J. Martin, "Shortened double-walled carbon nanotubes by high-energy ball milling," *Int J Nanotechnol*, vol. 4, no. 5, p. 618, 2007, doi: 10.1504/IJNT.2007.014756.
[448] S. Simões, F. Viana, M. A. L. Reis, and M. F. Vieira, "Microstructural Characterization of Aluminum-Carbon Nanotube Nanocomposites Produced Using Different Dispersion Methods," *Microscopy and Microanalysis*, vol. 22, no. 3, pp. 725–732, Jun. 2016, doi: 10.1017/S143192761600057X.
[449] D.-L. Shi, X.-Q. Feng, Y. Y. Huang, K.-C. Hwang, and H. Gao, "The Effect of Nanotube Waviness and Agglomeration on the Elastic Property of Carbon Nanotube-Reinforced Composites," *J Eng Mater Technol*, vol. 126, no. 3, pp. 250–257, Jul. 2004, doi: 10.1115/1.1751182.
[450] A. R. Alian, S. El-Borgi, and S. A. Meguid, "Multiscale modeling of the effect of waviness and agglomeration of CNTs on the elastic properties of nanocomposites," *Comput Mater Sci*, vol. 117, pp. 195–204, May 2016, doi: 10.1016/j.commatsci.2016.01.029.
[451] E. J. García, "Characterization of composites with aligned carbon nanotubes (CNTs) as reinforcement," Massachusetts Institute of Technology, 2006.
[452] J. D. Beard, D. Rouholamin, B. L. Farmer, K. E. Evans, and O. R. Ghita, "Control and modelling of capillary flow of epoxy resin in aligned carbon nanotube forests," *RSC Adv*, vol. 5, no. 49, pp. 39433–39441, 2015, doi: 10.1039/C5RA03393D.
[453] B. L. Wardle, J. H. Anastasios, E. J. Garcia, and A. H. Slocum, "Nanostructure-reinforced composite articles and methods," 2012
[454] B. G. Falzon, S. C. Hawkins, C. P. Huynh, R. Radjef, and C. Brown, "An investigation of Mode I and Mode II fracture toughness enhancement using aligned carbon nanotubes

forests at the crack interface," *Compos Struct*, vol. 106, pp. 65–73, Dec. 2013, doi: 10.1016/j.compstruct.2013.05.051.
[455] N. Arora and N. N. Sharma, "Arc discharge synthesis of carbon nanotubes: Comprehensive review," *Diam Relat Mater*, vol. 50, pp. 135–150, Nov. 2014, doi: 10.1016/j.diamond.2014.10.001.
[456] P. Sharma, V. Pavelyev, S. Kumar, P. Mishra, S. S. Islam, and N. Tripathi, "Analysis on the synthesis of vertically aligned carbon nanotubes: growth mechanism and techniques," *Journal of Materials Science: Materials in Electronics*, vol. 31, no. 6, pp. 4399–4443, Mar. 2020, doi: 10.1007/s10854-020-03021-6.
[457] X. Cai, H. Cong, and C. Liu, "Synthesis of vertically-aligned carbon nanotubes without a catalyst by hydrogen arc discharge," *Carbon N Y*, vol. 50, no. 8, pp. 2726–2730, Jul. 2012, doi: 10.1016/j.carbon.2012.02.031.
[458] C. Bower, W. Zhu, S. Jin, and O. Zhou, "Plasma-induced alignment of carbon nanotubes," *Appl Phys Lett*, vol. 77, no. 6, pp. 830–832, Aug. 2000, doi: 10.1063/1.1306658.
[459] N. Arora and N. N. Sharma, "Arc discharge synthesis of carbon nanotubes: Comprehensive review," *Diam Relat Mater*, vol. 50, pp. 135–150, Nov. 2014, doi: 10.1016/j.diamond.2014.10.001.
[460] T. Okada, T. Kaneko, and R. Hatakeyama, "Conversion of toluene into carbon nanotubes using arc discharge plasmas in solution," *Thin Solid Films*, vol. 515, no. 9, pp. 4262–4265, Mar. 2007, doi: 10.1016/j.tsf.2006.02.067.
[461] J.-S. Su, "Direct Route to Grow CNTs by Micro-Electrodischarge Machining without Catalyst in Open Air," *Materials and Manufacturing Processes*, vol. 25, no. 12, pp. 1432–1436, Dec. 2010, doi: 10.1080/10426914.2010.500339.
[462] K. K. Kia and F. Bonabi, "Electric field induced needle-pulsed arc discharge carbon nanotube production apparatus: Circuitry and mechanical design," *Review of Scientific Instruments*, vol. 83, no. 12, Dec. 2012, doi: 10.1063/1.4772575.
[463] Y. Murooka, Y. Maede, M. Ozaki, and M. Hibino, "Self-assembling of hot carbon nanoparticles observed by short pulse-arc-discharge," *Chem Phys Lett*, vol. 341, no. 5–6, pp. 455–460, Jun. 2001, doi: 10.1016/S0009-2614(01)00493-6.
[464] Y. Y. Tsai, J. S. Su, and C. Y. Su, "A novel method to produce carbon nanotubes using EDM process," *Int J Mach Tools Manuf*, vol. 48, no. 15, pp. 1653–1657, Dec. 2008, doi: 10.1016/j.ijmachtools.2008.07.005.
[465] H. Zeng, L. Zhu, G. Hao, and R. Sheng, "Synthesis of various forms of carbon nanotubes by AC arc discharge," *Carbon N Y*, vol. 36, no. 3, pp. 259–261, 1998, doi: 10.1016/S0008-6223(97)00167-X.
[466] L. P. Biró *et al.*, "Continuous carbon nanotube production in underwater AC electric arc," *Chem Phys Lett*, vol. 372, no. 3–4, pp. 399–402, Apr. 2003, doi: 10.1016/S0009-2614(03)00417-2.
[467] H. H. Kim and H. J. Kim, "Preparation of carbon nanotubes by DC arc discharge process under reduced pressure in an air atmosphere," *Materials Science and Engineering: B*, vol. 133, no. 1–3, pp. 241–244, Aug. 2006, doi: 10.1016/j.mseb.2006.06.017.
[468] S. Scalese, V. Scuderi, S. Bagiante, S. Gibilisco, G. Faraci, and V. Privitera, "Order and disorder of carbon deposit produced by arc discharge in liquid nitrogen," *J Appl Phys*, vol. 108, no. 6, Sep. 2010, doi: 10.1063/1.3475726.
[469] D. He, T. Zhao, Y. Liu, J. Zhu, G. Yu, and L. Ge, "The effect of electric current on the synthesis of single-walled carbon nanotubes by temperature controlled arc discharge,"

Diam Relat Mater, vol. 16, no. 9, pp. 1722–1726, Sep. 2007, doi: 10.1016/j.diamond.2007.05.006.
[470] E. S. Choi *et al.*, "Enhancement of thermal and electrical properties of carbon nanotube polymer composites by magnetic field processing," *J Appl Phys*, vol. 94, no. 9, pp. 6034–6039, Nov. 2003, doi: 10.1063/1.1616638.
[471] X. Zhao, S. Inoue, M. Jinno, T. Suzuki, and Y. Ando, "Macroscopic oriented web of single-wall carbon nanotubes," *Chem Phys Lett*, vol. 373, no. 3–4, pp. 266–271, May 2003, doi: 10.1016/S0009-2614(03)00610-9.
[472] D. S. Tang *et al.*, "Evidence for an open-ended nanotube growth model in arc discharge," *Carbon N Y*, vol. 38, no. 3, pp. 480–483, 2000, doi: 10.1016/S0008-6223(99)00249-3.
[473] Y. Liu, S. Xiaolong, Z. Tingkai, Z. Jiewu, M. Hirscher, and F. Philipp, "Amorphous carbon nanotubes produced by a temperature controlled DC arc discharge," *Carbon N Y*, vol. 42, no. 8–9, pp. 1852–1855, 2004, doi: 10.1016/j.carbon.2004.01.069.
[474] Z. Shi *et al.*, "Large scale synthesis of single-wall carbon nanotubes by arc-discharge method," *Journal of Physics and Chemistry of Solids*, vol. 61, no. 7, pp. 1031–1036, Jul. 2000, doi: 10.1016/S0022-3697(99)00358-3.
[475] S. Farhat *et al.*, "Diameter control of single-walled carbon nanotubes using argon–helium mixture gases," *J Chem Phys*, vol. 115, no. 14, pp. 6752–6759, Oct. 2001, doi: 10.1063/1.1390526.
[476] S. Arepalli, "Laser Ablation Process for Single-Walled Carbon Nanotube Production," *J Nanosci Nanotechnol*, vol. 4, 2004.
[477] C. Scott, S. Arepalli, P. Nikolaev, and E. Al., "Growth mechanisms for single-wall carbon nanotubes in a laser-ablation process," *Appl Phys A*, vol. 72, pp. 573–580, 2001, doi: https://doi.org/10.1007/s003390100761.
[478] J. Chrzanowska *et al.*, "Synthesis of carbon nanotubes by the laser ablation method: Effect of laser wavelength," *physica status solidi (b)*, vol. 252, no. 8, pp. 1860–1867, 2015, doi: https://doi.org/10.1002/pssb.201451614.
[479] H. Zhang *et al.*, "The effect of laser power on the formation of carbon nanotubes prepared in CO2 continuous wave laser ablation at room temperature," *Physica B Condens Matter*, vol. 325, pp. 224–229, Jan. 2003, doi: 10.1016/S0921-4526(02)01528-4.
[480] J. Chrzanowska *et al.*, "Synthesis of carbon nanotubes by the laser ablation method: Effect of laser wavelength," *physica status solidi (b)*, vol. 252, no. 8, pp. 1860–1867, 2015, doi: https://doi.org/10.1002/pssb.201451614.
[481] M. Kumar, *Carbon Nanotube Synthesis and Growth Mechanism*. London: Intech Open, 2010.
[482] M. Kumar and Y. Ando, "Chemical Vapor Deposition of Carbon Nanotubes: A Review on Growth Mechanism and Mass Production," *J Nanosci Nanotechnol*, vol. 10, no. 6, pp. 3739–3758, Jun. 2010, doi: 10.1166/jnn.2010.2939.
[483] R. BAKER, "Nucleation and growth of carbon deposits from the nickel catalyzed decomposition of acetylene," *J Catal*, vol. 26, no. 1, pp. 51–62, Jul. 1972, doi: 10.1016/0021-9517(72)90032-2.
[484] S. Helveg *et al.*, "Atomic-scale imaging of carbon nanofibre growth," *Nature*, vol. 427, no. 6973, pp. 426–429, Jan. 2004, doi: 10.1038/nature02278.
[485] R. Rao, R. Sharma, F. Abild-Pedersen, J. K. Nørskov, and A. R. Harutyunyan, "Insights into carbon nanotube nucleation: Cap formation governed by catalyst interfacial step flow," *Sci Rep*, vol. 4, no. 1, p. 6510, Oct. 2014, doi: 10.1038/srep06510.

[486] M. Chhowalla *et al.*, "Growth process conditions of vertically aligned carbon nanotubes using plasma enhanced chemical vapor deposition," *J Appl Phys*, vol. 90, no. 10, pp. 5308–5317, Nov. 2001, doi: 10.1063/1.1410322.
[487] T. Yanase, T. Miura, T. Shiratori, M. Weng, T. Nagahama, and T. Shimada, "Synthesis of Carbon Nanotubes by Plasma-Enhanced Chemical Vapor Deposition Using Fe1−xMnxO Nanoparticles as Catalysts: How Does the Catalytic Activity of Graphitization Affect the Yields and Morphology?," *C (Basel)*, vol. 5, no. 3, p. 46, Aug. 2019, doi: 10.3390/c5030046.
[488] Z. Ghorannevis, T. Kato, T. Kaneko, and R. Hatakeyama, "Growth of Single-Walled Carbon Nanotubes from Nonmagnetic Catalysts by Plasma Chemical Vapor Deposition," *Jpn J Appl Phys*, vol. 49, no. 2S, p. 02BA01, Feb. 2010, doi: 10.1143/JJAP.49.02BA01.
[489] T. Kato and R. Hatakeyama, "Direct Growth of Short Single-Walled Carbon Nanotubes with Narrow-Chirality Distribution by Time-Programmed Plasma Chemical Vapor Deposition," *ACS Nano*, vol. 4, no. 12, pp. 7395–7400, Dec. 2010, doi: 10.1021/nn102379p.
[490] "Library," *MRS Bull*, vol. 30, no. 11, pp. 899–901, Nov. 2005, doi: 10.1557/mrs2005.242.
[491] E. C. Neyts, "PECVD growth of carbon nanotubes: From experiment to simulation," *Journal of Vacuum Science & Technology B, Nanotechnology and Microelectronics: Materials, Processing, Measurement, and Phenomena*, vol. 30, no. 3, May 2012, doi: 10.1116/1.3702806.
[492] S. Hofmann, C. Ducati, J. Robertson, and B. Kleinsorge, "Low-temperature growth of carbon nanotubes by plasma-enhanced chemical vapor deposition," *Appl Phys Lett*, vol. 83, no. 1, pp. 135–137, Jul. 2003, doi: 10.1063/1.1589187.
[493] M. Chhowalla *et al.*, "Growth process conditions of vertically aligned carbon nanotubes using plasma enhanced chemical vapor deposition," *J Appl Phys*, vol. 90, no. 10, pp. 5308–5317, Nov. 2001, doi: 10.1063/1.1410322.
[494] C. Bower, W. Zhu, S. Jin, and O. Zhou, "Plasma-induced alignment of carbon nanotubes," *Appl Phys Lett*, vol. 77, no. 6, pp. 830–832, Aug. 2000, doi: 10.1063/1.1306658.
[495] J.-M. Ting and K.-H. Liao, "Low-temperature, nonlinear rapid growth of aligned carbon nanotubes," *Chem Phys Lett*, vol. 396, no. 4–6, pp. 469–472, Oct. 2004, doi: 10.1016/j.cplett.2004.08.084.
[496] T. Kato, G.-H. Jeong, T. Hirata, R. Hatakeyama, K. Tohji, and K. Motomiya, "Single-walled carbon nanotubes produced by plasma-enhanced chemical vapor deposition," *Chem Phys Lett*, vol. 381, no. 3–4, pp. 422–426, Nov. 2003, doi: 10.1016/j.cplett.2003.10.007.
[497] T. Kato and R. Hatakeyama, "Formation of Freestanding Single-Walled Carbon Nanotubes by Plasma-Enhanced CVD," *Chemical Vapor Deposition*, vol. 12, no. 6, pp. 345–352, Jun. 2006, doi: 10.1002/cvde.200506451.
[498] R. Hatakeyama, T. Kaneko, T. Kato, and Y. F. Li, "Plasma-synthesized single-walled carbon nanotubes and their applications," *J Phys D Appl Phys*, vol. 44, no. 17, p. 174004, May 2011, doi: 10.1088/0022-3727/44/17/174004.
[499] Z. Ghorannevis, T. Kato, T. Kaneko, and R. Hatakeyama, "Narrow-Chirality Distributed Single-Walled Carbon Nanotube Growth from Nonmagnetic Catalyst," *J Am Chem Soc*, vol. 132, no. 28, pp. 9570–9572, Jul. 2010, doi: 10.1021/ja103362j.

[500] S. Huang, X. Du, M. Ma, and L. Xiong, “Recent progress in the synthesis and applications of vertically aligned carbon nanotube materials,” *Nanotechnol Rev*, vol. 10, no. 1, pp. 1592–1623, Oct. 2021, doi: 10.1515/ntrev-2021-0102.
[501] S. Trivedi and K. Alameh, “Effect of vertically aligned carbon nanotube density on the water flux and salt rejection in desalination membranes,” *Springerplus*, vol. 5, no. 1, p. 1158, Dec. 2016, doi: 10.1186/s40064-016-2783-3.
[502] P. Krishnakumar *et al.*, “Mass transport through vertically aligned large diameter MWCNTs embedded in parylene,” *Nanotechnology*, vol. 23, no. 45, p. 455101, Nov. 2012, doi: 10.1088/0957-4484/23/45/455101.
[503] S. Li, C. Zhou, S. Raju, and M. Chan, “Catalyst design for high-density and low-temperature CNT synthesis on conductive Ti silicide substrate,” *Diam Relat Mater*, vol. 75, pp. 39–43, May 2017, doi: 10.1016/j.diamond.2017.01.003.
[504] A. Krittayavathananon, P. Iamprasertkun, and M. Sawangphruk, “Enhancing the charge-storage performance of N -doped reduced graphene oxide aerogel supercapacitors by adsorption of the cationic electrolytes with single-stand deoxyribonucleic acid,” *Carbon N Y*, vol. 109, pp. 314–320, Nov. 2016, doi: 10.1016/j.carbon.2016.08.018.
[505] C. Querne, T. Vignal, M. Pinault, P. Banet, M. Mayne-L’Hermite, and P.-H. Aubert, “A comparative study of high density Vertically Aligned Carbon Nanotubes grown onto different grades of aluminum – Application to supercapacitors,” *J Power Sources*, vol. 553, p. 232258, Jan. 2023, doi: 10.1016/j.jpowsour.2022.232258.
[506] O. T. Gul, “A simple method to grow millimeters long vertically aligned carbon nanotube forests,” *Diam Relat Mater*, vol. 120, p. 108637, Dec. 2021, doi: 10.1016/j.diamond.2021.108637.
[507] J.-S. Chen, V. Stolojan, and S. R. P. Silva, “Towards type-selective carbon nanotube growth at low substrate temperature via photo-thermal chemical vapour deposition,” *Carbon N Y*, vol. 84, pp. 409–418, Apr. 2015, doi: 10.1016/j.carbon.2014.12.023.
[508] M. Kumar, “Carbon Nanotube Synthesis and Growth Mechanism,” in *Carbon Nanotubes - Synthesis, Characterization, Applications*, InTech, 2011. doi: 10.5772/19331.
[509] Q. N. Pham *et al.*, “Effect of growth temperature on the synthesis of carbon nanotube arrays and amorphous carbon for thermal applications,” *physica status solidi (a)*, vol. 214, no. 7, Jul. 2017, doi: 10.1002/pssa.201600852.
[510] J. Hansson *et al.*, “Effects of high temperature treatment of carbon nanotube arrays on graphite: increased crystallinity, anchoring and inter-tube bonding,” *Nanotechnology*, vol. 31, no. 45, p. 455708, Nov. 2020, doi: 10.1088/1361-6528/ab9677.
[511] W. Z. Li, J. G. Wen, and Z. F. Ren, “Effect of temperature on growth and structure of carbon nanotubes by chemical vapor deposition,” *Appl Phys A Mater Sci Process*, vol. 74, no. 3, pp. 397–402, Mar. 2002, doi: 10.1007/s003390201284.
[512] S. Huang, X. Du, M. Ma, and L. Xiong, “Recent progress in the synthesis and applications of vertically aligned carbon nanotube materials,” *Nanotechnol Rev*, vol. 10, no. 1, pp. 1592–1623, Oct. 2021, doi: 10.1515/ntrev-2021-0102.
[513] A. DUPUIS, “The catalyst in the CCVD of carbon nanotubes—a review,” *Prog Mater Sci*, vol. 50, no. 8, pp. 929–961, Nov. 2005, doi: 10.1016/j.pmatsci.2005.04.003.
[514] X. Zhao, C. Johnston, and P. S. Grant, “A novel hybrid supercapacitor with a carbon nanotube cathode and an iron oxide/carbon nanotube composite anode,” *J Mater Chem*, vol. 19, no. 46, p. 8755, 2009, doi: 10.1039/b909779a.

[515] V. SUBRAMANIAN, H. ZHU, and B. WEI, “Synthesis and electrochemical characterizations of amorphous manganese oxide and single walled carbon nanotube composites as supercapacitor electrode materials,” *Electrochem commun*, vol. 8, no. 5, pp. 827–832, May 2006, doi: 10.1016/j.elecom.2006.02.027.
[516] M. S. Chang, “An investigation on the dynamic behavior and thermal properties of MWCNTs/FRP laminate composites,” *Journal of Reinforced Plastics and Composites*, vol. 29, no. 24, 2010.
[517] J. Pan, L. M. Wang, S. Gu, Y. Li, and Q. Zhang, “Hybrid effect of carbon nanotube film and ultrathin carbon fiber prepreg composites,” *Journal of Reinforced Plastics and Composites*, vol. 36, no. 6, pp. 452–463, 2017, doi: https://doi.org/10.1177/0731684416684020.
[518] E. F. R. da Costa, A. A. Skordos, I. K. Partridge, and A. Rezai, “RTM processing and electrical performance of carbon nanotube modified epoxy/fibre composites,” *Composites Part A-Applied Science and Manufacturing*, vol. 43, no. 4, pp. 593–602, 2012, doi: DOI10.1016/j.compositesa.2011.12.019.
[519] S. V. Lomov and S. G. Abaimov, “Influence of the Nanostitch Sensor Embedment on the Fibrous Microstructure of Glass Fiber Prepreg Laminates,” *Polymers (Basel)*, vol. 14, no. 21, p. 4644, Oct. 2022, doi: 10.3390/polym14214644.
[520] R. Cross, B. A. Cola, T. Fisher, X. Xu, K. Gall, and S. Graham, “A metallization and bonding approach for high performance carbon nanotube thermal interface materials,” *Nanotechnology*, vol. 21, no. 44, p. 445705, Nov. 2010, doi: 10.1088/0957-4484/21/44/445705.
[521] M. H. Islam, S. Afroj, M. A. Uddin, D. V. Andreeva, K. S. Novoselov, and N. Karim, “Graphene and CNT-Based Smart Fiber-Reinforced Composites: A Review,” *Adv Funct Mater*, vol. 32, no. 40, Oct. 2022, doi: 10.1002/adfm.202205723.
[522] U.-H. Shin, D.-W. Jeong, S.-H. Kim, H. W. Lee, and J.-M. Kim, “Elastomer-Infiltrated Vertically Aligned Carbon Nanotube Film-Based Wavy-Configured Stretchable Conductors,” *ACS Appl Mater Interfaces*, vol. 6, no. 15, pp. 12909–12914, Aug. 2014, doi: 10.1021/am502851e.
[523] S. P. Mulvaney and C. D. Keating, “Raman Spectroscopy,” *Anal Chem*, vol. 72, no. 12, pp. 145–158, Jun. 2000, doi: 10.1021/a10000155.
[524] P. Puech *et al.*, “Similarities in the Raman RBM and D bands in double-wall carbon nanotubes,” *Phys Rev B*, vol. 72, no. 15, p. 155436, Oct. 2005, doi: 10.1103/PhysRevB.72.155436.
[525] M. Szybowicz, A. B. Nowicka, and A. Dychalska, “Characterization of Carbon Nanomaterials by Raman Spectroscopy,” in *Characterization of Nanomaterials*, Elsevier, 2018, pp. 1–36. doi: 10.1016/B978-0-08-101973-3.00001-8.
[526] L. Acauan, A. C. Dias, M. B. Pereira, F. Horowitz, and C. P. Bergmann, “Influence of Different Defects in Vertically Aligned Carbon Nanotubes on TiO 2 Nanoparticle Formation through Atomic Layer Deposition,” *ACS Appl Mater Interfaces*, vol. 8, no. 25, pp. 16444–16450, Jun. 2016, doi: 10.1021/acsami.6b04001.
[527] N. A. Asli *et al.*, “Mechanism of vertically arrays of carbon nanotubes by camphor based catalysed in-situ growth,” *Fullerenes, Nanotubes and Carbon Nanostructures*, vol. 30, no. 4, pp. 476–486, Apr. 2022, doi: 10.1080/1536383X.2021.1958317.

[528] D. Li and L. Pan, “Growth of carbon nanocoils using Fe–Sn–O catalyst film prepared by a spin-coating method,” *J Mater Res*, vol. 26, no. 16, pp. 2024–2032, Aug. 2011, doi: 10.1557/jmr.2011.227.
[529] A. Abdollahi, A. Abnavi, S. Ghasemi, S. Mohajerzadeh, and Z. Sanaee, “Flexible free-standing vertically aligned carbon nanotube on activated reduced graphene oxide paper as a high performance lithium ion battery anode and supercapacitor,” *Electrochim Acta*, vol. 320, p. 134598, Oct. 2019, doi: 10.1016/j.electacta.2019.134598.
[530] P. Landois *et al.*, “In situ time resolved wide angle X-ray diffraction study of nanotube carpet growth: Nature of catalyst particles and progressive nanotube alignment,” *Carbon N Y*, vol. 87, pp. 246–256, Jun. 2015, doi: 10.1016/j.carbon.2015.01.046.
[531] D. Ürk, F. Ç. Cebeci, M. L. Öveçoğlu, and H. Cebeci, “Structure-controlled growth of vertically-aligned carbon nanotube forests using iron–nickel bimetallic catalysts,” *Mater Adv*, vol. 2, no. 6, pp. 2021–2030, 2021, doi: 10.1039/D0MA00826E.
[532] M. R. M. Asyraf *et al.*, “Study on micro-patterning process of vertically aligned carbon nanotubes (VACNTs),” *Fullerenes, Nanotubes and Carbon Nanostructures*, vol. 24, no. 2, pp. 88–99, Feb. 2016, doi: 10.1080/1536383X.2015.1119126.
[533] S. Zhang, D. Peng, H. Xie, Q. Zheng, and Y. Zhang, “Investigation on the Formation Mechanism of Double-Layer Vertically Aligned Carbon Nanotube Arrays via Single-Step Chemical Vapour Deposition,” *Nanomicro Lett*, vol. 9, no. 1, p. 12, Jan. 2017, doi: 10.1007/s40820-016-0113-5.
[534] V. Svatoš, W. Sun, R. Kalousek, I. Gablech, J. Pekárek, and P. Neužil, “Single Measurement Determination of Mechanical, Electrical, and Surface Properties of a Single Carbon Nanotube via Force Microscopy,” *Sens Actuators A Phys*, vol. 271, pp. 217–222, Mar. 2018, doi: 10.1016/j.sna.2018.01.014.
[535] O. A. Ageev *et al.*, “Study of modification methods of probes for critical-dimension atomic-force microscopy by the deposition of carbon nanotubes,” *Semiconductors*, vol. 49, no. 13, pp. 1743–1748, Dec. 2015, doi: 10.1134/S1063782615130023.
[536] M. Lu, Y. Li, X. Zhang, C. Xu, Z. Dai, and L. Ding, “Performance evaluation of VACNT arrays under simulated LEO plasma environment,” *Vacuum*, vol. 216, p. 112486, Oct. 2023, doi: 10.1016/j.vacuum.2023.112486.
[537] A. Eitan, K. Jiang, D. Dukes, R. Andrews, and L. S. Schadler, “Surface Modification of Multiwalled Carbon Nanotubes: Toward the Tailoring of the Interface in Polymer Composites,” *Chemistry of Materials*, vol. 15, no. 16, pp. 3198–3201, Aug. 2003, doi: 10.1021/cm020975d.
[538] J. Lee, L. H. Acauan, E. Kalfon-Cohen, S. S. Kessler, and B. L. Wardle, “Hierarchical Nano- and Micro-engineered Interlaminar Reinforcement of Advanced Aerospace Grade Composites with Carbon Nanotube Arrays,” in *AIAA Scitech 2021 Forum*, Reston, Virginia: American Institute of Aeronautics and Astronautics, Jan. 2021. doi: 10.2514/6.2021-0443.
[539] L. Tong, A. P. Mouritz, and M. Bannister, *3D Fibre Reinforced Polymer Composites*. Elsevier, 2002.
[540] Y. A. Kim *et al.*, “Enhanced thermal conductivity of carbon fiber/phenolic resin composites by the introduction of carbon nanotubes,” *Appl Phys Lett*, vol. 90, no. 9, Feb. 2007, doi: 10.1063/1.2710778.

[541] Y. Song, B. Suberu, V. Shanov, and M. Schulz, “Multiscale Laminated Composite Materials,” in *Nanotube Superfiber Materials*, Elsevier, 2014, pp. 627–647. doi: 10.1016/B978-1-4557-7863-8.00022-0.
[542] A. Cao, P. L. Dickrell, W. G. Sawyer, M. N. Ghasemi-Nejhad, and P. M. Ajayan, “Super-Compressible Foamlike Carbon Nanotube Films,” *Science (1979)*, vol. 310, no. 5752, pp. 1307–1310, Nov. 2005, doi: 10.1126/science.1118957.
[543] J. E. Masters, “Improved Impact and Delamination Resistance through Interleafing,” *Key Eng Mater*, vol. 37, pp. 317–0, Jan. 1991, doi: 10.4028/www.scientific.net/KEM.37.317.
[544] A. T. Le, Q. Govignon, S. Rivallant, and T. Cutard, “Mode I and mode II fracture behavior in nano-engineered long fiber reinforced composites,” *Polym Compos*, vol. 44, no. 7, pp. 4016–4026, Jul. 2023, doi: 10.1002/pc.27374.
[545] M. Todo and P.-Y. B. Jar, “Study of mode-I interlaminar crack growth in DCB specimens of fibre-reinforced composites,” *Compos Sci Technol*, vol. 58, no. 1, pp. 105–118, Jan. 1998, doi: 10.1016/S0266-3538(97)00102-4.
[546] L. K. Jain, K. A. Dransfield, and Y.-W. Mai, “On the effects of stitching in CFRPs—II. Mode II delamination toughness,” *Compos Sci Technol*, vol. 58, no. 6, pp. 829–837, Jan. 1998, doi: 10.1016/S0266-3538(97)00186-3.
[547] I. K. Partridge and D. D. R. Cartié, “Delamination resistant laminates by Z-Fiber® pinning: Part I manufacture and fracture performance,” *Compos Part A Appl Sci Manuf*, vol. 36, no. 1, pp. 55–64, Jan. 2005, doi: 10.1016/j.compositesa.2004.06.029.
[548] T.-W. Chou, L. Gao, E. T. Thostenson, Z. Zhang, and J.-H. Byun, “An assessment of the science and technology of carbon nanotube-based fibers and composites,” *Compos Sci Technol*, vol. 70, no. 1, pp. 1–19, Jan. 2010, doi: 10.1016/j.compscitech.2009.10.004.
[549] Y. Dzenis, “Structural Nanocomposites,” *Science (1979)*, vol. 319, no. 5862, pp. 419–420, Jan. 2008, doi: 10.1126/science.1151434.
[550] S. S. Wicks, R. G. de Villoria, and B. L. Wardle, “Interlaminar and intralaminar reinforcement of composite laminates with aligned carbon nanotubes,” *Compos Sci Technol*, vol. 70, no. 1, pp. 20–28, Jan. 2010, doi: 10.1016/j.compscitech.2009.09.001.
[551] Y. Zeng, L. Ci, B. J. Carey, R. Vajtai, and P. M. Ajayan, “Design and Reinforcement: Vertically Aligned Carbon Nanotube-Based Sandwich Composites,” *ACS Nano*, vol. 4, no. 11, pp. 6798–6804, Nov. 2010, doi: 10.1021/nn101650p.
[552] R. J. Allen, O. Ghita, B. Farmer, M. Beard, and K. E. Evans, “Mechanical testing and modelling of a vertically aligned carbon nanotube composite structure,” *Compos Sci Technol*, vol. 77, pp. 1–7, Mar. 2013, doi: 10.1016/j.compscitech.2013.01.001.
[553] S. Shen, L. Yang, C. Wang, and L. Wei, “Effect of CNT orientation on the mechanical property and fracture mechanism of vertically aligned carbon nanotube/carbon composites,” *Ceram Int*, vol. 46, no. 4, pp. 4933–4938, Mar. 2020, doi: 10.1016/j.ceramint.2019.10.230.
[554] L. Miao *et al.*, “Anisotropic tensile mechanics of vertically aligned carbon nanotube reinforced silicon carbide ceramic nanocomposites,” *Carbon N Y*, vol. 199, pp. 241–248, Oct. 2022, doi: 10.1016/j.carbon.2022.07.049.
[555] A. Mikhalchan, T. Gspann, and A. Windle, “Aligned carbon nanotube–epoxy composites: the effect of nanotube organization on strength, stiffness, and toughness,” *J Mater Sci*, vol. 51, no. 22, pp. 10005–10025, Nov. 2016, doi: 10.1007/s10853-016-0228-6.

[556] T. H. Nam *et al.*, "Mechanical property enhancement of aligned multi-walled carbon nanotube sheets and composites through press-drawing process," *Advanced Composite Materials*, vol. 25, no. 1, pp. 73–86, Jan. 2016, doi: 10.1080/09243046.2014.985419.
[557] S. Jangam, S. Raja, and K. H. Reddy, "Effect of multiwalled carbon nanotube alignment on the tensile fatigue behavior of nanocomposites," *J Compos Mater*, vol. 52, no. 17, pp. 2365–2374, Jul. 2018, doi: 10.1177/0021998317745585.
[558] K. Aly, A. Li, and P. D. Bradford, "In-situ monitoring of woven glass fiber reinforced composites under flexural loading through embedded aligned carbon nanotube sheets," *J Compos Mater*, vol. 52, no. 20, pp. 2777–2788, Aug. 2018, doi: 10.1177/0021998317754128.
[559] K. Kim, P. R. Mantena, S. S. Daryadel, V. M. Boddu, M. W. Brenner, and J. S. Patel, "Dynamic Mechanical Analysis and High Strain-Rate Energy Absorption Characteristics of Vertically Aligned Carbon Nanotube Reinforced Woven Fiber-Glass Composites," *J Nanomater*, vol. 2015, pp. 1–7, 2015, doi: 10.1155/2015/480549.
[560] R. MANTENA, B. PRAMANIK, T. TADEPALLI, V. BODDU, M. BRENNER, and A. KUMAR, "Effect of Process Parameters on the Dynamic Modulus, Damping and Energy Absorption of Vertically Aligned Carbon Nano-Tube (VACNT) Forest Structures," *Journal of Multifunctional Composites*, vol. 2, no. 2, pp. 93–100, 2015, doi: 10.12783/issn.2168-4286/2.2/Mantena.
[561] S. Chen, Y. Feng, M. Qin, T. Ji, and W. Feng, "Improving thermal conductivity in the through-thickness direction of carbon fibre/SiC composites by growing vertically aligned carbon nanotubes," *Carbon N Y*, vol. 116, pp. 84–93, May 2017, doi: 10.1016/j.carbon.2017.01.103.
[562] T. Ji *et al.*, "Thermal conductive and flexible silastic composite based on a hierarchical framework of aligned carbon fibers-carbon nanotubes," *Carbon N Y*, vol. 131, pp. 149–159, May 2018, doi: 10.1016/j.carbon.2018.02.002.
[563] Q. M. Zou *et al.*, "Thermally Stable and Electrically Conductive, Vertically Aligned Carbon Nanotube/Silicon Infiltrated Composite Structures for High-Temperature Electrodes," *ACS Appl Mater Interfaces*, vol. 9, no. 42, pp. 37340–37349, Oct. 2017, doi: 10.1021/acsami.7b12087.
[564] Y. Cai, H. Yu, C. Chen, Y. Feng, M. Qin, and W. Feng, "Improved thermal conductivities of vertically aligned carbon nanotube arrays using three-dimensional carbon nanotube networks," *Carbon N Y*, vol. 196, pp. 902–912, Aug. 2022, doi: 10.1016/j.carbon.2022.05.050.
[565] Q. Zhang, B. A. Calderon, C. R. Ebbing, L. J. Elston, L. W. Byrd, and B.-H. Tsao, "Thermal Properties Enhancement of Vertically Aligned Carbon Nanotubes-Based Metal Nanocomposites as Thermal Interface Materials," *Front Mater*, vol. 7, Oct. 2020, doi: 10.3389/fmats.2020.572956.
[566] M. Wang *et al.*, "Enhancing Thermal Conductive Performance of Vertically Aligned Carbon Nanotube Array Composite by Pre-Annealing Treatment," *J Nanosci Nanotechnol*, vol. 15, no. 4, pp. 3212–3217, Apr. 2015, doi: 10.1166/jnn.2015.9675.
[567] M. Wang *et al.*, "Crack-Free and Scalable Transfer of Carbon Nanotube Arrays into Flexible and Highly Thermal Conductive Composite Film," *ACS Appl Mater Interfaces*, vol. 6, no. 1, pp. 539–544, Jan. 2014, doi: 10.1021/am404594m.
[568] O. Yildiz, M. M. Lubna, V. P. Ramesh, M. Ozturk, and P. D. Bradford, "Microporous vertically aligned CNT nanocomposites with tunable properties for use in flexible heat

sinks," *Journal of Science: Advanced Materials and Devices*, vol. 7, no. 4, p. 100509, Dec. 2022, doi: 10.1016/j.jsamd.2022.100509.
[569] L. Ping, P.-X. Hou, C. Liu, and H.-M. Cheng, "Vertically aligned carbon nanotube arrays as a thermal interface material," *APL Mater*, vol. 7, no. 2, Feb. 2019, doi: 10.1063/1.5083868.
[570] Y.-J. Kwon, J.-B. Park, Y.-P. Jeon, J.-Y. Hong, H.-S. Park, and J.-U. Lee, "A Review of Polymer Composites Based on Carbon Fillers for Thermal Management Applications: Design, Preparation, and Properties," *Polymers (Basel)*, vol. 13, no. 8, p. 1312, Apr. 2021, doi: 10.3390/polym13081312.
[571] M. Saghafi, F. Mahboubi, S. Mohajerzadeh, and R. Holze, "Preparation of Co-Ni Oxide/Vertically Aligned Carbon Nanotube and Their Electrochemical Performance in Supercapacitors," *Materials and Manufacturing Processes*, vol. 30, no. 1, pp. 70–78, Jan. 2015, doi: 10.1080/10426914.2014.952026.
[572] H. Wang *et al.*, "Development of stretchable membrane based nanofilters using patterned arrays of vertically grown carbon nanotubes," *Nanoscale*, vol. 5, no. 18, p. 8488, 2013, doi: 10.1039/c3nr02742b.
[573] B. J. Lyon, A. I. Aria, and M. Gharib, "Fabrication of carbon nanotube—polyimide composite hollow microneedles for transdermal drug delivery," *Biomed Microdevices*, vol. 16, no. 6, pp. 879–886, Dec. 2014, doi: 10.1007/s10544-014-9892-y.
[574] M. Abdolahad, S. Mohajerzadeh, M. Janmaleki, H. Taghinejad, and M. Taghinejad, "Evaluation of the shear force of single cancer cells by vertically aligned carbon nanotubes suitable for metastasis diagnosis," *Integrative Biology*, vol. 5, no. 3, pp. 535–542, Mar. 2013, doi: 10.1039/c2ib20215h.
[575] S. J. Paul, I. Elizabeth, and B. K. Gupta, "Ultrasensitive Wearable Strain Sensors based on a VACNT/PDMS Thin Film for a Wide Range of Human Motion Monitoring," *ACS Appl Mater Interfaces*, vol. 13, no. 7, pp. 8871–8879, Feb. 2021, doi: 10.1021/acsami.1c00946.
[576] D. P. Linklater *et al.*, "High Aspect Ratio Nanostructures Kill Bacteria via Storage and Release of Mechanical Energy," *ACS Nano*, vol. 12, no. 7, pp. 6657–6667, Jul. 2018, doi: 10.1021/acsnano.8b01665.
[577] I. Malek, C. F. Schaber, T. Heinlein, J. J. Schneider, S. N. Gorb, and R. A. Schmitz, "Vertically aligned multi walled carbon nanotubes prevent biofilm formation of medically relevant bacteria," *J Mater Chem B*, vol. 4, no. 31, pp. 5228–5235, 2016, doi: 10.1039/C6TB00942E.
[578] A. Pantano, D. M. Parks, and M. C. Boyce, "Mechanics of deformation of single- and multi-wall carbon nanotubes," *J Mech Phys Solids*, vol. 52, no. 4, pp. 789–821, Apr. 2004, doi: 10.1016/j.jmps.2003.08.004.
[579] Y. Yang, M. Li, and Z. Zhu, "A novel electrochemical sensor based on carbon nanotubes array for selective detection of dopamine or uric acid," *Talanta*, vol. 201, pp. 295–300, Aug. 2019, doi: 10.1016/j.talanta.2019.03.096.
[580] H. Sugime, T. Ushiyama, K. Nishimura, Y. Ohno, and S. Noda, "An interdigitated electrode with dense carbon nanotube forests on conductive supports for electrochemical biosensors," *Analyst*, vol. 143, no. 15, pp. 3635–3642, 2018, doi: 10.1039/C8AN00528A.
[581] H. Fayazfar, A. Afshar, M. Dolati, and A. Dolati, "DNA impedance biosensor for detection of cancer, TP53 gene mutation, based on gold nanoparticles/aligned carbon nanotubes modified electrode," *Anal Chim Acta*, vol. 836, pp. 34–44, Jul. 2014, doi: 10.1016/j.aca.2014.05.029.

[582] S. Roy, H. Vedala, and W. Choi, “Vertically aligned carbon nanotube probes for monitoring blood cholesterol,” *Nanotechnology*, vol. 17, no. 4, pp. S14–S18, Feb. 2006, doi: 10.1088/0957-4484/17/4/003.
[583] L. Deng, G. Lai, L. Fu, C.-T. Lin, and A. Yu, “Enzymatic deposition of gold nanoparticles at vertically aligned carbon nanotubes for electrochemical stripping analysis and ultrasensitive immunosensing of carcinoembryonic antigen,” *Analyst*, vol. 145, no. 8, pp. 3073–3080, 2020, doi: 10.1039/C9AN02633A.
[584] X. Yu, S. N. Kim, F. Papadimitrakopoulos, and J. F. Rusling, “Protein immunosensor using single-wall carbon nanotube forests with electrochemical detection of enzyme labels,” *Mol Biosyst*, vol. 1, no. 1, p. 70, 2005, doi: 10.1039/b502124c.
[585] A. Wisitsoraat, C. Karuwan, K. Wong-ek, D. Phokharatkul, P. Sritongkham, and A. Tuantranont, “High Sensitivity Electrochemical Cholesterol Sensor Utilizing a Vertically Aligned Carbon Nanotube Electrode with Electropolymerized Enzyme Immobilization,” *Sensors*, vol. 9, no. 11, pp. 8658–8668, Oct. 2009, doi: 10.3390/s91108658.
[586] S. R. Shin *et al.*, “Aligned Carbon Nanotube–Based Flexible Gel Substrates for Engineering Biohybrid Tissue Actuators,” *Adv Funct Mater*, vol. 25, no. 28, pp. 4486–4495, Jul. 2015, doi: 10.1002/adfm.201501379.
[587] X. Gong, J. Liu, S. Baskaran, R. D. Voise, and J. S. Young, “Surfactant-Assisted Processing of Carbon Nanotube/Polymer Composites,” *Chemistry of Materials*, vol. 12, no. 4, pp. 1049–1052, Apr. 2000, doi: 10.1021/cm9906396.
[588] C. Velasco-Santos, A. L. Martínez-Hernández, F. T. Fisher, R. Ruoff, and V. M. Castaño, “Improvement of Thermal and Mechanical Properties of Carbon Nanotube Composites through Chemical Functionalization,” *Chemistry of Materials*, vol. 15, no. 23, pp. 4470–4475, Nov. 2003, doi: 10.1021/cm034243c.
[589] M. Cadek, J. N. Coleman, V. Barron, K. Hedicke, and W. J. Blau, “Morphological and mechanical properties of carbon-nanotube-reinforced semicrystalline and amorphous polymer composites,” *Appl Phys Lett*, vol. 81, no. 27, pp. 5123–5125, Dec. 2002, doi: 10.1063/1.1533118.
[590] T. Kashiwagi, E. Grulke, J. Hilding, R. Harris, W. Awad, and J. Douglas, “Thermal degradation and flammability properties of poly(propylene)/carbon nanotube composites,” *Macromol Rapid Commun*, vol. 23, no. 13, 2002, doi: https://doi.org/10.1002/1521-3927(20020901)23:13%3C761::AID-MARC761%3E3.0.CO;2-K.
[591] M. J. Biercuk, M. C. Llaguno, M. Radosavljevic, J. K. Hyun, A. T. Johnson, and J. E. Fischer, “Carbon nanotube composites for thermal management,” *Appl Phys Lett*, vol. 80, no. 15, pp. 2767–2769, Apr. 2002, doi: 10.1063/1.1469696.
[592] E. S. Choi *et al.*, “Enhancement of thermal and electrical properties of carbon nanotube polymer composites by magnetic field processing,” *J Appl Phys*, vol. 94, no. 9, pp. 6034–6039, Nov. 2003, doi: 10.1063/1.1616638.

Vita

Zackery Nieto started his educational path at The University of Texas at El Paso, where he attained his Bachelor's and Master's degree in Mechanical Engineering. During his undergraduate years, he began his research path working on statistical representation and machine learning with the Army Research Lab.

While pursuing his Master's and Doctoral degree, his research studies shifted to composite structures as a research assistant under Dr. Alejandra Castellanos. During his time under Dr. Castellanos he attended several conferences for the American Society of Composites where he presented his research each year and participated with her for three Air Force Summer Faculty Fellowship Programs.

His research interests focused on enhancing composite structure technologies from the manufacturing stage, to experimentation, and computational modeling.

Contact Information : Zackery.Nieto@gmail.com